

**GROWING AND MOVING
PLANETS IN DISKS**

GROWING AND MOVING PLANETS IN DISKS

Proefschrift

ter verkrijging van
de graad van Doctor aan de Universiteit Leiden,
op gezag van de Rector Magnificus Dr. D.D. Breimer,
hoogleraar in de faculteit der Wiskunde en
Natuurwetenschappen en die der Geneeskunde,
volgens besluit van het College voor Promoties
te verdedigen op donderdag 28 september 2006
te klokke 16.15 uur

door

Sijme-Jan Paardekooper

geboren te Alphen aan den Rijn in 1979

Promotiecommissie

Promotor: Prof. dr. V. Icke

Co-promotor: Dr. G. Mellema (Stockholm University)

Referent: Prof. dr. W. Kley (Universität Tübingen)

Overige leden: Prof. dr. E.F. van Dishoeck
Dr. C. Dominik (Universiteit van Amsterdam)
Dr. C. P. Dullemond (MPIA, Heidelberg)
Prof. dr. C. Keller (Universiteit Utrecht)
Dr. H. Klahr (MPIA, Heidelberg)
Dr. Y. Levin

Tell me: did Venus blow your mind?

TRAIN

Contents

1	Introduction	1
1.1	The Solar system	2
1.1.1	The role of whole numbers	2
1.1.2	Resonances	2
1.1.3	Structure	3
1.2	Planet formation	4
1.3	Extrasolar planets	5
1.4	Planet-disk interaction	5
1.5	Open questions	10
1.6	Numerical hydrodynamics	12
1.7	This thesis	14
1.7.1	Chapter 2	14
1.7.2	Chapter 3	14
1.7.3	Chapter 4	15
1.7.4	Chapter 5	15
1.7.5	Chapter 6	15
1.7.6	Chapter 7	16
1.7.7	Chapter 8	16
1.7.8	Main results	16
1.8	Outlook	17
2	RODEO: a new method for planet-disk interaction	21
2.1	Introduction	22
2.2	Physical Model	23
2.2.1	Basic equations	23
2.2.2	Equation of state	25
2.2.3	Viscosity	25
2.3	Numerical Method	26
2.3.1	Roe solver	27
2.3.2	Stationary Extrapolation	29
2.3.3	Adaptive Mesh Refinement	32
2.3.4	Accretion	33
2.4	Test Problems	33
2.4.1	Viscous ring spreading	34

2.5	Model design	34
2.5.1	Initial Conditions	35
2.5.2	Boundary conditions	35
2.6	Gap Formation	36
2.6.1	Source term integration	38
2.6.2	Flux limiter	40
2.7	Accretion rates	41
2.7.1	High mass planet	42
2.7.2	Low mass planet	45
2.7.3	Intermediate mass planet	46
2.7.4	Dependence on planetary mass	48
2.8	Migration	50
2.8.1	Numerical Parameters	50
2.8.2	Dependence on planetary mass	52
2.9	Summary and conclusions	53
2.A	Explicit expressions	54
2.A.1	Radial direction	54
2.A.2	Azimuthal direction	55
3	Gap opening by planets in inviscid disks	57
3.1	Introduction	58
3.2	Gap formation theory	59
3.2.1	Conditions for gap formation	59
3.2.2	Gap width	60
3.2.3	Time scale	61
3.3	Numerical method	62
3.3.1	Flux limiter	62
3.3.2	Potential smoothing	62
3.3.3	Model set-up	63
3.4	Results	64
3.4.1	Damping length	65
3.4.2	Angular momentum flux	67
3.4.3	Vortensity evolution	73
3.4.4	Time scales	77
3.4.5	Gap structure	81
3.5	Discussion	84
3.6	Summary and conclusion	86
3.A	Shock formation in isothermal disks	86
4	Orbital evolution of embedded planets	91
4.1	Introduction	92
4.2	Physical Model	94
4.2.1	Disk Model	94
4.2.2	Coordinate frame	94
4.3	Numerical Method	96

4.3.1	Roe Solver	97
4.3.2	Source Terms	97
4.3.3	Test	97
4.4	Results	98
4.4.1	Type I migration	98
4.4.2	Eccentricity damping for low-mass planets	101
4.4.3	A planet of $5 M_J$	106
4.4.4	A planet of $1 M_J$	109
4.4.5	A planet of $0.1 M_J$	115
4.5	Discussion	117
4.6	Summary and conclusion	118
5	Growing and moving low-mass planets in non-isothermal disks	121
5.1	Introduction	122
5.2	Cooling properties	124
5.3	Radiative effects	126
5.4	Convection	126
5.5	Model design	127
5.5.1	Central Star	127
5.5.2	Planet	127
5.5.3	Disk	128
5.6	Numerical method	131
5.6.1	Hydrodynamics	131
5.6.2	Flux-limited diffusion	132
5.6.3	Boundary conditions	135
5.6.4	Test problems	136
5.7	Results	138
5.7.1	Isothermal models	139
5.7.2	Near-Isothermal models	143
5.7.3	Radiation-Hydrodynamical models	149
5.7.4	Local, adiabatic models	157
5.8	Discussion	160
5.9	Summary and Conclusions	163
6	Planets opening dust gaps in gas disks	167
6.1	Introduction	168
6.2	Basic equations	169
6.2.1	Gas	169
6.2.2	Dust	170
6.2.3	Gas-dust interaction	171
6.3	Numerical method	173
6.3.1	Gas and dust advection	173
6.3.2	Accretion	174
6.3.3	Source terms	175
6.3.4	Test problem	175

6.3.5	Limits	176
6.4	Initial and boundary conditions	178
6.5	Results	178
6.5.1	Axisymmetric disk	178
6.5.2	Dust response to a spiral wave	179
6.5.3	Global disk evolution	180
6.5.4	Dependence on particle size	182
6.5.5	Dependence on planetary mass	184
6.5.6	Flow within the Roche lobe	186
6.5.7	Gas and dust accretion	187
6.5.8	Simulated observations	189
6.6	Discussion	190
6.7	Summary and conclusions	191
7	Dust accretion onto high-mass planets	195
7.1	Introduction	196
7.2	Equations of motion	198
7.2.1	Gas	198
7.2.2	Dust Particles	198
7.2.3	Drag Force	199
7.3	Numerical method	200
7.3.1	Gas	200
7.3.2	Dust	200
7.4	Initial and Boundary Conditions	203
7.5	Results	204
7.5.1	Perfect coupling	204
7.5.2	No coupling	206
7.5.3	Steady gas disk	209
7.5.4	Evolving gas disk	215
7.6	Discussion	221
7.7	Summary and conclusion	223
8	Planetary signatures in transitional circumstellar disks	227
8.1	Introduction	228
8.2	Physical background	231
8.2.1	Coupling of gas and dust	231
8.2.2	Protoplanetary disks	232
8.2.3	Debris disks	233
8.2.4	Transitional disks	233
8.3	Numerical method	234
8.3.1	Initial and boundary conditions	235
8.4	Results	236
8.4.1	Streaming instabilities	236
8.4.2	Planetary gaps	240
8.4.3	Radiation pressure	243

8.5 Discussion	248
8.6 Summary and conclusions	249
Bibliography	251
Nederlandse Samenvatting	253
Curriculum Vitae	265
Nawoord	267

CHAPTER 1

Introduction

IN this Chapter we introduce the basic concepts of planet formation theory, and in particular planet-disk interaction. We go through all mutual interactions, and discuss those parts of the theory that are not understood very well yet. We then give a short introduction to numerical hydrodynamics, because that is our preferred modeling technique for studying disk-planet interaction. We end this Chapter by giving an overview of the contents of this thesis.

1.1 THE SOLAR SYSTEM

We start this Chapter by reviewing some basic properties of our own Solar system. Until the discovery of the first extrasolar planet (Wolszczan & Frail 1992), planet formation theory was mainly aimed at understanding the small piece of the universe that we call the Solar system. With hindsight, we can state that this small piece has severely biased our view on planet formation.

1.1.1 The role of whole numbers

As early as in early Greece attempts were made to perceive order in the distribution of bodies in the Solar system. It was Anaximander of Miletus (611-547 B.C.) who postulated that the relative distances of the stars, the Moon and the Sun from the Earth were in the ratio 1:2:3 (see Bernal 1969). The belief in the importance of whole numbers by the Pythagorean school has influenced the work of Plato and Kepler to a great extent. Indeed, Kepler's views on the orbits of the planets had strong foundations in numerology, rather than science (Field 1988).

One of the most persistent misunderstandings regarding simple "laws" for the distributions of objects in the Solar system is the Titius-Bode law, which states that the distances d of the planets to the Sun are given by

$$d = 0.4 + 0.3 \cdot 2^i, \quad (1.1)$$

where $i = -\infty, 0, 1, 2, 4, 5, \dots$. The lack of physical basis of this "law" is often neglected because the fit is remarkably good, especially for the innermost planets. However, the question arises why not every value of i is filled. Sometimes the minor body Ceres is said to fill the $i = 3$ spot, but in addition, the Titius-Bode law would predict an infinite number of planets between Mercury and Venus! The most definitive proof that this law is mostly a coincidence is the fact that almost *any* distribution of planets generates its own Titius-Bode law (Murray & Dermott 2000).

1.1.2 Resonances

There are certain numerical relationships between various bodies in the Solar system that do have physical significance, however. They involve so-called *resonances*, and because they play an important role throughout this thesis we give a brief introduction here.

In general, resonances occur when there exists a simple numerical relationship between two frequencies. For example, the spin frequency of the Moon matches exactly its orbital frequency, so that the Moon always shows the same side to us on Earth. The Moon is said to be in a 1:1 spin-orbit resonance. It turns out that most natural satellites in the Solar system are in such a synchronous spin-orbit resonance. Mercury, on the other hand, is in a 3:2 spin-orbit resonance with the Sun.

Another kind of resonance can occur between the orbits of two different bodies. It turns out that Jupiter and Saturn are in a near 5:2 orbit-orbit resonance, while Neptune and Pluto are in a 3:2 resonance with each other. This means that in the time that Neptune orbits the Sun *three* times, Pluto will complete exactly *two* orbits. Such resonances are common in the Solar system, and this may even have some statistical significance (Murray & Dermott 2000). These orbit-orbit resonances also play a major role in planet-disk interaction (see Sect. 1.4).

1.1.3 Structure

The structure of the Solar system appears to be rather simple. Starting from the Sun, and moving outwards, we first find the four terrestrial planets: Mercury, Venus, Earth and Mars. They differ in mass, size and density, but they have in common that they have not succeeded in capturing a massive gaseous envelope. Typically, a core mass of a few Earth masses (M_{\oplus}) is needed to achieve this, depending on the local temperature. The boundary of the terrestrial zone is marked by the asteroid belt between Mars and Jupiter.

Outside the terrestrial region we find a whole different class of planets: the gas giants, of which Jupiter is the most impressive, in mass and in size. It is believed that the giants are built around solid cores of a few M_{\oplus} , but the exact value for example for Jupiter is highly uncertain due to uncertainties in the equation of state at the high pressures found near the center of the planet (Guillot 1999). It is even possible that Jupiter has no solid core at all.

The region of the giant planets stretches from 5 AU (the location of Jupiter) to 30 AU, where Neptune resides. In between we find Saturn and Uranus. We can further subdivide the giant planets in ordinary giants (Jupiter and Saturn) and Ice Giants (Uranus and Neptune), but in the rest of this thesis we only talk about "giants" in general.

Beyond the realm of the giant planets there is a belt of ice dwarfs, referred to as the Kuiper Belt. It is a matter of definition whether Pluto is the ninth planet or just a very large Kuiper Belt Object. We shall adopt the latter in this thesis, for two reasons. The first is that it nicely fits in the structure of the Solar system as discussed above: terrestrial planets, gas giants, Kuiper Belt, from the inside out. Second, Pluto does fit in the orbital structure of the Kuiper Belt: there is even a class of Kuiper Belt Object called the Plutino's, consisting of bodies in the same 3:2 orbital resonance with Neptune as Pluto.

For the contents of this thesis, we do not need to go further out into the Solar system than the Kuiper Belt. For the sake of completeness, we mention the Oort cloud: a huge spherical cloud of long-period comets with a radius of roughly 10000 AU. Passing stars occasionally stir up the bodies within the cloud, which may lead to a comet passing through the inner Solar system.

1.2 PLANET FORMATION

It has been suspected from approximately two centuries before the discovery of the first extrasolar planet that planets form in disks around young stars (Laplace 1796). The basis for this hypothesis is the observation that all the planets in the Solar system are confined into a single plane, which we call the ecliptic. Now, we have direct observations confirming the existence of disks around young stars (Beckwith & Sargent 1996).

Within these protoplanetary disks, interstellar dust grains, initially of sub-micron size, grow by binary collisions. As long as the relative velocities of two particles are not too high (of order 1 m s^{-1}) the intermolecular forces between the dust grains are large enough to stick the particles together upon collision. When particles become ever larger, molecular forces become less dominant until eventually gravity takes over for boulders of km-size. In between the two regimes, it is very hard to grow dust particles by collisions, because neither the molecular forces nor gravity may be strong enough to bind the particles together. One possible way around this is to invoke a gravitational instability of a thin, dense dust layer in the midplane of the disk (Goldreich & Ward 1973). However, such a thin dust layer embedded in a gas disk is subject to Kelvin-Helmholtz instabilities which may prevent the dust layer from reaching a gravitationally unstable state. The importance of this mechanism is still subject of debate (e.g. Youdin & Shu 2002; Garaud & Lin 2004; Yamoto & Sekiya 2004). For an overview of the physics of dust growth in disks, see Dominik et al. (2006).

The planetesimals formed by dust coagulation eventually merge into a few large bodies, which either become terrestrial planets, or, if they are massive enough, can capture a dense atmosphere that is comparable in mass or even much more massive than the solid core. This is how gas giant planets form in the so-called core-accretion model of planet formation (Pollack et al. 1996). An alternative model, originally proposed by Kuiper (1951), was recently revived by Boss (1997). This model relies on a gravitationally unstable gas disk, that will fragment directly into gas giant planets. It has the advantage that it is extremely fast compared to the core-accretion model, in which the build-up of the solid core takes approximately one million years, which is uncomfortably close to the total life time of the disk. In the disk instability scenario, giant planets form within a few thousand years. However, there are also two important problems with this models. First of all, disk fragmentation depends sensitively on the cooling properties of the disk (Pickett et al. 2003; Mejía et al. 2005). In disks with realistic cooling, fragmentation may well be prevented. Second, the fragments that are seen in numerical simulations are much more massive than the majority of the extrasolar giant planets found thus far; the objects that are produced by fragmentation are in the brown dwarf mass regime. Although the issue is not settled yet, currently the core-accretion scenario is the most widely adopted gas giant planet formation scenario.

Both scenarios for giant planet formation predict that they form in the outer parts of the disk (beyond approximately 5 AU): only there the temperatures are low enough for the disk to become unstable, and beyond the snow line, where water exists in solid form, accumulation of a large solid core is much faster due to ice coatings on the dust grains. It is therefore not surprising that the giant planets in our Solar system are found

further away from the Sun than the terrestrial planets. Planet formation theory thus predicted that this should be the case also for extrasolar planetary systems.

1.3 EXTRASOLAR PLANETS

Extrasolar planets have been anticipated long before their discovery. Even in ancient Greece, atomism of Leucippus and Democritus predicted other “worlds”, which would form in a rotating, turbulent nebula. Some of these worlds would have no moon, others would form with multiple suns, etc. It is remarkable how similar the newest concepts in extrasolar planet formation are to these ancient ideas (see also Dick 1982; Artymowicz 2004).

The Copernican principle states that we are not “special” observers, and it was this principle that formed the basis for our expectations of the structure and formation of extrasolar planetary systems. Planet formation theory had been aimed at explaining our Solar system since Laplace (1796), and in spite of the success of this “standard model” for planet formation, the scientific community was in for a big surprise when the first extrasolar planet around a main-sequence star was discovered (Mayor & Queloz 1995).

This first extrasolar Jupiter was found to reside on a very close orbit (well inside the orbit of Mercury, at a distance of 0.05 AU) around the star 51 Pegasi. The mass of the companion indicates that it is indeed a gas giant planet, but how could it have been formed where it is now? We have seen in the previous section that giant planets form in the cool outer parts of the protoplanetary disk, and certainly not in the hot environment close to the star. An entire class of such close-in giant planets was found, which were subsequently named Hot Jupiters.

The second major surprise was the high mean eccentricity of the orbits of these giant planets. In our own Solar system, $e < 0.06$, while $\bar{e} = 0.33$ for extrasolar giants. How did these eccentricities arise? The most obvious candidate is the interaction with another giant planet in the system. However, several of the extrasolar planets on eccentric orbits are not found to be interacting with other bodies. Moreover, numerical simulations reveal that when planets interact gravitationally with each other, mergers are a common phenomenon (Ford et al. 2001). The result of such a merging event is a single planet on a low-eccentricity orbit, and there are many fewer of these planets found than predicted by this scenario. For more arguments against planet-planet interactions see Goldreich & Sari (2003).

1.4 PLANET-DISK INTERACTION

The problem of the small orbital radius of the planet around 51 Pegasi was easily solved because the theoretical foundations were laid out 15 years earlier: planet migration due to tidal interaction with the surrounding gas disk (Goldreich & Tremaine 1980). Below, we go through the basics of this important theory.

In a cylindrical coordinate frame (r, ϕ) , with the central star located in the origin, we can expand the planetary potential as a Fourier cosine series:

$$\Phi(r, \phi, t) = \sum_m \psi_m(r) \cos(m\phi - m\Omega_p t), \quad (1.2)$$

where ψ is a radius-dependent amplitude, t denotes time and Ω_p is the angular velocity of the planet, which we have assumed to be on a circular orbit for simplicity. The response of the disk to the planet occurs at various resonances, where tidal waves are excited. Two kinds of resonances can be distinguished: corotation resonances and Lindblad resonances. Both occur where the angular velocity in the disk, Ω_d , is related in a simple way to Ω_p . Corotation resonances occur where $\Omega_d = \Omega_p$, while Lindblad resonances occur where $m(\Omega_d - \Omega_p) = \pm\kappa_d$, where κ_d is the epicyclic frequency of the disk, which is equal to Ω_d for a Keplerian disk. We can distinguish *inner* and *outer* Lindblad resonances, where inner Lindblad resonances have $m(\Omega_d - \Omega_p) = \kappa_d$.

Each potential component is constant in a frame rotating with the angular velocity of the planet, so the induced perturbations of the disk's energy and angular momentum preserve the Jacobi constant:

$$\frac{dE_d}{dt} = \Omega_p \frac{dL_d}{dt} = \Omega_p T_d, \quad (1.3)$$

where E denotes energy per unit mass, L denotes specific angular momentum and subscripts d refer to the disk. The quantity T is called the torque, and the sign of the total torque determines the direction in which the planet migrates.

Orbital eccentricity and energy are related through:

$$e^2 = 1 + \frac{2L^2 E}{(GM_*)^2}, \quad (1.4)$$

and upon replacing E with e in Eq. (1.3) we obtain:

$$(\Omega_p - \Omega_d)T_d = \frac{\Omega_d L_d}{2} \frac{de_d^2}{dt} \geq 0. \quad (1.5)$$

This last inequality holds as long as the unperturbed disk is circular. We see that whenever the disk angular velocity is *larger* than that of the planet, the torque on the disk is *negative*. Because $\Omega_p = \Omega_d$ at a corotation resonance, we cannot use Eq. (1.5) to determine its effect. The corotation torque is due to material on horseshoe orbits, and it turns out that it is proportional to $-d(\Sigma/B)/dr$, where B is Oort's second constant:

$$B = \frac{1}{2r} \frac{d(r^2 \Omega)}{dr}, \quad (1.6)$$

and Σ is the gas surface density. The corotation torque is much more complicated to evaluate than the Lindblad torque, because it is subject to saturation. This is because the effect of the corotation torque is to flatten the profile of Σ/B , and if no other physical processes in the disk such as viscosity are able to restore the gradient in Σ/B the corotation torque will tend to zero. See Ogilvie & Lubow (2003).

Conservation of angular momentum implies that because the disk loses angular momentum, the planet gains angular momentum by interaction with the faster moving part of the disk. In a Keplerian disk, this part is the inner part of the disk. On the other hand, interaction with the outer disk causes the angular momentum of the planet to decrease. It turns out that in general the outer disk wins (Ward 1997), mostly because in the outer disk resonances are located closer to the planet than in the inner disk. Therefore disks tend to push planets towards the central star. This mode of migration is called Type I migration, and it can be very fast, depending on the mass of the planet and the mass of the disk. In the most extreme case, for a Neptune-class planet embedded in a disk containing several Jupiter masses of gas, the migration time scale can be as short as a few thousand years. This is much shorter than the disk life time, and therefore all these planets should disappear into the central star. The problem of keeping planets alive long enough to survive inward migration is called the migration problem.

The analysis presented here is valid only for low-mass planets, for which the disk response is linear. In other words, the planet only creates small perturbations in the disk. The more massive a planet, the larger the perturbations, and for planets as massive as Jupiter a deep annular gap starts to form. In order for a gap to form, the angular momentum flux induced by the planet in the form of density waves needs to be damped locally. If this flux were constant, as is the case without any damping, any particular location in the disk does not gain or lose angular momentum because the amount of angular momentum the disk loses to one side is replaced exactly by an angular momentum flow from the other side.

There are two possibilities for a damping mechanism: viscosity, which is a representation of internal friction of the gas, and shock formation. Shocks, unlike linear waves, damp locally and are therefore capable of transferring their angular momentum to the disk. The criterion for shock formation is that the Roche lobe of the planet R_R , which is a measure of the gravitational sphere of influence of the planet, exceeds the disk pressure scale height H (Lin & Papaloizou 1993):

$$R_R = r_p \left(\frac{M_p}{3M_*} \right)^{1/3} \geq H, \quad (1.7)$$

which can be reformulated as:

$$q \geq 3h^3, \quad (1.8)$$

where $q = M_p/M_*$ and $h = H/r_p$. This condition implies that waves excited by the planet are non-linear *right from the start*. Goodman & Rafikov (2001) argue that this may be too strict, because waves that are linear in the beginning may well shock after traveling a certain distance, after which they deposit their angular momentum.

When damping is provided by viscosity, there is another criterion that has to be fulfilled. Because viscosity itself induces angular momentum transport in the disk by internal stresses, there is competition with the transport of angular momentum due to the waves excited by the planet. We show in Chapter 3 that the condition for the planet

to win can be written as:

$$q \geq \sqrt{\frac{10\nu h^3}{r_p^2 \Omega_p}}, \quad (1.9)$$

where ν is the kinematic viscosity coefficient.

For typical disk parameters, both conditions imply a minimum mass for gap-opening of approximately a tenth of the mass of Jupiter (around a solar mass star). When a planet gets more massive than this, a clean gap will open, which gives rise to a new mode of migration. Because there is no more material orbiting close to the planet, the planet becomes tidally locked inside the gap, and as the gas slowly accretes onto the central star the planet will accrete with it at the same speed. This mode of migration is called Type II migration. For this type of migration, the time scale is necessarily equal to the disk life time, because the planet accretes with the same velocity as the disk material. Therefore no migration problem exists for Type II migration. However, the prediction is still that all Jupiter-like planets would migrate inward to become Hot Jupiters, while there are a lot of examples of extrasolar giant planets that apparently did not migrate very far. This also holds for Jupiter itself.

Recently, a whole new migration mode has been discovered, which is called runaway or Type III migration (Masset & Papaloizou 2003; Artymowicz 2004). It is a very fast mode of migration which is driven by strong corotational flows, and it relies on a strong positive feedback of the corotation torque on the migration velocity of the planet; hence the term “runaway” migration. Type III migration may happen for planets that are just below the gap-opening mass. There is still mass inside the gap to drive migration, and if the disk mass that has been removed from the gap is comparable to the planet’s mass, Type III migration sets in (Masset & Papaloizou 2003). Because it is such a fast mode of migration its effects may well dominate over Type I and Type II migration. It is interesting that Type III migration can occur in both radial directions, depending on the migration history and the density profile in the disk. Therefore it has been suggested as a solution to the migration problem.

Disk-planet interaction is already quite complicated when considering migration, but the situation gets worse for eccentricity evolution of the planet. Because a planet on an eccentric orbit has a varying angular velocity, we need a double Fourier expansion of the planetary potential:

$$\Phi(r, \phi, t) = \sum_{l,m} \psi_{l,m}(r) \cos(m\phi - m\Omega_{l,m}t), \quad (1.10)$$

where $\Omega_{l,m}$ is the pattern speed for the (l, m) potential component:

$$\Omega_{l,m} = \Omega_p + \frac{l-m}{m} \kappa_d. \quad (1.11)$$

For a circular orbit, all $\psi_{l,m}$ are zero for $l \neq m$, and therefore $\Omega_{l,m} = \Omega_p$ for all m . For small eccentricities, $\psi_{l,m}$ can be taken zero for $|l-m| > 1$. Only when e becomes comparable to h , all components are needed to obtain convergence (Papaloizou & Larwood 2000).

Focusing on small eccentricities, for every value of m we have three pattern speeds: $\Omega_{m,m}$, $\Omega_{m-1,m}$ and $\Omega_{m+1,m}$. Each of these pattern speeds has three associated resonances: an inner Lindblad resonance, an outer Lindblad resonance and a corotation resonance. Therefore for each value of m we have *nine* resonances, each of which contribute in a specific way to the evolution of the eccentricity of the planet. For an overview see Goldreich & Sari (2003).

The density perturbation launched at a specific resonance rotates with its pattern speed. Therefore, the interaction of the planet with this perturbation conserves the planet's Jacobi constant:

$$\frac{dE_p}{dt} = \Omega_{l,m} \frac{dL_p}{dt} = -\Omega_{l,m} T_d. \quad (1.12)$$

We can again use the relation of orbital eccentricity to energy and angular momentum to get rid of the energy term, which yields:

$$e \frac{de}{dt} = \left[(1 - e^2)^{-1/2} \Omega_p - \Omega_{l,m} \right] \frac{L_p^2 T_d}{(GM_*)^2 M_p}. \quad (1.13)$$

For $e \ll 1$ this can be simplified to:

$$e \frac{de}{dt} = \left(\Omega_p - \Omega_{l,m} + \frac{1}{2} e^2 \Omega_p \right) \frac{L_p^2 T_d}{(GM_*)^2 M_p}. \quad (1.14)$$

First consider the case $l = m$. Because $\Omega_{m,m} = \Omega_p$ we have:

$$\frac{1}{e} \frac{de}{dt} = \frac{\Omega_p L_p^2 T_d}{2(GM_*)^2 M_p}. \quad (1.15)$$

For small eccentricities, the evolution of the semi-major axis a_p of the planet is directly related to the torque:

$$\frac{1}{a_p} \frac{da_p}{dt} = \frac{2}{L_p} \frac{dL_p}{dt} = -2 \frac{T_d}{L_p}. \quad (1.16)$$

Combining this equation with Eq. (1.15) yields:

$$\frac{1}{a_p} \frac{da_p}{dt} = -\frac{4(GM_*)^2}{\Omega_p L_p^3} \frac{1}{e} \frac{de}{dt} \approx -\frac{4}{e} \frac{de}{dt}, \quad (1.17)$$

where in the last step we again assume an almost circular orbit.

We have seen that in general, planets move inward, and Eq. (1.17) shows that the eccentricity increases due to interaction with principal (meaning $l = m$) Lindblad resonances. However, Eq. (1.17) also shows that the time scale for eccentricity evolution is four times the time scale for semi-major axis evolution, which means that principle Lindblad resonances can be safely ignored.

For the case $|l - m| = 1$, $\Omega_{m,m} \neq \Omega_p$ and for $e \ll 1$ we can ignore the term with e^2 in Eq. (1.14), which yields:

$$\text{sign} \left(\frac{de}{dt} \right) = \text{sign} ([\Omega_p - \Omega_{l,m}] T_d). \quad (1.18)$$

We can derive a similar relationship for the torque as in Eq. (1.5) for the eccentric case, only with Ω_p (the common pattern speed for all values of m) replaced by $\Omega_{l,m}$. Using this result, we finally obtain:

$$\text{sign} \left(\frac{de}{dt} \right) = \text{sign} \left([\Omega_p - \Omega_{l,m}] [\Omega_{l,m} - \Omega_d] \right). \quad (1.19)$$

We see that e decreases when the resonance is on the same side of corotation as the planet, and that e increases otherwise. Thus one can distinguish *coorbital* (eccentricity damping) and *external* (eccentricity pumping) Lindblad resonances.

For corotation resonances, the torque is proportional to $-d(\Sigma/B)/dr$, and therefore we have:

$$\text{sign} \left(\frac{de}{dt} \right) = \text{sign} \left([\Omega_{l,m} - \Omega_p] \frac{d(\Sigma/B)}{dr} \right). \quad (1.20)$$

Putting it all together, can disk-planet interaction account for the observed high eccentricities? The answer is not entirely clear yet, but we can comment on some necessary conditions.

First of all, in an unperturbed disk, coorbital Lindblad resonances damp eccentricity faster than external ones can excite it (Ward 1988; Artymowicz 1993); the difference is approximately a factor of 3. This means that in order for the eccentricity of the planet to grow, the coorbital Lindblad resonances must be rendered inactive by a gap in the disk. That leaves us with eccentricity driving Lindblad resonances.

Inside a gap, the density increases away from the planet, so the gradient of Σ/B will be such that corotation resonances damp eccentricity. Goldreich & Tremaine (1980) show that when the corotation torque operates at full power, the combined effect of Lindblad and corotation resonances will promote eccentricity decay, albeit at a small margin (4.6%). This means that the corotation torque only needs to be saturated for 5% to promote eccentricity growth. This puts a limit on the viscosity in the disk, together with a minimal eccentricity for the planet to begin with (Goldreich & Sari 2003; Ogilvie & Lubow 2003).

The maximum eccentricity that can be reached this way is approximately the size of the gap that is opened by the planet. If the radial excursions of the planet take it beyond the gap edge, coorbital Lindblad resonances will make sure that the eccentricity damps very fast. This again puts a limit on the viscosity in the disk. Goldreich & Sari (2003) and Sari & Goldreich (2004) argue that Jupiter-mass planets embedded in typical disks fulfill all criteria for eccentricity growth.

1.5 OPEN QUESTIONS

Planet-disk interaction is a promising candidate to account for the major surprises that were discovered during the extrasolar planet search. However, there are some details to be filled in, and also a new major problem that has been introduced by the necessary planet migration. This migration problem was already mentioned in the previous section, and we give some more details here.

The migration time scale for Type I migration can be written as (Tanaka et al. 2002):

$$\tau_{\text{mig}} = C \frac{h^2}{q q_d} \Omega_p^{-1}, \quad (1.21)$$

where q and q_d are the ratio of the planet and disk mass to the mass of the central star, respectively, and C is a constant of order unity. The precise value of C depends on the density structure and size of the disk. For typical values $h = 0.05$ and $q_d = 0.025$ a planet with $q = 10^{-4}$ would fall onto the central star in approximately 1000 orbits. If this planet is located at 1 AU initially this would correspond to a migration time scale of 1000 years, but even a planet originally located at the position of Neptune would migrate into the central star in 166,000 years. Because the typical life time of the disk is estimated to be ten times larger than this, it becomes very difficult for low-mass planets to survive the process of migration.

But the situation is even worse: in the core-accretion model of giant planet formation, giant planets are built around solid cores of a few M_{\oplus} . According to planet migration theory, these cores should undergo rapid migration before they can capture a dense atmosphere. Therefore also all gas giant planets are subject to the migration problem.

Clearly, a stopping mechanism is required. The simplest possibility is that the disk is truncated. When there is no disk inside a certain radius r_{in} , there is also no migration inside r_{in} . One of the best candidates for truncating the disk close to the star is the magnetic field of the protostar itself (Lin et al. 1996). However, this can not be the whole story because observations show that giant planets exist from 0.01 AU to more than 5 AU. Clearly a lot of planets stop migrating before they reach the magnetic cavity.

Another possible stopping mechanism is the interaction of the planet with a magnetized disk. Density perturbations due to a toroidal magnetic field in the disk are able to stop inward migration (Terquem 2003; Fromang et al. 2005). Magnetic turbulence is likely to play an important role as well. Turbulent density fluctuations due to the Magneto-Rotational Instability (MRI) (Balbus & Hawley 1991; Hawley & Balbus 1991) turn the gradual inward migration of planets into a stochastic process (Nelson & Papaloizou 2004). However, there may be large regions in the disk where the disk is too weakly ionized to couple to the magnetic field (Gammie 1996). To find out the location and width of these "dead zones" is currently an active field of research, see for example Ilgner & Nelson (2006a,b).

The most important shortcoming of most migration models, analytical as well as numerical, is that they do not solve for the temperature as an independent variable. Numerical hydrodynamical models of planet-disk interaction mostly use a locally isothermal equation of state, where the disk has a fixed temperature profile that stays constant throughout the simulation. There have been attempts to account for a more realistic disk temperature structure (Jang-Condell & Sasselov 2003, 2004, 2005) and opacity structure (Menou & Goodman 2004), and recently the first radiation-hydrodynamical models of the interaction of high-mass planets and disks were presented (Klahr & Kley 2006). In Chapter 5 we will present our results on radiation-hydrodynamical models for low-mass planets.

The other problem with planet-disk interaction concerns the eccentricities of the extrasolar planets. Although in theory eccentricity growth is possible for Jupiter-mass planets, in numerical simulations eccentric companions were only produced in the brown dwarf mass regime (Papaloizou et al. 2001).

1.6 NUMERICAL HYDRODYNAMICS

Because the major constituent of a protoplanetary disk is gas, the appropriate modeling tool for planet-disk interaction is numerical hydrodynamics. Hydrodynamics is hard. The complicating factor is that the governing equations (the Euler equations) are hyperbolic, and therefore that, in the absence of viscous forces, they allow *weak* (discontinuous) solutions. These discontinuities, where the spatial derivative is not defined, pose serious difficulties for numerical methods that rely on the approximation of derivatives.

Consider, as a simple example, mass conservation in one spatial dimension. For a particular volume V , which stretches from x_1 to x_2 , we denote the mass density inside V as $\rho(x, t)$. The flux of mass is given by $F(x, t) = \rho(x, t)v$, where for simplicity we take the velocity v constant. Therefore we have $F(x, t) = F(\rho)$. Conservation of mass states that

$$\frac{dM_V}{dt} = F(\rho(x_1, t)) - F(\rho(x_2, t)), \quad (1.22)$$

where M_V is the mass contained in volume V . The interpretation of Eq. (1.22) is straightforward: the change of mass in V is given by the amount of mass that flows in through the left (x_1) boundary minus the amount of mass that flows out through the right (x_2) boundary. Note that we do not consider the creation or destruction of mass here.

For smooth functions the right-hand side of Eq. (1.22) can be written as:

$$F(\rho(x_1, t)) - F(\rho(x_2, t)) = - \int_{x_1}^{x_2} \frac{\partial F}{\partial x} dx. \quad (1.23)$$

The mass inside V is the density, integrated over V :

$$M_V(t) = \int_{x_1}^{x_2} \rho(x, t) dx, \quad (1.24)$$

so that we can rewrite Eq. (1.22) as:

$$\int_{x_1}^{x_2} \left[\frac{\partial \rho}{\partial t} + \frac{\partial F}{\partial x} \right] dx = 0. \quad (1.25)$$

This equation must hold for all x_1 and x_2 , since mass is conserved for *any* volume under consideration. Therefore the expression under the integral sign must actually be zero everywhere:

$$\frac{\partial \rho}{\partial t} + \frac{\partial F}{\partial x} = 0, \quad (1.26)$$

which is just a rewritten form of conservation of mass, and it forms the basis of most numerical methods. For example, the most simple method for solving Eq. (1.26) is to update the density as:

$$\rho(t + \Delta t, x) = \rho(t, x) - \Delta t \frac{F(x + \Delta x, t) - F(x - \Delta x, t)}{2\Delta x}, \quad (1.27)$$

where we have approximated the spatial derivative by its finite difference version. It is a simple method, but it will not work when the flux derivative is not defined, as is the case near a discontinuity. More sophisticated methods yield accurate results even in the presence of discontinuities by going back to the original form of the conservation law, Eq. (1.22), which is always valid.

There are two basic classes of hydrodynamics solvers in use by the astrophysical community: the SPH methods and grid-based methods. For a review of Smoothed Particle Hydrodynamics (SPH), originally designed by Lucy (1977) and Gingold & Monaghan (1977), we refer to Benz (1990) and Monaghan (1992). Grid-based methods can be further subdivided into *shock-capturing* methods and *upwind* methods, where we follow the terminology of de Val-Borro et al. (2006). The main difference between the two is the way they treat flow discontinuities. The shock-capturing methods are specifically designed to treat these discontinuities in a physically correct way, so in problems containing shock waves these are the preferred methods of choice. Examples are the PPM-method (Woodward & Colella 1984) and the Roe solver (Roe 1981). The most commonly used upwind method is ZEUS (Stone & Norman 1992).

Now the question is: do we expect to see shocks near embedded planets? The answer is yes for planets more massive than approximately $30 M_{\oplus}$ around a Solar mass star (see Chapter 3). For planets of lower mass, Rafikov (2002) suggests that shocks play an important role as well. We will test this extensively in Chapter 3. The main point for now is that indeed shocks are important in planet-disk interaction, and therefore a shock-capturing scheme should be the method of choice. We chose for the Roe solver, and in particular the non-relativistic limit of the general relativistic Roe solver of Eulderink & Mellema (1995). Because of the general relativistic nature, gravity, which is a key element in planet-disk interaction, is built into the method in a very natural way. We explain the method in detail in Chapter 2.

Most numerical methods used in hydrodynamical simulations of disk-planet interaction were compared in de Val-Borro et al. (2006). Given the very different nature of the codes it is quite remarkable to see how much the results agree, especially on the density and vorticity structures. The spread in torques onto the planet is very large, but the adopted resolution is too low to yield reliable results on the torque. Small density differences close to the planet can have a big impact on the torque.

Among the three main outliers within the group of tested methods were two SPH methods, for which the number of particles was too small to provide sufficient resolution compared to the grid codes (see also Maschietto 2006). The increase in particle numbers needed for SPH to compare to the grid codes is not computationally feasible. The third outlier is a shock-capturing method that uses a Cartesian coordinate frame. It turns out that, while such a frame is inherently simple because no fictitious forces arise, it is very difficult to model a rotating disk in Cartesian coordinates. This shows

that adopting the best possible coordinate frame can be critical to obtain good results. In this respect, a very nice property of a covariant numerical recipe like ours is that it is valid for arbitrary coordinate frames. We will make use of this property to keep the planet at a fixed location in the grid, which is computationally advantageous (see also Chapter 4).

1.7 THIS THESIS

In this thesis we present the results of numerical hydrodynamical simulations of planets embedded in disks of gas and dust. We use our new method to study the open questions mentioned in Sect. 1.5. We add new physical processes to the models, and show how they change the basic picture outlined in this Chapter. The first part of the thesis (Chapters 2, 3, 4 and 5) is devoted to gas disks, while the later Chapters deal with disks of gas and dust.

1.7.1 Chapter 2

We kick off in Chapter 2 with a detailed description of the numerical method, which we have called RODEO (a ROe solver for Disk Embedded Objects). We give an overview of the two-dimensional version, with a locally isothermal equation of state. This provides the basic building block from which we build more complicated models, including detailed thermodynamics (Chapter 5) and dust (Chapters 6, 7 and 8). We also show which numerical parameters are important in hydrodynamical disk simulations, and we compare results on gas accretion and migration rates to previous analytical and numerical work.

1.7.2 Chapter 3

In Chapter 3 we focus on the criterion for gap opening. This is an important and not fully understood problem, for theory as well as for observations. There are two basic criteria for a planet to be able to open up a gap. The first one is that the waves of angular momentum launched by the planet should be damped locally. Otherwise, with a constant angular momentum flux, there is no region in the disk where the angular momentum changes with time, and therefore no gap opening. The two possible damping mechanisms include viscosity and shock formation. When viscosity provides the damping, there is an additional criterion for gap formation which states that the viscous flux of angular momentum should not exceed the planetary angular momentum flux. Otherwise, any gap that is being formed is quickly refilled by viscous flow. In Chapter 3, we focus on the inviscid limit, where shock formation is responsible for wave damping and therefore gap opening. The standard gap formation criterion in this case states that waves excited by the planet should be non-linear from the very beginning, while Rafikov (2002) argues that even when waves start out as linear waves, they will shock eventually due to the shear in the disk. Gap formation would then be

possible for arbitrary planets. We try to verify this claim through numerical simulations.

1.7.3 Chapter 4

Next, we focus on orbital evolution. We have developed a version of the RODEO method that is specifically designed to keep the planet at a fixed location in the grid, regardless of its orbital evolution. We show that this is advantageous especially when the eccentricity is small. We subsequently assess which conditions in the disk are favorable for eccentricity growth, for three planetary masses: $5 M_J$, $1 M_J$ and $0.1 M_J$. It turns out that in an inviscid disk, a $5 M_J$ planet will end up on an eccentric orbit when the disk is more massive than the planet. The gap opened by such a massive planet is wide and deep enough to sustain eccentricity growth. However, this is not the case for the $1 M_J$ planet, even in an inviscid disk. Only for a reduced disk thickness we find significant eccentricity growth. For the smallest mass we consider, vortices were found in the coorbital region of the planet (Koller et al. 2003). We show that these vortices do not affect eccentricity evolution (the planet remains on a circular orbit) but they are able to halt and even reverse migration.

1.7.4 Chapter 5

In Chapter 5 we present the results of radiation-hydrodynamical models of the interaction of low-mass planets with the disk in which they are embedded. First, we extend the method of Chapter 2 to three dimensions, and we compare the results on accretion and migration to previous analytical and numerical work, just as in Chapter 2. Next, we describe the results of simulations with radiation included. These are very expensive computationally, because due to the large value of the speed of light compared to the speed of sound the radiation update has to be implicit. This comes down to solving a large matrix equation, which can only be done iteratively. We were awarded a special grant from the Dutch national supercomputer facility to run these very expensive simulations. The results are very interesting: depending on the cooling efficiency in the disk, low-mass planets may move *outward* instead of inward. Especially in the dense inner part of the disk inward moving planets will halt their migration towards the central star, and therefore they can be saved before they plunge into the Sun.

1.7.5 Chapter 6

We move to a different extension of classical planet-disk interaction in Chapter 6, where we focus on the differences between the flow of gas and the flow of dust. We show that planets of intermediate mass (comparable to Neptune), which do not open gaps in the gas disk, do so in the dust disk. Because large dust particles of approximately 1 mm are only marginally coupled to the gas, they move up the pressure gradients induced by the planet which results in a deep dust gap. We derive a minimum

mass for a planet to create such a gap ($16 M_{\oplus}$), and a minimum particle size for this effect to occur ($150 \mu\text{m}$). We also briefly consider the effect of the dust gap on accretion of solids.

1.7.6 Chapter 7

In Chapter 7 we focus on dust accretion in more detail. In particular, using a different numerical method we consider the whole dust size spectrum, from micron-size dust grains to km-sized planetesimals. We show that it is extremely hard for dust particles to accrete onto a forming planet: only the smallest particles of micron size make it into the planetary atmosphere. Slightly larger particles are subject to dust gap formation (see Chapter 6) which reduces the accretion rate, and larger boulders are efficiently trapped in mean motion resonances with the planet. Therefore the mixture of gas and dust that is accreted onto the planet is relatively poor in solids, while observations for Jupiter suggest that it is *enriched* in solids. Therefore our results favor the core-accretion model of giant planet formation, because it is extremely hard to enrich a giant planet in solids after its formation.

1.7.7 Chapter 8

Finally, we consider planets embedded in transitional circumstellar disks. They differ from the protoplanetary disks considered in Chapter 6 in their gas content. They bridge the gap between gas-rich protoplanetary disks and gas-free circumstellar dust disks. In this Chapter we show that the reduced gas content in the disk leads to new interesting dynamical effects. We show that when there is as much gas as dust in the disk, this mixture is in fact unstable. This was predicted by Youdin & Goodman (2005). We discuss the effect of these instabilities on the process of dust gap formation that was outlined in Chapter 6. Finally, we consider the effect of radiation pressure on the dynamics of gas and dust. We show that this can enhance the asymmetry in the disk, and we tentatively compare the result of our simulation with observations of the transitional disk around HD 141569 A.

1.7.8 Main results

The main results presented in this thesis are:

- In favorable circumstances non-linear wave evolution may lead to gap opening for low-mass planets, as was predicted by Rafikov (2002).
- A low viscosity is not enough to favor eccentricity growth of Jupiter-mass planets. Only when the Roche lobe of the planet is more than 10 times larger than the scale height of the disk the gap created by the planet gets deep enough for the orbital eccentricity to grow.

- When planets migrate into a region where cooling of the disk through radiation can not keep up with heating due to the presence of the planet the torque on the planet reverses sign. In the Solar Nebula this happens in the high-density parts, within 15 AU from the Sun.
- Even when a low-mass planet is not able to open up a gap in the gas disk, the pressure gradients near the orbit of the planet may be able to create a *dust* gap in the mm-size part of the grain population. This opens up the possibility to observe Neptune-mass planets in protoplanetary disks at mm-wavelengths.
- The dust gap that emerges around the orbit of a planet hinders dust accretion onto the planet. Only particles larger than $10 \mu\text{m}$ may accrete onto a planet of $1 M_{\text{J}}$, while gas accretion slowly continues. This makes the mixture of gas and dust that is accreted by the planet relatively poor in solids. Therefore it is very hard to enrich a giant planet in solids *after* its formation.
- In transitional disks, where the dust-to-gas ratio can be of order unity and radiation pressure plays an important role, the signature of embedded planets changes significantly.

1.8 OUTLOOK

Disk-planet interaction is a fast evolving subject, and it is likely that it will remain this way in the near future. There are more planetary systems discovered every week, and the search will extend towards lower-mass, Earth-like planets in a few years. The orbits of extrasolar terrestrial planets will no doubt harbor their own surprises, some of which may be due to interaction with a former disk. In the next decade, ALMA will provide the necessary resolution to study the planet-forming zone in protoplanetary disks in nearby star-forming regions. The gaps and other planet-induced structures in these disks will teach us a lot about the process of planet formation, because then for the first time we will be looking directly into the cradle of Earth.

On the theoretical side, there are still important physical processes missing in the models. We have not considered magnetic fields, for example, in this thesis, while they may play an important role. Self-gravity of the gas is another important issue. Most of the mass of Jupiter resides in its gaseous envelope, and therefore it is clear that also self-gravity must have been important during the formation of Jupiter. And while we have included radiative transport into the models in Chapter 5, the radiation from the central star is not considered yet. The star is partly responsible for the geometry of the disk (how the disk thickness varies with radius), and this geometry plays a central role in migration, gap formation and eccentricity evolution.

So the story does not end here, and one might even say that, due to the increasing complexity of the models, it has only just begun. It will require the fastest computers in the world to run these simulations, and, more importantly, it will require very smart people to interpret them and thereby try to solve the outstanding problems in planet formation theory.

REFERENCES

- Artymowicz, P. 1993, *ApJ*, 419, 166
- Artymowicz, P. 2004, in *ASP Conf. Ser. 324: Debris Disks and the Formation of Planets*, ed. L. Caroff, L. J. Moon, D. Backman, & E. Praton, 39
- Balbus, S. A. & Hawley, J. F. 1991, *ApJ*, 376, 214
- Beckwith, S. V. W. & Sargent, A. I. 1996, *Nature*, 383, 139
- Benz, W. 1990, in *Numerical Modelling of Nonlinear Stellar Pulsations Problems and Prospects*, ed. J. R. Buchler, 269
- Bernal, J. D. 1969, *Science in History, Vol.I: The emergence of Science* (Pelican, Harmondsworth)
- Boss, A. P. 1997, *Science*, 276, 1836
- de Val-Borro, M., Edgar, R. G., Artymowicz, P., et al. 2006, *MNRAS*, 370, 529
- Dick, S. J. 1982, *Plurality of worlds* (Cambridge University Press)
- Dominik, C., Blum, J., Cuzzi, J., & Wurm, G. 2006, in *Protostars and Planets V* (astro-ph/0602617)
- Eulderink, F. & Mellema, G. 1995, *A&AS*, 110, 587
- Field, J. V. 1988, *Kepler's Geometric Cosmology* (Athlone Press, London)
- Ford, E. B., Havlickova, M., & Rasio, F. A. 2001, *Icarus*, 150, 303
- Fromang, S., Terquem, C., & Nelson, R. P. 2005, *MNRAS*, 363, 943
- Gammie, C. F. 1996, *ApJ*, 457, 355
- Garaud, P. & Lin, D. N. C. 2004, *ApJ*, 608, 1050
- Gingold, R. A. & Monaghan, J. J. 1977, *MNRAS*, 181, 375
- Goldreich, P. & Sari, R. 2003, *ApJ*, 585, 1024
- Goldreich, P. & Tremaine, S. 1980, *ApJ*, 241, 425
- Goldreich, P. & Ward, W. R. 1973, *ApJ*, 183, 1051
- Goodman, J. & Rafikov, R. R. 2001, *ApJ*, 552, 793
- Guillot, T. 1999, *Planet. Space Sci.*, 47, 1183
- Hawley, J. F. & Balbus, S. A. 1991, *ApJ*, 376, 223
- Ilgner, M. & Nelson, R. P. 2006a, *A&A*, 445, 205
- Ilgner, M. & Nelson, R. P. 2006b, *A&A*, 445, 223
- Jang-Condell, H. & Sasselov, D. D. 2003, *ApJ*, 593, 1116
- Jang-Condell, H. & Sasselov, D. D. 2004, *ApJ*, 608, 497
- Jang-Condell, H. & Sasselov, D. D. 2005, *ApJ*, 619, 1123
- Klahr, H. & Kley, W. 2006, *A&A*, 445, 747
- Koller, J., Li, H., & Lin, D. N. C. 2003, *ApJ*, 596, L91
- Kuiper, G. P. 1951, *Proc. Natl. Acad. Sci.*, 37, 1
- Laplace, P. S. 1796, *Le Systeme du Monde, Vol.II* (Paris)

- Lin, D. N. C., Bodenheimer, P., & Richardson, D. C. 1996, *Nature*, 380, 606
- Lin, D. N. C. & Papaloizou, J. C. B. 1993, in *Protostars and Planets III*, 749–835
- Lucy, L. B. 1977, *AJ*, 82, 1013
- Maschietto, F. 2006, Master thesis (Leiden Observatory)
- Masset, F. S. & Papaloizou, J. C. B. 2003, *ApJ*, 588, 494
- Mayor, M. & Queloz, D. 1995, *Nature*, 378, 355
- Mejía, A. C., Durisen, R. H., Pickett, M. K., & Cai, K. 2005, *ApJ*, 619, 1098
- Menou, K. & Goodman, J. 2004, *ApJ*, 606, 520
- Monaghan, J. J. 1992, *ARA&A*, 30, 543
- Murray, C. D. & Dermott, S. F. 2000, *Solar System Dynamics* (Cambridge University Press)
- Nelson, R. P. & Papaloizou, J. C. B. 2004, *MNRAS*, 350, 849
- Ogilvie, G. I. & Lubow, S. H. 2003, *ApJ*, 587, 398
- Papaloizou, J. C. B. & Larwood, J. D. 2000, *MNRAS*, 315, 823
- Papaloizou, J. C. B., Nelson, R. P., & Masset, F. 2001, *A&A*, 366, 263
- Pickett, B. K., Mejía, A. C., Durisen, R. H., et al. 2003, *ApJ*, 590, 1060
- Pollack, J. B., Hubickyj, O., Bodenheimer, P., et al. 1996, *Icarus*, 124, 62
- Rafikov, R. R. 2002, *ApJ*, 572, 566
- Roe, P. L. 1981, *J. Comp. Phys*, 43, 357
- Sari, R. & Goldreich, P. 2004, *ApJ*, 606, L77
- Stone, J. M. & Norman, M. L. 1992, *ApJS*, 80, 753
- Tanaka, H., Takeuchi, T., & Ward, W. R. 2002, *ApJ*, 565, 1257
- Terquem, C. E. J. M. L. J. 2003, *MNRAS*, 341, 1157
- Ward, W. R. 1988, *Icarus*, 73, 330
- Ward, W. R. 1997, *Icarus*, 126, 261
- Wolszczan, A. & Frail, D. A. 1992, *Nature*, 355, 145
- Woodward, P. & Colella, P. 1984, *J. Comp. Phys*, 54, 115
- Yamoto, F. & Sekiya, M. 2004, *Icarus*, 170, 180
- Youdin, A. N. & Goodman, J. 2005, *ApJ*, 620, 459
- Youdin, A. N. & Shu, F. H. 2002, *ApJ*, 580, 494

CHAPTER 2

RODEO: a new method for planet-disk interaction

Sijme-Jan Paardekooper and Garrelt Mellema

Astronomy & Astrophysics 450, 1203, 2006

IN this Chapter we describe a new method for studying the hydrodynamical problem of a planet embedded in a gaseous disk. We use a finite volume method with an approximate Riemann solver (the Roe solver), together with a special way to integrate the source terms. This new source term integration scheme sheds new light on the Coriolis instability, and we show that our method does not suffer from this instability. The first results on flow structure and gap formation are presented, as well as accretion and migration rates. For $M_p < 0.1 M_J$ and $M_p > 1.0 M_J$ ($M_J = \text{Jupiter's mass}$) the accretion rates do not depend sensitively on numerical parameters, and we find that within the disk's lifetime a planet can grow to 3 – 4 M_J . In between these two limits numerics play a major role, leading to differences of more than 50% for different numerical parameters. Migration rates are not affected by numerics at all as long as the mass inside the Roche lobe is not considered. We can reproduce the Type I and Type II migration for low-mass and high-mass planets, respectively, and the fastest moving planet of $0.1 M_J$ has a migration time of only $2.0 \cdot 10^4$ yr.

2.1 INTRODUCTION

It is now generally believed that planets are formed out of the same nebula as their parent star. When this cloud of gas collapses into a protostar, conservation of angular momentum leads to the formation of an accretion disk around the star. These disks are indeed observed around T-Tauri stars (Beckwith & Sargent 1996), and it is within these disks that planet formation should take place.

In standard theory, terrestrial planets as well as the rocky cores of gas giant planets arise slowly from collisions of dust particles. When a protoplanet reaches a certain critical mass ($\approx 15 M_{\oplus}$), it can no longer sustain a hydrostatic atmosphere, and dynamical accretion sets in. Eventually, this accretion process forms a gaseous envelope around the core, of a mass comparable to Jupiter. This scenario is known as the 'core accretion model'.

Recently, Boss (1997) revisited a model originally proposed by Cameron (1978), the "core collapse scenario", in which a giant planet is formed in much the same way as a star through a gravitational instability in the disk. However, Rafikov (2005) pointed out several problems with this scenario, and it is yet undecided which of these two scenarios is correct. In both cases we end up with a newly formed giant planet still embedded in the protoplanetary disk. It is this interesting stage of planet formation that we focus on in this Chapter.

The disk and the planet interact gravitationally with each other. The planet perturbs the disk through tidal forces, breaking its axisymmetry and, if the planet is massive enough, opens up a gap in the disk (Lin & Papaloizou 1993). The perturbed disk in its turn exerts a torque on the planet, leading possibly to orbital migration (Goldreich & Tremaine 1980). Inward migration is generally believed to be the mechanism responsible for creating 'Hot Jupiters': giant planets, comparable to Jupiter, with very small semi-major axes (< 0.1 AU).

The process of gap formation raises two interesting questions. First: does the presence of the gap prevent further gas accretion? If it does, this puts serious constraints on the maximum planet mass that can be reached. Secondly: how is the orbital evolution of the planet affected by the gap? If all planets move inward on much shorter time scales than the typical lifetime of the disk, how come we still have Jupiter in our Solar system at 5.2 AU?

The accretion issue has been investigated in detail numerically by Kley (1999) and by Lubow et al. (1999), and they find that accretion can continue through the gap, allowing more massive planets to be formed. Migration has been investigated both analytically (Goldreich & Tremaine 1980; Lin & Papaloizou 1986), recently by Rafikov (2002), and numerically by Nelson et al. (2000) and Kley (2000), and it seems that migration is always inward, allowing for Hot Jupiters but not for 'Cold' Jupiters. Recently Masset & Papaloizou (2003) and Artymowicz (2004) showed that there exists a runaway regime in which the orbital radius of the planet evolves on very short timescales, with possible outward migration.

However, the problem is complicated analytically, and hard to do numerically as well. A nice illustration of this is given by Kley (1998), who showed that the use of a corotating coordinate frame can lead to non-physical evolution in some numerical

codes. It therefore seems appropriate to introduce a numerical method which is new in this field of research, and which should handle rotating coordinate frames and the effects of gravity in a better way. We use a finite-volume method based on an approximate Riemann solver for arbitrary coordinate frames, which is specifically aimed to treat discontinuities in the flow correctly. Also, the numerical scheme is conservative, meaning that the method conserves mass, momentum and angular momentum up to second order.

In this Chapter, we aim to give a full description of RODEO (ROe solver for Disk-Embedded Objects), to show some differences in the gas flow in the disk and to present results on accretion and migration rates. The focus will be more on numerical effects than on physical effects, i.e. we do not consider different disk structures or different magnitudes of an anomalous viscosity as was done by Bryden et al. (1999) and Kley (1999). Instead, we consider the effect of various numerical parameters to assess their importance regarding gap formation, accretion and migration rates.

We focus on the two-dimensional, vertically integrated problem, which is formally only correct for planets for which the Roche lobe is larger than the disk scale height. For our disk, this comes down to $M_p > M_J$. However, because two-dimensional simulations are far less expensive in terms of computing time than three-dimensional simulations this allows us to do a detailed numerical study and compare our findings to previous two-dimensional results.

We start in Sect. 2.2 by describing the physical model that was used. Next, we focus on the numerical method in some detail in Sect. 2.3. In Sect. 2.4 we show the results of some test problems and in Sect. 2.5 we give the initial and the boundary conditions. We give our results on gap formation, accretion and migration in Sects. 2.6, 2.7 and 2.8. Section 2.9 is reserved for a short summary and the conclusions.

2.2 PHYSICAL MODEL

2.2.1 Basic equations

Protoplanetary disks are fairly thin, i.e. the ratio of the vertical thickness H and the radial distance from the center r is smaller than unity. Typically $H/r = 0.05$. We can therefore vertically integrate the hydrodynamical equations, and work with vertically averaged state variables. We will use cylindrical coordinates (r, ϕ) , with the central star of $1 M_\odot$ located at $r = 0$.

The flow of the gas is determined by the Euler equations, which express conservation of mass, momentum in all spatial directions, and energy. These equations can be written in a simple form:

$$\frac{\partial \mathbf{W}}{\partial t} + \frac{\partial \mathbf{F}}{\partial r} + \frac{\partial \mathbf{G}}{\partial \phi} = \mathbf{S}, \quad (2.1)$$

where \mathbf{W} is called the state, \mathbf{F} and \mathbf{G} are the radial and the polar flux, respectively, and \mathbf{S} is the source term. The state consists of the conserved quantities, and Eq. (2.1) expresses the fact that any change in time of the state in a specific volume is due to flow

r	radial coordinate
ϕ	azimuthal coordinate
Σ	surface density
v_r	radial velocity
v_ϕ	angular velocity in the corotating frame
p	vertically integrated pressure
Φ	gravitational potential
Ω	angular velocity coordinate system
r_p	orbital radius of the planet
ϕ_p	angular position of the planet
P	orbital period of the planet

Table 2.1: Definition of symbols

across the boundary of the volume (the flux terms) or due to a source inside the volume (the source term). We will omit the energy equation for now, because we will work with a simple (isothermal) equation of state, which does not require an energy equation. The method still includes the energy equation as an option, however, and this way we have another way of simulating isothermal flow: a run with a very low adiabatic exponent Γ , as was done for example in Nelson & Benz (2003). We will present the method only for the isothermal equations; for the full method including the energy equation we refer to Eulderink & Mellema (1995).

In cylindrical coordinates, the vectors \mathbf{W} , \mathbf{F} , \mathbf{G} and \mathbf{S} can be written in the following form:

$$\mathbf{W} = r(\Sigma, \Sigma v_r, \Sigma v_\phi) \quad (2.2)$$

$$\mathbf{F} = r(\Sigma v_r, \Sigma v_r^2 + p, \Sigma v_r v_\phi) \quad (2.3)$$

$$\mathbf{G} = r(\Sigma v_\phi, \Sigma v_r v_\phi, \Sigma v_\phi^2 + p/r^2), \quad (2.4)$$

$$\mathbf{S} = \begin{pmatrix} 0 \\ \Sigma r^2 (v_\phi + \Omega)^2 - \Sigma r \frac{\partial \Phi}{\partial r} + p \\ -2\Sigma v_r (\Omega + v_\phi) - \frac{\Sigma}{r} \frac{\partial \Phi}{\partial \phi} \end{pmatrix}. \quad (2.5)$$

The symbols used are listed in Table 2.1.

Note that in this form there are no derivatives of dependent variables in the source term, keeping \mathbf{S} finite even in the presence of discontinuities. Also, there are no viscous terms present, because we deal with viscosity in a separate way (see Sect. 2.2.3).

The gravitational potential contains terms due to the central star and due to the direct and indirect influence of the planet:

$$\Phi(r, \phi) = -\frac{GM_\odot}{r} - \frac{GM_p}{r_2} + \frac{GM_p}{r_p^2} r \cos(\phi - \phi_p). \quad (2.6)$$

Here $r_2 = |r - r_p|$ denotes the distance to the planet. Because this potential is singular at the position of the planet, and to account for the three-dimensional structure of the

disk, we use a smoothed version of r_2 :

$$r_2 = \sqrt{r^2 + r_p^2 - 2r r_p \cos(\phi - \phi_p)} + \epsilon^2. \quad (2.7)$$

The smoothing parameter ϵ is taken to be a certain fraction of the Roche lobe of the planet:

$$\epsilon = b R_R = b r_p \sqrt[3]{\frac{M_p}{3M_\odot}}. \quad (2.8)$$

Throughout this Chapter we have used $b = 0.2$. The results do not depend much on its value, as long as $b < 1$. The indirect term in the potential (the last term on the right-hand side in Eq. (2.6)) arises due to the fact that a coordinate system centered on the central star is not an inertial frame, because the star feels the gravitational pull of the planet. A similar (small) term for the disk is omitted for simplicity.

2.2.2 Equation of state

Equation (2.1) needs to be complemented by an equation of state. We assume an isothermal equation of state:

$$p = c_s^2 \Sigma. \quad (2.9)$$

This choice is based on the assumption that the gas is able to radiate away all its excess energy very efficiently. In vertical hydrostatic equilibrium, the isothermal sound speed c_s is given by:

$$c_s = \frac{H}{r} \sqrt{\frac{G M_\odot}{r}}. \quad (2.10)$$

2.2.3 Viscosity

The nature of the viscosity in accretion disks was unknown for a long time. Currently, the Magneto-Rotational Instability (MRI) is the best candidate for providing a turbulent viscosity (Balbus & Hawley 1990). In regions where the ionization fraction in the disk is high enough to sustain the MRI one would need to do Magneto-Hydrodynamics (MHD) to study planet-disk interaction, as was done in Nelson & Papaloizou (2003). MHD simulations are very expensive however, and it is not yet clear if the MRI operates throughout the disk. In so-called dead-zones (Gammie 1996) there may be no turbulent viscosity at all. However, in order to compare our results to previous studies we include an anomalous turbulent viscosity in our models.

Viscosity comes in as two extra source terms for the momentum, one in the radial and one in the azimuthal direction. We deal with these source terms separately in the numerical method (see Sect. 2.3).

The form of these source terms can be found for example in D'Angelo et al. (2002):

$$f_r = \frac{1}{r} \frac{\partial(r \mathcal{S}_{rr})}{\partial r} + \frac{1}{r} \frac{\partial(\mathcal{S}_{r\phi})}{\partial \phi} - \frac{\mathcal{S}_{\phi\phi}}{r} \quad (2.11)$$

$$f_\phi = \frac{1}{r} \frac{\partial(r^2 \mathcal{S}_{r\phi})}{\partial r} + \frac{\partial(\mathcal{S}_{\phi\phi})}{\partial \phi}, \quad (2.12)$$

where the components of the viscous stress tensor \mathcal{S} are:

$$\mathcal{S}_{rr} = 2\nu\Sigma \left(\frac{\partial v_r}{\partial r} - \frac{1}{3}\nabla \cdot \mathbf{v} \right) \quad (2.13)$$

$$\mathcal{S}_{\phi\phi} = 2\nu\Sigma \left(\frac{\partial v_\phi}{\partial \phi} + \frac{v_r}{r} - \frac{1}{3}\nabla \cdot \mathbf{v} \right) \quad (2.14)$$

$$\mathcal{S}_{r\phi} = \nu\Sigma \left(\frac{1}{r} \frac{\partial v_r}{\partial \phi} + r \frac{\partial v_\phi}{\partial r} \right) \quad (2.15)$$

$$\nabla \cdot \mathbf{v} = \frac{1}{r} \frac{\partial(rv_r)}{\partial r} + \frac{\partial v_\phi}{\partial \phi}. \quad (2.16)$$

We can either use an α -prescription for the viscosity parameter ν (Shakura & Sunyaev 1973):

$$\nu = \alpha c_s H, \quad (2.17)$$

or we can take ν constant throughout the disk. Note that for the α -disk with constant aspect ratio H/r , $\nu \propto \sqrt{r}$, leading to enhanced viscosity in the outer disk.

2.3 NUMERICAL METHOD

We can integrate Eq. (2.1) over the finite volume of a grid cell to obtain:

$$\begin{aligned} & \frac{1}{\Delta t \Delta r \Delta \phi} \left(\int dr \int d\phi (\mathbf{W}^{n+1} - \mathbf{W}^n) + \right. \\ & \quad \int dt \int d\phi (\mathbf{F}_{i+1/2,j} - \mathbf{F}_{i-1/2,j}) + \\ & \quad \left. \int dt \int dr (\mathbf{G}_{i,j+1/2} - \mathbf{G}_{i,j-1/2}) - \right. \\ & \quad \left. \int dt \int dr \int d\phi \mathbf{S} \right) = 0. \end{aligned} \quad (2.18)$$

Here $A_{i,j}^n$ means the physical quantity A , evaluated at time index n , at grid coordinates (i, j) . The volume term ($r^2 \sin \theta$ for spherical coordinates, r for cylindrical coordinates) of the grid cell is already present in \mathbf{W} , \mathbf{F} and \mathbf{S} . A second order accurate integration scheme for this equation is:

$$\begin{aligned} & \frac{1}{\Delta t} (\langle \mathbf{W} \rangle^{n+1} - \langle \mathbf{W} \rangle^n) + \\ & \frac{1}{\Delta r} (\mathbf{F}_{i+1/2,j}^{n+1/2} - \mathbf{F}_{i-1/2,j}^{n+1/2}) + \\ & \frac{1}{\Delta \phi} (\mathbf{G}_{i,j+1/2}^{n+1/2} - \mathbf{G}_{i,j-1/2}^{n+1/2}) - \\ & \quad \mathbf{S}_{i,j}^{n+1/2} = 0, \end{aligned} \quad (2.19)$$

where $\langle \rangle$ denotes arithmetic mean. A numerical scheme like this is called *conservative* because the conserved quantities are indeed conserved by the numerical method: what goes into one cell must come out of another.

We will use Eq. (2.19) to find an update for the state. What is left to be done is to find expressions for the interface fluxes (Sect. 2.3.1) and to account for the source terms (Sect. 2.3.2).

2.3.1 Roe solver

First, we use the technique of dimensional splitting to obtain the two one-dimensional equations

$$\begin{aligned}\frac{\partial \mathbf{W}}{\partial t} + \frac{\partial \mathbf{F}}{\partial r} &= \mathbf{X} \\ \frac{\partial \mathbf{W}}{\partial t} + \frac{\partial \mathbf{G}}{\partial \phi} &= \mathbf{Y}.\end{aligned}\tag{2.20}$$

The order in which these equations are solved is alternated to avoid systematic numerical effects (Strang 1968). We have the freedom of choosing the splitting of the source term any suitable way. We discuss a special way in Sect. 2.3.2.

From now on, we focus on the radial direction; the azimuthal integration is done in a similar way. We split Eq. (2.20) once more to obtain an equation without source terms, and solve this equation with a method originally proposed by Roe (1981), and extended by Eulerink & Mellema (1995) to a general relativistic method. The non-relativistic limit of this method yields a solver for the Euler equations in arbitrary coordinates.

Characteristics

Given the state (or the flux) immediately left and right of an interface of two grid cells, the Roe solver computes the resulting interface flux by solving:

$$\frac{\partial \mathbf{W}}{\partial t} + \mathcal{A}(\mathbf{W}) \frac{\partial \mathbf{W}}{\partial r} = 0,\tag{2.21}$$

where $\mathcal{A}(\mathbf{W}) = \partial \mathbf{F} / \partial \mathbf{W}$ is the Jacobian matrix. Roe's central idea is to approximate $\mathcal{A}(\mathbf{W})$ by a constant matrix $\tilde{\mathcal{A}}$. Since the Euler equations are hyperbolic, this matrix $\tilde{\mathcal{A}}$ has eigenvectors \mathbf{e}_k and corresponding eigenvalues λ_k . These can be used to diagonalize $\tilde{\mathcal{A}}$:

$$\mathcal{Q}^{-1} \tilde{\mathcal{A}} \mathcal{Q} = \mathcal{D},\tag{2.22}$$

where \mathcal{Q} is the matrix with right eigenvectors of $\tilde{\mathcal{A}}$. Now we can cast Eq. (2.21) into characteristic form:

$$\frac{\partial \mathbf{C}}{\partial t} + \mathcal{D} \frac{\partial \mathbf{C}}{\partial r} = 0,\tag{2.23}$$

where \mathbf{C} is the vector of characteristic variables, defined by

$$d\mathbf{C} = \mathcal{Q}^{-1} d\mathbf{W},\tag{2.24}$$

and \mathcal{D} is the diagonal matrix with eigenvalues of $\tilde{\mathcal{A}}$. From Eq. (2.23) it is easy to see that $d\mathbf{C} = 0$ along the path $\mathbf{r} = \mathcal{D}t$. These paths are called characteristics, and

are essential in the study of hyperbolic differential equations. Discontinuities (shocks) travel along characteristics, and the domains of influence and dependence are bounded by the characteristics.

We can integrate Eq. (2.23) to find a relation between the state and the characteristic variables:

$$\mathbf{W} = \mathcal{Q}\mathbf{C} = \sum_k a_k \mathbf{e}_k, \quad (2.25)$$

where a_k is the k -th characteristic variable. As the a_k are used to project the state on the eigenvectors of $\tilde{\mathcal{A}}$, they are called *projection coefficients*.

We can use the projection coefficients for calculating the interface flux, because we know that they are constant along characteristics. If we can figure out from which point in space the characteristics that cross the interface originate at the current time, we can just calculate the projection coefficients at that point in space and use Eq. (2.25) to find the state at the interface.

The interface flux is related to the interface state by:

$$\mathbf{F} = \tilde{\mathcal{A}}\mathbf{W} = \tilde{\mathcal{A}}\mathcal{Q}\mathbf{C} = \mathcal{Q}\mathcal{D}\mathbf{C} = \sum_k b_k \mathbf{e}_k, \quad (2.26)$$

where $b_k = \lambda_k a_k$. We present the exact expressions for the eigenvalues, eigenvectors and projection coefficients in Appendix 2.A.

We can project the flux difference at the interface we are considering on the eigenvectors of $\tilde{\mathcal{A}}$:

$$\mathbf{F}_R - \mathbf{F}_L = \sum b_k \mathbf{e}_k, \quad (2.27)$$

where \mathbf{F}_R and \mathbf{F}_L are the fluxes immediately right and left of the interface, respectively. Then the first order interface flux is approximated by:

$$\mathbf{F}_{i+1/2}^{n+1/2} = \frac{1}{2}(\mathbf{F}_L + \mathbf{F}_R) - \frac{1}{2} \sum \sigma_k b_k \mathbf{e}_k, \quad (2.28)$$

where $\sigma_k = \text{sign}(\lambda_k)$.

Flux limiter

The first order expression for the flux, Eq. (2.28), assumes a jump in the projection coefficients. That is: depending on the sign of the eigenvalue λ_k , we use the b_k corresponding to either the left or the right state. This procedure is correct if there is a shock right at that interface, so the state makes a jump there. In regions of smooth flow however, linear interpolation between the different b_k seems to be a better approach. To switch between the two kinds of interpolation a flux limiter ψ is used. We follow the suggestion by Roe (1985), in which one uses the ratio of the state difference at the interface $a_0 = [a_k]_{i+1/2}$ to the upwind state difference:

$$a_u = \begin{cases} (a_k)_{i-1/2} & \text{if } \lambda_k \geq 0; \\ (a_k)_{i+3/2} & \text{if } \lambda_k < 0. \end{cases}$$

Let

$$\psi(a_0, a_u) = \max(0, \min(pa_u, \max(a_0, \min(a_u, pa_0)))) + \min(0, \max(pa_u, \min(a_0, \max(a_u, pa_0))))). \quad (2.29)$$

This form of the flux limiter allows us to tune the way the method deals with sharp discontinuities through the parameter p . When $p = 2$, for example, the flux limiter is called "superbee". This limiter tends to create very sharp shocks, but tends to steepen shallow gradients, leading to numerical problems such as under- and overshoots. For $p = 1$ the limiter is called "minmod", which is more diffusive. To get the best of both worlds (sharp shocks but no under- or overshoots), we set $p = 1.5$ as our standard value.

With this flux limiter, the second order interface flux becomes:

$$\mathbf{F}_{i+1/2}^{n+1/2} = \frac{1}{2}(\mathbf{F}_L + \mathbf{F}_R) - \frac{1}{2} \sum (\sigma_k a_k - (\sigma_k - \nu_k) \psi_k) \lambda_k \mathbf{e}_k, \quad (2.30)$$

where $\nu_k = \lambda_k \Delta t / \Delta r$, the coefficient needed for linear interpolation. When $\psi_k = 0$ (shock), Eq. (2.28) is retrieved, while for $\psi_k = 1$ (smooth flow) the σ_k in Eq. (2.28) is replaced by ν_k and we interpolate linearly between the projection coefficients.

2.3.2 Stationary Extrapolation

The usual way for dealing with source terms is to split Eq. (2.20) once more to end up with an ordinary differential equation for the state:

$$\frac{\partial \mathbf{W}}{\partial t} = \mathbf{X}, \quad \frac{\partial \mathbf{F}}{\partial r} = 0, \quad (2.31)$$

thereby assuming that the flux is constant in space. The ordinary differential equation can be solved with any second-order integration scheme to yield a second-order update for the state.

However, it is also possible to take the opposite approach:

$$\frac{\partial \mathbf{W}}{\partial t} = 0, \quad \frac{\partial \mathbf{F}}{\partial r} = \mathbf{X}. \quad (2.32)$$

This is a method we call *stationary extrapolation*, because it assumes a stationary state within one grid cell. This equation is more difficult to solve, but it has certain advantages:

- The Roe solver solves a Riemann problem at the interface, a configuration with two *stationary* states separated by a discontinuity. Using actual stationary states on either side of the interface ensures that the Roe solver deals with a genuine Riemann problem.

- Physical stationary states are recognized. When the actual states *are* stationary, the Roe solver will produce no (unwanted) numerical evolution of these states. This property is related to the numerical instability found by Kley (1998) concerning the Coriolis force. We will see below that a scheme using stationary extrapolation does not suffer from this instability.

If we split the source terms appropriately:

$$\mathbf{X} = \begin{pmatrix} 0 \\ \Sigma r^2 (v_\phi + \Omega)^2 - \Sigma r \frac{\partial \Phi}{\partial r} + p \\ -2\Sigma v_r (\Omega + v_\phi) \end{pmatrix} \quad (2.33)$$

$$\mathbf{Y} = \begin{pmatrix} 0 \\ 0 \\ -\frac{\Sigma}{r} \frac{\partial \Phi}{\partial \phi} \end{pmatrix}, \quad (2.34)$$

the integrations can be done analytically (Eulderink & Mellema 1995). For isothermal, stationary flow in the radial direction Eq. (2.32) can be rewritten:

$$\frac{\partial}{\partial r} \begin{pmatrix} r\Sigma v_r \\ \frac{1}{2}(v_r^2 + r^2 v_\phi^2) + \Phi + c_s^2 \log(\Sigma) \\ r^2(v_\phi + \Omega) \end{pmatrix} = 0. \quad (2.35)$$

That is: the mass flux, the Bernoulli constant and the specific angular momentum are invariant. From these invariants the state at a cell interface can be computed from the state at the cell center. However, this procedure is computationally expensive, therefore it is feasible to adopt a first order approximation to calculate the interface fluxes:

$$\begin{aligned} \mathbf{F}_{i-1/2,R} &= \mathbf{F}_i - \frac{1}{2}\Delta r \mathbf{X}_i \\ \mathbf{F}_{i-1/2,L} &= \mathbf{F}_{i-1} + \frac{1}{2}\Delta r \mathbf{X}_{i-1}. \end{aligned} \quad (2.36)$$

This procedure can conserve stationary states up to second order (Mellema et al. 1991). However, Kley (1998) showed that the angular momentum in disk simulations deserves special attention. We illustrate this with a simple example. Consider the radial transport of angular momentum:

$$\frac{\partial}{\partial t}(r\Sigma v_\phi) + \frac{\partial}{\partial r}(r\Sigma v_r v_\phi) = -2\Sigma v_r (v_\phi + \Omega). \quad (2.37)$$

For stationary radial flow the mass flux and the specific angular momentum are constant: $r\Sigma v_r = D$ and $r^2(v_\phi + \Omega) = L$. For simplicity we assume here that D is constant for the whole computational domain. Consider the interface between cells i and $i - 1$. Stationary extrapolation from the cell centers to the interface $i - 1/2$ leads to the fluxes

$$F_L = D \left(\frac{L_{i-1}}{r_{i-1/2}^2} - \Omega \right) \quad (2.38)$$

$$F_R = D\left(\frac{L_i}{r_{i-1/2}^2} - \Omega\right). \quad (2.39)$$

With $v_r > 0$, the first order interface flux produced by the Roe solver is $F_{i-1/2} = F_L$. Therefore

$$L_{i-1/2} = r_{i-1/2}^2(F_L/D + \Omega) = L_{i-1}. \quad (2.40)$$

Stationary extrapolation from the interface back to the cell center i gives the final flux coming from the left for cell i :

$$F_{L,i} = D\left(\frac{L_{i-1}}{r_i^2} - \Omega\right). \quad (2.41)$$

From the same analysis for interface $i + 1/2$ we find the flux going to the right for cell i :

$$F_{R,i} = D\left(\frac{L_i}{r_i^2} - \Omega\right). \quad (2.42)$$

The first order update for the state is:

$$\Delta(r\Sigma v_\phi) = \frac{\Delta t}{\Delta r}(F_{L,i} - F_{R,i}) = \frac{\Delta t}{\Delta r} \frac{D}{r_i^2}(L_{i-1} - L_i). \quad (2.43)$$

The change in angular momentum $J = r^2\Sigma(v_\phi + \Omega)$ due to this update is given by:

$$\Delta J = \frac{\Delta t}{\Delta r} \frac{D}{r_i}(L_{i-1} - L_i). \quad (2.44)$$

It is easy to see that the conservative formulation of Kley (1998):

$$\frac{\partial}{\partial t}(r\Sigma L) + \frac{\partial}{\partial r}(r\Sigma v_r L) = 0, \quad (2.45)$$

leads to the same change in angular momentum. This shows that this new method does not suffer from the numerical instability due to the explicit treatment of the Coriolis force that was noted by Kley (1998). Note however that this does not hold for the approximate extrapolation of Eq. (2.36). Therefore we always use the exact extrapolation for the specific angular momentum, while keeping the method of approximate extrapolation to deal with the other source terms. This way we do not need to do the computationally intensive full stationary extrapolation, while keeping angular momentum nicely conserved.

Stationary extrapolation therefore provides a different point of view on the Coriolis instability: the failure of numerical hydrodynamic schemes to properly conserve angular momentum can be traced back to the failure to recognize stationary states. Rewriting the angular momentum equation as done by Kley (1998) is a way to solve this problem, but it only deals with the Coriolis source term while similar problems may exist due to the other source terms as well. Therefore we feel that it is a good idea to integrate *all* source terms using stationary extrapolation.

One disadvantage of stationary extrapolation is that it is not known a-priori if the assumption of stationary flow is valid. This is especially important when the source

terms are large, in our case very close to the planet. When dealing with more massive planets ($> 0.5 M_J$) the assumption of stationary flow along the coordinate axes breaks down, leading to numerical instabilities. A physical explanation is that the gas in this case will try to orbit the planet, perhaps forming a Keplerian disk, rather than to orbit the star. The flow is still semi-stationary, but only in a cylindrical coordinate frame centered on the planet, and this flow is at some points even orthogonal to the stationary flow in the frame of the star. Therefore, it seems appropriate to treat these larger source terms as external (see below). This transition from stationary to non-stationary extrapolation is applied smoothly at a typical distance R_R from the planet with a \sin^2 ramp.

External source terms

The stationary extrapolation deals with the geometrical source terms (including gravity, which is merely a geometrical effect in general relativity). Any other source term which we will call \mathbf{Z} is better integrated using Eq. (2.31):

$$\mathbf{W}^{n+1} = \mathbf{W}^n + \Delta t \mathbf{Z}. \quad (2.46)$$

In our case, \mathbf{Z} consists of the viscous source terms. The derivatives in these terms are calculated using a finite-difference method, and the resulting source is fed into Eq. (2.46).

2.3.3 Adaptive Mesh Refinement

Resolution is always an issue in numerical hydrodynamics, and a compromise has to be found between resolution and computational cost. Adaptive Mesh Refinement (AMR) is a very economic way of refining your grid where the highest resolution is needed, whereas keeping large parts of the grid at low resolution.

We have implemented the PARAMESH algorithm (MacNeice et al. 2000) to be able to resolve the region near the planet accurately. Usually the refinement criterion is taken to be the second derivative of the density, but we can also predefine the region that has to be refined. When running in this mode, and switching off additional refining and derefining, the algorithm works like the nested grid technique of D'Angelo et al. (2002). However, since our grid can be fully adaptive it is suited to let the planet migrate through the disk while keeping a high resolution near the planet. This will be the subject of a future study.

We use linear interpolation to communicate boundary cells between the different levels of refinement. The implementation of the monotonised harmonic mean (van Leer 1977) used by D'Angelo et al. (2002) made no significant difference. For every boundary between different levels we reset the flux into the lower level in order to conserve mass and momentum across the boundary.

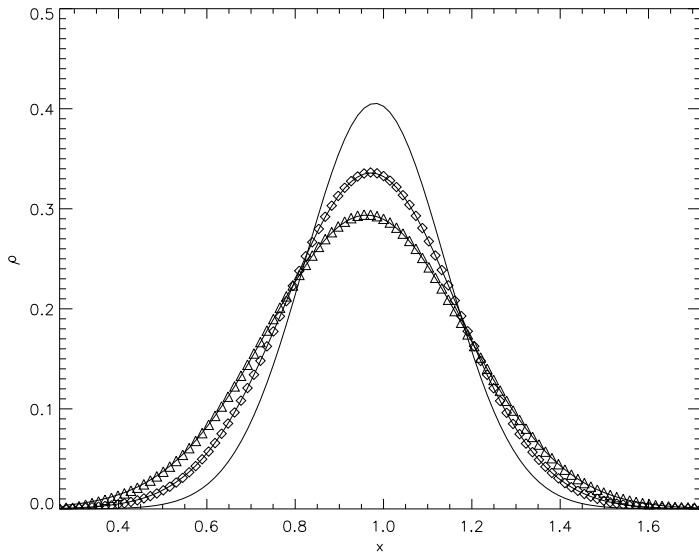


Figure 2.1: The evolution of the axisymmetric gas ring, initially located at $x=1$, shown at $\tau = 0.05$, and after 50 and 100 orbits. For the last two the numerical results are also plotted (diamonds and triangles, respectively).

2.3.4 Accretion

We follow D’Angelo et al. (2002) in modeling the accretion by taking away some fraction of the density within a distance of r_{acc} of the planet. Basically, the density is reduced with a factor

$$1 - f \Delta t, \quad (2.47)$$

where Δt is the magnitude of the time step. The two parameters that determine the accretion rate are r_{acc} and f , where f is taken to be twice its value in the inner half of r_{acc} . The mass taken out is monitored, assuming it has been accreted onto the planet, but without changing the dynamical mass of the planet.

Equation (2.47) can be seen as a first order approximation to the solution of the differential equation

$$\frac{d\rho}{dt} = -\frac{\rho}{\tau_{\text{acc}}}, \quad (2.48)$$

with the solution

$$\rho(t + \Delta t) = \rho(t)e^{-\Delta t/\tau_{\text{acc}}} \approx \rho(t)(1 - \Delta t/\tau_{\text{acc}}). \quad (2.49)$$

From this equation we see that the typical time scale τ_{acc} for emptying the accretion region is f^{-1} .

2.4 TEST PROBLEMS

We tested the RODEO method against several hydrodynamical test problems. First of all, the standard Sod shock tube (Sod 1978), in one and in two dimensions. For the two-dimensional problem, we have placed the initial discontinuity diagonal along the

grid, making it a genuine two-dimensional problem. The analytic solution was nicely recovered, except at the boundaries where some reflections were seen.

A more complicated test is the wind tunnel with step (Woodward & Colella 1984), which was previously used as a test problem by Mellema et al. (1991) using the same method. The results agreed very well. Note that both tests do use an energy equation.

2.4.1 Viscous ring spreading

To test the implementation of the viscous terms, we set up an axisymmetric ring of gas in Keplerian rotation about a central object. If we neglect pressure forces, the evolution of the surface density, which initially is a delta function, is given by (Pringle 1981):

$$\Sigma(r, t) = \frac{1}{\pi r_0^2 \tau x^{1/4}} e^{-\frac{1+x^2}{\tau}} I_{1/4} \left(\frac{2x}{\tau} \right), \quad (2.50)$$

where x denotes the normalized radial coordinate r/r_0 , with the ring initially located at $r = r_0$, and τ denotes the dimensionless time ($\tau = t/t_v$) in units of the viscous spreading time $t_v = r_0^2/12\nu$. $I_{1/4}$ denotes the Bessel function of the first kind of fractional order $1/4$.

As the analytical solution neglects any forces due to a pressure gradient, we have to make sure that we set the temperature to a very low value, or else pressure waves will dominate the pattern. We have used the same resolution as for simulations with the planet, and with a viscosity parameter $\alpha = 0.004$ at $x = 1$, comparable to the value used in the disk-planet simulations. We have placed the ring in the middle of the computational domain of $x \in [0.27, 1.73]$, with $\tau = 0.05$ initially because we cannot model a delta function numerically.

We have also performed a test run of this problem using $\alpha = 0$ to check for numerical viscosity, and it turned out that this (unwanted) numerical diffusion was very much lower than any physical viscosity at a low resolution of 128×384 . Note that this also shows that we can maintain a stable disk in Keplerian rotation. This is a nice result, showing that our conservative scheme conserves angular momentum very well.

Figure 2.1 shows the results for $\alpha = 0.004$. It is clear that the numerical solution agrees very well with Eq. (2.50), indicating that the implementation of the viscosity works. Only at the boundaries there are minor deviations from the analytical solution.

2.5 MODEL DESIGN

Throughout we use non-dimensional units. The unit of distance is the orbital radius of the planet, and the unit of time is the inverse orbital frequency. Note that this differs by a factor 2π from the orbital period of the planet.

2.5.1 Initial Conditions

The base resolution in all our simulations is $(n_r, n_\phi) = (256, 768)$, which leads to square cells near the position of the planet. We set $h = H/r = 0.05$, which determines the temperature through Eq. (2.10). We take a constant initial surface density. Because we do not consider the self-gravity of the disk the density can be given in any desirable unit, and we normalize it to 1 at the planet's position. We set the radial velocity to zero, although another possibility is to take an exact α -disk initially. The initial angular velocity is set to the value for a Keplerian disk, with a small correction for the pressure force.

We take a constant kinematic viscosity $\nu = 10^{-5}$, corresponding to $\alpha = 0.004$ at the location of the planet. We put in a planet at location $(r, \phi) = (1, \pi)$. This planet can be allowed to accrete matter (without changing its dynamical mass).

2.5.2 Boundary conditions

The inner and the outer boundary are located at 0.4 and 2.5, respectively. Imposing proper boundary conditions is not trivial, because waves are continuously hitting both edges of the grid, changing the sign of the radial velocity. A standard outflow boundary assumes that the velocity is always directed outward, and in combination with outgoing waves this leads to instabilities near the inner radius of the disk. A reflecting boundary, on the other hand, will lead to reflected waves traveling into the computational domain, which interact with the outgoing waves, destroying the flow structure.

Therefore we decided to take a *non-reflecting* boundary, following Godon (1996). This boundary treatment is based on characteristics, and as a result the implementation is particularly simple in our numerical scheme. The idea is to impose the boundary conditions on the characteristic variables, rather than on density, momentum or energy directly. Godon (1996) showed that this leads to a non-reflective boundary.

A ghost cell has to be updated according to incoming characteristics: when a characteristic leaves the last regular cell into the ghost cell, the corresponding characteristic variable of the ghost cell is updated accordingly. When a characteristic enters the ghost cell from outside the numerical domain, the characteristic variable is updated using the unperturbed (Keplerian) value. Using the Roe solver, this comes down to having *two* ghost cells: the outer one is never updated, so density and velocities remain at the initial values, and the inner one serves as the actual ghost cell. The latter is automatically updated by the Roe solver using characteristic variables, thereby following the suggestion by Godon (1996).

It turns out that these boundary conditions work especially well with stationary extrapolation, because then the hydrodynamics part as well as the boundary prescription are dealing with small fluctuations over a stationary background state. When we switch to the ordinary integration of source terms of Eq. (2.31) this is no longer true. In this case small numerical artifacts can be seen near the boundaries.

Therefore, as an addition we can add a wave-damping mechanism (de Val-Borro et al. 2006) that operates in the regions $0.4 < r < 0.5$ and $2.1 < r < 2.5$. In these regions

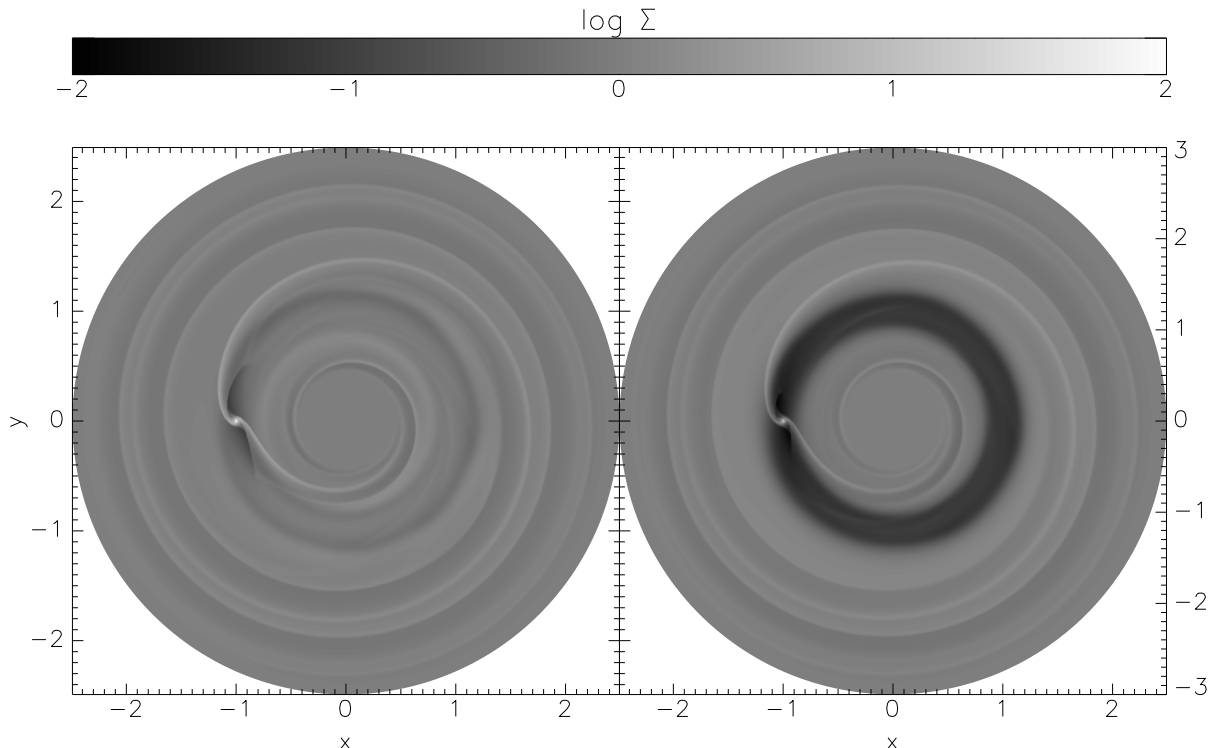


Figure 2.2: Greyscale plot in (x, y) after 10 orbits (left panel) and after 200 orbits (right panel) of a $1 M_J$ planet.

the state is relaxed to the initial (stationary) state on a time scale varying from infinity at $r = 0.5$ and $r = 2.1$ to 1 orbital period at the location of the boundary. Using this prescription, outgoing waves are damped gently as they approach the boundary of the computational domain.

2.6 GAP FORMATION

Only massive planets are able to open gaps in gas disks. There are two criteria that have to be fulfilled: firstly, the torques arising due to the presence of the planet must be able to overcome the viscous torques, leading to a minimum mass of (Bryden et al. 1999):

$$M_{\min, \nu} = \frac{40\nu}{\Omega_K r_p^2} M_\odot. \quad (2.51)$$

Secondly, Lin & Papaloizou (1993) suggested that at a distance of R_R from the planet the planet's gravity should be more important than pressure, which leads to another minimum mass for gap opening:

$$M_{\min, h} = 3 h^3 M_\odot. \quad (2.52)$$

For our disk, with $\nu = 10^{-5}$ and $h = 0.05$ both criteria yield approximately the same minimum mass, namely $0.4 M_J$. These criteria were shown to be valid within a factor

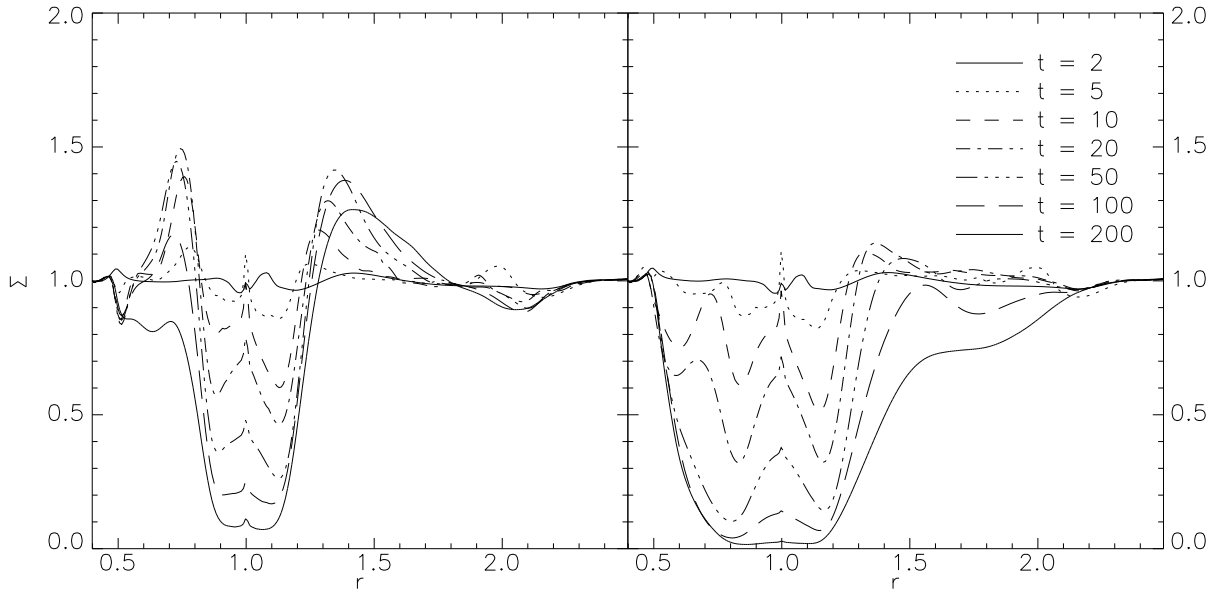


Figure 2.3: Gap formation for a $1 M_J$ planet. Left panel: azimuthally averaged surface density for the case of exact stationary extrapolation. Right panel: azimuthally averaged surface density for the case of approximate extrapolation. The indicated times are in planetary orbits.

of 2 in Bryden et al. (1999).

In our simulations, we found the density reduction factor near the orbit of the planet to be more than 100 for a $1 M_J$ planet, 10 for a $0.5 M_J$ planet and 2 for a $0.1 M_J$ planet. All factors were measured after 500 orbits of the planet. In view of these results, we can confirm that both criteria give a good estimate of the minimum mass for gap opening. This seems to contradict recent results from Rafikov (2002), who found that it takes only a fraction of $M_{\min,h}$ to open a gap. This fraction depends on viscosity and disk mass, and it can be as low as 0.1. We will look at this in detail in Chapter 3, where we show that in the inviscid limit we can reproduce the results of Rafikov (2002).

Figure 2.2 (left panel) shows a greyscale plot of the surface density after 10 orbits of a $1 M_J$ planet, and all the basic features in the flow are already visible. We can see two trailing spiral arms leaving the planet: the inner arm moves all the way down to the inner boundary, while the outer arm reaches to about $r = 1.5$. Note also the secondary waves excited in the inner and in the outer disk.

All spiral waves are stationary in the corotating frame. For this run we did not take out any matter inside the Roche lobe, so the density reaches very high values near the planet.

The formation of the gap is quite a violent process. There are structures visible in the corotating region and in the outer edge of the gap. The physical viscosity is able to damp these fluctuations, leading to a stable gap after 200 orbits (Fig. 2.2, right panel).

The left panel of Fig. 2.3 shows the azimuthally averaged surface density for the same run at different times. The gap that is formed is approximately $0.5 r_p$ wide, with two density bumps on either side. After 100 orbits the inner disk is starting to be

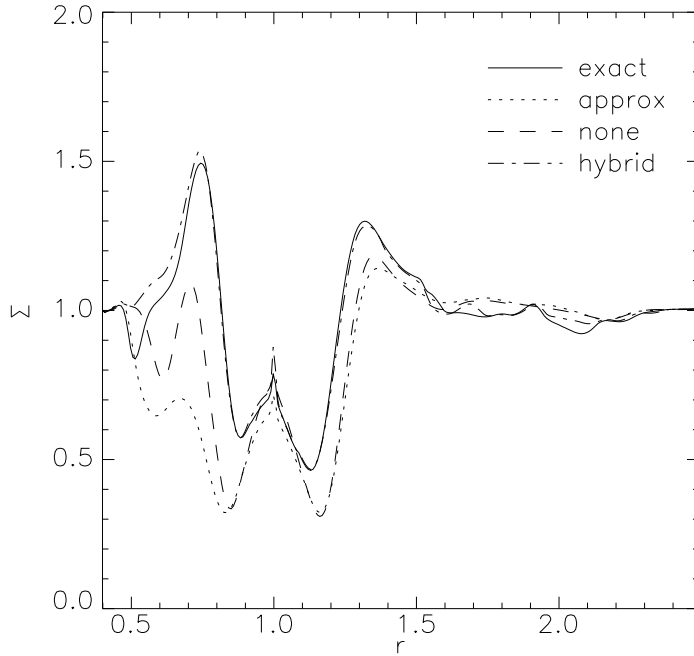


Figure 2.4: Azimuthally averaged density profile after 20 orbits for different implementations of the source term integration: exact stationary extrapolation, approximate extrapolation and no stationary extrapolation.

accreted onto the central star. At all times the position of the planet is visible as a small spike at $r = 1$.

The process of gap formation is numerically challenging, as was already shown by Kley (1998). In the remainder of this section we study the formation of gaps as a function of numerical parameters.

2.6.1 Source term integration

First of all we focus on the integration of source terms. We consider four different methods. First of all our standard scheme, in which we solve for the angular momentum exactly, and integrate all other source terms using Eq. (2.36). Secondly, we have the approximate scheme, where all source terms are integrated using Eq. (2.36). Next, we consider the case of no stationary extrapolation at all (see Eq. (2.31)), which is what ordinary Riemann-type schemes would use. Finally, we again integrate the angular momentum exactly, and all other source terms using Eq. (2.31). This mimics the fix found by Kley (1998), and we will refer to this scheme as *hybrid*, because it combines the two extremes of stationary extrapolation and no stationary extrapolation.

In Fig. 2.3 we show the formation of the gap for the exact stationary extrapolation (left panel) and the approximate stationary extrapolation (right panel). The difference between the two plots is quite dramatic. While both methods keep angular momentum conserved up to second order, approximate extrapolation leads to a much wider and deeper gap. After 200 orbits of the planet, even the region $1.5 < r < 2.1$ is participating in gap formation. From Fig. 2.3 it is clear that approximate extrapolation, while it preserves stationary states up to second order, is not the way to go in case of a strongly rotating fluid. Only the exact stationary extrapolation produces results comparable to

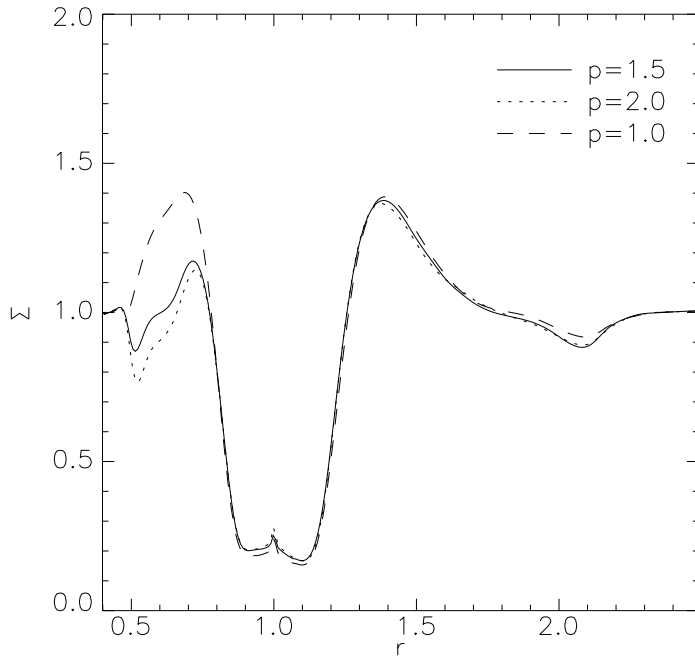


Figure 2.5: Azimuthally averaged density profile for a $1 M_J$ planet after 100 orbits for different flux limiters: $p = 1.5$ (standard value), $p = 2.0$ and $p = 1.0$ (see Eq. (2.29))

other codes (see de Val-Borro et al. 2006).

For these runs the wave damping boundary regions were employed to be able to compare to runs with no stationary extrapolation at all. The effect of the damping zones is clearly visible after 200 orbits, especially at the inner boundary.

Both models of Fig. 2.3 were also run in an inertial frame for comparison. For the case of exact extrapolation it made no difference at all, while only small changes were seen for approximate extrapolation. However, even in an inertial frame there is a Coriolis force term, see Eq. (2.5), so an inertial frame calculation is in this case not a valid check for the instability found by Kley (1998).

In Fig. 2.4 we compare the azimuthally averaged surface density profile for the four methods of source integration: standard, approximate, no stationary extrapolation at all, and the hybrid form. This figure shows that both the approximate extrapolation and the case of no stationary extrapolation overestimate the angular momentum transport, which leads to spurious gap widening. It is remarkable, however, that approximate extrapolation does the worst job, worse even than the run without stationary extrapolation. This is especially clear for the inner disk ($r < 1$). It is interesting to note that in this case trying to deal with the issue raised by Kley (1998) in an approximate way actually makes matters worse than for the standard source term integration.

The hybrid extrapolation reproduces the correct gap width and gap depth after 20 orbits, and follows closely the exact extrapolation almost everywhere. Only in regions where the strongest waves exist, near the planet and in the inner disk, the two methods give different results. Qualitatively hybrid extrapolation gives similar results as a more diffusive flux limiter (see Sect. 2.6.2).

We also performed the same simulations at a lower resolution. For the case of exact and hybrid extrapolation no differences were found, but for both other cases the

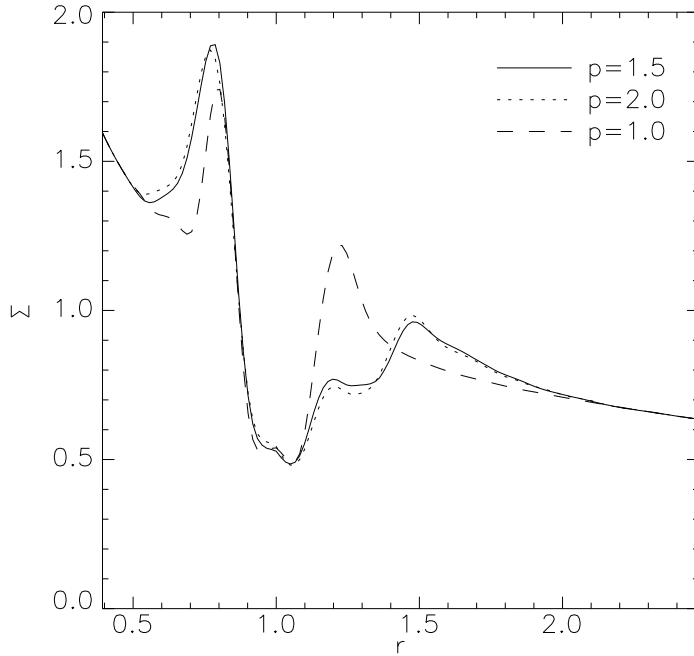


Figure 2.6: Azimuthally averaged density profile for a $0.1 M_J$ planet after 200 orbits in a non-viscous disk for different flux limiters: $p = 1.5$ (standard value), $p = 2.0$ and $p = 1.0$ (see Eq. (2.29))

width and structure of the gap changed significantly, especially for the approximate stationary extrapolation. It is clear from Eq. (2.36) that the error made in this approximate scheme will depend on the spatial resolution of the grid. On a grid of only $(n_r, n_\phi) = (128, 384)$ the effect of gap widening is even more dramatic than seen in Fig. 2.3. The inner disk is cleared away even faster, leading to an unstable situation near the boundary. For the case of no stationary extrapolation the effect is not that severe, but still the gap is wider than in Fig. 2.4.

2.6.2 Flux limiter

The flux limiter is basically a switch between using a first or second order interface flux for the state update. Near shocks it should be first order, in smooth flow it should be second order. Applying a second order flux near a discontinuity leads to numerical smearing of the state, and therefore the flux limiter that switches the fastest to first order fluxes gives the least numerical diffusion. Here we study the effect of this numerical diffusion on the formation and appearance of the gap. In Fig. 2.5 we show the gap structure for three different limiters (see Eq. (2.29)): $p = 1.0$ (minmod, most diffusive), $p = 2.0$ (superbee, least diffusive) and $p = 1.5$ which we call soft superbee. In the outer disk all limiters give more or less the same result. But in regions where the waves induced by the planet are the strongest, the inner disk and close to the planet, we see clear differences. The diffusive minmod limiter damps the ingoing waves more than the other limiters, leading to an enhanced surface density near $r = 0.7$. Close to the planet this higher diffusion also leads to an enhanced surface density, seen as a spike at $r = 1$ in Fig. 2.5.

There are no large differences in the results obtained with the superbee limiter and

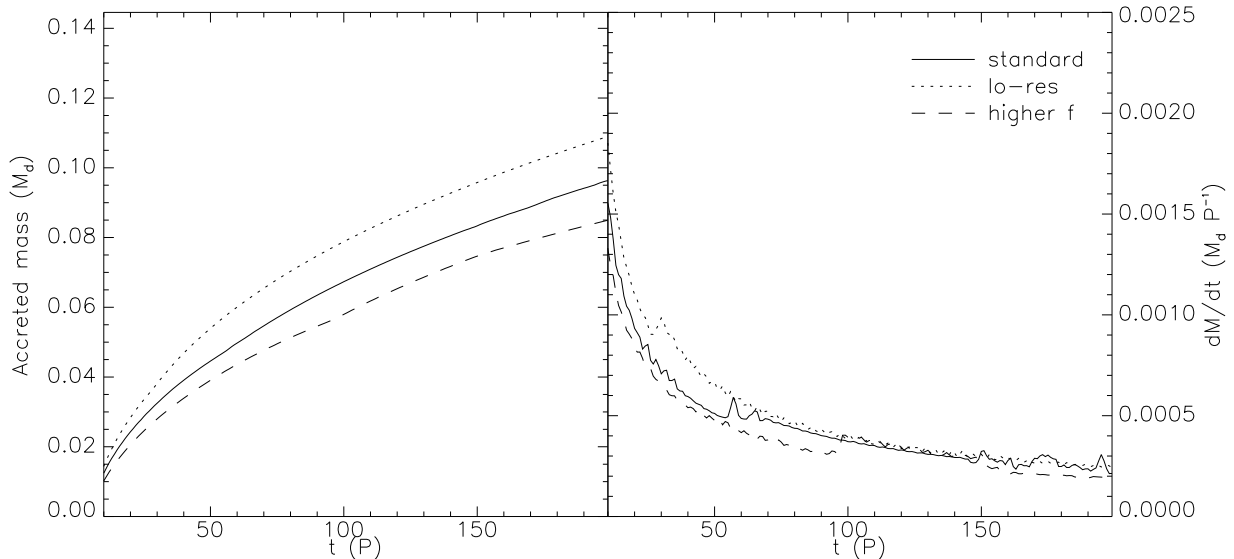


Figure 2.7: Accretion onto a $1 M_J$ planet. Left panel: total accreted mass in units of the initial disk mass. Right panel: accretion rate, in units of disk masses per orbit.

its softer version. This indicates that our choice of $p = 1.5$ (see Sect. 2.3.1) is a good trade-off between the two extremes minmod and superbee. It inherits the low numerical diffusion from superbee, as is clear from Fig. 2.5, while it is more stable against numerical overshoots.

Since the different limiters imply different numerical viscosities, it is interesting to study how they influence the result in the case when there is no physical viscosity added to the simulations. Then the situation changes drastically, because numerical viscosity starts to play a major role, in particular the length over which shocks are damped. As an illustration, we show the azimuthally averaged surface density for a $0.1 M_J$ planet in a viscosity-free disk in Fig. 2.6, for the three different flux limiters. It is clear that for the diffuse minmod limiter the waves are damped much faster, and the angular momentum is deposited much closer to the planet. For the superbee limiter, as well as its softer version, a much wider gap results.

2.7 ACCRETION RATES

Now we turn to the problem of accretion onto the planet. The growth rate of the planet is important because it determines the ultimate mass the planet will reach. Two-dimensional studies of D’Angelo et al. (2002) and Lubow et al. (1999) showed that a planet of $1 M_J$ grows approximately at a rate of $10^{-4} M_d P^{-1}$, where M_d is the disk mass within the computational domain. However, the study by Kley (1999) done at lower resolution indicated an accretion rate more than ten times higher.

In this section we look at three different mass regimes: high-mass planets, which open clear gaps in the disk, low-mass planets, which do not open gaps, and intermediate mass planets, which create only small density dips around their orbit.

2.7.1 High mass planet

We start by discussing the results for a $1 M_J$ planet. Because this planet is able to open up a gap in the disk, the accretion rate is determined by the amount of mass that flows through the gap (Kley 1999), and less by the density structure close to the planet.

In Fig. 2.7 we show the accreted mass and the accretion rate as a function of time for our standard resolution, accretion parameters, source term integration and flux limiter (solid lines). Because we do not start with an initial gap the accretion rate is very high at the beginning of the simulation, dropping about one order of magnitude in 200 orbits to a value of $2 \cdot 10^{-4}$ (disk masses per orbit). We ran one model to 500 orbits, and the final accretion rate turned out to be $1.5 \cdot 10^{-4}$. The fact that the accretion rate approaches a constant value after about 500 orbits and the actual value found agree within a factor 2 with D'Angelo et al. (2002) and Lubow et al. (1999). The planet accretes approximately 10 percent of the total disk mass during the simulation.

Accretion parameters

The accretion procedure is described by two parameters: the radius within which we take out material (r_{acc}) and the value of f (see Eq. (2.47)). We can vary these to see if this influences the final accretion rate.

In Fig. 2.7 the accretion rates onto a $1 M_J$ planet are shown for the standard case ($r_{\text{acc}} = 0.5 R_R$ and $f = 0.5$) and for parameters $r_{\text{acc}} = 0.1 R_R$ and $f = 5/3$ (the curve labeled with "higher f "). The standard set was used by Kley (1999), and the other case by D'Angelo et al. (2002). Note that the accretion areas differ by a factor 25, while f varies only by a factor 3.3. So for identical density distributions close to the planet the standard parameters yield 7.5 times more accreted mass during one time step. Despite this the final accretion rate is the same for both sets of parameters.

Because of the different accretion radii any difference in accretion rate would imply that the flow within the Roche lobe is important for the accretion process. Disk material that makes it to $0.5 R_R$ is accreted for the standard parameters, while it has to make it all the way to $0.1 R_R$ to be accreted in the second case. The fact that we do not see any differences indicates that the accretion rate is determined by the amount of mass the disk is able to supply, independent of local processes near the planet.

Resolution

Our base resolution corresponds to approximately 8 cells per R_R , which means that the standard accretion area is resolved by only a few grid cells. This might be of influence on the inferred accretion rate, and therefore we performed simulations on different resolutions.

First of all we lowered the resolution with a factor of 2, the same resolution as in Kley (1999). In this case we do not resolve the Roche lobe, so if the flow close to the planet is important for accretion we would expect differences. However, since the two sets of accretion parameters did not yield different accretion rates we expect no big resolution effects. Indeed, Fig. 2.7 shows that for this low resolution case (dotted line)

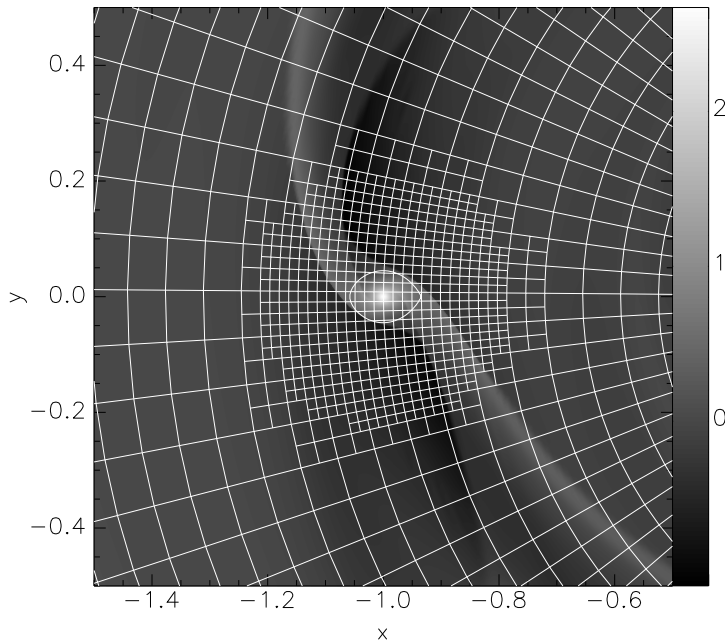


Figure 2.8: Close-up on the logarithm of the surface density near the planet. Overplotted is the AMR mesh structure, where each block consists of 8×8 cells.

the accretion rate is the same as for our standard resolution. This shows that resolving the flow within the Roche lobe is not important for gap-opening planets, at least not for determining accretion rates.

It is computationally very expensive to go up a factor of 2 in resolution on the whole grid, therefore we used our AMR module to refine the region around the planet. Figure 2.8 shows a close-up on the density pattern after 20 orbital periods. Overplotted are the Roche lobe and the grid structure. Each block represents 8×8 cells, so that we have approximately 1500 cells within the Roche lobe. Therefore we can really resolve the flow inside the Roche lobe with this resolution. Nevertheless also this resolution yielded the same accretion rate of $2 \cdot 10^{-4} M_d P^{-1}$.

Equation of state

It is interesting to compare accretion rates for a truly isothermal simulation and a run that does include an energy equation, but at a very low adiabatic exponent Γ . This has been done before to mimic isothermal flow for planet-disk interaction (Nelson & Benz 2003). The basic idea is that for a low value of Γ the gas can be compressed without a large change in temperature. In order to check the validity of this approach regarding planet-disk interaction, we ran simulations including an energy equation but with a low value of Γ .

We performed two simulations including an energy equation, one with $\Gamma = 1.001$ and one with $\Gamma = 1.01$. The latter value was also used by Nelson & Benz (2003). We found that the basic flow structures remain the same, and that the temperature profile does not change anywhere but very close to the planet. For $\Gamma = 1.001$ the temperature rises already by a factor 10, and for $\Gamma = 1.01$ by a factor of 60. This steep temperature gradient slows down the gas flow towards the planet considerably.

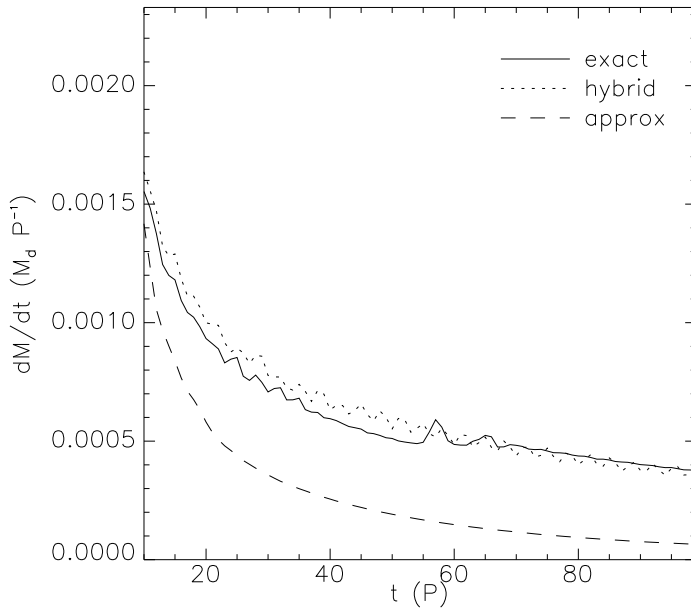


Figure 2.9: Accretion rates onto a $1 M_J$ planet for three different methods of source term integration.

Due to the higher temperatures close to the planet the accretion slows down. Already for $\Gamma = 1.001$ the accretion rate drops by a factor of 2, and even a factor of 10 for $\Gamma = 1.01$. This shows that the accretion rate depends very much on the temperature near the planet, and that “nearly” isothermal simulations can produce very different results from truly isothermal runs.

This effect is different from the one described in Kley (1999), who found that a polytropic equation of state leads to a reduction in the accretion rate. Because the temperature is proportional to the density in that case (for $\Gamma = 2$), the gap region is much cooler and therefore the viscosity is reduced when the α -formalism is used. In our case, there is a temperature *rise* very close to the planet, which leads to a pressure barrier that is able to slow down accretion considerably, even when Γ is as low as 1.001. Therefore we conclude that these kinds of simulations are not able to mimic isothermal flow for this specific case, due to the deep potential well of the planet.

Source term integration

In Fig. 2.3 we demonstrated that the way source terms are included has dramatic effects on the process of gap formation. In this section we show that this also affects the accretion onto the planet.

Figure 2.9 shows the accretion rates for three different methods of source term integration: exact, hybrid and approximate extrapolation. See Sect. 2.6 for their definition. Again, as in Fig. 2.3 approximate extrapolation is the odd one out, yielding a 4 times lower accretion rate. This clearly has to do with the difference in gap formation time scale, and again it is clear that approximate extrapolation is not the way to go.

Both the exact and hybrid method give the same results. This is not surprising, because the region where the methods differ most is where the source terms are large: close to the planet. And as we mentioned before, this region is not important for the

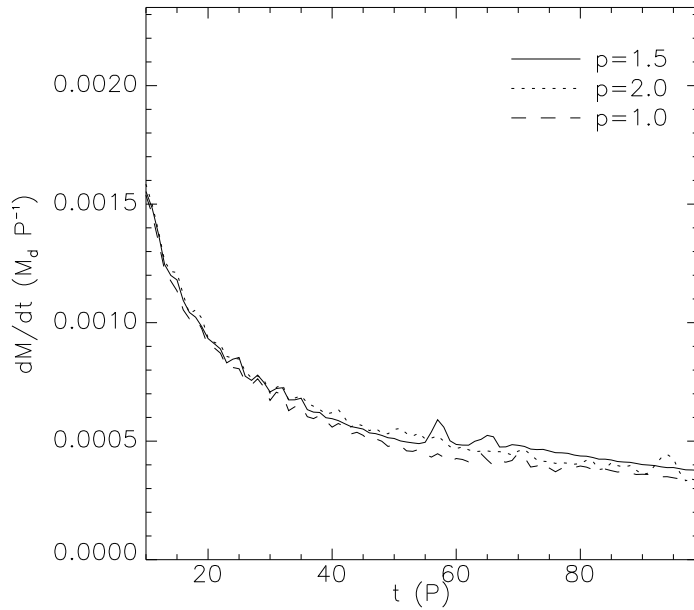


Figure 2.10: Accretion rates onto a $1 M_J$ planet for three different flux limiters.

accretion rate.

Flux Limiter

The flux limiter did not play a major role in gap formation (see Fig. 2.5), only at the inner parts of the disk some differences can be seen. Figure 2.10 shows the accretion rates for the three different limiters discussed in Sect. 2.6. It is clear that the accretion rate does not depend at all on the flux limiter.

This can be understood if one realizes that it is the flow from the outer disk to the inner disk that governs the accretion rate (see Kley 1999). But in the outer disk the waves are weaker than in the inner disk, so a different flux limiter should not change the mass flux from the outer disk very much.

2.7.2 Low mass planet

We now move to the other side of the planetary mass spectrum to investigate accretion onto planets that do not open gaps in the disk. Specifically we focus on a planet with mass $M_J/64$. Because $R_R \propto M_p^{1/3}$ the Roche lobe of this planet is 4 times as small as the Roche lobe of a Jupiter-mass planet.

In Fig. 2.11 the solid line gives the accretion rate for our standard parameters and 4 levels of AMR. For our base resolution the Roche lobe would only be resolved by only 1 grid cell, clearly not enough to study accretion. Figure 2.11, dashed line, shows that 2 levels of refinement, yielding 4 cells per R_R , is still not enough to reproduce the result for 4 levels of AMR. The accretion rates for 3 and 4 levels of AMR agree very well, showing that at least 8 cells per R_R are needed for accurately modeling accretion.

All accretion rates have reached their final value after 30 orbits. The model with 4 levels of refinement was run until 200 orbits with no change in the accretion rate. This

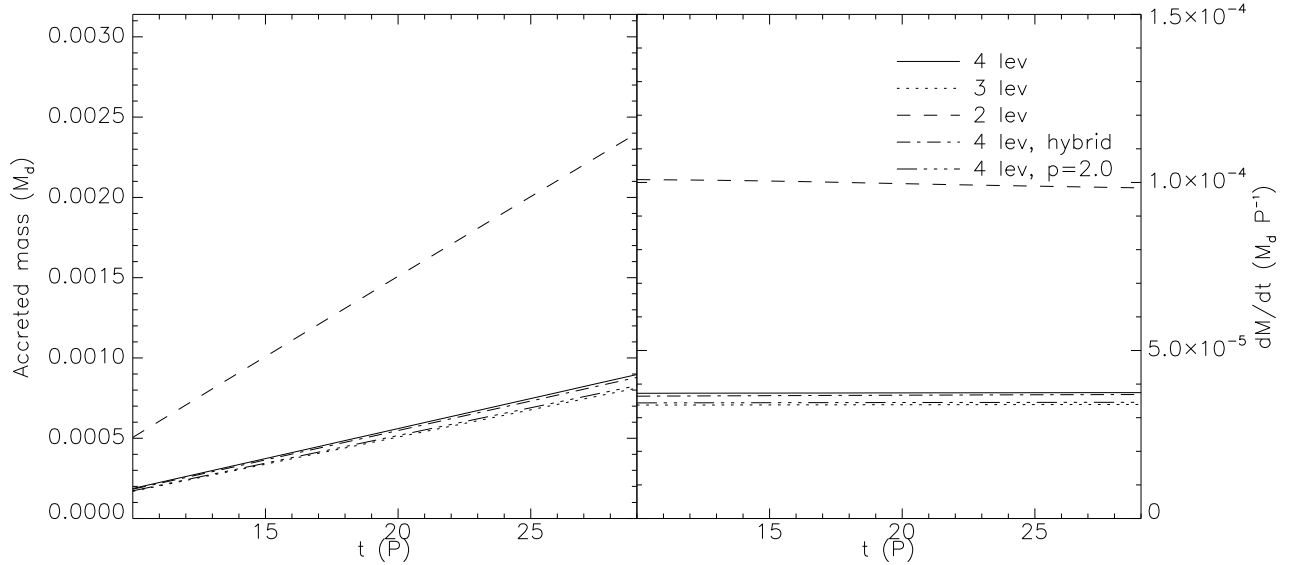


Figure 2.11: Accretion onto a $1/64 M_J$ planet. Left panel: total accreted mass in units of the initial disk mass. Right panel: accretion rate, in units of disk masses per orbit.

is because the planet does not open up a gap, which would take about 200 orbits (see Sect. 2.6). The value of $3.5 \cdot 10^{-5}$ that we find is in good agreement with the results of D’Angelo et al. (2002). Note however that they need 7 grid levels, corresponding to approximately 6 levels of AMR for our simulations, while we need only 3 levels to obtain the same result.

Because we have already discarded the approximate extrapolation scheme in Sect. 2.6 and Sect. 2.6.1 we looked only at the difference between exact extrapolation and hybrid extrapolation for the low-mass case. However, we point out that in this case approximate extrapolation gave identical results. This is because the waves from this planet are too weak to make a difference in angular momentum flow. From Fig. 2.11 we see that both methods we considered for source term integration give identical results. In this case the planetary gravitational source terms are too small to cause a large difference in accretion rate.

Also different flux limiters gave identical results. In Fig. 2.11 we only show the superb-ee-result, but the minmod limiter yielded exactly the same accretion rate. This was to be expected, because in the limit of smooth flow (or, equivalently, no strong waves, as is the case for a low-mass planet) all limiters produce the same flux (see Eq. (2.29) with $a_0 = a_u$).

2.7.3 Intermediate mass planet

The masses that lie in between the two extremes we have considered so far are perhaps the most interesting. In this regime the transition from linear disk response to gap formation takes place, and therefore also the transition from Type I to Type II migration. D’Angelo et al. (2002) find the highest accretion and migration rates here. Also, the

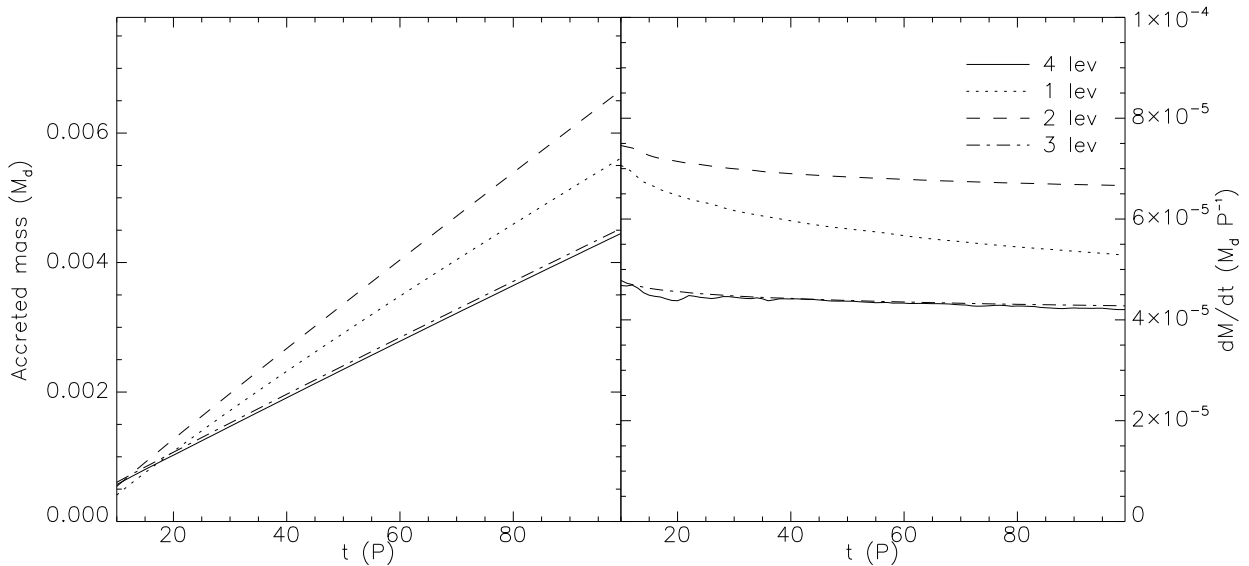


Figure 2.12: Accretion onto a $1/8 M_J$ planet. Left panel: total accreted mass in units of the initial disk mass. Right panel: accretion rate, in units of disk masses per orbit.

cores of giant planets may well be in this mass range.

For this section we focus on a planet of mass $1/8 M_J$, which makes its Roche lobe twice as small as for a Jupiter-sized planet. In Fig. 2.12 we compare the accretion rates for different resolutions. First of all, note that we need a relatively high resolution to obtain convergence (3 levels of refinement, which amounts to 16 cells per R_R). This is already an indication that interesting things are going on. Secondly, we find an accretion rate that is about twice as low as was found by D’Angelo et al. (2002). In view of the good agreement for the low-mass planet this is remarkable.

In Fig. 2.13 we compare the standard model with the method of hybrid extrapolation and the minmod flux limiter. While for the high-mass planet as well as the low-mass planet these three methods gave identical results, for a $1/8 M_J$ planet they differ significantly, giving a 66 % and 100 % higher accretion rate for the hybrid extrapolation and minmod limiter, respectively. With the most diffusive flux limiter we can reproduce the result of D’Angelo et al. (2002). This shows that numerical diffusion is a very important issue in these kinds of simulations.

It is not surprising that the diffusive minmod limiter increases the accretion rate, because it tends to smear out the strong density and velocity gradients near the planet, allowing mass to diffuse into the Roche lobe. For this planet local conditions determine the accretion rate, unlike the previous cases. Low-mass planets do not excite strong enough waves to alter their environment significantly, while high-mass planets open up gaps, and the accretion rate is therefore determined by the global evolution of the disk. Planets of intermediate mass, however, do not clear a gap while they excite reasonably strong waves, making the dynamics very interesting.

A similar story applies to the source term integration. We have seen no differences between exact and hybrid extrapolation for high and low-mass planets, while for our $1/8 M_J$ planet the difference is quite dramatic. Again, the gravitational forces due to

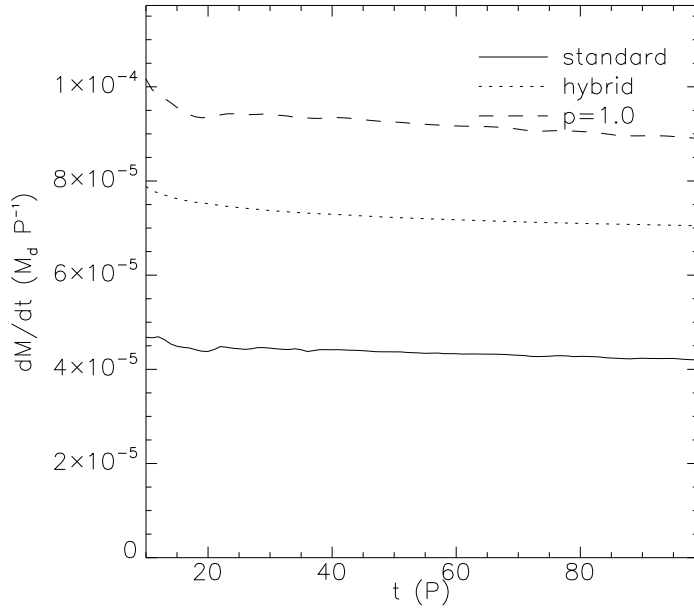


Figure 2.13: Accretion rates onto a $1/8 M_J$ planet for the standard case (solid line), hybrid extrapolation (dotted line) and the minmod limiter (dashed line).

low-mass planets are too weak to cause a difference, while for high-mass planets the local conditions are irrelevant.

2.7.4 Dependence on planetary mass

In the previous sections we have looked in detail at three characteristic planetary masses. Here we focus on how the accretion rate depends on the mass of the planet. We have run simulations for planets from $0.5 M_{\oplus}$ up to $8 M_J$, or, in other words, from deep in the linear regime to well above the gap-opening mass.

In the left panel of Fig. 2.14 we show the accretion rate for all planetary masses, as well as the relation found by D’Angelo et al. (2002). As was mentioned in Sect. 2.7.2 the results for the low-mass planets agree very well with those found by D’Angelo et al. (2002). However, as soon as the disk response to the planet approaches the non-linear regime around $M_p \approx 0.1 M_J$ the results start to differ significantly. At first, the accretion rate stays low, but around $M_p \approx 0.2 M_J$ there is a strong rise leading to a maximum at $0.5 M_J$, followed by a steep decline.

The general features of the plot are consistent with the results of D’Angelo et al. (2002): the accretion rate rises with planetary mass, with a maximum around $0.5 M_J$, followed by a steeper decline. However, the rise as well as the decline are much more dramatic in our case, leading to a higher maximum accretion rate and lower accretion rates for the highest mass planets.

The diamonds in Fig. 2.14 represent the results obtained with the diffusive minmod limiter wherever they differed significantly from the standard case. We conclude that a diffusive flux limiter always tends to increase accretion onto the planet, especially in the mass regime in which the transition from linear to non-linear disk response takes place.

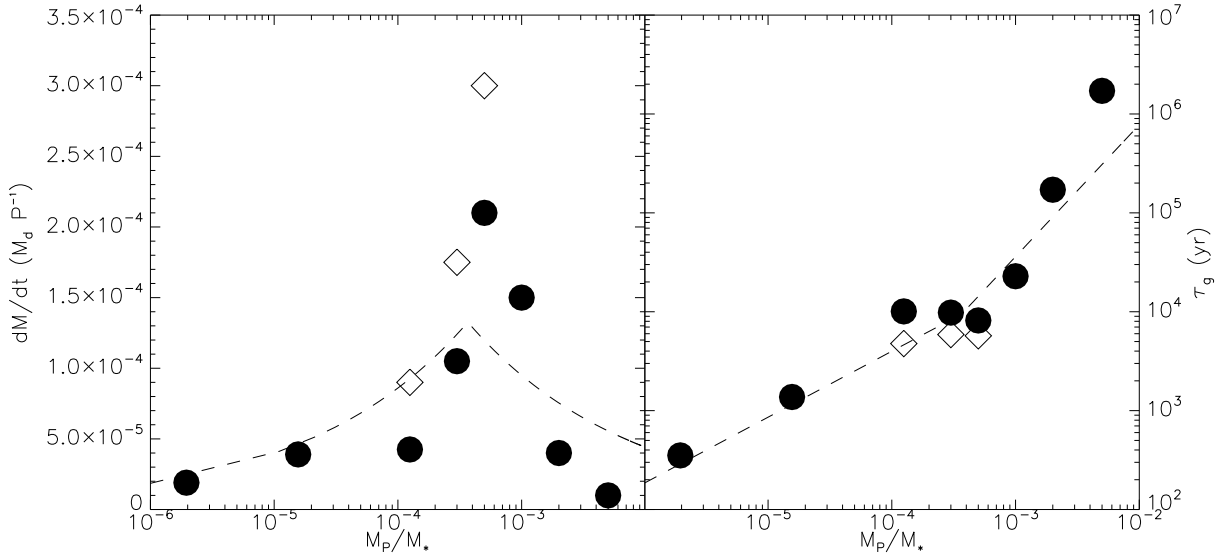


Figure 2.14: Left panel: accretion as a function of planet mass. Right panel: growth time (see Eq. (2.53)). Filled circles indicate our standard result, diamonds give the results for the diffusive minmod limiter wherever they were different. In both panels the fit of D’Angelo et al. (2002) is shown by the dashed line.

The difference between the results obtained with the minmod flux limiter and our standard limiter can be as large as 50% (see Fig. 2.14). Because these differences are caused by purely numerical effects, one can interpret these as an estimate of the error in the values of the accretion rates in this mass regime. Keeping these error estimates in mind, we see that our results are roughly in agreement with the relation found by D’Angelo et al. (2002). Note, however, that our standard results always represent the lowest possible accretion rate. Different flux limiters or different source term integrations always lead to a higher accretion rate.

The growth time scale is defined as the time it takes for a planet to double its mass at a given accretion rate:

$$\tau_g \equiv \frac{M_p}{dM_p/dt}. \quad (2.53)$$

In order to express τ_g in years we took a disk mass of $0.0035 M_\odot$. When for a given mass τ_g becomes comparable to the total disk life time the planet can not grow beyond this mass. This limiting mass is of the order of several M_J (D’Angelo et al. 2002). However, they do not consider planets more massive than $1 M_J$.

In the right panel of Fig. 2.14 we show τ_g for all planet masses. Again, the dashed curve shows the fit from D’Angelo et al. (2002). Because of the logarithmic scale on the y-axis the differences are much less pronounced. However, we still see the two different regimes and the sharp transition. Very important is the steep rise in τ_g for the highest masses. Assuming that the planet spends maximal 10^6 years inside this disk the maximum mass it can reach is $4 M_J$. Note that if we exclude the planets more massive than $1 M_J$ the slope of the growth time scale is in excellent agreement with the relation found by D’Angelo et al. (2002). Extrapolating this slope we would

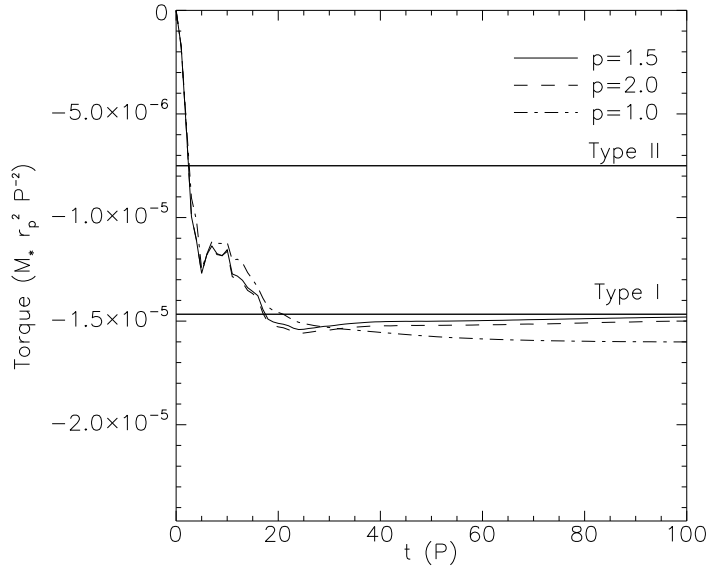


Figure 2.15: Torque exerted on a $1/8 M_J$ planet, for three different flux limiters. The whole Roche lobe is excluded for these calculations.

find that the maximum mass that can be reached is about $10 M_J$. This shows that it is really necessary to include the highest mass planets to obtain a reliable estimate of the maximum planetary mass that can be reached through disk accretion.

The decline in accretion rate that we find for high-mass planets is steeper than found by Lubow et al. (1999), who used the ZEUS code for their simulations. We have shown that this is not due to the flux limiter or the source term integration, and the reason for this difference may be found in the intrinsic difference between the finite-difference approach and Riemann solvers. However, this is impossible to verify within our numerical method.

2.8 MIGRATION

It has become clear in recent years that protoplanets can be extremely mobile within their protoplanetary disk. Three types of migration can be distinguished: Type I, which concerns low-mass planets that do not open gaps in the disk, Type II for migration inside a clear gap, and Type III, for which the radial movement of the planet drives its migration (Masset & Papaloizou 2003). Because our planet stays at a fixed location, we are only dealing with Type I and Type II migration.

For the torque calculations, we exclude material orbiting within the Roche lobe of the planet, and we assume an initial disk mass of $0.0035 M_\odot$.

2.8.1 Numerical Parameters

Migration rates turn out to be very robust once the Roche lobe as well as the disk scale height is well resolved. Across the whole mass spectrum we found no significant torque differences for the various methods of source term integration and flux

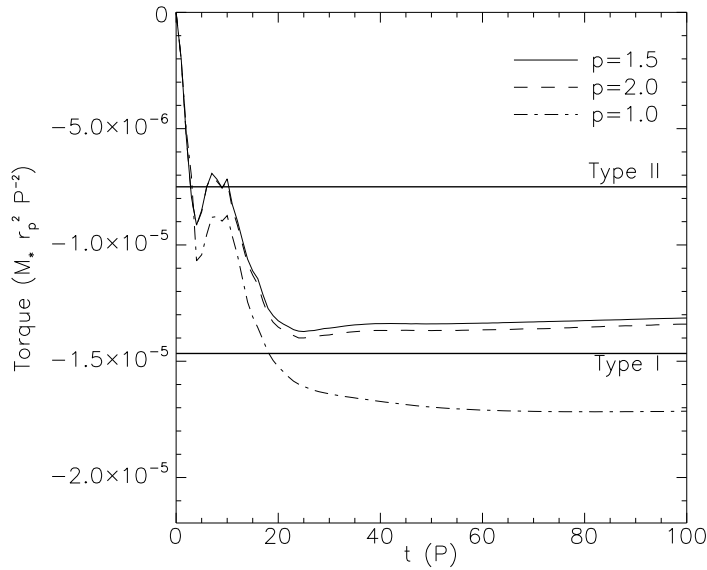


Figure 2.16: Torque exerted on a $1/8 M_J$ planet, for three different flux limiters. Only the inner half of the Roche lobe is excluded for these calculations.

limiters. Even approximate extrapolation, which was shown to lead to spurious numerical evolution of the gap, does not affect the torque on the planet. This is because for low-mass planets approximate extrapolation does not alter the density structure around the planet (see Sect. 2.7.2), and for high-mass planets it only speeds up gap formation, which leads to Type II migration.

As an example we show in Fig. 2.15 the torque as a function of time for a $1/8 M_J$ planet for different flux limiters. All three limiters lead to a torque that is comparable to Type I migration. As with gap formation, the difference between $p = 1.5$ and $p = 1.0$ is larger than the difference between $p = 1.5$ and $p = 2.0$ (see Fig. 2.5), but for the torque the effect is not significant. This shows that the sensitivity of the accretion rate on numerical parameters found in Sect. 2.7.3 is due to effects *inside* the Roche Lobe, while we explicitly excluded this region for the torque calculations of Fig. 2.15.

This is further illustrated in Fig. 2.16, where we again show the total torque on the planet, but now we exclude only the inner half of the Roche lobe. The first thing to note is that the minmod limiter now gives a significantly different result compared to the other two. We found similar behavior for the accretion rate in Sect. 2.7.3.

Secondly, we observe that the torque is less negative for $p = 1.5$ and $p = 1.0$. This is the torque reversal also observed by D’Angelo et al. (2002): material within the Roche lobe exerts a *positive* torque on the planet, slowing down migration. However, it is not clear exactly where the disk ends and the envelope of the planet starts. A gas giant is usually assumed to fill its Roche lobe during formation (Pollack et al. 1996), so all material orbiting inside the Roche lobe is part of the envelope. Therefore the question rises whether a planet should change its orbit due to its own envelope. On the other hand, important physical processes are not included in the current hydrodynamical simulations of planet-disk interaction, namely heat transport (due to the isothermal assumption) and self-gravity. Both can have dramatic influence on the direct surroundings of the planet, where the density is highest and the temperature may

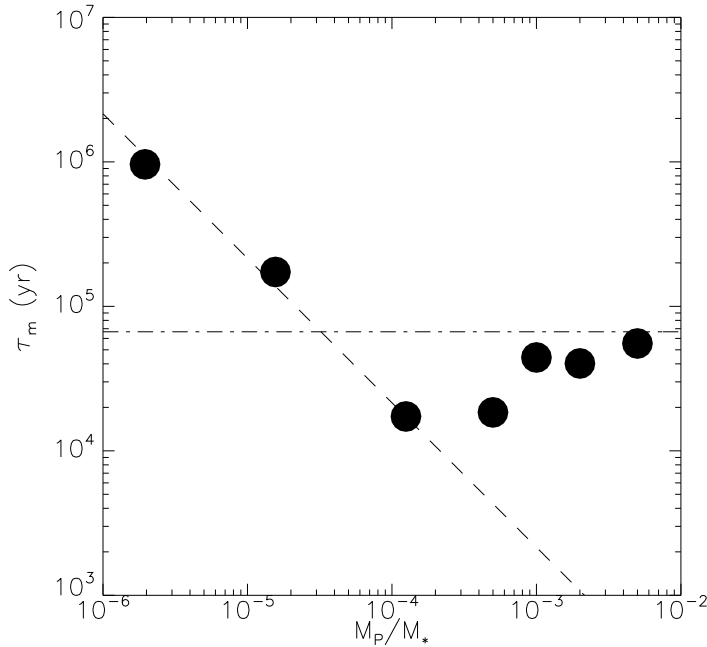


Figure 2.17: Migration time scales for planets of different mass. Dashed line: analytical solution by Tanaka et al. (2002) for Type I migration. Dash-dotted line: result by Ward (1997) for Type II migration.

differ significantly from the ambient disk, and therefore it is not feasible yet to make a connection between the one-dimensional planet formation models of Pollack et al. (1996) and the hydrodynamic models of planet-disk interaction. For now, we are only interested in comparing our values to previous analytical and numerical results, which will be done in the next section.

2.8.2 Dependence on planetary mass

For the low-mass case of Type I migration there exists a nice analytical prediction of the migration rate as a function of planetary mass (Tanaka et al. 2002). For gap-opening planets, the migration rate should not depend on planetary mass, only on the viscosity in the disk (Ward 1997). Numerical simulations show that in between these two extremes the fastest migration takes place, in two-dimensional simulations (D’Angelo et al. 2002) as well as in three-dimensional simulations (Bate et al. 2003; D’Angelo et al. 2003).

In Fig. 2.17 we show the migration time scale τ_m defined by:

$$\tau_m = \frac{r_p}{|v_{r,p}|}, \quad (2.54)$$

where the radial velocity of the planet due to a torque \mathcal{T} is given by:

$$v_{r,p} = 2r_p \frac{\mathcal{T}}{L_p}. \quad (2.55)$$

Here \mathcal{T} is the torque due to the disk *on* the planet.

From Fig. 2.17 we see that we can reproduce Type I as well as Type II migration. The transition region extends approximately from $M_p = 0.1 M_J$ to $M_p = 1.0 M_J$, consistent

with the three-dimensional results of Bate et al. (2003). A planet of mass $0.1 M_J$ has the fastest migration time scale of approximately 10^4 years.

Comparing Figs. 2.14 and 2.17 we see that for the low-mass planets the growth time scale is much shorter than the migration time scale, while for the high-mass planets it is the other way around. In the intermediate case, both time scales are approximately equal.

2.9 SUMMARY AND CONCLUSIONS

We have presented a new method for modeling disk-planet interaction. Key features of the RODEO method are: it is a conservative method, it treats shocks and discontinuities correctly, and it uses stationary extrapolation to integrate the geometrical and gravitational source terms.

We found that the RODEO method performs very well on the problem of disk-planet interaction, not in the least because we do not experience serious computational difficulties as for example in Kley (1998). We have shed some new light on this matter in that this instability can be seen to result from the failure of most hydrodynamic schemes to recognize stationary states.

We find that the process of gap formation crucially depends on source term integration. Only exact and hybrid extrapolation produce gaps of correct width. A diffusive flux limiter leads to a more pronounced inner edge of the gap.

The accretion rates turn out to be very robust in the low-mass regime ($M_p < 0.1 M_J$) as well as in the high-mass regime ($M_p \geq 1.0 M_J$): they are independent of numerical resolution, accretion parameters and source term integration. A different equation of state affects the accretion rates significantly: even a very low Γ of 1.001 that is used frequently to mimic isothermal flow the accretion rate drops by a factor of 2.

For intermediate mass planets the accretion rates are far less certain. They are dependent on the flux limiter used as well as on the way source terms are integrated. Within our method we find differences of 50%, and the differences between our results and the similar study of D'Angelo et al. (2002) are of the same order. This shows that the error bars on these values are very large.

For the highest mass planets we find significantly lower accretion rates than in previous numerical studies, limiting the maximum planet mass that can be reached to about $4 M_J$. Note that this is in fact the first numerical study that consistently goes beyond this limiting mass so that no extrapolation is required.

Migration rates are far more robust than accretion rates, as long as we limit the disk region that exerts a torque on the planet to outside the planetary Roche lobe. Therefore the region where most differences arise in the accretion rates is located deep within the Roche lobe.

We can nicely reproduce the analytical results for Type I and Type II migration, with a transition region extending from $M_p = 0.1 M_J$ to $M_p = 1.0 M_J$. In this transition region the fastest migration rate corresponds to a mass of $0.1 M_J$.

The RODEO method can also be used for two-fluid calculations (see Paardekooper & Mellema 2004) to model dust-gas interaction in protoplanetary disks. Also, the

method can easily be extended to three dimensions, and is also suited to treat an energy equation in a multi-dimensional set-up. We will consider these extensions in forthcoming Chapters.

ACKNOWLEDGMENTS

The authors would like to thank Pawel Artymowicz for stimulating discussions and useful suggestions. The research of GM has been made possible by a fellowship of the Royal Netherlands Academy of Arts and Sciences. This work was sponsored by the National Computing Foundation (NCF) for the use of supercomputer facilities, with financial support from the Netherlands Organization for Scientific Research (NWO).

2.A EXPLICIT EXPRESSIONS

Here we give explicit expressions of the eigenvalues, eigenvectors and projection coefficients for the isothermal Euler equations in cylindrical coordinates.

2.A.1 Radial direction

The Jacobian matrix \mathcal{A} is given by:

$$\mathcal{A} = \begin{pmatrix} 0 & 1 & 0 \\ c_s^2 - v_r^2 & 2v_r & 0 \\ -v_r v_\phi & v_\phi & v_r \end{pmatrix}. \quad (2.56)$$

The eigenvalues of this matrix are:

$$\begin{aligned} \lambda_1 &= v_r - c_s \\ \lambda_2 &= v_r + c_s \\ \lambda_3 &= v_r. \end{aligned} \quad (2.57)$$

The corresponding eigenvectors:

$$\begin{aligned} \mathbf{e}_1 &= (1, v_r - c_s, v_\phi) \\ \mathbf{e}_2 &= (1, v_r + c_s, v_\phi) \\ \mathbf{e}_3 &= (0, 0, 1). \end{aligned} \quad (2.58)$$

A vector $\Delta \equiv (\Delta_\rho, \Delta_r, \Delta_\phi)$ can be projected on these eigenvalues using the following projection coefficients, found by solving the system $\mathcal{C}\mathbf{a} = \Delta$, where \mathcal{C} is the matrix with the eigenvectors:

$$\begin{aligned} a_1 &= \frac{1}{2c_s}((c_s + v_r)\Delta_\rho - \Delta_r) \\ a_2 &= \frac{1}{2c_s}((c_s - v_r)\Delta_\rho + \Delta_r) \\ a_3 &= \Delta_\phi - v_\phi \Delta_\rho. \end{aligned} \quad (2.59)$$

2.A.2 Azimuthal direction

The Jacobian matrix \mathcal{A} is given by:

$$\mathcal{A} = \begin{pmatrix} 0 & 1 & 0 \\ -v_r v_\phi & v_\phi & v_r \\ \frac{c_s^2}{r^2} - v_\phi^2 & 0 & 2v_\phi \end{pmatrix}. \quad (2.60)$$

The eigenvalues of this matrix are:

$$\begin{aligned} \lambda_1 &= v_\phi - c_s/r \\ \lambda_2 &= v_\phi + c_s/r \\ \lambda_3 &= v_\phi. \end{aligned} \quad (2.61)$$

The corresponding eigenvectors:

$$\begin{aligned} \mathbf{e}_1 &= (1, v_r, v_\phi - c_s/r) \\ \mathbf{e}_2 &= (1, v_r, v_\phi + c_s/r) \\ \mathbf{e}_3 &= (0, 1, 0). \end{aligned} \quad (2.62)$$

A vector $\Delta \equiv (\Delta_\rho, \Delta_r, \Delta_\phi)$ can be projected on these eigenvalues using the following projection coefficients, found by solving the system $\mathcal{C}\mathbf{a} = \Delta$, where \mathcal{C} is the matrix with the eigenvectors:

$$\begin{aligned} a_1 &= \frac{1}{2c_s} ((c_s + rv_\phi)\Delta_\rho - r\Delta_\phi) \\ a_2 &= \frac{1}{2c_s} ((c_s - rv_\phi)\Delta_\rho + r\Delta_\phi) \\ a_3 &= \Delta_r - v_r\Delta_\rho. \end{aligned} \quad (2.63)$$

REFERENCES

- Artymowicz, P. 2004, in ASP Conf. Ser. 324: Debris Disks and the Formation of Planets, 39
- Balbus, S. A. & Hawley, J. F. 1990, BAAS, 22, 1209
- Bate, M. R., Lubow, S. H., Ogilvie, G. I., & Miller, K. A. 2003, MNRAS, 341, 213
- Beckwith, S. V. W. & Sargent, A. I. 1996, Nature, 383, 139
- Boss, A. P. 1997, Science, 276, 1836
- Bryden, G., Chen, X., Lin, D. N. C., Nelson, R. P., & Papaloizou, J. C. B. 1999, ApJ, 514, 344
- Cameron, A. G. W. 1978, Moon and Planets, 18, 5
- D'Angelo, G., Henning, T., & Kley, W. 2002, A&A, 385, 647
- D'Angelo, G., Kley, W., & Henning, T. 2003, ApJ, 586, 540

- de Val-Borro, M., Edgar, R. G., Artymowicz, P., et al. 2006, *MNRAS*, 370, 529
- Eulderink, F. & Mellema, G. 1995, *A&AS*, 110, 587
- Gammie, C. F. 1996, *ApJ*, 457, 355
- Godon, P. 1996, *MNRAS*, 282, 1107
- Goldreich, P. & Tremaine, S. 1980, *ApJ*, 241, 425
- Kley, W. 1998, *A&A*, 338, L37
- Kley, W. 1999, *MNRAS*, 303, 696
- Kley, W. 2000, *MNRAS*, 313, L47
- Lin, D. N. C. & Papaloizou, J. 1986, *ApJ*, 309, 846
- Lin, D. N. C. & Papaloizou, J. C. B. 1993, in *Protostars and Planets III*, 749–835
- Lubow, S. H., Seibert, M., & Artymowicz, P. 1999, *ApJ*, 526, 1001
- MacNeice, P., Olson, K. M., Mobarry, C., de Fainchtein, R., & Packer, C. 2000, *Computer Physics Communications*, 126, 330
- Masset, F. S. & Papaloizou, J. C. B. 2003, *ApJ*, 588, 494
- Mellema, G., Eulderink, F., & Icke, V. 1991, *A&A*, 252, 718
- Nelson, A. F. & Benz, W. 2003, *ApJ*, 589, 556
- Nelson, R. P. & Papaloizou, J. C. B. 2003, *MNRAS*, 339, 993
- Nelson, R. P., Papaloizou, J. C. B., Masset, F., & Kley, W. 2000, *MNRAS*, 318, 18
- Paardekooper, S.-J. & Mellema, G. 2004, *A&A*, 425, L9
- Pollack, J. B., Hubickyj, O., Bodenheimer, P., et al. 1996, *Icarus*, 124, 62
- Pringle, J. E. 1981, *ARA&A*, 19, 137
- Rafikov, R. R. 2002, *ApJ*, 572, 566
- Rafikov, R. R. 2005, *ApJ*, 621, L69
- Roe, P. L. 1981, *J. Comp. Phys*, 43, 357
- Shakura, N. I. & Sunyaev, R. A. 1973, *A&A*, 24, 337
- Sod, G. A. 1978, *J. Comp. Phys*, 27, 1
- Strang, G. 1968, *Siam. J. Num. Analysis*, 5, 506
- Tanaka, H., Takeuchi, T., & Ward, W. R. 2002, *ApJ*, 565, 1257
- van Leer, B. 1977, *Journal of Computational Physics*, 23, 276
- Ward, W. R. 1997, *Icarus*, 126, 261
- Woodward, P. & Colella, P. 1984, *J. Comp. Phys*, 54, 115

CHAPTER 3

Gap opening by planets in inviscid disks

Sijme-Jan Paardekooper

To be submitted

WE study the process of gap formation in protoplanetary disks by tidal waves launched by low-mass planets. The non-linear evolution of these waves may lead to shock formation, and the subsequent dissipation of angular momentum flux opens up the possibility even for low-mass planets to create a deep annular gap in the disk. We focus on the inviscid limit, to separate dissipation by shocks from viscous dissipation. We perform two-dimensional numerical hydrodynamical simulations using the RODEO method, which uses an approximate Riemann solver to treat shock waves in a correct way. This is necessary, since we are specifically interested in shock formation. We find that indeed in the inviscid limit the tidal waves carrying angular momentum flux dissipate locally due to shock formation, even for a planet of only $6 M_{\oplus}$ around a $1 M_{\odot}$ star. Therefore also low-mass planets are able to open up gaps in protoplanetary disks, although the time scale for gap opening for a $6 M_{\oplus}$ planet around a $1 M_{\odot}$ star is already 10000 orbits and even longer for planets of lower mass.

3.1 INTRODUCTION

It is generally believed that planets are born inside circumstellar disks around young stars, and it is the gravitational interaction of the planets with their place of birth that determines the final outcome of the planetary formation process in terms of the final masses and orbits of the planets. Gravitational torques induced by the planet lead to transport of angular momentum by spiral density waves (Goldreich & Tremaine 1979, 1980), which gives rise to inward planet migration. When the planet is massive enough an annular gap may be opened by the planet (Lin & Papaloizou 1986). These gaps are of critical importance for the evolution of the planet.

First of all, the formation of the gap slows down gas accretion onto the planet, and although it does not stop completely (Kley 1999) there exists a maximum mass that a planet may reach through disk accretion (Lubow et al. 1999; D'Angelo et al. 2002; Paardekooper & Mellema 2006). This mass is of the order of a few Jupiter masses (M_J).

Secondly, the opening of the gap marks the transition from the rapid Type I migration to the much slower Type II migration (Ward 1997). When a gap forms, the planet is basically locked to the evolution of the disk and migrates inward on a viscous time scale. This transition from fast to slow migration is critical for the survival of high-mass planets.

Gaps in disks can also be used to detect newly formed planets in protoplanetary disks (Wolf & D'Angelo 2005) in nearby star-forming regions. These observations will provide important constraints on the theory of planet formation. It is therefore necessary to study the dependence of gap formation on planetary mass and disk parameters (Bryden et al. 1999).

Another interesting effect is that what continuum observations trace (the distribution of dust) may not be the same as what gasdynamical simulations predict (the gas distribution). Paardekooper & Mellema (2004) showed that gaps form much more easily in the dust than in the gas, lowering the minimum planetary mass for gap formation *in the dust* from approximately $1 M_J$ to $0.05 M_J$.

However, even for the gas alone the situation is not entirely clear yet. Bryden et al. (1999) confirmed the standard gap formation criteria, which we will discuss in Sect. 3.2, to within a factor of 2 through numerical simulations, while Rafikov (2002b) claims that planets of much lower mass may open gaps in disks. In this Chapter, we will test the analytical gap-opening criteria through numerical simulations of a planet embedded in an inviscid disk

The reason for focusing on inviscid disks is three-fold. First of all, the viscosity driving accretion onto the central star is probably either due to the Magneto-Rotational Instability (Balbus & Hawley 1990), which leads to very turbulent disks (Nelson & Papaloizou 2003) or absent altogether in so-called dead zones (Gammie 1996). The anomalous turbulent viscosity that has been widely used in simulations of planet-disk interaction is capable of describing neither of the two cases.

Secondly, in the inviscid limit new physical effects may show up that are otherwise damped by viscosity. One example is the absence of the corotation torque in inviscid disks (Masset 2001, 2002) which may lead to eccentricity evolution of the planet because corotation resonances tend to damp eccentricity (Goldreich & Sari 2003). An-

other interesting effect that only seems to show up in the inviscid limit is the formation of vortices near the edges of a shallow gap (Koller et al. 2003; Li et al. 2005).

The third reason is of numerical origin. The inviscid case is much more challenging for any numerical method because the physical viscosity tends to smear out sharp gradients, regardless of the intrinsic numerical viscosity. Therefore non-viscous simulations provide better insight in the abilities and limitations of the numerical method used.

The plan of the Chapter is as follows. In Sect. 3.2 we start by reviewing the analytical estimates of the minimum planetary mass for gap formation. Then, in Sect. 3.3 we describe the numerical method, and in Sect. 3.4 we show the results. We give a brief discussion on the results in Sect. 3.5 and conclude in Sect. 3.6.

3.2 GAP FORMATION THEORY

In this section we take a closer look at the processes that lead to gap formation. We adopt a cylindrical two-dimensional coordinate system (r, ϕ) , centered on the primary star. We will keep track of the viscous terms in the equations although we are mainly aiming at inviscid disks. Throughout we will use units in which the orbital radius of the planet r_p , the orbital frequency of the planet Ω_p and the gravitational constant times the central mass GM_* are all equal to 1.

We consider a thin disk with a constant relative thickness $h = H/r$ where H is the pressure scale height. The two-dimensional treatment of the disk is only valid when $h \ll 1$, and in this study we use $h = 0.05$. The temperature profile is calculated assuming vertical hydrostatic equilibrium, and it is taken to be constant with time. Basically we assume that the disk is able to radiate all excess energy away very efficiently. We do not include self-gravity of the gas, therefore the analysis is only valid in the limit $Q \rightarrow \infty$, where Q is Toomre's parameter. This approximation is valid for typical protoplanetary disks with masses of approximately $0.01 M_\odot$.

3.2.1 Conditions for gap formation

In general, the evolution of the surface density Σ of an axisymmetric disk is governed by conservation of mass and angular momentum (Pringle 1981):

$$\frac{\partial(r\Sigma)}{\partial t} + \frac{\partial(r\Sigma v_r)}{\partial r} = 0 \quad (3.1)$$

$$\frac{\partial(r\Sigma L)}{\partial t} + \frac{\partial(r\Sigma v_r L)}{\partial r} = -\frac{1}{2\pi} \frac{\partial(G - F)}{\partial r} \quad (3.2)$$

where $L = r^2\Omega$ is the angular momentum, Ω is the angular velocity, v_r is the radial velocity, and G and F are the viscous and planetary angular momentum fluxes, respectively. The viscous transport of angular momentum is governed by a kinematic viscosity ν :

$$G = -2\pi r^3 \nu \Sigma \frac{\partial \Omega}{\partial r} \quad (3.3)$$

The total angular momentum flux induced by the planet through wave excitation at Lindblad resonances can be written as (Goldreich & Tremaine 1980):

$$F_0 = 0.93q^2\Sigma r^4\Omega^2h^{-3} \quad (3.4)$$

where q is the secondary to primary mass ratio.

The most straightforward condition for a gap to form is that the angular momentum transport due to density waves exceeds the viscous angular momentum transport: $F > G$. This leads to a minimum planetary mass of:

$$q_\nu = \sqrt{\frac{10\nu h^3}{r_p^2\Omega_p}} \quad (3.5)$$

Note that this expression differs from the one for q_ν found by Bryden et al. (1999). For the typical values $h = 0.05$ and $\nu = 10^{-5}$ that are commonly used in simulations of planet-disk interaction this minimum mass amounts to $q_\nu \approx 10^{-4}$.

Lacking any form of viscosity, this linear theory predicts that no gap should form for any planetary mass because the angular momentum needs to be deposited locally. However, when non-linear waves come into play the situation is different, because non-linear waves (i.e. shocks) indeed dissipate locally and therefore they will promote gap formation.

The condition for shocks to form at the location of the planet was found by Lin & Papaloizou (1993) and Korycansky & Papaloizou (1996) to be that a planet should be more massive than:

$$q_H = 3h^3 \quad (3.6)$$

This condition is equivalent with requiring that the Roche lobe of the planet ($R_R = r_p(q/3)^{1/3}$) should exceed the disk thickness H at the location of the planet.

However, as pointed out by Goodman & Rafikov (2001) this condition may be too strict, because a wave that starts as a linear wave at the location of the planet may shock after traveling a certain distance, after which the angular momentum carried by the wave is dissipated. Rafikov (2002b) showed that this mechanism leads to much less strict conditions for gap formation, even in the presence of an anomalous turbulent viscosity. For inviscid disks, the claim is that *all* planets open up gaps. In this Chapter we would like to verify this through a series of dedicated numerical simulations.

3.2.2 Gap width

The width Δ of a gap opened by a planet depends on the length over which the angular momentum waves are damped. For viscous disks Δ depends on the magnitude of the turbulent viscosity ν . For inviscid disks damping only sets in when the wave shocks, which happens after traveling a distance (Goodman & Rafikov 2001):

$$l_{\text{sh}} \approx 1.4 \frac{2H}{3} \left(\frac{\Gamma + 1}{8/15} \frac{q}{q_H} \right)^{-2/5} \quad (3.7)$$

where Γ is the adiabatic exponent of the gas. Since we will compare these results to isothermal numerical simulations we take $\Gamma = 1$. Goodman & Rafikov (2001) consider a barotropic equation of state with $\Gamma > 1$, but in Appendix 3.A we show that a similar analysis can be carried out for an isothermal equation of state.

At distances larger than l_{sh} the angular momentum waves are damped by non-linear wave evolution. The angular momentum flux F is then:

$$F(r) = F_0 \left(1 - \zeta \left(\frac{r - r_p}{l_{\text{sh}}} \right) \right) \quad (3.8)$$

where ζ is the damping function found by Goodman & Rafikov (2001), which can be approximated by (Rafikov 2002b):

$$\zeta(z) = \begin{cases} 1 & z < z_{\text{sh}} \\ (1 + (z/z_{\text{sh}} - 1)^2)^{-1/4} & z > z_{\text{sh}} \end{cases} \quad (3.9)$$

Angular momentum is most readily deposited where the derivative of ζ has a minimum, which happens at $z = 1.43$. At this distance from the planet the effect of the planet is largest, and it can be used as an approximate half-width of the gap that may be formed:

$$\Delta \approx 1.43 l_{\text{sh}} \quad (3.10)$$

This analysis is valid when the region of wave excitation is well-separated from the point at which the wave becomes non-linear, so when $l_{\text{sh}} \gg H$. In view of Eq. (3.7) this amounts to the requirement

$$q \ll q_1 \equiv \left(1.4 \frac{2}{3} \right)^{5/2} \frac{8/15}{\Gamma + 1} q_H. \quad (3.11)$$

Note that the estimate of Eq. (3.10) gives the distance from the planet at which the angular momentum is deposited most readily, so at that location the gap grows fastest. The final gap may be much larger.

3.2.3 Time scale

In order to open a gap of half-width Δ the planet has to remove the total angular momentum between $r = r_p$ and $r = r_p + \Delta$:

$$L_\Delta = \frac{1}{2} \pi \Sigma \Omega r_p^2 \Delta^2 \quad (3.12)$$

The time needed to transport this amount of angular momentum is given by:

$$\tau = \frac{L_\Delta}{F_0} = 1.69 \frac{\Delta^2 h^3}{r_p^2 q^2} \Omega^{-1} \quad (3.13)$$

When we put in the estimate for the gap width, Eq. (3.10), we see that

$$\tau \approx 2.52 h^{37/5} q^{-14/5} \Omega^{-1}. \quad (3.14)$$

Putting in the requirement $q \ll q_H$ leads to $\tau \gg 0.116 h^{-1}$ as a lower limit on the time scale for gap formation. For a typical value of $h = 0.05$ we find $\tau \gg 2 \Omega^{-1}$. We see immediately Eq. (3.14) breaks down for $q \approx q_H$, because gap-opening for high-mass planets takes several hundreds of orbits (Bryden et al. 1999; Paardekooper & Mellema 2006).

3.3 NUMERICAL METHOD

We use the RODEO method (Paardekooper & Mellema 2006) to solve the Euler equations in two dimensions. The method makes use of an approximate Riemann solver (Roe 1981) for the advection and stationary extrapolation (Eulderink & Mellema 1995) to integrate the source terms. Because we are interested in non-linear wave evolution we need the correct treatment of shocks that is intrinsic to Riemann solvers, as opposed to ZEUS-type finite-difference schemes.

3.3.1 Flux limiter

There is no explicit artificial viscosity in the code. However, to obtain second-order accuracy in regions of smooth flow a flux-limiter is used. This limiter is responsible for switching to first-order accuracy whenever a discontinuity is present at a specific location in the flow. Different limiter functions may lead to different results in a discontinuous flow. For an overview of flux limiters and their applications see LeVeque (2002). A diffusive limiter tends to stick to second-order accuracy, which leads to artificial smearing of shocks. On the other hand, a very non-diffusive limiter may lead to instabilities due to numerical overshoots. We discuss results obtained by three different limiter functions: the diffusive minmod limiter, the non-diffusive superbee limiter and its softer version. See Paardekooper & Mellema (2006) for their definition.

The importance of the adopted flux limiter in the context of non-linear wave evolution is clear: a very non-diffusive limiter like superbee may artificially shock the planetary wake at smaller distances than l_{sh} , which would lead to smaller gaps. On the other hand, the wave is less easily damped, which would lead to wider gaps. It is not immediately clear which of these two effects will be dominant.

3.3.2 Potential smoothing

The gravitational potential in the models consists of three parts. There is the potential of the central star, the potential of the planet and there are indirect potential components due to the fact that a coordinate system based on the primary star is accelerated. Because we are mainly dealing with planets of low mass, these indirect terms are relatively unimportant.

The planetary component of the potential is singular at the location of the planet. There are two main reasons for working with a smoothed version of this potential rather than the singular version. One is to avoid numerical instabilities near the planet.

Name	n_r	n_ϕ	Δr
low	128	384	0.0164
medium	192	576	0.0110
high	256	768	0.0082
ultra	384	1152	0.0055

Table 3.1: Resolution parameters. First column: name by which the resolution is referred to in the text. Second and third column: number of radial and azimuthal cells, respectively. Fourth column: radial size of a grid cell (in units of r_p).

Although one can avoid infinite forces by placing the planet on a corner of a grid cell while the forces are calculated at the cell centers, still the very large planetary source terms may lead to large errors or even instabilities. A common approach is to take the smoothing length ϵ a small fraction of the Roche lobe, where the canonical value of ϵ is $0.2 R_R$ (see Kley 1999; Lubow et al. 1999). However, for very low-mass planets this smoothing length may well be smaller than a single grid cell, which is essentially the same as using no smoothing at all. Alternatively one could smooth the potential over a fixed amount of computational cells (D’Angelo et al. 2002). This has the advantage that the potential is always resolved, but care must be taken that ϵ should always be much smaller than the scale of interest. For wave excitation, this scale is H , while for gas accretion onto the planet this scale is R_R . In this Chapter we focus on non-linear wave evolution, therefore we need to resolve the pressure scale height rather than the Roche lobe.

The second reason for smoothing the potential is to account for three-dimensional effects in an approximate way. Material orbiting at high altitudes above the midplane of the disk does not feel much of the planet, while in a two-dimensional set-up it comes as close to the planet as midplane material. In this case, ϵ should be a fraction of the disk scale height H . Masset (2001) found that an optimal value for ϵ is $0.76 H$, so that the Lindblad torques are of equal strength in two dimensions as they are in three dimensions.

However, we are aiming at a comparison with two-dimensional analytical results, and therefore we consider smoothing only as a fraction of the Roche lobe or as a fixed number of grid cells.

3.3.3 Model set-up

The lowest resolution runs have 128 radial and 384 azimuthal cells, where the computational domain spans $0.4 \leq r \leq 2.5$ and $0 \leq \phi \leq 2\pi$. The factor 3 difference in azimuthal cells compared to radial cells leads to approximately square cells near the planet. The corresponding resolution is approximately $h/3$ for $h = 0.05$. We do not use the Adaptive Mesh Refinement (AMR) option in the RODEO code, because waves traveling over AMR boundaries may damp in a non-trivial way. Therefore if we increase the resolution we do it globally. This puts constraints on the maximum resolution we can achieve, but since we are only interested in changes on a scale of approximately H

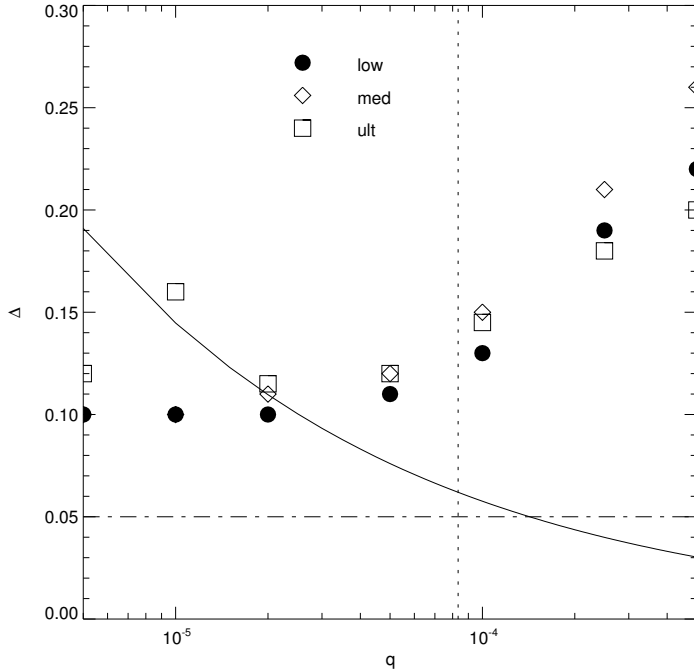


Figure 3.1: Damping length as a function of planetary mass for three different resolutions. The solid line represents the relation of Eq. (3.10). The vertical dotted line and the horizontal line indicate $q = q_H$ and $\Delta = H$, respectively. The adopted flux limiter is the soft superbee limiter, and the potential was smoothed with $\epsilon = 0.2 R_R$.

this is not a serious problem. In Table 3.1 we show the parameters for the four different resolutions we have used, together with the name by which they will be referred to in the text.

As initial conditions we use a Keplerian disk, with a small correction in the azimuthal velocity to account for the radial pressure gradient. The initial surface density is constant, and we set the radial velocity to zero.

We use the non-reflecting boundaries discussed in Paardekooper & Mellema (2006) to make sure that no outgoing waves are reflected back into the computational domain. This way the angular momentum transported by density waves can freely propagate through the boundaries.

We do not monitor accretion onto the planet by taking away mass from its Roche lobe. Rather, we let a pressure-supported envelope develop. Taking into account accretion would mean that we would have to resolve the Roche lobe of even the smallest planets, which is impossible to achieve without AMR.

We use a coordinate frame that corotates with the planet. The planet is not allowed to migrate, therefore it stays at a fixed location on the grid. This is advantageous because moving the planet through the grid introduces artificial smearing.

3.4 RESULTS

Density and velocity perturbations due to the presence of an embedded planet in a two-dimensional disk are described in detail in D’Angelo et al. (2002) and for high-mass planets in Lubow et al. (1999). For the inviscid case the basic flow patterns are the same: the planet launches two spiral density waves into the disk and a high-density

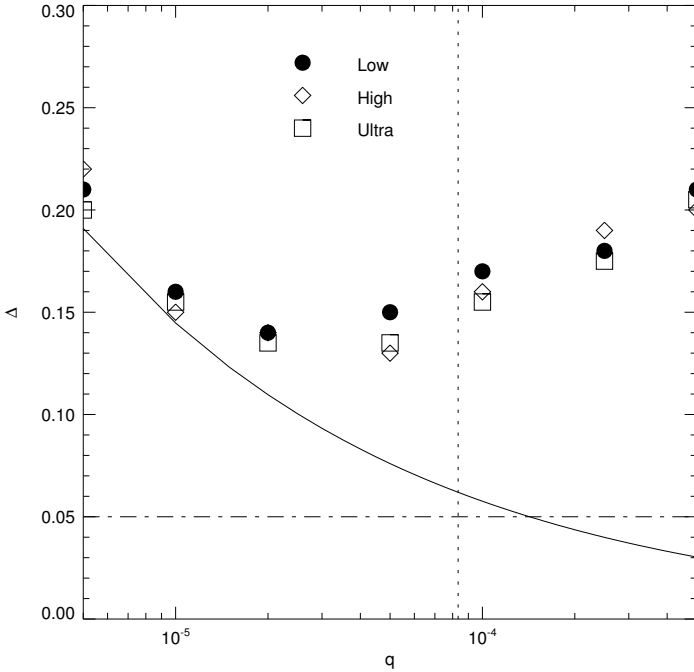


Figure 3.2: Same as Fig. 3.1, but using a smoothing length $\epsilon = 2 \Delta r$ for three different resolutions.

envelope emerges inside the Roche lobe. The tidal waves are less readily damped, however, in the inviscid simulations and they travel all the way to the boundaries. No reflections were observed, showing that our boundary conditions are capable of absorbing the outgoing waves.

3.4.1 Damping length

We start our analysis by verifying Eq. (3.10), which states that angular momentum is deposited most readily at a distance $1.43 l_{\text{sh}}$ from the planet. The most straightforward way of measuring Δ is to see at which location the gap starts to form, and therefore we looked at the azimuthal averaged density profile after 10 orbits of the planet. For the low-mass planets we consider, the disk has settled to a quasi-stationary state after this time, but no clear gap has formed. This way we do not measure the final gap width, but rather the length over which the waves are damped, for which analytical considerations led to Eq. (3.10). We will look at the final gap structure in Sect. 3.4.5.

We define Δ as the distance from the planet at which the surface density passes through its unperturbed value. Δ is therefore a measure for the location of the gap edge, which is always in the region where the tidal waves are being damped. This way, this definition of Δ is a good measure to characterize wave damping.

In Fig. 3.1 we show the damping length Δ as a function of q for different resolutions, together with the relation of Eq. (3.10) (solid line). For these runs, the planetary potential was smoothed with $\epsilon = 0.2 R_{\text{R}}$, the canonical value for two-dimensional planet-disk interaction. Only for the highest mass planet together with the ultra resolution ϵ is resolved by more than 1 grid cell. Thus effectively no smoothing was used.

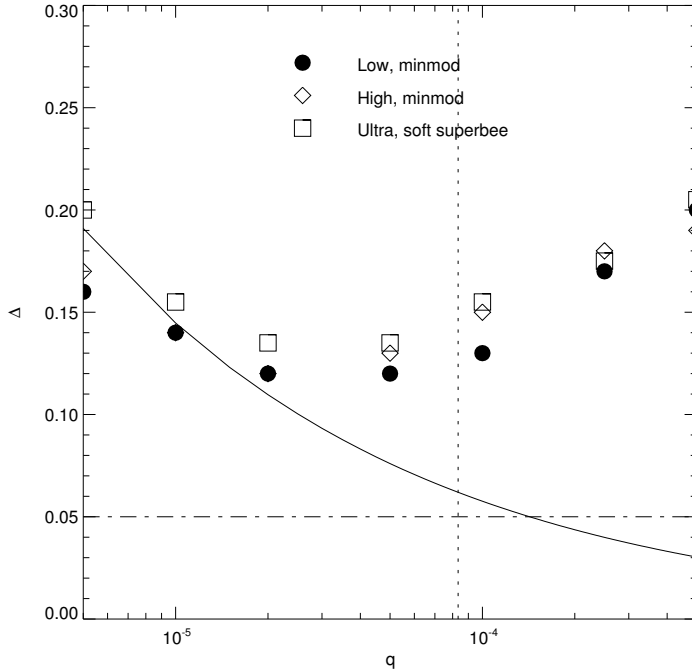


Figure 3.3: Same as Fig. 3.1, but for the minmod flux limiters at two different resolutions. For comparison, the results at ultra resolution for the soft superbee flux limiter are also shown.

For $q = q_H/4$ we see that Δ agrees nicely with Eq. (3.10) for all resolutions. Moving towards higher masses, we approach q_H where the analytical derivation of Eq. (3.10) is no longer valid and Δ shows a steady increase for all resolutions. However, for the highest masses the three resolutions shown only marginally agree on the damping length. We will show later that this is a consequence of the fact that the smoothed potential is not resolved.

For $q < q_H/4$, the low resolution runs give a constant damping length of $2H$, while we expect on the basis of Eq. (3.10) that Δ would rise towards smaller masses. The ultra resolution run for $q = 10^{-5}$ shows that this is a consequence of the potential not being resolved. For the lowest mass, however, even the ultra resolution is not high enough and Δ drops again.

In Fig. 3.2 we compare the previous results with results for a larger smoothing length of $\epsilon = 2\Delta r$. For this choice of ϵ the planetary potential is always resolved. The first thing to note is that with this smoothing we can nicely reproduce the relation of Eq. (3.10) for the smallest masses, even at low resolution. This is an indication that the mechanism outlined in Goodman & Rafikov (2001) and Rafikov (2002a,b) is indeed operating. Moreover, a high resolution run for the same smoothing gives identical results, also for the higher masses. This shows that it is necessary to resolve the potential in order to obtain accurate results. Therefore from now on we will stick with a smoothing length $\epsilon = 2\Delta r$. A smoothing length of $0.6 H$ gave similar results for all resolutions. Note that for the low resolution case, both smoothing lengths are approximately equal.

In Fig. 3.3 we compare Δ for the two different flux limiters. The minmod limiter is known to be more diffusive, which will lead to stronger dissipation of angular momentum flux. Indeed, for all planetary masses the minmod limiter gives lower estimates for the damping length. Increasing the resolution improves the situation, but not by

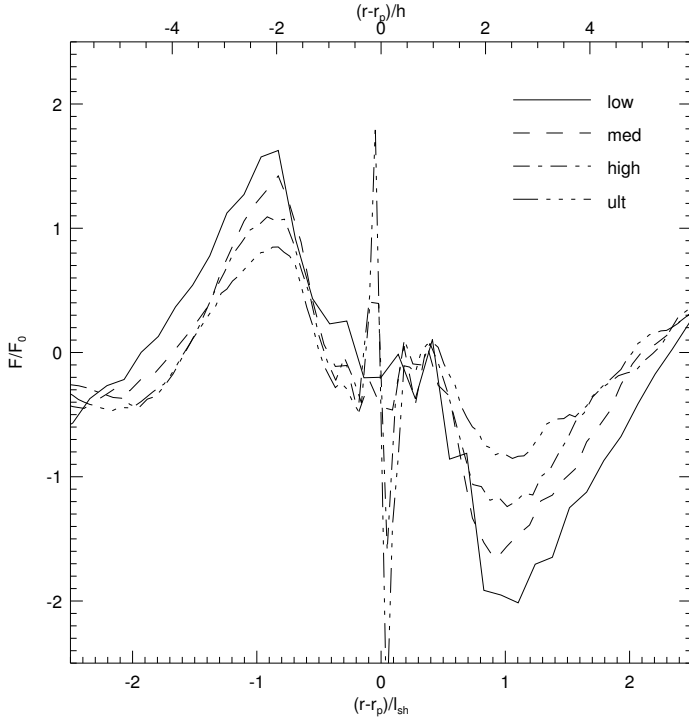


Figure 3.4: Azimuthally averaged angular momentum flux after 10 planetary orbits, normalized by F_0 , for different resolutions with $q = 10^{-5}$. The adopted smoothing is $2\Delta r$, together with the minmod flux limiter. The x-axis at the top and at the bottom give the radial distance to the planet in units of H and l_{sh} , respectively.

much for the lower-mass planets. Note that the results on Δ for the minmod limiter are always below the results obtained with the soft superbee limiter. Results with the full superbee limiter coincide with the latter. This indicates that the more diffusive limiter overestimates the wave damping considerably, especially when the waves are relatively weak. In Paardekooper & Mellema (2006) a comparison was shown between the gap structure for $q = 10^{-4}$, and again the conclusion was that the minmod limiter leads to much stronger wave damping compared to the other two limiters.

This analysis shows that numerical dissipation plays an important role in this problem, together with the way shocks are treated. The agreement of the results for different resolutions indicate that the measured wave damping is really physical, and that we are probing the effect described in Goodman & Rafikov (2001) and Rafikov (2002a,b).

3.4.2 Angular momentum flux

In order to investigate in some detail the angular momentum flow we look at the azimuthally averaged angular momentum flux F^* (see Eq. (3.2)):

$$F^* = r\Sigma v_r L \quad (3.15)$$

In a stationary state there is a direct link between F^* and F (see Eq. (3.2)), but since we are dealing with gap-opening planets this will not be the case. Still, we can obtain a lot of information on wave excitation and damping by looking at F^* . In this section

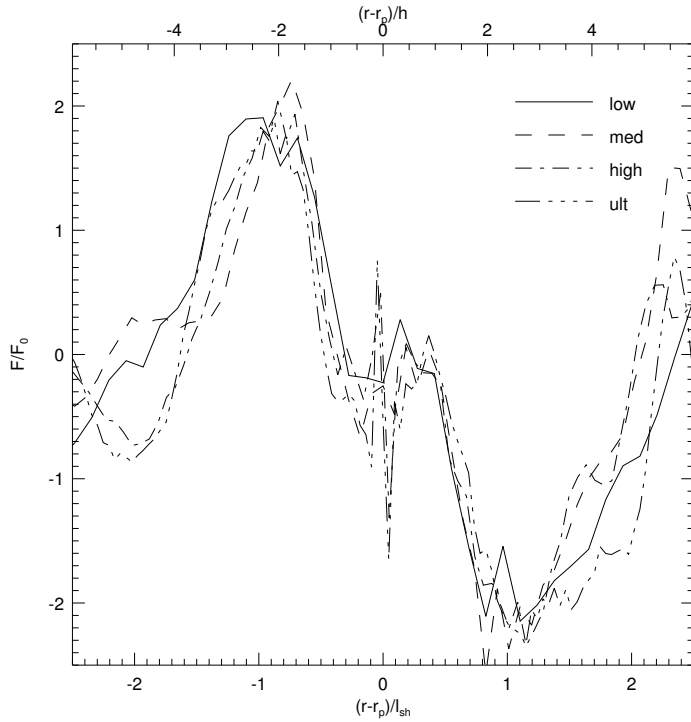


Figure 3.5: Same as Fig. 3.4, but for the soft superbee flux limiter.

we focus on the case where $q = 10^{-5}$, and unless otherwise stated, we show F^* after 10 orbits of the planet.

In Fig. 3.4 we show the radial angular momentum flux for the minmod flux limiter at different resolutions. We see that close to the planet F^* is essentially zero. This is the so-called torque cut-off (Goldreich & Tremaine 1980), and is a consequence of the fact that a stationary perturber does not excite sound waves in a subsonic background flow (Landau & Lifshitz 1959). Beyond approximately $2H/3$ the background flow becomes supersonic with respect to the planet due to the Keplerian shear, and from this distance to the planet waves are excited that transport angular momentum. It is hard to measure the exact location of this cut-off in Fig. 3.4 because the flux near the planet exhibits a lot of noise, but it is clear that F^* starts to rise in the inner disk and to drop in the outer disk at a distance of approximately one pressure scale height H from the planet.

For the higher resolution runs two strong peaks emerge in the angular momentum flux. These peaks are caused by circumplanetary material, and they do not show up in the lower resolution simulations because there the Roche lobe is not resolved. Since the Roche lobe for this planet is much smaller than H the peaks are localized within the cut-off region.

Beyond a distance of approximately H from the planet the angular momentum flux quickly rises to its maximum value, which is reached at the shocking distance l_{sh} . This distance does not depend on resolution, but the maximum value of F^* does, as can be seen in Fig. 3.4. The flux profile clearly does not converge upon increasing the resolution.

Figure 3.5 shows the results for the same models, but now obtained with the soft superbee flux limiter. The angular momentum flux appears to be a little more noisy

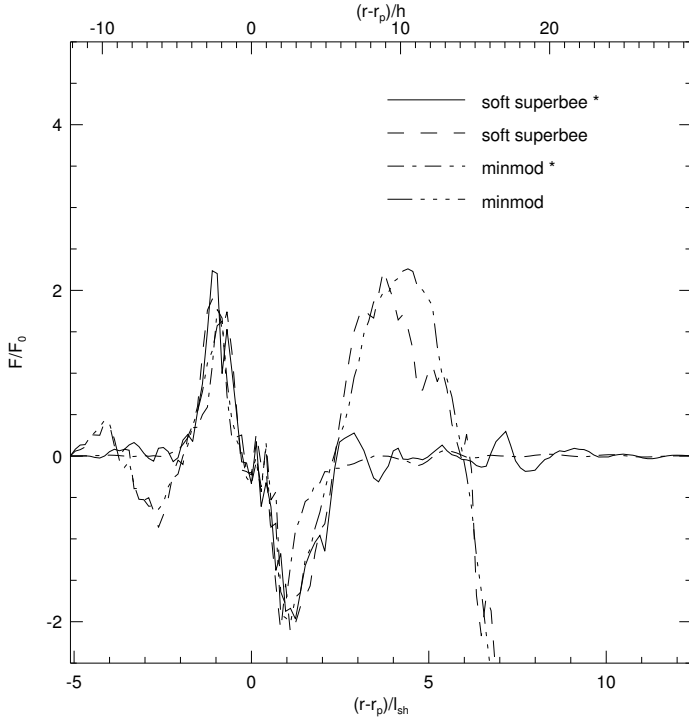


Figure 3.6: Azimuthally averaged angular momentum flux after 10 orbits of the planet, normalized by F_0 , for the full planetary potential and the cut-off potential (indicated with an asterisk), both with $q = 10^{-5}$, for two different flux limiters.

than in Fig. 3.4, but that is to be expected for a less diffusive limiter. But the most important thing to note is that for this limiter the flux profile *has* converged. The extreme values for F^* are the same for all resolutions. Note that only for the low resolution case in Fig. 3.4 the magnitude of F^* agrees with the converged value of the soft superbee limiter. Again in Fig. 3.5, for the highest resolutions we see the two circumplanetary peaks emerge, but they are far less pronounced than for the minmod limiter in Fig. 3.4. This indicates that the diffusive minmod limiter has great difficulty handling the large gravitational forces close to the planet, which may well be the cause of the different extreme values in Fig. 3.4. We saw already in Sect. 3.4.1 that effects very close to the planet (the smoothing length ϵ) can affect the wave structure much further out (the damping length Δ). In this case the strong gravitational forces close to the planet affect the angular momentum flux at a much larger distance of l_{sh} . One other thing to note from Figs. 3.4 and 3.5 is that F^* changes sign after a distance of approximately $2 l_{\text{sh}}$ from the planet. This is in conflict with Eq. (3.8), which states that after traveling a distance l_{sh} the wave is only damped due to non-linear evolution. However, this is only true if one neglects wave excitation by resonances beyond l_{sh} . They play no major role in the evolution of the surface density of the disk or in the forces on the planet, but they do show up in the angular momentum flux.

This is illustrated in Fig. 3.6, which shows F^* for the whole radial domain. Both the minmod limiter and the soft superbee limiter produce a peak in the angular momentum flux at approximately $10 H$ from the planet ($r = 1.5 r_p$) in the outer disk, which is close to the 1:2 resonance located at $r = 1.58 r_p$. When we switch off the planetary gravitational potential beyond l_{sh} this peak disappears (see Fig. 3.6) for both limiters. In order to focus only on wave damping beyond l_{sh} we use this potential cut-off for the

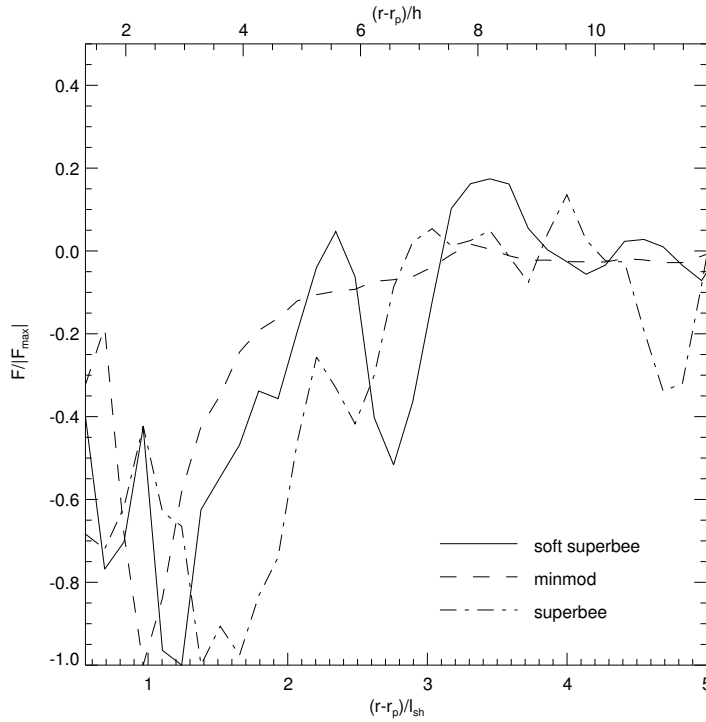


Figure 3.7: Azimuthally averaged angular momentum flux after 10 orbits of the planet, normalized to its extreme value, with the cut-off potential for $q = 10^{-5}$ for three different flux limiters.

remainder of this section.

Figure 3.7 zooms in on the angular momentum flux in the outer disk, now normalized to its maximum absolute value. The minmod flux limiter gives a smooth profile that gradually approaches zero, as expected from Eq. (3.8). Note that the damping sets in immediately after the wake shocks. The angular momentum is deposited most readily where the derivative of F^* has a maximum, and in Sect. 3.4.1 we measured Δ to be $1.43 l_{\text{sh}}$ for this limiter. Although the resolution is too low for the calculation of an accurate derivative inspection by eye of Fig. 3.7 shows that indeed beyond this distance the curve of F^* starts to level off.

For the other two limiters the angular momentum flux is not smooth at all, with significant positive excursions. Maxima and minima in general do not coincide for the two limiters, but their amplitude decreases outward. Note that the position of the global minimum is not the same for the different limiters: the less diffusive the flux limiter, the farther out the minimum. This confirms the results shown in Fig. 3.3. Note also that these oscillations in the flux are also seen in Fig. 3.6 for the simulations without the potential cut-off. Therefore they are not an artifact produced by the sudden disappearance of the planetary potential.

In Fig. 3.8 we show the angular momentum flux for the soft superbee flux limiter at different resolutions. We find these oscillations for all resolutions, and while the downward excursions are getting less deep for the higher resolutions, the upward excursions are all of the same amplitude. Note also that the curves do not get smoother for the higher resolutions, only the wavelength of the oscillations seems to get shorter. Again, the different resolutions do not agree on the positions of the maxima and minima of the oscillations.

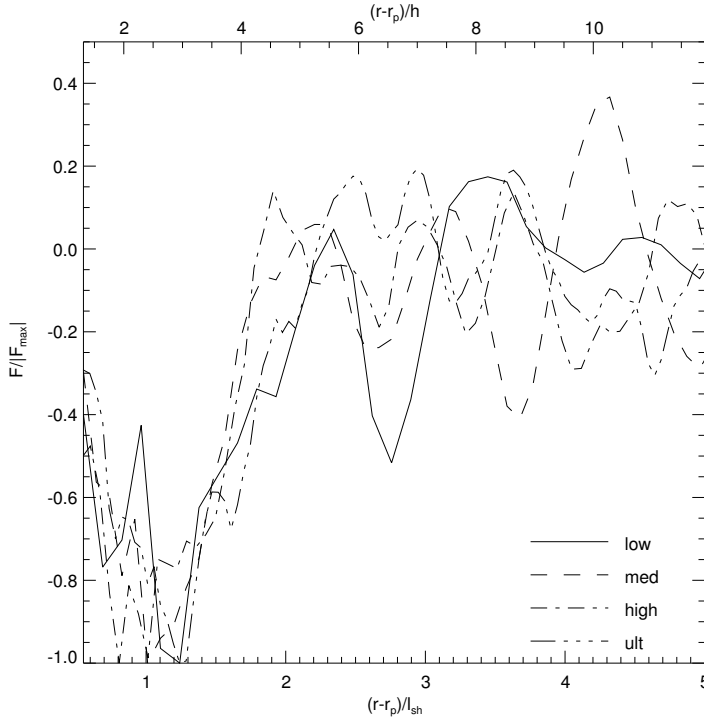


Figure 3.8: Same as Fig. 3.7, but only for the soft superbee flux limiter at different resolutions.

Even more, we find that for the less diffusive flux limiters the angular momentum flux is strongly time-dependent. See Fig. 3.9. The only thing the three curves agree on is that there is a minimum between 0.8 and $1.5 l_{\text{sh}}$, and that beyond approximately $3 l_{\text{sh}}$ the mean flux tends to zero. The damping length Δ as measured in Sect. 3.4.1 is actually a mean value, with quite a large spread. Note also that the amplitude of the oscillations does not decrease with time.

The oscillations are traveling waves, generated near l_{sh} . This is illustrated in Fig. 3.10 where we show snapshots of the angular momentum flux every tenth of the orbital timescale of the planet. All features outside l_{sh} are slowly moving outward, while a new wave is appearing at a distance of approximately $1.5 l_{\text{sh}}$ from the planet. From Fig. 3.10 we can measure the speed v_{wave} at which the waves move, and if we look at the peak near $r - r_p = 5 H$ we see that it travels approximately $1.75 H$ in 0.4 orbits, so $v_{\text{wave}} \approx 4.375 r_p \Omega_p^{-1}$. The distance between this peak and the other high peak near $r - r_p = 10 H$ is $5.5 H$, and with $v_{\text{wave}} \approx 4.375$ this means that the time interval between the waves is $1.257 \Omega_p^{-1}$. This is also the inverse orbital frequency at $r = 1.165 r_p$, or $r - r_p \approx 1.5 l_{\text{sh}}$. This again suggests that the disturbances are generated at a distance of $1.5 l_{\text{sh}}$ from the planet. Note that this is approximately the same as the damping length given by Eq. (3.10).

These results show that in the inviscid limit, the planetary wake produces a time-dependent angular momentum flux. Only the most diffusive flux limiter is able to damp these oscillations, and only then we can reproduce the results from Rafikov (2002b).

For higher mass planets the angular momentum flux is dominated by the fluctuations. This is illustrated in Fig. 3.11 for $q = 10^{-4}$. Again, an analysis of the velocity

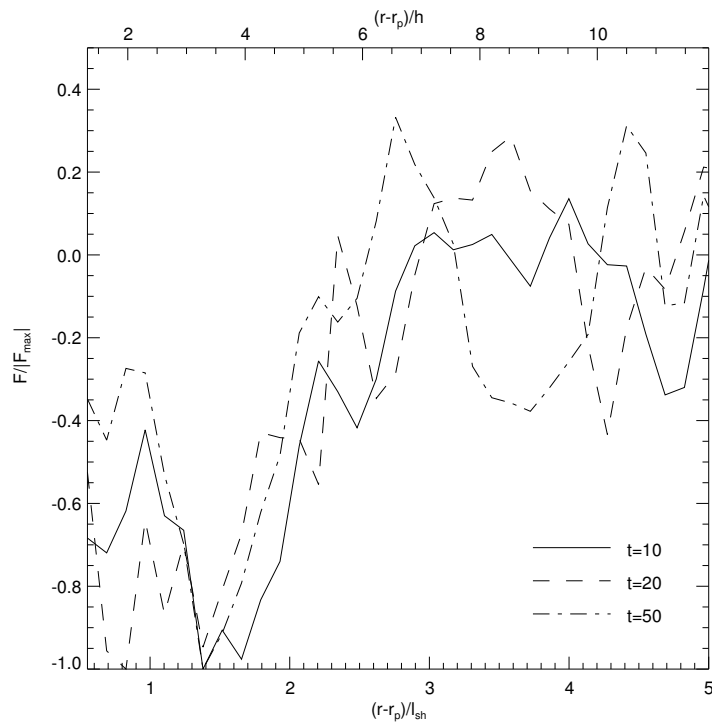


Figure 3.9: Same as Fig. 3.8, but for the superbee flux limiter at different times.

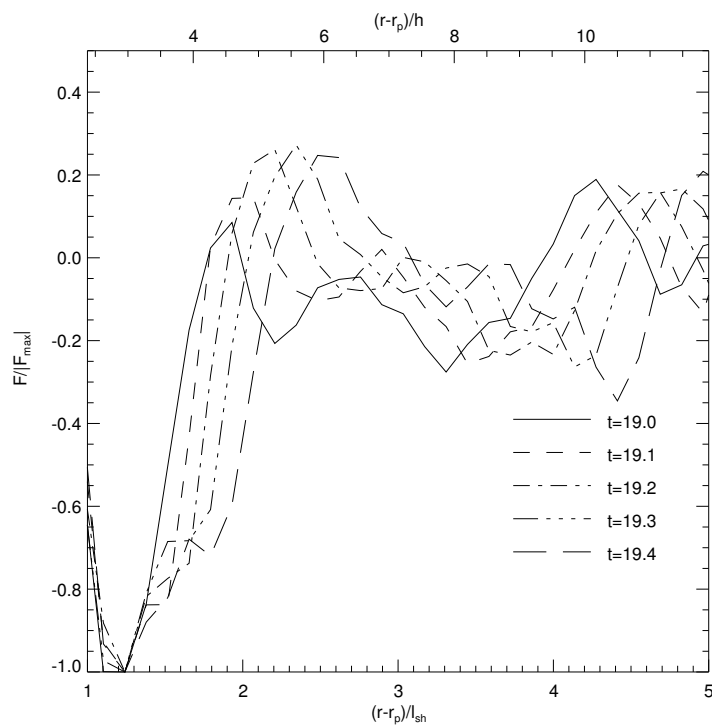


Figure 3.10: Same as Fig. 3.9, but for shorter time intervals.

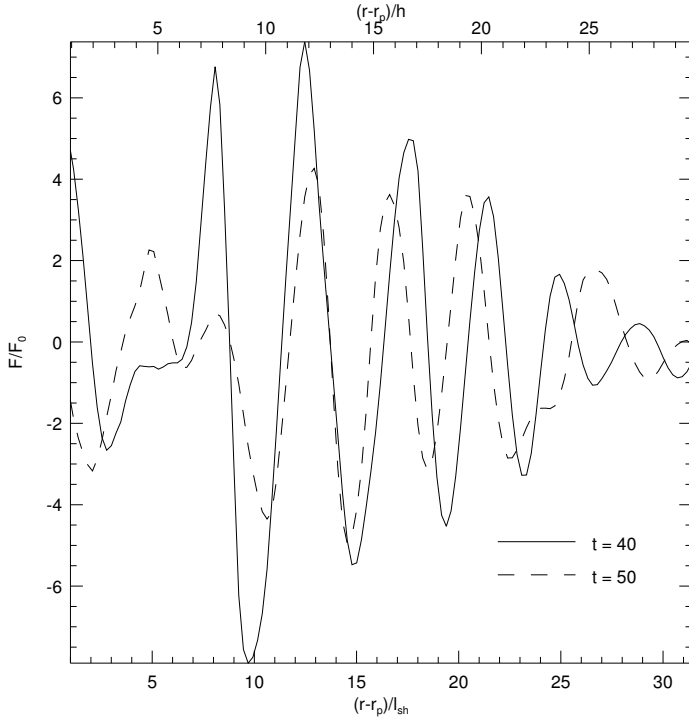


Figure 3.11: Same as Fig. 3.9, but for $q = 10^{-4}$.

and spatial frequency of the oscillations yields that the fluctuations are created around $r - r_p = 1.5 l_{\text{sh}}$. In the next section, we will link these large fluctuations to the appearance of vortices at the same location.

3.4.3 Vortensity evolution

One possible explanation for the appearance of the waves in the angular momentum flux was given by Koller et al. (2003), who looked at the creation of vortices in the coorbital region of the planet. They suggested that the planet-induced shocks are able to modify the potential vorticity profile in the disk in such a way that vortices appear near the separatrix. At this location there exists an inflection point, which is a necessary but not sufficient condition for instability (Balmforth & Morrison 1996). Balmforth & Korycansky (2001) also found fluctuations in the angular momentum flux due to vortices in the coorbital region.

The potential vorticity, in astrophysics often called vortensity, is defined by:

$$\omega = \frac{(\nabla \times \mathbf{v})_z}{\Sigma} \quad (3.16)$$

where \mathbf{v} is the velocity vector. One can show that ω is conserved along streamlines in two dimensions (Korycansky & Papaloizou 1996). However, near shocks streamlines are broken and therefore in these regions ω is no longer conserved, which may lead to the appearance of vortices. The fact that the fluctuations in angular momentum flux develop just beyond the point where the planetary wake shocks suggests that the same

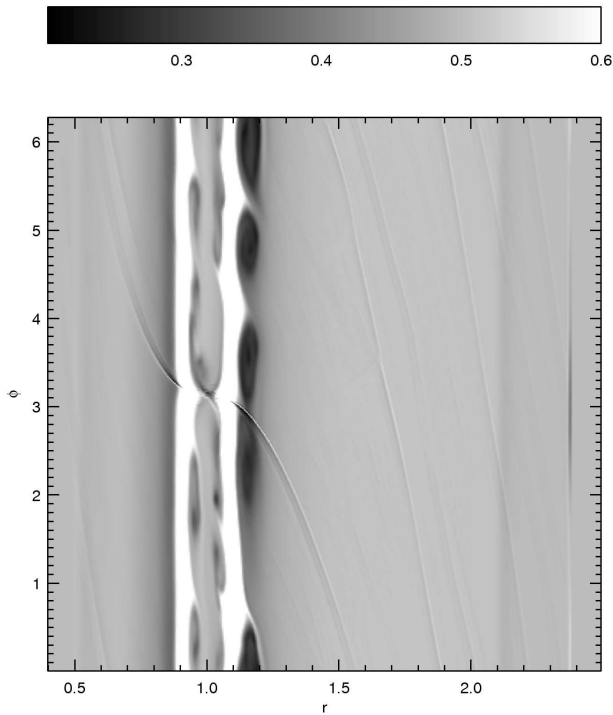


Figure 3.12: Greyscale plot of the vortensity ω for $q = 10^{-4}$ after 100 orbits of the planet. Vortices appear as minima in ω , and can most clearly be identified near $r \approx 1.2$.

mechanism is operating here, although perhaps in a weaker form because of the low mass of the planet compared to the $q = 10^{-4}$ case from Koller et al. (2003).

We start discussing the evolution of the vortensity with a set-up that is similar as in Koller et al. (2003) and Li et al. (2005). That is, we set the initial surface density to a power law with index $-3/2$ so that the initial profile of ω is constant, and we put in a planet of $q = 10^{-4}$. By comparing our results to the results from Li et al. (2005), obtained using a different numerical method we can get a good handle on any numerical issues.

In Fig. 3.12 we show the vortensity after 100 orbits with the soft superbee flux limiter. There are four vortices orbiting at $r \approx 1.18$ in the outer disk, and a lot of smaller structures can be seen in the coorbital region. Note that there is a lot of filamentary substructure visible in the whole outer disk.

The appearance of vortices does not strongly depend on resolution. For all but the lowest resolution case we find the same result as shown in Fig. 3.12 for the high resolution case. This is further illustrated in Fig. 3.13, where we show the azimuthally averaged vortensity profile for runs with different resolution. The profile we find is similar to the results of Li et al. (2005), with two peaks at $\Delta r \approx \pm 3R_R$. The vortices are associated with the minima just outside from the peaks (Koller et al. 2003), and we see that in this regions all resolutions give the same vortensity profile. The only exception is the shallower minimum of the low resolution case, which did not show vortices at this point in time. However, the minimum is getting deeper with time, and after 100

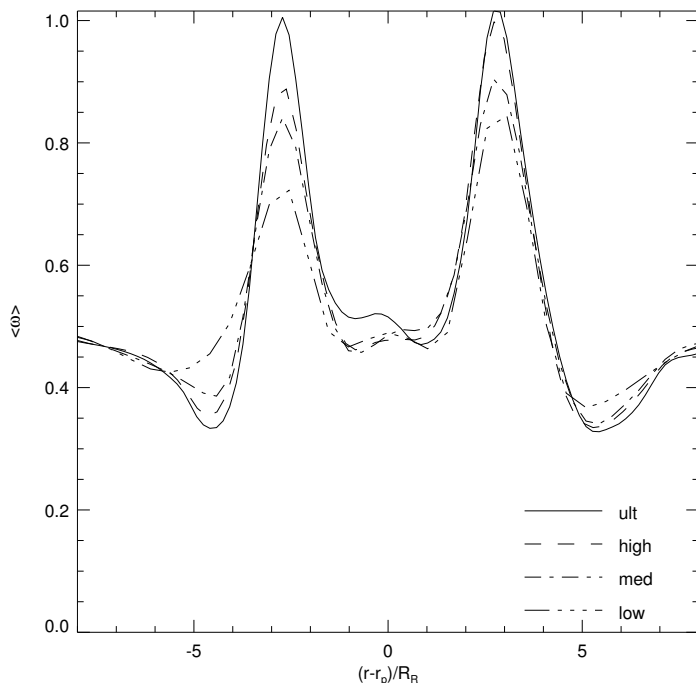


Figure 3.13: Azimuthally averaged vortensity profile for $q = 10^{-4}$ after 50 orbits of the planet for different resolutions for the soft superbee flux limiter.

orbits also the low resolution case shows the vortices.

For the peaks as well as the minimum in the inner disk the case is not so simple. The peaks are getting higher upon increasing the resolution, and we do not find convergence even for the ultra resolution. This is in agreement with the results of Li et al. (2005) who found that one needs a resolution that is two times higher than our highest resolution to obtain convergence. However, our results differ from theirs for the lower resolutions. For example, we find the same position of the peak for all resolutions, and near the outer minimum the solution is converged at much lower resolution.

The differences may have to do with the different treatment of shocks in the respective numerical methods. The importance of shock treatment can be illustrated by looking at results for different flux limiters, see Fig. 3.14. First thing to note is that the superbee limiter and its softer version agree very well everywhere except at the outer peak. The minmod limiter differs from the other ones most clearly in the inner part of the disk. The three curves in Fig. 3.14 are models at high resolution, and it is clear that in regions where the ultra resolution differs most from the high resolution models (indicating no convergence, see Fig. 3.13) also the diffusive minmod limiter does not agree with the other two. This confirms that the treatment of shocks, which is different for different limiters, is critical for determining the height of the peaks and the depth of the inner minimum. The inner minimum is again related to the appearance of vortices in the inner disk (see Fig. 3.12). Note that all flux limiters agree on the outer minimum, and therefore on the creation of vortices.

Figure 3.13 suggests that the depth of the minima determines whether vortices appear. However, this is not entirely true. In Fig. 3.14 the inner minimum for the minmod limiter is actually deeper than for the soft superbee limiter, but no vortices can be seen in the minmod results while they can be clearly seen in Fig. 3.12. This suggests that

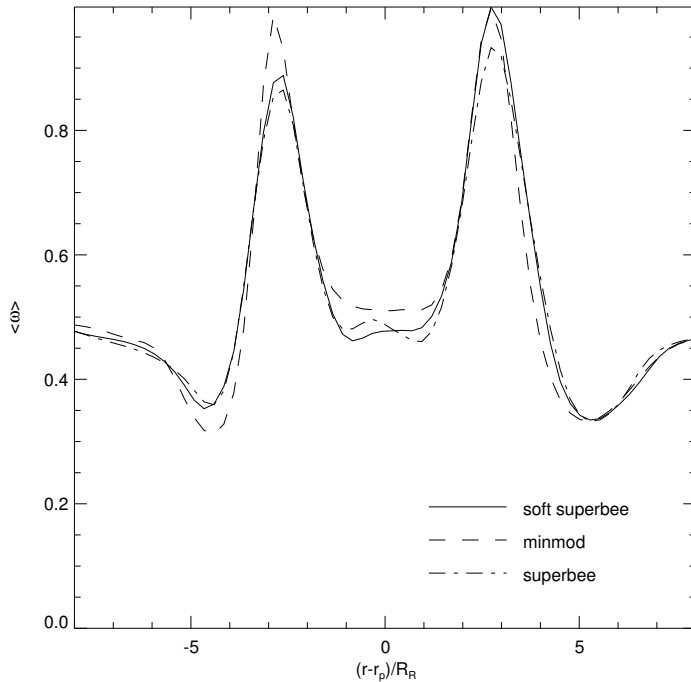


Figure 3.14: Azimuthally averaged vortensity profile for $q = 10^{-4}$ after 50 orbits of the planet for different flux limiters at high resolution.

also numerical dissipation of shocks plays a big role in the formation of vortices. This is also confirmed in a recent comparison problem for hydrodynamical codes on planet-disk interaction (de Val-Borro et al. 2006).

Another difference between our results and those of Li et al. (2005) is the relatively fast appearance of vortices. They find that vortices only appear after 160 orbits, while we already find them after 50 orbits. Part of this can be explained in terms of a different smoothing length. Although Li et al. (2005) do not specify their exact smoothing length, for the higher resolution runs our smoothing length of 2 grid cells is probably smaller than theirs because they try to correct for 3D effects. However, for the lowest resolution our smoothing is approximately the same as the value of $0.76 H$ needed for this correction (Masset 2001), and even in this case we find vortices as early as 100 orbits. Increasing the smoothing length even further does lead to slower evolution of the vortensity profile, see Fig. 3.15, but then the minimum shifts outward too far compared to the results from Li et al. (2005). Introducing the planet more slowly into the disk did not change these results. Therefore we conclude that vortices form much more readily when shocks are treated correctly by our adopted numerical method.

The time evolution of the vortensity profile is the same as in Li et al. (2005), see Fig. 3.16. The peaks and the minima slowly move away from the planet, and Li et al. (2005) showed that this leads to ever larger vortices. This process did not stop during a period of more than 500 orbits.

In Fig. 3.17 we show the time scale for the appearance of vortices as a function of planetary mass. For the lowest mass we consider here, $q = 3.5 \cdot 10^{-5}$, it takes approximately 300 orbits before vortices appear. For lower masses, this time scale becomes prohibitively long, but the trend is clear. The apparently linear relation between τ_{vort} and q in log-log scale in Fig. 3.17 indicates that there exists a relation between the two

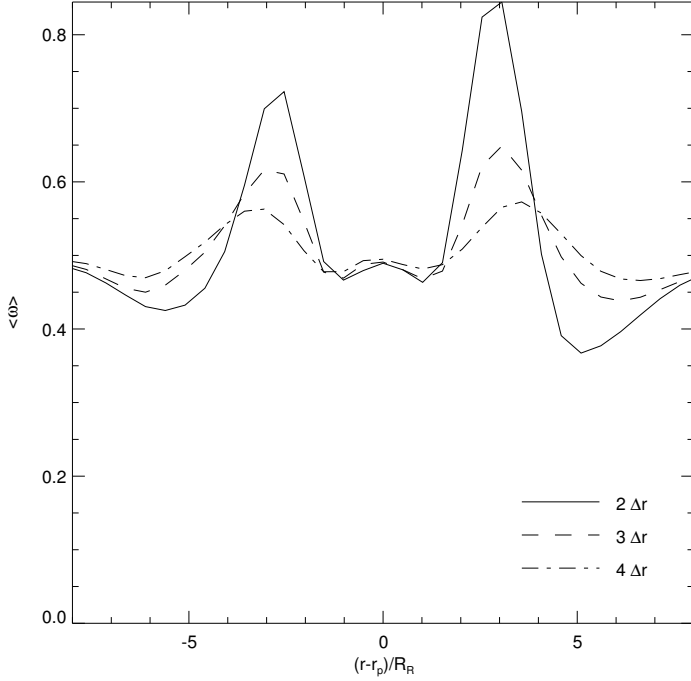


Figure 3.15: Azimuthally averaged vortensity profile for $q = 10^{-4}$ after 50 orbits of the planet for different smoothings at low resolution.

of the form:

$$\tau_{\text{vort}} = \beta q^\alpha. \quad (3.17)$$

The best-fit parameters are given by $\alpha = -2.51 \pm 0.5$ and $\beta = 1.74 \cdot 10^{-9} \pm 7.5 \cdot 10^{-8}$. The resulting fit is remarkably good and is shown in Fig. 3.17 by the dashed line.

The fact that $\alpha \approx -5/2$ suggests that the time scale for vortex formation is inversely proportional to l_{sh} (see Eq. (3.7)). This is an interesting result, because the way in which the vortensity is changed by spiral shocks depends in a complicated way on the shock structure (Li et al. 2005). However, since the errors in the best fit parameters are rather large due to uncertainties in the timing of the appearance of vortices further study is required to pin down the exact relation.

3.4.4 Time scales

From Eq. (3.14), together with the results from Fig. 3.17 we can deduce that the time scale for vortex formation is always much smaller than the time scale for gap formation if $q < 0.02$ for $h = 0.05$. Around a solar mass star $q = 0.02$ would correspond to a 20 M_J brown dwarf. For $q \ll q_H$ we can safely assume that $\tau_{\text{vort}} \ll \tau_{\text{gap}}$. This means that the appearance of vortices may be of major importance for the formation of the gap.

In order to measure the time scale for gap formation within numerical simulations we need to define what we mean by a gap: at what density contrast do we call a density depression a 'gap'? In view of the definition of τ_{gap} in Eq. (3.14) we define a gap as a density depression with a minimum that is a factor e lower than the initial surface density:

$$\Sigma_{\text{min}}(t_{\text{gap}}) = \Sigma(0) e^{-1}. \quad (3.18)$$

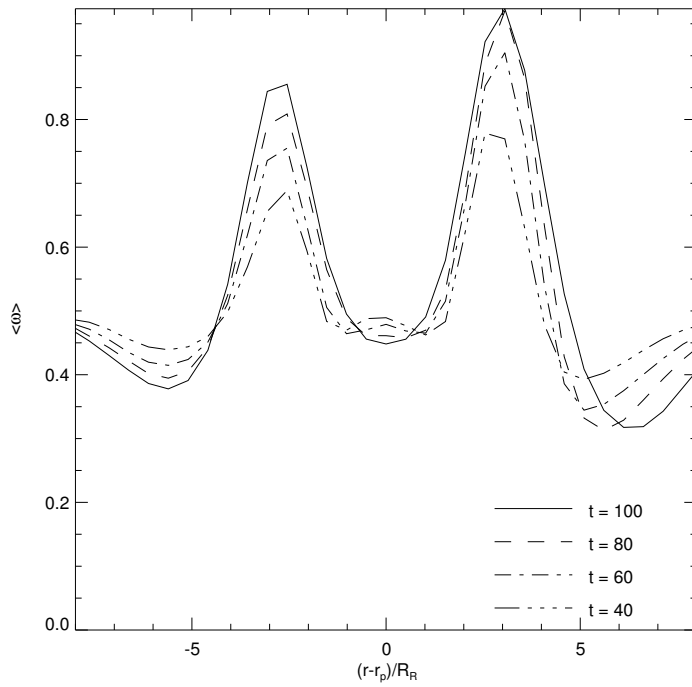


Figure 3.16: Azimuthally averaged vortensity profile for $q = 10^{-4}$ at low resolution for the soft superbee flux limiter at different times.

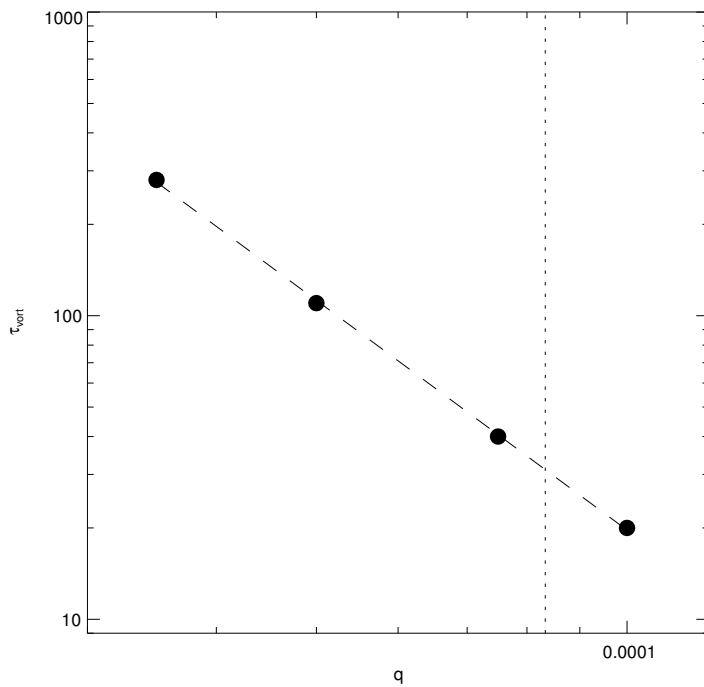


Figure 3.17: Time scales for vortex formation. The vertical line marks $q = q_H$, and the dashed line indicates the best fit of the form $\tau_{\text{vort}} = \beta q^\alpha$. The best-fit parameters read $\alpha = -2.51$ and $\beta = 1.74 \cdot 10^{-9}$.

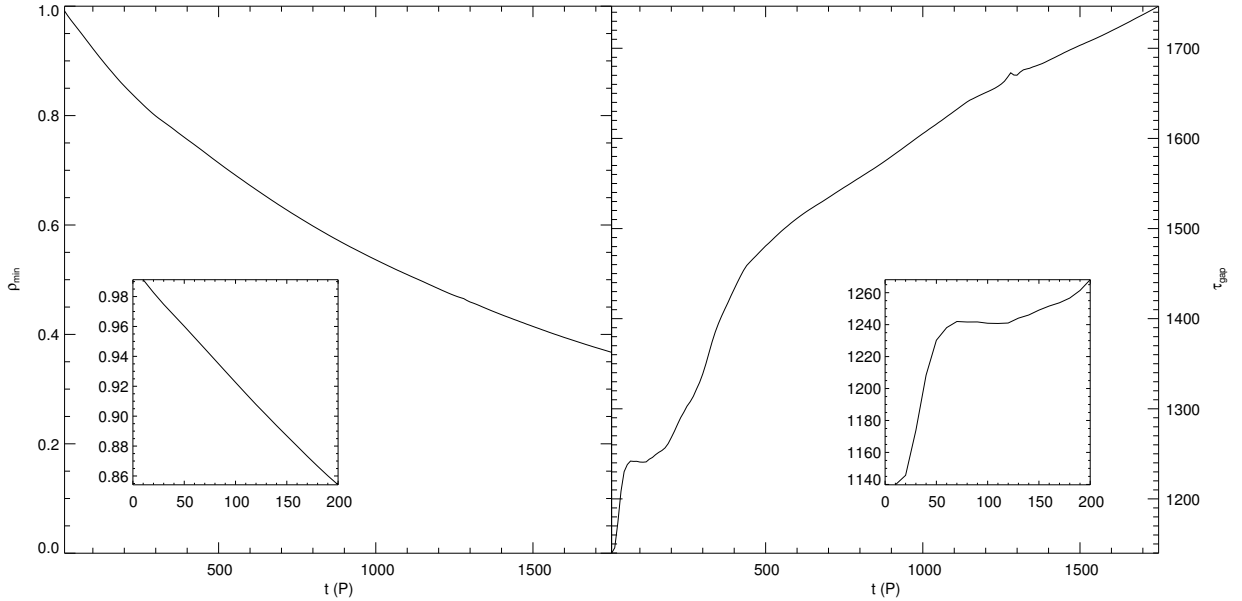


Figure 3.18: Left panel: Depth of the gap opened by a $q = 5 \cdot 10^{-5}$ planet as a function of time. Right panel: corresponding gap opening time scale. The small panels provide a close-up on the time of vortex appearance ($t \approx 100$, see Fig. 3.17).

The first thing to note is that the time scale for gap formation as estimated in Eq. (3.14) will break down for $q > 2 \cdot 10^{-5}$ because the damping lengths do not match Δ (see Fig. 3.3). For $q = 5 \cdot 10^{-5}$, for example, we expect τ_{gap} to be a factor 2-3 larger than the value predicted by Eq. (3.14). This is important when assessing the possible effect of the appearance of vortices.

When the surface density evolution due to gap formation proceeds in the simple form:

$$\Sigma_{\min}(t) = \Sigma_0 e^{-t/\tau_{\text{gap}}}, \quad (3.19)$$

we can solve for τ_{gap} :

$$\tau_{\text{gap}} = -\frac{t}{\log \Sigma(t)/\Sigma_0}, \quad (3.20)$$

in which τ_{gap} would be constant. In reality gap formation does not proceed according to Eq. (3.19), but still Eq. (3.20) provides a useful measure of the speed at which the gap is forming as a function of time. We interpret $\tau_{\text{gap}}(t)$, which will be a function of time in general, as the time scale for gap formation if it would proceed with the mean speed until time t .

In the left panel of Fig. 3.18 we show the evolution of the minimum density Σ_{\min} as a function of time for $q = 5 \cdot 10^{-5}$. It decays at a decreasing rate until it crosses the value e^{-1} after 1750 orbits. Although the curve for Σ_{\min} does not show much substructure, the curve of $\tau_{\text{gap}}(t)$, shown in the right panel of Fig. 3.18, does. The first thing to note is that $\tau_{\text{gap}}(t)$ is not constant, which indicates that gap formation does not proceed

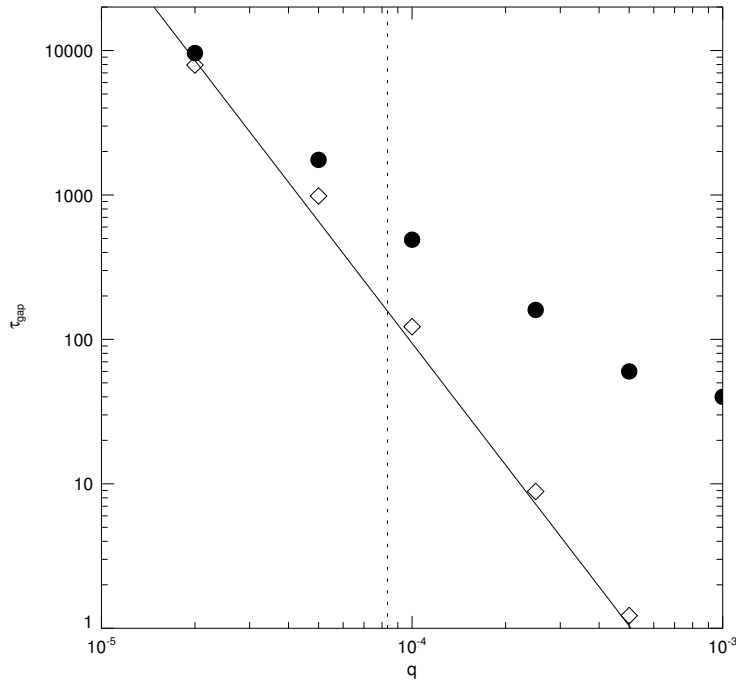


Figure 3.19: Time scales for gap formation. The vertical dotted line marks $q = q_H$, and the solid line indicates the estimate of Eq. (3.14). Closed symbols indicate the measured time scales, open symbols indicate the same results but corrected for the different damping length Δ as measured in Fig. 3.2 compared to Eq. (3.10).

according to the simple law of Eq. (3.19). Beyond 200 orbits, $\tau_{\text{gap}}(t)$ keeps rising until the gap actually forms. It is because $d\tau_{\text{gap}}/dt < 1$ that a gap is able to form eventually.

More interesting is the behavior of $\tau_{\text{gap}}(t)$ around 100 orbits, of which a close-up is shown in the small panels in Fig. 3.18. Between approximately 50 and 120 orbits the curve of $\tau_{\text{gap}}(t)$ seems to level off at a value of 1240 orbits, after which it begins to rise steadily. This timing is interesting, because from Fig. 3.17 we see that this is exactly the time at which vortices begin to form. It seems that the angular momentum transport due to the vortices works against gap formation.

The estimate of the gap formation time scale given by Eq. (3.14), 750 orbits, is much lower than the measured value of 1750 orbits. However, when taking into account the measured damping length Δ from Fig. 3.2 rather than from Eq. (3.10), we find a gap formation time scale of 1250 orbits. This equals the formation time scale *before* the onset of vortex creation (see Fig. 3.18). This shows that the vortices do change the angular momentum flux, working against gap formation.

In Fig. 3.19 we show how the measured gap formation time scale depends on planetary mass. We see that for all planets we measure a longer time scale than predicted by Eq. (3.14). When we correct for the larger damping length the time scales agree reasonably well, but still the measured formation time scales are all longer than the analytical estimate of Eq. (3.14). This can be interpreted as the effect of vortex formation on the angular momentum flux. Note, however, that the effect of vortices is small compared to the effect of the difference in Δ .

For the smallest planet mass considered here, $q = 2 \cdot 10^{-5}$, the measured gap formation time scale is consistent with the analytical estimate of Eq. (3.14). The importance of the vortices in the angular momentum transport is apparently low for this planet. Unfortunately, as the gap formation time scale for this planet is already close to 10000

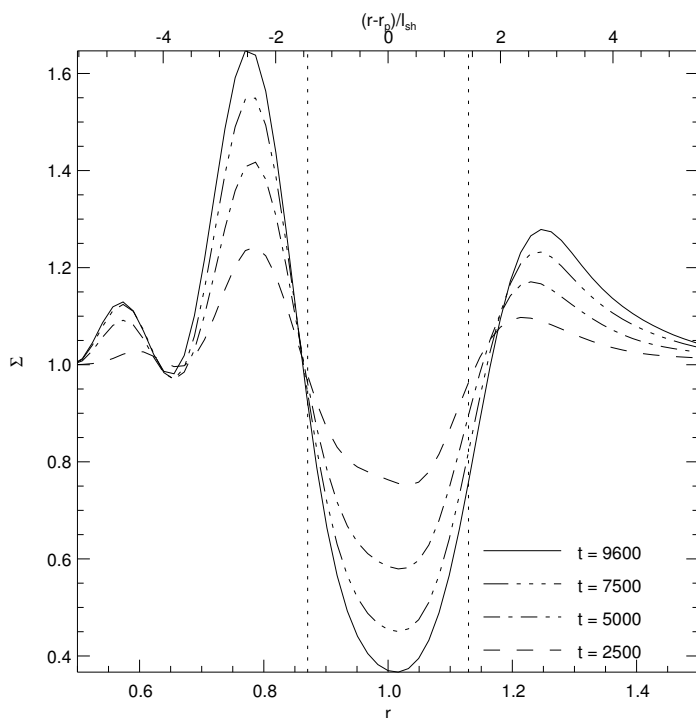


Figure 3.20: Azimuthally averaged density profile for $q = 2 \cdot 10^{-5}$, the minmod flux limiter at low resolution for different times. After 9600 orbits, the density in the gap is approximately a factor e lower than the initial density. The vertical dotted lines indicate the theoretical gap width of Eq. (3.10).

orbits, computations for lower-mass planets are too expensive to perform.

3.4.5 Gap structure

In this section, we will study the structure of gaps opened by low-mass planets. In particular, we focus on the width of the gap and the density structure near the coorbital region. The analytical theory of Goodman & Rafikov (2001) and Rafikov (2002a) only considers effects occurring several pressure scale heights away from the planet, thereby ignoring the coorbital region as well as the direct influence of the potential of the planet. Both are included in our numerical simulations, and we will try to establish their importance.

We will concentrate on the lowest mass planet that still allows us to run a simulation until a gap has formed, $q = 2 \cdot 10^{-5}$. Figures 3.2 and 3.19 show that here there is reasonable agreement between the theory of Rafikov (2002a) and the numerical results on wave damping and gap formation time scale. Planets of higher mass severely deviate from the theory because q comes too close to q_H , while planets of lower mass form gaps only after more than 10000 orbits, which makes the simulations too expensive computationally.

In Fig. 3.20 we show the surface density evolution for this planet with $q = 2 \cdot 10^{-5}$ for the minmod flux limiter at low resolution. Only after 9600 orbits the density has decreased by a factor of e , which is our working definition of a gap. The vertical dotted lines mark the edges of a gap of half-width Δ , where Δ is given by Eq. (3.10). It is immediately clear that there is no clear defined edge for the gap. In the inner

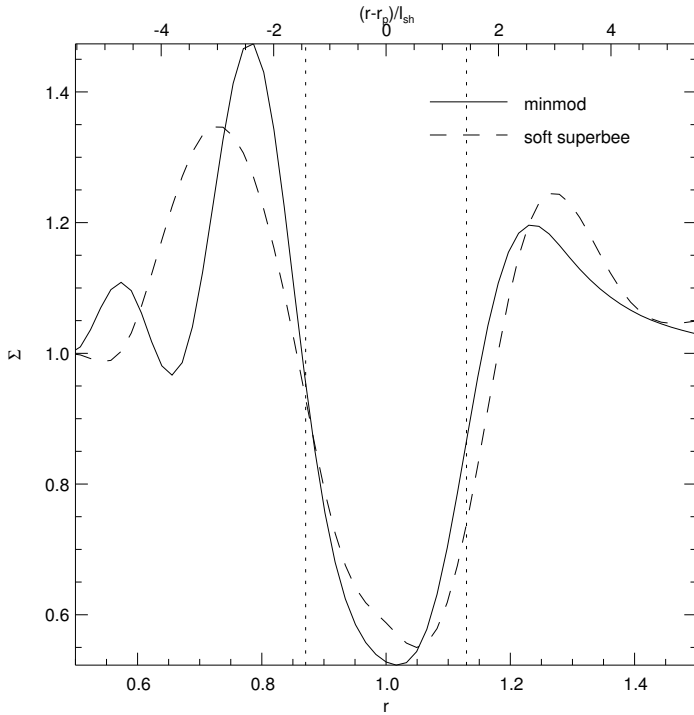


Figure 3.21: Azimuthally averaged density profile for $q = 2 \cdot 10^{-5}$ after 6000 orbits at low resolution for different flux limiters. The vertical dotted lines indicate the theoretical gap width of Eq. (3.10).

disk, the density slowly rises from the minimum near $r = 1$ to the maximum at $r = 0.75$. The analytical estimate of Eq. (3.10) is located approximately half way between the minimum and the maximum, where also the density is approximately half way between the minimum and maximum density.

It is interesting to note that the gap is not symmetrically located with respect to the planet's radial position. The different heights of the peaks near the inner edge and the outer edge reflect the fact that mass is conserved rather than density. In cylindrical coordinates, the mass in a given grid cell of size $(\Delta r, \Delta \phi)$ is:

$$M = r \Sigma \Delta r \Delta \phi. \quad (3.21)$$

For constant Δr and $\Delta \phi$ as we consider here, the mass ratio for a ring located at $r = 0.75$ and a ring located at $r = 1.25$ is 1.67 when the rings have equal widths and equal density. This effect is more than able to account for the different heights of the peaks at the gap edges, and it even tells us that more mass is transported to the outer disk than to the inner disk.

The theory outlined in Goodman & Rafikov (2001) and Rafikov (2002a) predicts no disk evolution at distances closer than l_{sh} from the planet. In Fig. 3.20 we see that this is not the case in our simulations, due to coorbital effects. These are aimed at flattening the vortensity profile locally near the orbit of the planet. This profile is continuously disturbed by the process of gap-opening by non-linear wave damping, and the attempt to flatten the profile again leads to surface density evolution in the coorbital region.

In Fig. 3.21 we show the surface density profile after 6000 orbits for the same planet, but now for two different flux limiters. The most important difference is the change in location of the peaks that mark the gap edges. The soft superbee flux limiter, which is

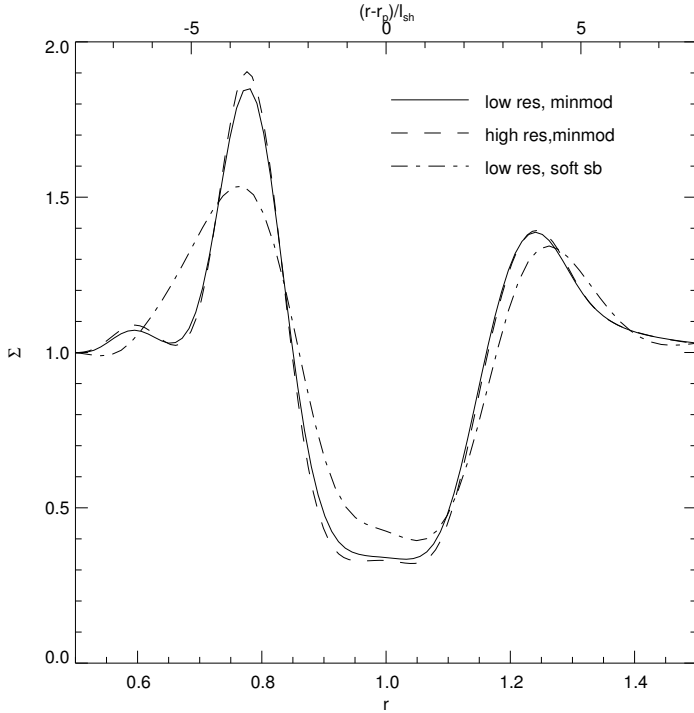


Figure 3.22: Azimuthally averaged density profile after 1600 orbits of a $0.05 M_J$ planet. The solid line indicates a low resolution run with the minmod limiter, the dashed line the corresponding high resolution run, and the dot-dashed line indicates a low resolution run with the soft superbee flux limiter.

less diffusive, deposits the angular momentum of the waves noticeably further away from the planet than the minmod limiter. This is another indication that it really is non-linear wave evolution that promotes gap opening. Note that also the coorbital density profile is different for both limiters. This is due to the vortices, which are suppressed using the minmod limiter but are present in the run using the soft superbee flux limiter. We again see that it leads to slower gap formation.

Because it takes several thousands of orbits for a planet with $q \ll q_H$ to open up a gap, a resolution study is very difficult. Our results on wave damping suggest that numerical resolution does not play an important role. However, coorbital effects can be very sensitive to numerical resolution, because the width of the coorbital region is closely related to the size of the Roche lobe and the pressure structure close to the planet. For an overview see Masset (2001, 2002). Because our low-resolution runs do not resolve the Roche lobe of the lowest-mass planets coorbital effects may be enhanced significantly for resolutions that do resolve the Roche lobe. We try to assess the importance of coorbital effects for a planet of $0.05 M_J$, for which we do not resolve the Roche lobe in our lowest resolution runs. However, from Fig. 3.2 we see that this planet is not in the regime where we find agreement with the theory of non-linear wave damping by Rafikov (2002a). Nevertheless, it is the lowest-mass planet we can consider at high resolution.

We compare the gap profile for a $0.05 M_J$ planet for two resolutions using the minmod limiter with a low-resolution run with the soft superbee flux limiter in Fig. 3.22. For both runs with the minmod limiter, a gap has formed according to Eq. (3.18), while for the run with the soft superbee flux limiter no gap has formed yet. We see that both runs with the minmod limiter show almost the same structure, while the

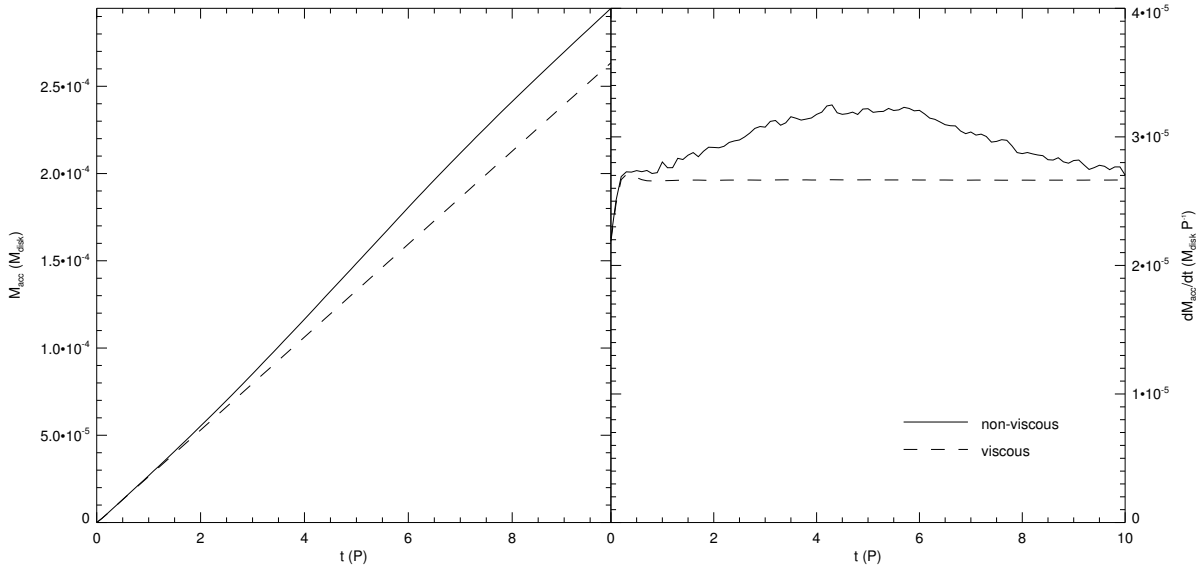


Figure 3.23: Left panel: mass accreted by a $q = 2 \cdot 10^{-5}$ planet, in units of total disk mass. Right panel: corresponding mass accretion rate, in units of disk mass per orbit.

soft superbee limiter appears to be the odd one out. This indicates that, at least for planets of this mass, resolution is not an issue, while non-linear wave damping is. To find out whether this also holds for planets of lower mass would require simulations of thousands of orbits at high resolution, which is beyond present-day computational resources.

3.5 DISCUSSION

The major shortcoming of the simulations presented here is that they consider only two spatial dimensions, while especially for low-mass planets three-dimensional effects may be very important. Because of the agreement we find between two-dimensional analytic theory and two-dimensional numerical simulations, a theory of the non-linear evolution of the three-dimensional planetary wake would be very useful. However, because of the high computational costs already in two dimensions the numerical confirmation of such a theory would be very difficult. Moreover, even for high-mass planets gap formation is not well-studied numerically in the three-dimensional case, the only exception being Kley et al. (2001). More work on this subject is definitely needed.

Migration switches from fast Type I to slow Type II when a planet opens up a gap. Gap formation by low-mass planets is therefore an interesting candidate for saving planets from catastrophic Type I migration into the central star. For this, the gap formation time scale would need to be smaller than the migration time scale. For a planet located at 5 AU in a two-dimensional disk of $5 M_J$ with $h = 0.05$ the Type I migration time scale equals approximately (Tanaka et al. 2002):

$$\tau_{\text{mig}} \approx 0.167 q^{-1}. \quad (3.22)$$

Comparing this with Eq. (3.14) we see that gap formation is faster than migration for planets less massive than $q_{\text{eq}} = 2.0 \cdot 10^{-5}$, or $6 M_{\oplus}$ around a solar mass star. Note that at this mass Eq. (3.14) agrees with numerical simulations (see Fig. 3.19). In more massive disks, q_{eq} will be smaller because the migration time scale is inversely proportional to the disk mass in the linear regime. In a 3D disk, Type I migration is found to be a factor of 2 slower (Tanaka et al. 2002), moving q_{eq} to higher masses, but the time scales for 3D gap formation may be larger as well, if a gap forms at all.

We have not considered accretion in this Chapter, because that requires us to resolve the Roche lobe of the planet, which is not possible for the long integration times needed. However, since the gap-opening time scales for low-mass planets are very long, it is important to compare them with the time scale for mass accretion. Focusing on a planet of $q = 2.0 \cdot 10^{-5}$, we found in Chapter 2 that the equilibrium accretion rate in a viscous disk is approximately $3.0 \cdot 10^{-5}$ disk masses per orbit. When a gap forms, further accretion is possible at a limited rate due to viscously-driven flow across the gap. In an inviscid disk, as considered in this Chapter, the mass accretion rate is expected to approach zero when the gap is fully formed around a low-mass planet. However, before the gap is empty the planet can accrete at a rate that is comparable to the viscous rate. This is shown in Fig. 3.23, where we compare the accretion rate for a viscous disk with that for an inviscid disk. Both simulations used the AMR module to achieve high resolution close to the planet, just as in Chapter 2. The accretion rate in an inviscid disk turns out to be comparable to the viscous accretion rate, at least before the gap starts to form. The time scale for accreting the whole disk is approximately 10^5 orbits, and therefore:

$$-\frac{\dot{M}_d}{M_d} = \frac{\dot{M}_d}{\dot{M}_p} = \frac{M_d}{M_p} \tau_g \approx 10^5 \Omega_p^{-1}, \quad (3.23)$$

where M_d and M_p denote disk and planet mass, respectively, and τ_g denotes the growth time scale of the planet. Time derivatives are denoted by dotted quantities. When we assume that the disk contains a few M_J in gas, and note that we are dealing with Earth-mass planets, we can approximate M_d/M_p by 100, which yields $\tau_g \approx 10^3$ orbits. This is much shorter than the time scale for gap formation of this planet. However, a $q = 2.0 \cdot 10^{-5}$ might be not massive enough to capture that amount of gas from the nebula. The measured accretion rates are upper limits to the true accretion rate, because they measure the amount of gas that the disk is able to supply to the planet. How much of this mass the planet is willing to accept is an open question, and answering this will require detailed modeling of the thermodynamical state of the planetary envelope.

Vortex creation and evolution is another issue that should be studied in three dimensions. Because they are of influence on the torque and thus on the migration behavior they may be of vital importance for the evolution of the planet's orbit (Koller et al. 2003; Li et al. 2005). It is not clear if they appear in 3D simulations, and whether they are long-lived structures.

3.6 SUMMARY AND CONCLUSION

We have presented fully non-linear two-dimensional simulations of planets embedded in an inviscid gaseous disk. We have compared wave damping and gap formation with the analytical work of Goodman & Rafikov (2001) and Rafikov (2002a) on non-linear wave evolution, and although a direct comparison is difficult we have found good agreement for $q \ll q_H$. We have found gap formation to occur for a planet 20 times less massive than the commonly applied thermal criterion for gap formation in disks with low viscosity, Eq. (3.6).

We have confirmed the results of Koller et al. (2003) and Li et al. (2005) that vortices form in the coorbital region of low-mass planets. The appearance of vortices affects the process of gap formation, but does not change the overall picture. A diffusive flux limiter is able to suppress the appearance of vortices at low resolution, but at high resolution all limiters give consistent results.

The time scale for gap formation becomes comparable to the disk life time for Earth-mass planets. But also for $q = 2.0 \cdot 10^{-5}$ it takes already 10000 dynamical time scales to create a gap, which severely limits the results that can be obtained by numerical simulations, even in two dimensions. Future work should be aimed at obtaining a three-dimensional theory of non-linear wave evolution in accretion disks, and on three-dimensional simulations of vortices near embedded planets.

3.A SHOCK FORMATION IN ISOTHERMAL DISKS

In this appendix, we show that the results from Goodman & Rafikov (2001) are immediately applicable to disks with an isothermal equation of state. We will work in a coordinate frame (x, y) corotating with the planet, where $x = r - r_p$ and $y = r_p(\phi - \phi_p)$. The state of the background flow is expanded to lowest order in x/r_p . We assume a constant unperturbed surface density Σ_0 , sound speed c , rotation rate Ω , shear rate $2A$ and vorticity $2B$. Here, A and B denote the Oort constants. The same set-up was used by Goodman & Rafikov (2001).

In the absence of source terms due to the planet, the steady state fluid equations read:

$$\begin{aligned} (2Ax + v)\partial_y u + u\partial_x u - 2\Omega v + \frac{c^2}{\Sigma}\partial_x \Sigma &= 0 \\ (2Ax + v)\partial_y v + u\partial_x v + 2Bu + \frac{c^2}{\Sigma}\partial_y \Sigma &= 0 \\ (2Ax + v)\partial_y \Sigma + u\partial_x \Sigma + \Sigma\partial_x u + \Sigma\partial_y v &= 0, \end{aligned} \tag{3.24}$$

where we write the velocity $\mathbf{v} = (u, v)^T$ and ∂_q is short for $\partial/\partial q$. For $|x| \gg l \equiv c/|2A|$ the system (3.24) simplifies because then $\partial_y \ll \partial_x$ and $v \ll u$ (Goodman & Rafikov 2001). Then we can drop v entirely and keep ∂_y only in the combination $2Ax\partial_y$, yielding:

$$\begin{aligned} \partial_y u + u\partial_x u + \frac{c^2}{\Sigma}\partial_x \Sigma &= 2\Omega v \\ \partial_y \Sigma + u\partial_x \Sigma + \Sigma\partial_x u &= -\Sigma\partial_y v, \end{aligned} \tag{3.25}$$

where, following Goodman & Rafikov (2001), $\xi \equiv Ax^2$. The source terms on the right hand side are necessary in order to conserve angular momentum flux (Goodman & Rafikov 2001). The homogeneous version of the system (3.25) can be solved by defining Riemann invariants

$$R_{\pm} = u \pm \int \frac{dp}{c\Sigma}, \quad (3.26)$$

yielding

$$\partial_{\pm} R_{\pm} = 0, \quad (3.27)$$

where ∂_{\pm} is short for $\partial_y + (u \pm c)\partial_{\xi}$. For an isothermal equation of state, the Riemann invariants read

$$R_{\pm} = u \pm c \log \left(\frac{\Sigma}{\Sigma_0} \right). \quad (3.28)$$

Upon including the source terms, we obtain

$$\partial_{\pm} R_{\pm} = \frac{2\Omega v \mp c\partial_y v}{2Ax} \equiv S_{\pm} \quad (3.29)$$

As explained in Goodman & Rafikov (2001) we can neglect the source term for R_+ , which is therefore constant along the corresponding characteristic. Because this characteristic propagates *towards* the planet from the unperturbed disk we can replace R_+ by $u_0 + c \log(\Sigma_0/\Sigma) = 0$. This means that $u = -c \log(\Sigma/\Sigma_0)$ everywhere, and therefore

$$R_- = -2c \log \left(\frac{\Sigma}{\Sigma_0} \right). \quad (3.30)$$

We use the second equation of the system (3.24) to approximate the source term S_- . To an adequate approximation, we have

$$\partial_y v \approx -\frac{1}{2Ax} (2Bu + c^2 \partial_y \log \Sigma). \quad (3.31)$$

Only those parts of S_- that are in phase with u or $\Sigma - \Sigma_0$ are important (Goodman & Rafikov 2001); therefore we have for the terms in S_- :

$$\partial_y v \approx -\frac{Bu}{Ax}, \quad (3.32)$$

$$v \approx -\frac{c^2}{2Ax} \log \left(\frac{\Sigma}{\Sigma_0} \right), \quad (3.33)$$

and for S_-

$$S_- = -\frac{2Bcu + \Omega c^2 \log \left(\frac{\Sigma}{\Sigma_0} \right)}{2A\xi}, \quad (3.34)$$

which, upon substituting the Keplerian value $B = A + \Omega$, together with $u = -c \log(\Sigma/\Sigma_0)$, simplifies to:

$$S_- = \frac{c^2}{2\xi} \log \left(\frac{\Sigma}{\Sigma_0} \right). \quad (3.35)$$

Now define $\psi = \log \Sigma / \Sigma_0$, which transforms the equation for $R_- = -2c\psi$ into:

$$\partial_y \psi - (1 + \psi) c \partial_\xi \psi = -\frac{c}{4\xi} \psi, \quad (3.36)$$

which is the same as Eq. A4 from Goodman & Rafikov (2001), but with a different definition of ψ . This equation can be further simplified by making the substitutions

$$\eta \equiv \frac{y}{l} + \text{sign}(x) \frac{x^2}{2l^2} \quad (3.37)$$

$$t \equiv \frac{4}{5} \left| \frac{y}{l} \right|^{5/4} \quad (3.38)$$

$$\chi \equiv \left| \frac{y}{l} \right|^{-1/4} \psi, \quad (3.39)$$

which yield

$$\partial_t \chi - \chi \partial_\eta \chi = 0, \quad (3.40)$$

which is just the inviscid Burger's equation. This is the same result as found by Goodman & Rafikov (2001), except for the definition of χ , which they found to be, for a polytropic equation of state:

$$\chi_\Gamma \equiv \left| \frac{y}{l} \right|^{-1/4} \frac{\Gamma + 1}{\Gamma - 1} \frac{c^* - c}{c} \approx \left| \frac{y}{l} \right|^{-1/4} \frac{\Gamma + 1}{2} \frac{\Sigma - \Sigma_0}{\Sigma_0}, \quad (3.41)$$

where c^* denotes the perturbed value of the sound speed. But

$$\chi \equiv \left| \frac{y}{l} \right|^{-1/4} \psi = \left| \frac{y}{l} \right|^{-1/4} \log \left(\frac{\Sigma_0 + \Delta \Sigma}{\Sigma_0} \right), \quad (3.42)$$

where $\Delta \Sigma \equiv \Sigma - \Sigma_0$. Anticipating that $\Delta \Sigma$ is small compared to Σ_0 we expand the logarithm to obtain:

$$\chi \approx \left| \frac{y}{l} \right|^{-1/4} \frac{\Sigma - \Sigma_0}{\Sigma_0}, \quad (3.43)$$

which is equivalent to χ_Γ for $\Gamma = 1$. Alternatively we can write, using the polytropic equation of state, $c^* = c(\Sigma/\Sigma_0)^{(\Gamma-1)/2}$, and therefore:

$$\chi_\Gamma = \left| \frac{y}{l} \right|^{-1/4} \frac{\Gamma + 1}{\Gamma - 1} \left[\left(\frac{\Sigma}{\Sigma_0} \right)^{\frac{\Gamma-1}{2}} - 1 \right]. \quad (3.44)$$

Upon inserting the definition of ψ and taking the limit $\Gamma \rightarrow 1$ we obtain finally:

$$\lim_{\Gamma \rightarrow 1} \chi_\Gamma = \left| \frac{y}{l} \right|^{-1/4} 2 \lim_{\Gamma \rightarrow 1} \frac{e^{\psi \frac{\Gamma-1}{2}} - 1}{\Gamma - 1} = \left| \frac{y}{l} \right|^{-1/4} \psi, \quad (3.45)$$

where we have invoked l'Hôpital's rule to evaluate the limit. Again, we see that χ_Γ transforms smoothly into χ when $\Gamma \rightarrow 1$.

This shows that we can use the results obtained by Goodman & Rafikov (2001) for our isothermal simulations by substituting $\Gamma = 1$ where appropriate. In particular, we can use Eq. (3.7) to estimate the distance over which the planetary wake shocks.

REFERENCES

- Balbus, S. A. & Hawley, J. F. 1990, *BAAS*, 22, 1209
- Balmforth, N. J. & Korycansky, D. G. 2001, *MNRAS*, 326, 833
- Balmforth, N. J. & Morrison, P. J. 1996, *APS Meeting Abstracts*, 12
- Bryden, G., Chen, X., Lin, D. N. C., Nelson, R. P., & Papaloizou, J. C. B. 1999, *ApJ*, 514, 344
- D'Angelo, G., Henning, T., & Kley, W. 2002, *A&A*, 385, 647
- de Val-Borro, M., Edgar, R. G., Artymowicz, P., et al. 2006, *MNRAS*, 370, 529
- Eulderink, F. & Mellema, G. 1995, *A&AS*, 110, 587
- Gammie, C. F. 1996, *ApJ*, 457, 355
- Goldreich, P. & Sari, R. 2003, *ApJ*, 585, 1024
- Goldreich, P. & Tremaine, S. 1979, *ApJ*, 233, 857
- Goldreich, P. & Tremaine, S. 1980, *ApJ*, 241, 425
- Goodman, J. & Rafikov, R. R. 2001, *ApJ*, 552, 793
- Kley, W. 1999, *MNRAS*, 303, 696
- Kley, W., D'Angelo, G., & Henning, T. 2001, *ApJ*, 547, 457
- Koller, J., Li, H., & Lin, D. N. C. 2003, *ApJ*, 596, L91
- Korycansky, D. G. & Papaloizou, J. C. B. 1996, *ApJS*, 105, 181
- Landau, L. D. & Lifshitz, E. M. 1959, *Fluid mechanics (Course of theoretical physics, Oxford: Pergamon Press, 1959)*
- LeVeque, R. J. 2002, *Finite Volume Methods for Hyperbolic Problems (Cambridge texts in applied mathematics, Cambridge:University press, 2002)*
- Li, H., Li, S., Koller, J., et al. 2005, *ApJ*, 624, 1003
- Lin, D. N. C. & Papaloizou, J. 1986, *ApJ*, 307, 395
- Lin, D. N. C. & Papaloizou, J. C. B. 1993, in *Protostars and Planets III*, 749–835
- Lubow, S. H., Seibert, M., & Artymowicz, P. 1999, *ApJ*, 526, 1001
- Masset, F. S. 2001, *ApJ*, 558, 453
- Masset, F. S. 2002, *A&A*, 387, 605
- Nelson, R. P. & Papaloizou, J. C. B. 2003, *MNRAS*, 339, 993
- Paardekooper, S.-J. & Mellema, G. 2004, *A&A*, 425, L9
- Paardekooper, S.-J. & Mellema, G. 2006, *A&A*, 450, 1203
- Pringle, J. E. 1981, *ARA&A*, 19, 137
- Rafikov, R. R. 2002a, *ApJ*, 569, 997
- Rafikov, R. R. 2002b, *ApJ*, 572, 566
- Roe, P. L. 1981, *J. Comp. Phys*, 43, 357
- Tanaka, H., Takeuchi, T., & Ward, W. R. 2002, *ApJ*, 565, 1257
- Ward, W. R. 1997, *Icarus*, 126, 261
- Wolf, S. & D'Angelo, G. 2005, *ApJ*, 619, 1114

CHAPTER 4

Orbital evolution of embedded planets

Sijme-Jan Paardekooper

To be submitted

EXTRASOLAR giant planets are mostly found to be on highly eccentric orbits. In this Chapter, we investigate whether planet-disk interaction can account for significant eccentricity growth. We focus on the most favorable conditions: inviscid disks of high mass. This is a different part of parameter space than has been considered so far. We use the RODEO hydrodynamics solver to evolve the gas disk. We make use of the ability of the method to treat arbitrary spatial coordinates to choose a coordinate frame that keeps the planet at a fixed location on the grid even when its orbit is eccentric. We find that this new coordinate frame is advantageous for small values of e , especially when it becomes comparable to the size of a single grid cell. A planet of 5 Jupiter masses can grow significant eccentricity in a massive, inviscid disk (up to $e = 0.15$). A planet of 1 Jupiter mass remains largely on a circular orbit, even for very low viscosity. Short excursions to $e = 0.1$ can be seen, especially at high resolution, but never for more than 10 orbits of the planet. It requires a very low pressure scale height for the planet to be able to maintain an eccentric orbit. Intermediate-mass planets also remain on circular orbits. Their migration behavior is interesting, though, in an inviscid disk. Due to vortex formation at the edge of their shallow gap they can temporarily move outward instead of the usual fast inward migration that is found in viscous disks.

4.1 INTRODUCTION

Planet-disk interaction is a very important stage in planet formation, because it determines the final shape of the planetary system. Disk-induced orbital migration (Goldreich & Tremaine 1979, 1980) is invoked to explain for example the planets that are known as ‘Hot Jupiters’: massive planets orbiting very close to their parent star. Indeed, it is very unlikely that these planets were formed at their present position where the temperatures are very high and there was only a very limited supply of gas to attract from the nebula.

While the process of orbital migration is able to explain the Hot Jupiters, it poses a serious problem as well. The migration time scale for certain planetary masses (several Earth masses (M_{\oplus}), typically) is much shorter than the disk life time, and therefore these planets are quickly lost into the central star. This type of migration is referred to as Type I, and it holds for planets that are not able to substantially change the surface density of the surrounding disk.

Planets more massive than about 1 Jupiter mass (M_J) are able to tidally truncate the disk and to carve a deep annular gap near their orbit. In this case the planet will migrate on the viscous time scale of the disk ($10^6 - 10^7$ years), and this much slower type of migration is referred to as Type II migration. Because during this stage of migration the planet behaves like a disk fluid particle the migration timescale is on the order of the disk life time, and therefore the rate of survival for the more massive planets is substantially higher. However, these planets also pass through a stage of Type I migration before they have accreted enough mass. Indeed, the bottleneck for giant planet formation is the phase in which the massive core of several M_{\oplus} is built and these cores are subject to Type I migration.

Both types of migration have been studied extensively using analytic theory (e.g. Tanaka et al. 2002; Ward 1997) and numerical simulations in two and in three dimensions confirming the analytic results (e.g. Bate et al. 2003; D’Angelo et al. 2002, 2003). The migration rates, however, were calculated in a stationary situation, i.e. where the planet does not actually move inwards. This is only valid in the limit where the radial velocity of the planet is much smaller than the viscous inward drift of the gas, that is for very small planets ($M_p < 0.01 M_J$). The dramatic impact of a moving planet on the gas flow was shown by Masset & Papaloizou (2003) and Artymowicz (2004) who discovered a whole new, very rapid type of migration due to dynamic corotational torques. This runaway or Type III migration takes place on time scales of several hundredths of orbits.

Another important issue is the large mean value of the eccentricity found in systems of extrasolar planets ($\bar{e} = .0.33$), while in our own Solar system the eccentricities of the giant planets are smaller than 0.06. It is not yet clear how these large eccentricities came about. One popular scenario involves interactions among planets (Rasio & Ford 1996; Lin & Ida 1997; Weidenschilling & Marzari 1996; Ford et al. 2001; Chiang et al. 2002), but Goldreich & Sari (2003) argue that this scenario fails to reproduce the eccentricity distribution of isolated extrasolar planets.

Disk-planet interaction is another potential candidate for inducing high eccentricities. Unfortunately, analytic theory is not capable of resolving whether these inter-

actions are able to promote eccentricity growth (Goldreich & Sari 2003). The balance between resonances that excite and those that damp orbital eccentricity proves to be very delicate (Goldreich & Tremaine 1980; Artymowicz 1993a,b), and there is some debate over the role of apsidal resonances (Ward & Hahn 1998, 2000; Goldreich & Sari 2003). In general, a deep gap is needed for the coorbital resonances that damp eccentricity to be of minor importance. At the same time, the density gradients near the planet need to be sufficiently small in order to prevent eccentricity damping by corotation resonances (Goldreich & Sari 2003). The latter are subject to saturation (Ogilvie & Lubow 2003), which makes them far less effective in disks with a small viscosity.

Until now, numerical hydrodynamical simulations of disk-planet interaction did not succeed in producing a Jupiter-mass planet on a highly eccentric orbit (Nelson et al. 2000). Papaloizou et al. (2001) found eccentricity growth only in the Brown Dwarf mass regime. However, there are a few possibilities for disk-planet interaction to excite the orbital eccentricity of a planet. It was found by Koller et al. (2003) and Li et al. (2005) that intermediate-mass planets of approximately $0.1 M_J$ produce vortices near their orbit. These change the torque on the planet (Koller et al. 2003) and possibly can promote eccentricity growth. In a comparison problem on disk-planet interaction (de Val-Borro et al. 2006) it was found that also Jupiter-mass planets are capable of creating large vortices near the edges of their gap.

Recently, Kley & Dirksen (2006) found that planets of a few M_J are capable of exciting large ($e \approx 0.25$) eccentricity in the disk. The eccentric disk is capable of transferring more mass to the planet than a circular disk, but the effects on the orbital evolution of the planet remain to be investigated. In particular, the coupling of the disk's eccentricity to the orbital eccentricity of the planet is an interesting subject.

Finally, orbital eccentricity growth may occur when a massive planet is in the process of gap formation (Sari & Goldreich 2004). One condition is that the mass expelled from the gap region needs to be larger than the planet's mass, and it is interesting to note that this is also the criterion for fast Type III migration (Masset & Papaloizou 2003; Artymowicz 2004). Masset & Papaloizou (2003) did not find eccentricity growth in their simulations, and more work is needed to study the connection between Type III migration and eccentricity growth.

In this Chapter we investigate the orbital evolution of embedded planets using a new numerical method which has certain advantages over the conventional methods used until now. In particular, we keep the location of the planet in the computational grid fixed, while we still solve the full equations of motion of the planet. This way, the planet migrates, and may pick up eccentricity, without changing its location on the grid. Especially in the limit of small eccentricities this method should be an improvement over conventional methods in which the planet moves through the grid. We investigate all possible mechanisms of eccentricity growth through planet-disk interaction mentioned above.

The plan of the Chapter is as follows. In Sect. 4.2 we present the physical aspects of the coordinate frame and disk model we use. Section 4.3 is devoted to the numerical method, and in Sect. 4.4 we present our results. In Sect. 4.5 we give a brief discussion on the results and we conclude in Sect. 4.6.

4.2 PHYSICAL MODEL

In this section we describe the physics of our coordinate system, which is specifically designed to keep the planet on a fixed location in the computational grid, together with the physical model for the disk itself.

4.2.1 Disk Model

The disk model is the same as used in (Paardekooper & Mellema 2006, Chapter 2), and for details we refer to that Chapter. Because we focus on high-mass planets for the major part of this Chapter, we can safely work in a two-dimensional geometry and thereby reduce the computational costs significantly.

The disk is assumed to start in Keplerian rotation, with a small correction due to the radial pressure gradient. All radial velocities are zero, initially. The density follows a power-law with an index that varies from simulation to simulation. In most models we set it to zero for simplicity. As mentioned in the previous section, we work with a locally isothermal equation of state, which removes the need to solve the energy equation. In viscous models, we include a constant kinematic viscosity ν as described in Paardekooper & Mellema (2006).

Our base grid size is $(n_u, n_\phi) = (128, 184)$, which gives approximately square cells near the planet. The disk extends from $u = 0.4$ to $u = 2.5$ radially, which yields a cell size near the planet of 0.0164. We have not used the AMR module in this Chapter. For high-mass planets (more massive than $1 M_J$) we use a larger computational domain: $u \in [0.4, 4.6]$, with twice the amount of radial cells.

For calculating the gravitational force due to the disk on the planet, we assume a disk mass of $M_d = 0.05 M_\odot$. This relatively massive disk ensures that the conditions for eccentricity growth are favorable: the disk is always more massive than the planet. Also, effects that would be secular for less massive disks are significantly sped up.

4.2.2 Coordinate frame

In order to study migration it is desirable to work with a ‘free’ planet: one that is able to move through the grid and perhaps pick up eccentricity. However, moving the potential well of the planet with respect to the grid can lead to numerical difficulties:

- The coarseness of the computational grid shows up as a stair step pattern in the migration rate (Nelson & Benz 2003). This can be circumvented by smoothing the planetary potential over several grid cells.
- When migration is very fast, the planet rapidly approaches the boundary of the computational domain (Masset & Papaloizou 2003).
- An adaptive grid with higher resolution near the planet needs to be constantly adapted to the new position of the planet. The interpolations needed in this process may come to dominate the numerical solution.

In this Chapter we exploit the fact that our numerical method (Paardekooper & Mellema 2006) can handle arbitrary coordinate frames (Eulerink & Mellema 1995) and work in a frame that keeps the planet at a fixed location at all times.

We start with ordinary cylindrical coordinates (r, ϕ) , for which the covariant metric tensor reads

$$g_{\mu\nu} = \begin{pmatrix} -1 - 2\Phi & 0 & 0 \\ 0 & 1 & 0 \\ 0 & 0 & r^2 \end{pmatrix}, \quad (4.1)$$

where Φ is the gravitational potential. Now we transform to a frame with $\theta = \phi - \Omega_p t$ and $u = r/r_p$:

$$g_{\mu\nu} = \begin{pmatrix} -1 - 2\Phi + u^2(v_{r,p}^2 + r_p^2\Omega_p^2) & ur_p v_{r,p} & u^2 r_p^2 \Omega_p \\ ur_p v_{r,p} & r_p^2 & 0 \\ u^2 r_p^2 \Omega_p & 0 & u^2 r_p^2 \end{pmatrix}, \quad (4.2)$$

where $v_{r,p} = dr_p/dt$ is the radial velocity of the planet. This coordinate frame rotates with the angular velocity of the planet, Ω_p , and contracts or expands if the planet moves inward or outward, respectively. The corresponding contravariant metric tensor reads, in the non-relativistic limit:

$$g^{\mu\nu} = \begin{pmatrix} -1 & uv_{r,p}/r_p & \Omega_p \\ uv_{r,p}/r_p & 1/r_p^2 & 0 \\ \Omega_p & 0 & 1/u^2 r_p^2 \end{pmatrix}. \quad (4.3)$$

In this frame, the potential Φ is given by:

$$\Phi = -\frac{GM_*}{r_p u} - \frac{GM_p}{r_p |u - 1|} + \frac{GM_p}{r_p} u \cos(\theta - \theta_p), \quad (4.4)$$

where G is the gravitational constant, M_* is the central mass, M_p is the mass of the planet and θ_p is the (fixed) angular position of the planet.

As in Paardekooper & Mellema (2006) we write the Euler equations in the form:

$$\frac{\partial \mathbf{W}}{\partial t} + \frac{\partial \mathbf{F}}{\partial u} + \frac{\partial \mathbf{G}}{\partial \theta} = \mathbf{X} + \mathbf{Y} + \mathbf{T}, \quad (4.5)$$

where \mathbf{W} is called the state vector, \mathbf{F} and \mathbf{G} are the radial and azimuthal flux vectors, and \mathbf{X} , \mathbf{Y} and \mathbf{T} are the source terms. The total source vector $\mathbf{S} = \mathbf{X} + \mathbf{Y} + \mathbf{T}$ is split into a radial part \mathbf{X} , an azimuthal part \mathbf{Y} and a temporal part \mathbf{T} .

Armed with Eqs. (4.2) and (4.3) we are in a position to derive expressions for the state, fluxes and source terms from the formulae of Eulerink & Mellema (1995) in the non-relativistic limit. The state \mathbf{W} and the fluxes in the radial and azimuthal direction \mathbf{F} and \mathbf{G} are written as:

$$\begin{aligned} \mathbf{W} &= u r_p^2 (\Sigma, \Sigma v_u, \Sigma v_\theta)^T, \\ \mathbf{F} &= u r_p^2 (\Sigma v_u, \Sigma v_u^2 + \frac{p}{r_p^2}, \Sigma v_u v_\theta)^T, \\ \mathbf{G} &= u r_p^2 (\Sigma v_\theta, \Sigma v_u v_\theta, \Sigma v_\theta^2 + \frac{p}{r_p^2 u^2})^T, \end{aligned} \quad (4.6)$$

where Σ denotes the gas surface density, v_u and v_θ the radial and azimuthal velocities, respectively, and p is the pressure. Note that the volume term scales with r_p^2 . We will work with a locally isothermal equation of state, so that

$$p = c_s^2 \Sigma, \quad (4.7)$$

where the sound speed c_s is a constant fraction of the Kepler velocity:

$$c_s = h v_K. \quad (4.8)$$

In vertical hydrostatic equilibrium, h is the relative thickness of the disk. For the two-dimensional approximation to be valid, h needs to be much smaller than 1. Typically we use $h = 0.05$.

Looking at the pressure terms in the fluxes we see that they both scale with r_p^{-2} . In view of Eq. (4.7) we can interpret this as a rescaling of the sound speed according to the change in position of the planet.

The sources \mathbf{X} and \mathbf{Y} read:

$$\mathbf{X} = \begin{pmatrix} 0 \\ \Sigma u^2 r_p^2 (v_\theta + \Omega_p)^2 - \Sigma u \frac{\partial \Phi}{\partial u} + p + \Sigma u^2 v_{r,p}^2 \\ -2\Sigma r_p^2 v_u (\Omega_p + v_\theta) \end{pmatrix}, \quad (4.9)$$

$$\mathbf{Y} = \begin{pmatrix} 0 \\ 0 \\ -\frac{\Sigma}{u} \frac{\partial \Phi}{\partial \theta} \end{pmatrix}. \quad (4.10)$$

There is an extra source term for the u -direction associated with the radial velocity of the planet.

Because the metric is time-dependent an extra source vector \mathbf{T} arises:

$$\mathbf{T} = \begin{pmatrix} 0 \\ -\Sigma u^2 r_p \frac{\partial v_{r,p}}{\partial t} - \Sigma u^2 v_{r,p}^2 - 2u \Sigma v_{r,p} r_p v_u \\ -\Sigma u r_p^2 \frac{\partial \Omega_p}{\partial t} - 2u \Sigma v_{r,p} r_p (v_\theta + \Omega_p) \end{pmatrix}. \quad (4.11)$$

The first terms are due to the acceleration of the coordinate frame, and the second term in the θ -component represents the Coriolis force. The third term in the u -component is due to the change of the volume element that scales with r_p^2 . The term $\Sigma u^2 v_{r,p}^2$ is special, because it also appears in \mathbf{X} and therefore it is absent in the total source \mathbf{S} .

The splitting of the total source \mathbf{S} in this way is correct for one-dimensional stationary solutions in the two spatial dimensions, and for homogeneous flow in the time direction (Eulerink & Mellema 1995). This has advantages for the numerical integration of the source terms.

4.3 NUMERICAL METHOD

In this section we discuss the two main ingredients of the numerical method: the approximate Riemann solver and the integration of the source terms. In particular, we focus on the difference between the method used in this Chapter and the method described in Paardekooper & Mellema (2006).

4.3.1 Roe Solver

Looking at Eqs. (4.6) we see that when we write $\mathbf{W} = (W_0, W_1, W_2)^T$ the radial flux \mathbf{F} can be written as:

$$\mathbf{F} = (W_1, W_1^2/W_0 + c_s^2 W_0/r_p^2, W_1 W_2/W_0)^T, \quad (4.12)$$

which has the same form as the Euler equations with $v_{r,p} = 0$ except for the transformation $c_s \rightarrow c_s/r_p$. The same holds for the azimuthal flux \mathbf{G} . This means that we can go back to the original method (see Paardekooper & Mellema 2006) and replace c_s by c_s/r_p in the projection coefficients, eigenvalues and eigenvectors, after which the new Roe solver can be used to solve the source-free version of Eq. (4.5). The major difference in the implementation of the new coordinate system lies in the source term integration, which we discuss next.

4.3.2 Source Terms

With the source term splitting given by Eqs. (4.9), (4.10) and (4.11) the integration of the source terms may be done algebraically assuming one-dimensional stationary solutions for the spatial source terms:

$$\frac{\partial \mathbf{F}}{\partial u} = \mathbf{X}, \quad (4.13)$$

$$\frac{\partial \mathbf{G}}{\partial \theta} = \mathbf{Y}, \quad (4.14)$$

and a homogeneous solution for the temporal source term:

$$\frac{\partial \mathbf{W}}{\partial t} = \mathbf{T}. \quad (4.15)$$

The use of stationary extrapolation was discussed extensively in Paardekooper & Mellema (2006). Here, we focus on the integration of the new temporal source term \mathbf{T} . Equation (4.15) may be integrated analytically to obtain the vector \mathbf{C} that is constant:

$$\mathbf{C} = r_p^2 \begin{pmatrix} \Sigma \\ v_u + u \frac{v_{r,p}}{r_p} \\ v_\theta + \Omega_p \end{pmatrix}. \quad (4.16)$$

This vector is used to update the state according to the changing orbital distance r_p and velocities $v_{r,p}$ and Ω_p of the planet.

4.3.3 Test

The hydrodynamics solver has been tested extensively on one- and two dimensional shock tubes, the wind tunnel with step, and a viscously spreading ring (see Paardekooper & Mellema 2006, Chapter 2). For the planet-disk problem, it was compared

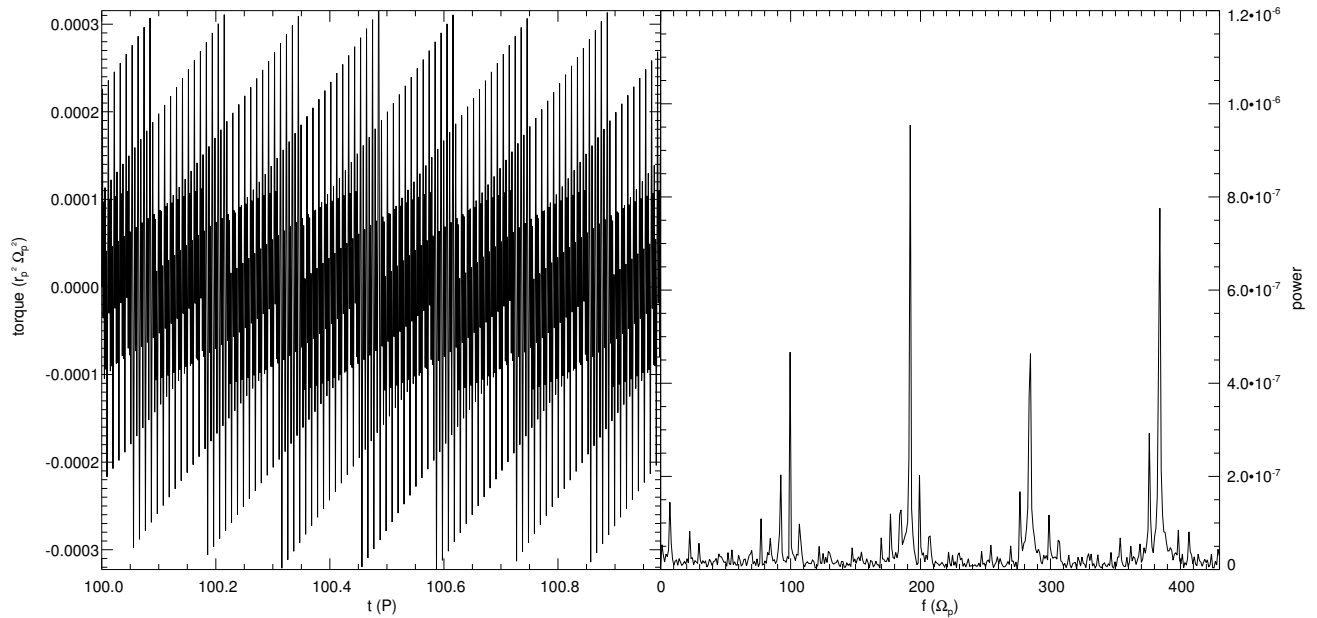


Figure 4.1: Left panel: torque on a $5 M_{\oplus}$ planet as a function of time for a run in an inertial frame. The torque is very noisy, but the average value is negative and comparable to the Type I analytical value of Tanaka et al. (2002). Right panel: Fourier power spectrum of the same torque series. The planet crosses 384 grid cells every orbit, and this frequency clearly shows up in the spectrum. However, most power lies in half this frequency.

with other methods in de Val-Borro et al. (2006). The new coordinate frame was tested by considering a massless planet on an eccentric orbit, for which the disk should not evolve. For $e = 0.1$, we have found density perturbations of less than 1% after 100 orbits. Although the temporal source terms \mathbf{T} are taken into account exactly, the extra term in \mathbf{X} is taken into account using approximate extrapolation (see Chapter 2). This approximation is responsible for the small perturbations.

4.4 RESULTS

In this section we present the results. We start by discussing low-mass planets, for which analytical results on migration rates and eccentricity damping exist. Because the two-dimensional approximation is not valid for these low-mass planets, we regard these results mostly as a test case for the method.

4.4.1 Type I migration

As a start, we do not let the planet migrate radially but calculate the torque on the planet only. This is usually done in two (D’Angelo et al. 2002; Koller et al. 2003) and in

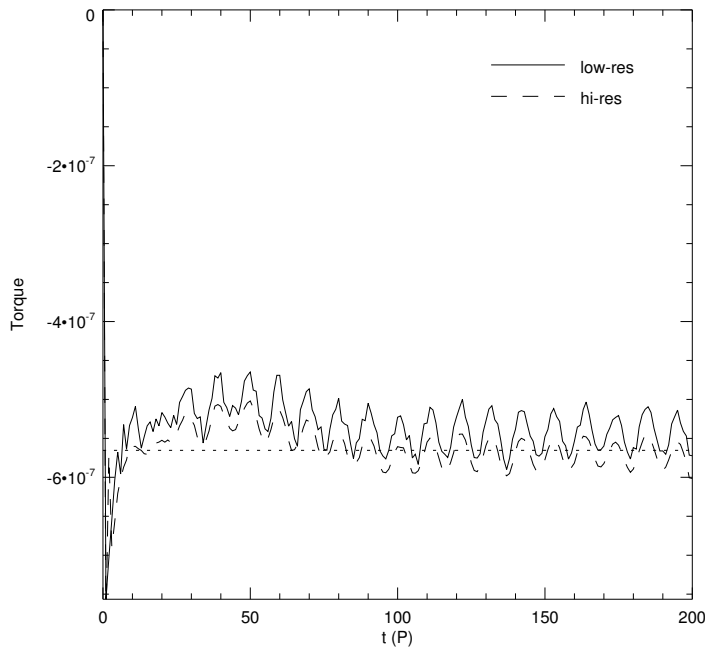


Figure 4.2: Torque evolution on a $5 M_{\oplus}$ planet for a rotating frame calculation at two different resolutions. Low resolution corresponds to $(n_r, n_{\phi}) = (128, 384)$; high resolution to $(n_r, n_{\phi}) = (256, 768)$.

three (Bate et al. 2003; D’Angelo et al. 2003) dimensions to avoid smearing effects due to the movement of the planet through the grid. We would like to see explicitly what the effect of this movement is, therefore we compare a simulation run in an inertial frame (where the planet moves through the grid in the azimuthal direction) to a simulation run in a rotating frame. We focus on a planet with a mass ratio of $M_p/M_* \equiv q = 1.6 \cdot 10^{-5}$, which corresponds approximately to a $5 M_{\oplus}$ planet around a Solar mass star. This puts the planet well inside the linear regime of Type I migration.

In the left panel of Fig. 4.1 we show the torque between $t = 100$ and $t = 101$ orbits for a planet in an inertial frame. It is clear that the torque varies dramatically within one orbit, reaching large positive as well as large negative values. The analytical result of Tanaka et al. (2002) for this disk and planet mass yields a torque of $-5.7 \cdot 10^{-7} r_p^2 \Omega_p^2$. The mean value of the torque in Fig. 4.1 is indeed negative, and comparable in magnitude to this analytical result.

A Fourier-analysis of the time series of the torque shown in the left panel of Fig. 4.1 is shown in the right panel of Fig. 4.1. There are four distinct peaks visible in the spectrum, at approximately $f = 95, 192, 290$ and 385 . Because the grid in the azimuthal direction is 384 cells large, the latter frequency matches exactly the frequency at which the planet is crossing grid cells, $f_0 = 384$. Moreover, all three other peaks can be related to this frequency as well: they occur approximately at $f = f_0/4, f_0/2$ and $3f_0/4$. Therefore we conclude that *all* oscillations seen in the torque in the left panel of Fig. 4.1 are of numerical origin: they are manifestations of the movement of the planet through the grid.

When we switch to a rotating frame, in which the planet resides at a fixed location, all these spurious oscillations disappear, see Fig. 4.2. The torque slowly converges to the analytical value of Tanaka et al. (2002). The small fluctuations occur approximately

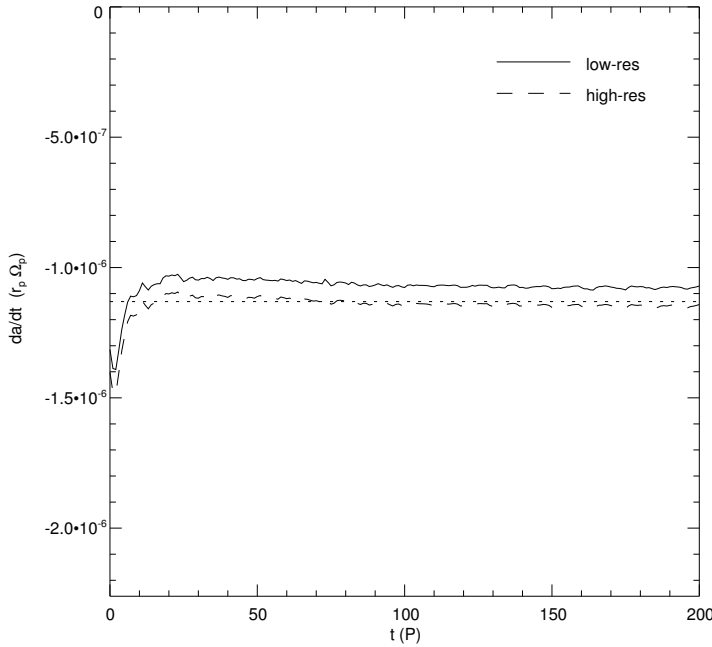


Figure 4.3: Evolution of the semi-major axis for a $5 M_{\oplus}$ planet embedded in a $0.001 M_{\odot}$ protoplanetary disk for two different resolutions.

at the libration time scale, and start to disappear upon increasing the resolution. Comparing Figs. 4.1 and 4.2 we conclude that a rotating frame is the preferred choice.

If we now free the planet also in the radial direction the situation becomes even worse for the inertial frame calculation. Because of the movement of the planet we get the same effect as seen in Fig. 4.1 but now also for the force in the radial direction. Because the radial velocity of the planet is much smaller than its azimuthal velocity the frequency of the force fluctuations is much lower. Therefore the planet experiences large periods of outward migration, for example, followed by large periods of inward migration. Again, this is entirely a numerical effect.

If we choose our coordinate frame as described in Sect. 4.2 the planet stays at a fixed location of the grid even though its radial coordinate changes. We show the resulting evolution in semi-major axis in Fig. 4.3. The torque on the planet is negative always, and because the planet stays at a fixed radial location in the grid no spurious outward migration is observed. The migration rate settles at a constant value after approximately 30 orbits of the planet. For the low resolution run, the measured migration rate is slightly less than predicted by Tanaka et al. (2002). This is not a consequence of the radial movement of the planet, because this disk of $0.001 M_{\odot}$ is not massive enough to induce sufficient migration in order to change the dynamical corotation torque (Masset & Papaloizou 2003). Indeed, for a run at higher resolution ($(n_r, n_{\phi}) = (256, 768)$) we nicely reproduce the correct migration rate. Note that the migration rate is not very sensitive to the torque fluctuations on the libration time scale as seen in Fig. 4.2, because the migration time scale for this low-mass disk is much larger than the libration time scale.

We conclude that at least for this low-mass planet a coordinate frame that keeps the planet at a fixed location is to be preferred over an inertial frame.

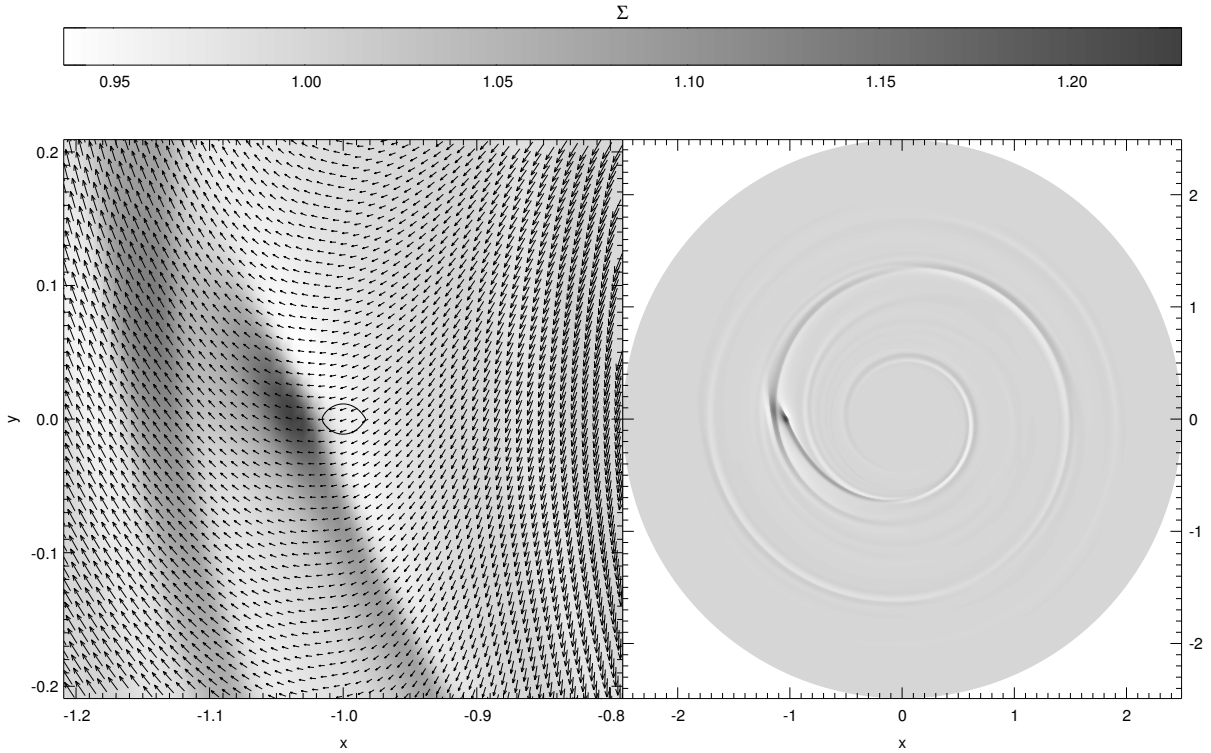


Figure 4.4: Greyscale plot of the gas surface density around a $5 M_{\oplus}$ planet after $5\frac{1}{4}$ orbits with $e = 0.1$. At this time, the planet is moving inward with a speed twice as high as the local sound speed. The left panel shows a close-up on the planet together with the velocity field *relative to the planet*. The Roche lobe of the planet is indicated by the black curve. The right panel shows the whole computational domain.

4.4.2 Eccentricity damping for low-mass planets

In the previous section the orbit of the planet remained nearly circular. Now, we want to look at eccentricity evolution and in order to do that we start the planet on an eccentric orbit.

The orbit of a planet in the plane of the disk can be characterized by the orbital energy

$$E = \frac{1}{2} \left(v_{r,p}^2 + r_p^2 \Omega_p^2 \right) - \frac{GM_{\odot}}{r_p}, \quad (4.17)$$

and the z-component of the orbital angular momentum

$$L = r_p^2 \Omega_p. \quad (4.18)$$

From these, the semi-major axis a and the eccentricity e can be calculated as follows:

$$a = -\frac{GM_{\odot}M_p}{2E}, \quad (4.19)$$

$$e^2 = 1 + \frac{2L^2E}{M_p^3(GM_{\odot})^2}. \quad (4.20)$$

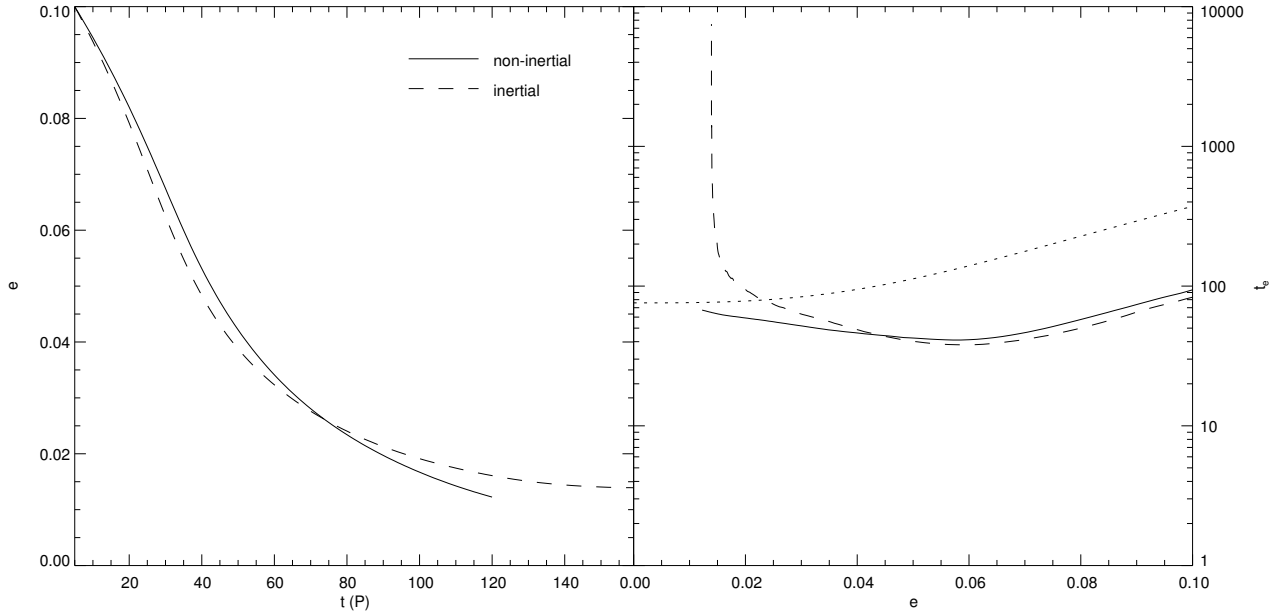


Figure 4.5: Eccentricity evolution for a $5 M_{\oplus}$ planet embedded in a $0.01 M_{\odot}$ disk for two different coordinate frames. Left panel: eccentricity as a function of time. Right panel: eccentricity damping time scale.

For bound orbits, $E < 0$ which results in a being larger than zero and an eccentricity smaller than 1.

Taking the derivative of Eq. (4.19) with respect to time, and using Eq. (4.20) to replace \dot{E} by a combination of \dot{e} and \dot{L} , we arrive at:

$$\frac{\dot{a}}{a} = \frac{2\dot{L}}{L} + \frac{2e^2}{1-e^2} \frac{\dot{e}}{e} \quad (4.21)$$

Here, \dot{x} means the derivative of x with respect to time. Adopting the definitions of Papaloizou & Larwood (2000) for the migration time scale $t_m = L/\dot{L}$ and the circulation time scale $t_e = e/\dot{e}$ we can rewrite this equation as:

$$\frac{\dot{a}}{a} = \frac{2}{t_m} + \frac{e^2}{1-e^2} \frac{2}{t_e} \quad (4.22)$$

Note that the term ‘migration time scale’ is somewhat misleading: it applies to the semi-major axis alone only when the eccentricity is very small.

Papaloizou & Larwood (2000) calculated t_e and t_m as a function of eccentricity, and they found that t_m , or, rather, \dot{L} switches sign above $e \approx 1.1 h$. This means that the angular momentum of a planet will actually increase due to disk-planet interaction when the orbital eccentricity becomes large enough. Cresswell & Nelson (2006) showed, however, that this does not lead to outward migration because, looking at Eq. (4.22),

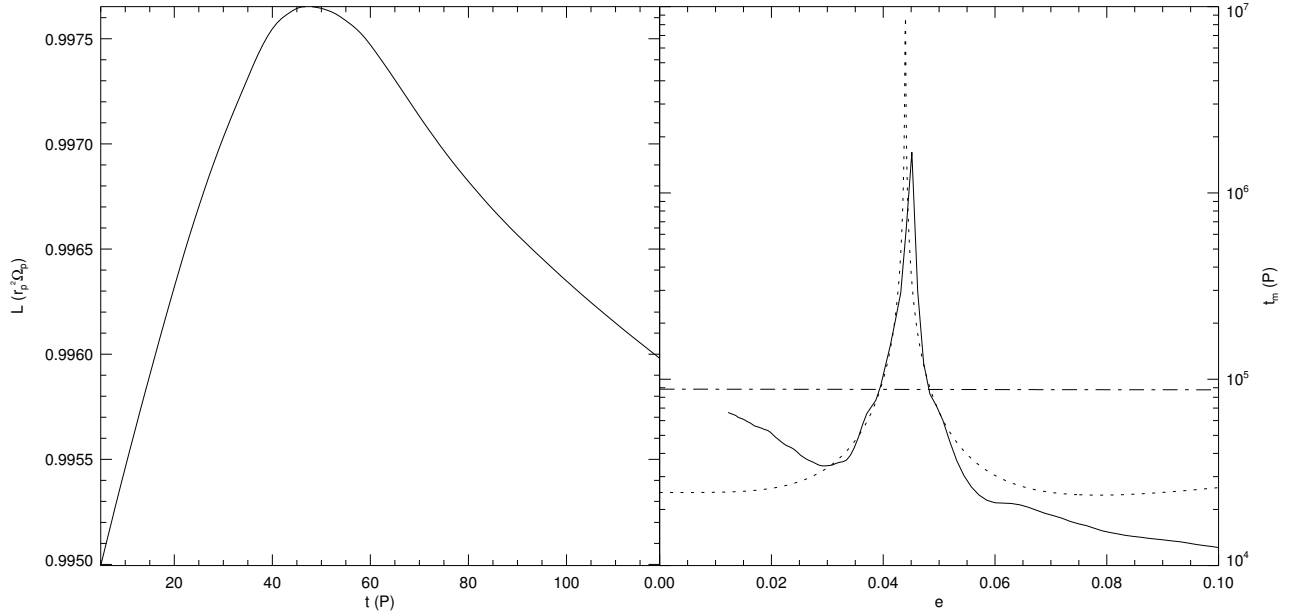


Figure 4.6: Left panel: evolution of a specific angular momentum of the $5 M_{\oplus}$ planet embedded in a $0.01 M_{\odot}$ protoplanetary disk. The angular momentum reaches a maximum at $e = 0.045$. Right panel: corresponding migration time scales. Note that for $e > 1.1 h = 0.04$ the angular momentum *increases*. The dotted line shows the analytical result from Papaloizou & Larwood (2000), and the dash-dotted line the result from Tanaka et al. (2002), valid for $e = 0$.

the negative contribution of eccentricity damping overcomes the positive contribution from angular momentum growth.

In this section, we start our $5 M_{\oplus}$ planet at an eccentric orbit ($e = 0.1$) in a massive disk ($M_d/M_{\odot} \equiv q_d = 0.01$). We set the aspect ratio of the disk to $h = 0.04$. This disk is able to significantly damp the planet's eccentricity within 100 orbits. We again compare an inertial frame with a frame that keeps the planet at a fixed location. Due to the large radial velocity of the planet, as well as the large *changes* in the velocity of the planet, such an eccentric orbit really puts our method to the test, in particular the source term integration.

In Fig. 4.4 we show the surface density around a $5 M_{\oplus}$ planet after $5\frac{1}{4}$ orbits with $e = 0.1$. Around this time, the planet reaches its maximum inward radial velocity (at $t = 5$ the planet is at apocenter), which affects the surface density close to the planet significantly. Some of the spiral structure remains intact, but due to the high inward (supersonic) velocity of the planet it has overtaken the former inner spiral wave which shows up as the leftmost dark filament in the left panel of Fig. 4.4. Also, the planet is not able to capture a dense envelope because its potential well is not deep enough to gravitationally bind the material that is streaming by at high velocity. Simulations with higher resolution close to the planet, and therefore a deeper potential well, may reveal gas that is bound to the planet. Simulations using an inertial coordinate frame

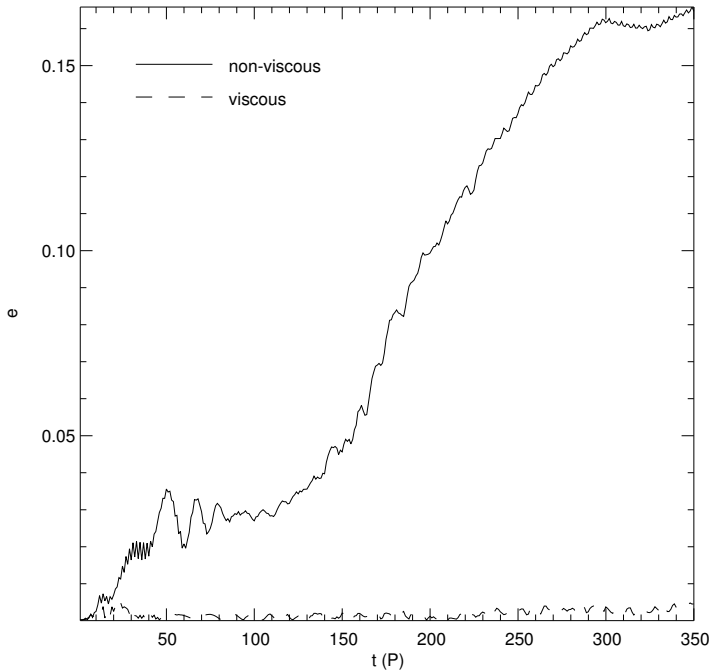


Figure 4.7: Eccentricity evolution for a $5 M_J$ planet embedded in a non-viscous disk (solid line) and a viscous disk, with $\alpha = 0.004$ (dashed line).

show the same result.

In the left panel of Fig. 4.5 we show the evolution of the orbital eccentricity for a run in an inertial frame (dashed line) and a run in our coordinate system of Sect. 4.2 (solid line). We see that both runs give approximately the same results until 80 orbits, after which for the inertial frame e comes to a stop around $e = 0.014$, while for our new coordinate frame e continues to decrease, as expected (Papaloizou & Larwood 2000).

When we look at t_e as a function of e in the right panel of Fig. 4.5 we see that the inertial frame and our new frame agree reasonably well above $e \approx 0.04 = h$. Below that, t_e starts to increase for the inertial frame, until it quickly rises to infinity for $e \approx 0.014$. Clearly this is not physical. Interesting is that at this point the eccentricity is comparable to the size of a single grid cell. As the planet makes its radial excursions from $r = a(1 - e)$ to $r = a(1 + e)$ it will cross only two cells. The coarseness of the grid at this scale leads to spurious eccentricity evolution.

For the coordinate frame that keeps the planet fixed on the grid no such thing happens. Instead, t_e slowly rises to approximately the analytical estimate of Papaloizou & Larwood (2000) for low values of e , that is broadly consistent with the results of Ward (1997), Tanaka & Ward (2004) and Artymowicz (1993a, 1994). However, for larger values of e the difference between our results (also for an inertial frame) and the analytical result of Papaloizou & Larwood (2000) is approximately a factor of 3. This is interesting, because Cresswell & Nelson (2006) needed the same factor to get their semi-major axis evolution consistent with the results from Papaloizou & Larwood (2000), while this was not necessary for the eccentricity evolution.

In the left panel of Fig. 4.6 we show the specific angular momentum as a function of time for the same planet. Indeed, as found by Papaloizou & Larwood (2000), L actually *increases* for $e > 1.1 h$. It is at $e = 0.045 = 1.125 h$ that \dot{L} switches sign. However,

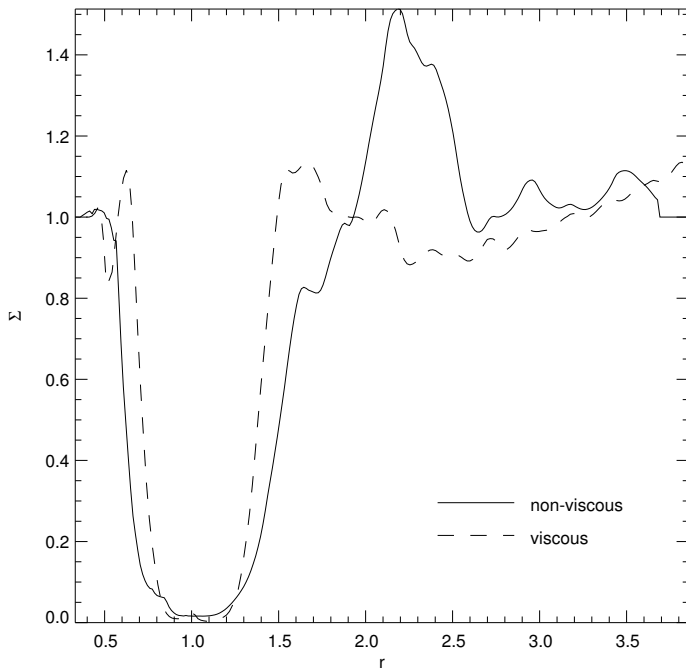


Figure 4.8: Azimuthally averaged surface density profile after 300 orbits of a $5 M_J$ planet embedded in an inviscid disk (solid line) and a viscous disk (dashed line) with $\alpha = 0.004$.

as was also observed by Cresswell & Nelson (2006), the semi-major axis continues to decrease. In the right panel of Fig. 4.6 we show the corresponding migration time scale. We see that for $e > h$ our results agree reasonably with those of Papaloizou & Larwood (2000). Towards lower eccentricities our results approach the analytical result of Tanaka et al. (2002), for which the migration time scale is more than a factor of 3 larger than found by Papaloizou & Larwood (2000). This is related to the factor of 3 that Cresswell & Nelson (2006) needed to match their migration rates with those of Papaloizou & Larwood (2000).

The most apparent difference between our results and those of Cresswell & Nelson (2006) can be seen at high eccentricities. This is interesting, because when $e > h$ the planet starts to move supersonically through the disk and therefore shocks start to play an important role. Note that it is not the coordinate system that causes the difference, because from Fig. 4.5 we see that we obtained the same results in an inertial frame for $e > h$. We have verified that the differences are also not due to the particular disk model used: although both eccentricity and semi-major axis evolution depend on for example the power law index of the surface density, a model run with the same parameters as in Cresswell & Nelson (2006) still differed from their results for high eccentricities.

One possible explanation for this behavior is the different way in which shocks are handled within the two numerical methods. When $e > h$, the planet moves supersonically with respect to the disk material at certain phases of its orbit. During these phases, a bow shock may form in front of the planet, which changes the torque balance on the planet. More work is necessary to elucidate the importance of shocks in this regime, but in view of the low masses of the planets this study should be carried out in three dimensions. Here, we are interested in the onset of eccentricity growth for

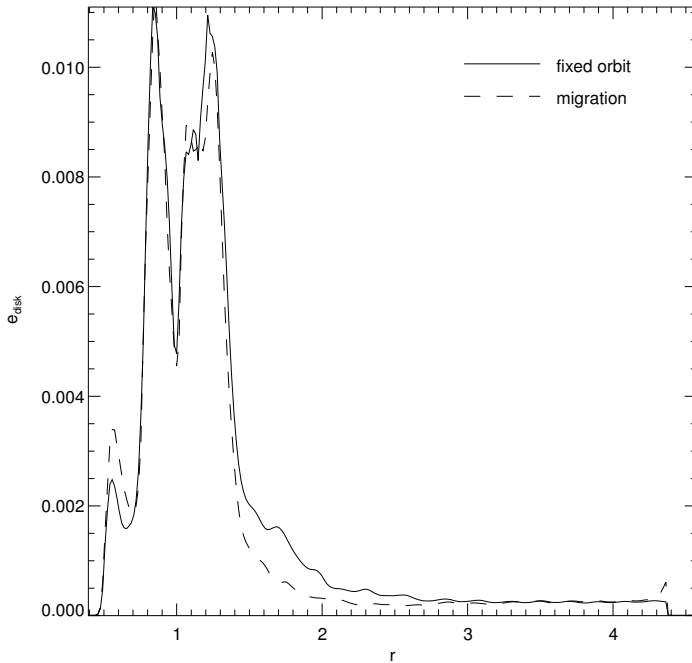


Figure 4.9: Disk eccentricity after 500 orbits of a $5 M_J$ planet in a viscous disk with $\alpha = 0.004$. Solid line: planet on a fixed, circular orbit. Dashed line: planet is free to migrate.

high-mass planets.

4.4.3 A planet of $5 M_J$

In this section, we consider a high-mass planet of $5 M_J$ around a $1 M_\odot$ star. This planet is massive enough to open up a deep gap even in a moderately viscous disk (Bryden et al. 1999) and therefore it is a good candidate to find eccentricity growth. However, according to the results of Papaloizou et al. (2001) this planet is still not massive enough for its eccentricity to be excited by interaction with the disk. They only find significant eccentricity growth for planet in the Brown Dwarf mass regime ($M_p > 10 M_J$). In this section, we investigate whether the absence of viscosity may help the growth of orbital eccentricity.

In Fig. 4.7 we show the evolution of the orbital eccentricity with time for an inviscid disk (solid line) compared to a viscous disk (dashed line). While the eccentricity in the viscous case is indeed rising slowly, this is nothing compared what happens in the inviscid disk. In the latter case, the gap quickly becomes deep enough to sustain an eccentricity of $e \approx 0.03$ up to $t = 100$ orbits. After 100 orbits, the gap gets wide enough to reduce the eccentricity damping effect of the $m = 1, l = 0$ corotation resonance, which is located at $r \approx 1.6$. This is illustrated in Fig. 4.8, where we show the density profile of the gap for the inviscid as well as the viscous case. It is clear that the density is strongly reduced near $r = 1.6$ for the inviscid disk, while in the viscous case the gap does not extend far enough to reduce the effect of the corotation resonance located at $r = 1.6$.

For longer integration times than presented here, Kley & Dirksen (2006) found that the gap eventually becomes wide enough to sustain an eccentric disk even in the vis-

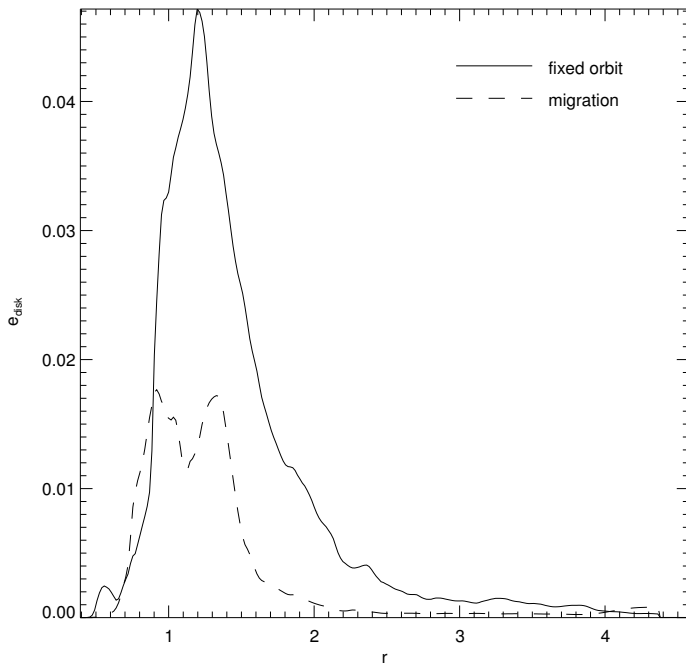


Figure 4.10: Disk eccentricity after 400 orbits of a $5 M_J$ planet in an inviscid disk. Solid line: planet on a fixed, circular orbit. Dashed line: planet is free to migrate.

cous case. Although our integration times are not as long as in Kley & Dirksen (2006), we can give some comments on the start of eccentricity exchange between planet and disk. In particular, we can inquire whether the eccentricity generated at the 1:3 resonance can be efficiently transferred to the planet. For this to happen, the disk needs to be more massive than the planet; otherwise, only an eccentric disk results. This is also what happens if the planet is forced to remain on a circular orbit (Kley & Dirksen 2006), which makes its effective inertia infinitely large. For our nominal disk mass, we expect the eccentricity of the planet to grow.

In Fig. 4.9 we show the eccentricity of two viscous disks: one with a planet on a fixed orbit (solid line) and one with a migrating planet (dashed line). The disk eccentricity is calculated using Eq. (4.20) on the azimuthally averaged disk quantities (see also Kley & Dirksen 2006). Although after 500 orbits the disk has not been able to grow significant eccentricity, it is clear that especially in the region $r \in [1.5, 2.0]$ the disk is more eccentric for a planet on a fixed circular orbit than for a free planet. This is an indication that eccentricity is being transferred from the disk to the planet.

The difference is even more pronounced for an inviscid disk (see Fig. 4.10). For the fixed circular orbit, the eccentricity profile resembles closely that of a $5 M_J$ planet in a *viscous* disk after 2500 orbits (Kley & Dirksen 2006), although the maximum eccentricity is much lower. This is because even after 500 orbits the eccentricity damping corotation resonance still plays a role. Only when the gap extends towards $r = 1.6$ the disk eccentricity may grow to several tenths. Most important, however, is the fact that the same mechanism as outlined in Kley & Dirksen (2006) is able to produce an eccentric disk much faster in an inviscid disk than in a viscous disk. Moreover, the eccentric disk is able to transfer some of its eccentricity to the planet. Because of the high disk mass compared to the planet mass, the orbital eccentricity picked up by the

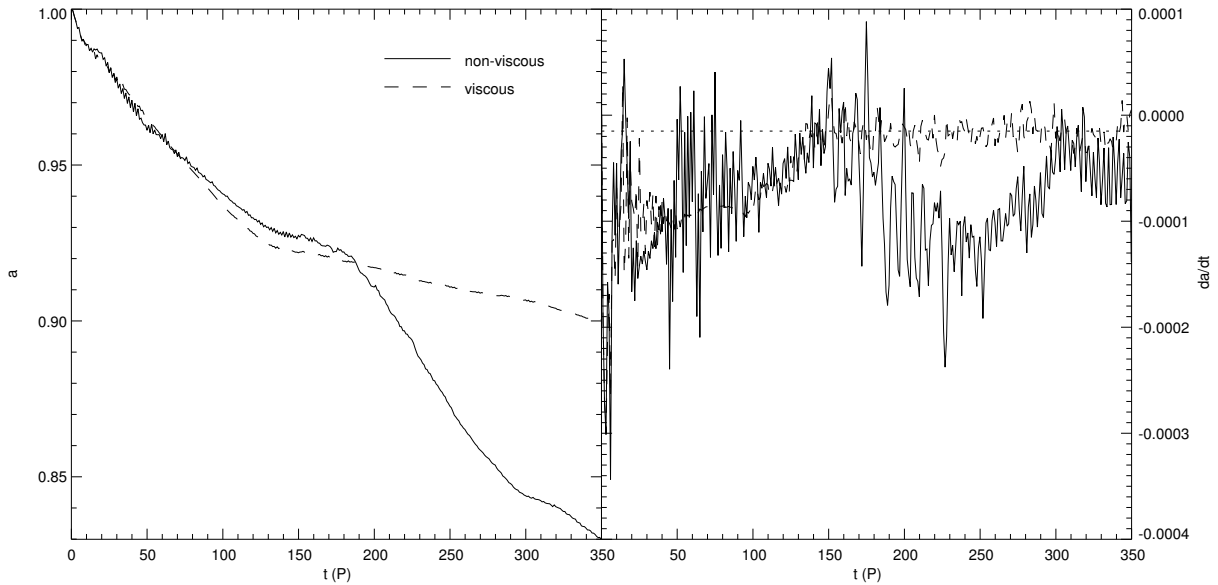


Figure 4.11: Migration behavior of a $5 M_J$ planet embedded in a non-viscous disk (solid line) and a viscous disk, with $\alpha = 0.004$ (dashed line). Left panel: evolution of the semi-major axis a . Right panel: the corresponding migration rate. The analytical Type II migration rate (given by the viscous evolution time scale of the disk) is indicated by the horizontal dotted line.

planet exceeds the maximum eccentricity of the disk in the case of a planet on a fixed circular orbit.

We have shown that in the most favorable limit of an inviscid, massive disk eccentricity growth does occur for a $5 M_J$ planet. It remains to be seen, however, what happens in a more realistic setting of a less massive disk with finite viscosity through MHD turbulence.

Finally, we compare the migration behavior of the $5 M_J$ planet in an inviscid disk to that in a viscous calculation. In Fig. 4.11 we show the evolution of the semi-major axis (left panel) and the corresponding migration rates (right panel). As was found also in Papaloizou et al. (2001) migration is directed inward as long as the eccentricity grows. For the viscous case, where the orbit of the planet remains nearly circular, we find excellent agreement with the analytical Type II migration rate after approximately 150 orbits. This is again a confirmation that our coordinate frame that moves with the planet gives reliable results. For the inviscid case, we find an increase in the migration rate when the eccentricity starts to grow. A simple explanation for this can be given using Eq. (4.19) and Eq. (4.20) for the disk: at a fixed value of a (for example, the location of the eccentricity driving 1:3 resonance), which corresponds to a fixed disk energy, in order for the disk to become eccentric its angular momentum needs to increase. This angular momentum is extracted from the planet's orbit, which leads to an enhanced inward migration rate. As soon as the orbital eccentricity growth of the planet starts to slow down (around 300 orbits, see Fig. 4.7) the migration rate goes down as well. Longer integration times may show oscillatory behavior of the planet's eccentricity (Papaloizou et al. 2001), which may lead to temporary outward migration.

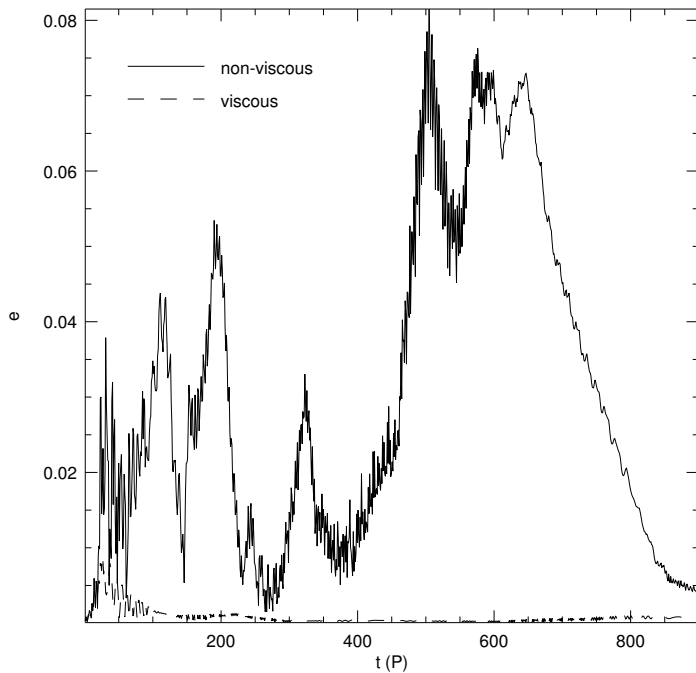


Figure 4.12: Eccentricity evolution for a $1 M_J$ planet embedded in a non-viscous disk (solid line) and a viscous disk, with $\alpha = 0.004$ (dashed line).

4.4.4 A planet of $1 M_J$

Now we turn to the important case of a planet of $1 M_J$. Although this planet is massive enough to open up a gap in the disk, no eccentricity growth was observed in numerical simulations (Nelson et al. 2000). Observations, however, show that even planets with masses much lower than Jupiter’s can have large eccentricities, up to $e = 0.6$. It has been suggested (Papaloizou et al. 2001) that a lower viscosity in the disk may help to create a large enough gap to promote eccentricity growth for planets of $1 M_J$. In the previous section we have shown that for a more massive planet this is indeed the case: in the absence of viscosity the orbital eccentricity of a $5 M_J$ planet grows to $e \approx 0.16$ within 350 dynamical time scales, while in a viscous disk the orbit remained almost circular during the same amount of time. However, as was shown by Kley & Dirksen (2006), a planet of $1 M_J$ is not able to produce an eccentric disk even on the viscous time scale.

In Fig. 4.12 we compare the evolution of the orbital eccentricity of the planet in a viscous and an inviscid disk. First of all, note that for the viscous run the eccentricity first rises to $e \approx 0.01$ in the gap-opening phase, which may be connected to the mechanism outlined in Sari & Goldreich (2004). There it is argued that during the phase in which the planet has opened up a partial gap it is more susceptible to eccentricity growth. It is a general feature of all models that during this phase the eccentricity grows. As can be seen from Fig. 4.12, for an inviscid disk the effect is stronger.

After the eccentricity in the viscous model has reached its maximum value, the eccentricity starts to decline and $e \ll 0.01$ after 100 orbits. Around 600 orbits, e start to grow slightly, but after 800 orbits it levels off already around $e \approx 0.0005$. This agrees with the result of Nelson et al. (2000): for a viscous disk, a $1 M_J$ planet does not pick

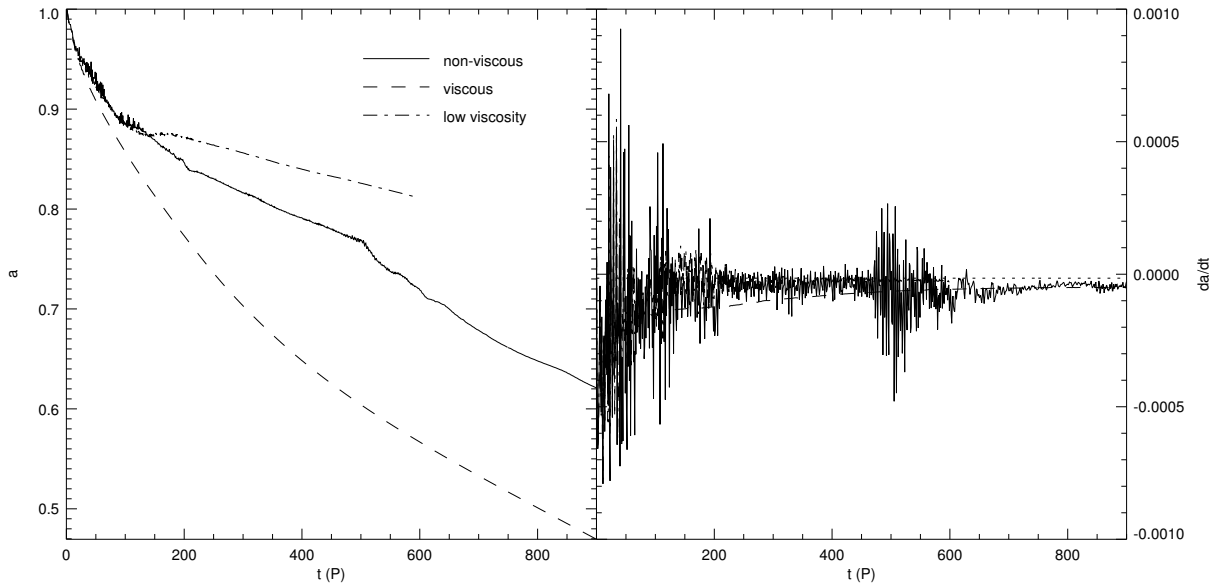


Figure 4.13: Semi-major axis evolution for a $1 M_J$ planet in an inviscid disk (solid line), in a viscous disk with $\alpha = 0.004$ (dashed line), and a low-viscosity disk with $\alpha = 0.0004$ (dash-dotted line).

up eccentricity.

For an inviscid disk, the evolution of the orbital eccentricity is shown by the solid line in Fig. 4.12. There are episodes of eccentricity growth as well as strong damping, and the overall behavior of e is highly erratic. There are no long periods with either high or low eccentricity, and the maximum value of e that is reached is approximately 0.08.

The main reason for the absence of eccentricity growth is that the gap does not get deep enough, even for the inviscid model. This is illustrated in Fig. 4.13, where we show the semi-major axis evolution together with the corresponding migration rates for three disks with different viscosity levels. The smooth curve from the high-viscosity model ($\alpha = 0.004$) gives the fastest migration, which leaves the planet at approximately $a = 0.47$ after 900 orbits. Note that in an inertial frame run, where the inner disk edge would be located at $r = 0.4 a_0$ the planet would hit the boundary of the computational domain. This illustrates one other advantage of this new coordinate frame: no matter how fast and how far the planet migrates, it will never hit the boundary of the computational grid. There is some influence of the boundary conditions, because at the boundaries we assume the disk to be unperturbed. This means that when the planet is moving inward, in which case the gas is moving *outward* in our coordinate frame, the state of the gas that is flowing through the inner boundary into the computational domain is that of the unperturbed disk. In reality, this inflowing gas would have been perturbed by the planet because the inner spiral wave reaches all the way to the physical inner edge of the disk. However, this does not influence the torque on the planet as long as it takes long enough for the inflowing material to reach the planet so that the gas has no memory of the unperturbed state it was in at the boundary. This is the case

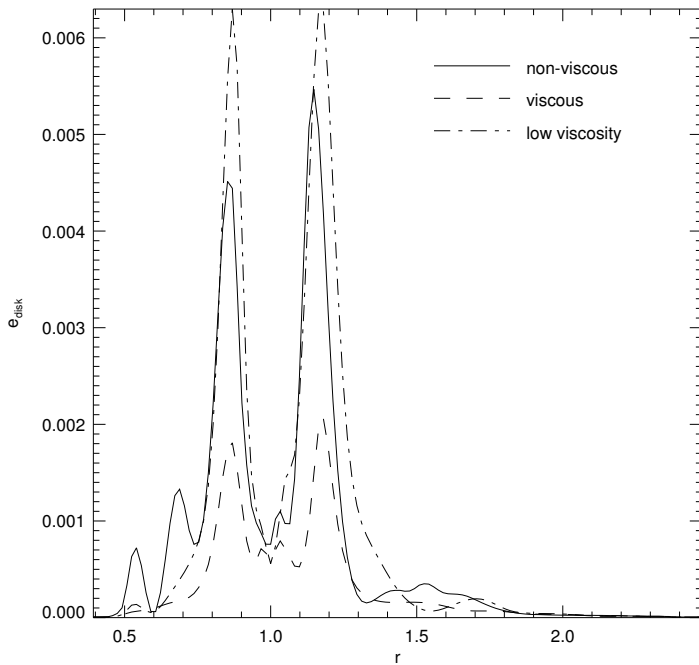


Figure 4.14: Disk eccentricity after 400 orbits of a $1 M_J$ planet in an inviscid disk (solid line), a viscous disk (dashed line) with $\alpha = 0.004$, and a low-viscosity disk (dash-dotted line) with $\alpha = 0.0004$.

for all simulations presented here.

After approximately 700 orbits the migration rate reaches a steady value. However, this migration rate does not correspond to Type II migration; in fact, it is more than a factor 2 faster. This is due to the fact that the gap simply does not get empty enough, and therefore resonant torques continue to play a role. A related issue is that a $1 M_J$ planet is still able to accrete disk material (Kley 1999; D’Angelo et al. 2002; Paardekooper & Mellema 2006). For higher-mass planets, mass flow through the gap becomes ever more difficult, and in the previous section we saw that for a $5 M_J$ planet the gap is clean enough to reproduce Type II migration.

It is interesting to see that also for the inviscid disk the gap does not become clean enough to halt migration completely. In fact, matter piles up around the Lagrangian points L4 and L5 (see de Val-Borro et al. 2006), from which it may slowly spread into the rest of the gap region. After 600 orbits, the migration rate in the inviscid disk is comparable to that in the viscous disk. The coorbital material responsible for this migration is also responsible for eccentricity damping.

Viscosity removes the material from the Lagrangian points (de Val-Borro et al. 2006), and it is therefore possible that there exists a certain level of viscosity that results in a deep enough gap together with empty Lagrangian points. Although we did not perform a full parameter study, results with a reduced value of α suggest that it is not possible. The dash-dotted line in Fig. 4.13 shows the semi-major axis evolution and the corresponding migration rate for a low-viscosity disk ($\alpha = 0.0004$). The migration rate reaches a steady value after 200 orbits, which is only a little longer than for the $5 M_J$ planet (see Fig. 4.11). However, the migration rate is still too large for Type II. In fact, we find that the migration rate for the $\alpha = 0.0004$ disk approximately corresponds to the viscous velocity of the $\alpha = 0.004$ disk. In other words, the migration rate in

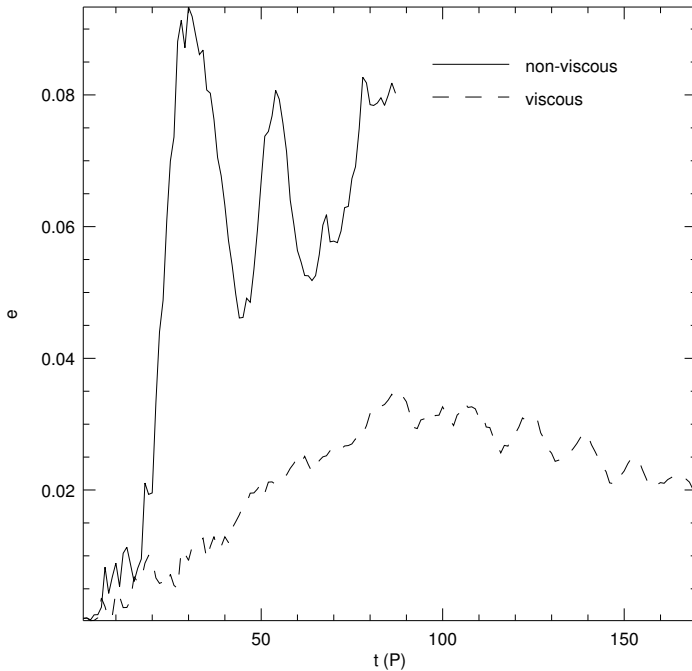


Figure 4.15: Eccentricity evolution for a $1 M_J$ planet embedded in a non-viscous disk (solid line) and a viscous disk, with $\alpha = 0.004$ (dashed line). The disk scale height was set to $h = 0.025$.

the low-viscosity disk is approximately a factor of 10 higher than the Type II estimate. This is because the viscosity is too low to clear L4 and L5, so we are approaching the inviscid result. From Fig. 4.13 we see that for the low-viscosity run the planet migrates slower than in the inviscid disk. No eccentricity growth was observed, however.

For no level of viscosity we found eccentricity growth in the disk. In Fig. 4.14 we show the disk eccentricity after 400 orbits of the planet for three different levels of viscosity. Note that from Fig. 4.12 we see that the planet is on a nearly circular orbit at that time in the inviscid disk. We see that eccentricity growth in the disk is highly dependent on the level of viscosity, which was also found by Kley & Dirksen (2006). The low-viscosity disk gets a little more eccentric than the inviscid disk, but this may be due to the higher eccentricity of the planet in the inviscid disk. Indeed, after 600 orbits, when the planet in the inviscid disk reaches an eccentricity of approximately $e = 0.075$ we find that the peak value of the disk eccentricity is reduced by a factor 2 compared to Fig. 4.14, while e_{disk} slowly grows for the viscous models, for which the orbital eccentricity of the planet does not grow during that time. This again points at a strong coupling between the eccentricity of the disk and the planet.

The pressure scale height H at the location of the planet plays an important role in gap formation theory. The angular momentum flux due to the planet is proportional to h^{-3} (see Chapter 3), which means that when H increases, F_0 decreases and gap formation is more difficult. Eccentricity growth should therefore be easier in disks with a low value of h . However, the width of the gap decreases with decreasing values of h (Bryden et al. 1999), which makes eccentricity growth more difficult. It is therefore not clear what the combined effect will be on the evolution of e .

In Fig. 4.15 we show the eccentricity evolution of a $1 M_J$ planet in a disk with $h = 0.025$. Because our base resolution is not sufficient to accurately resolve one pressure

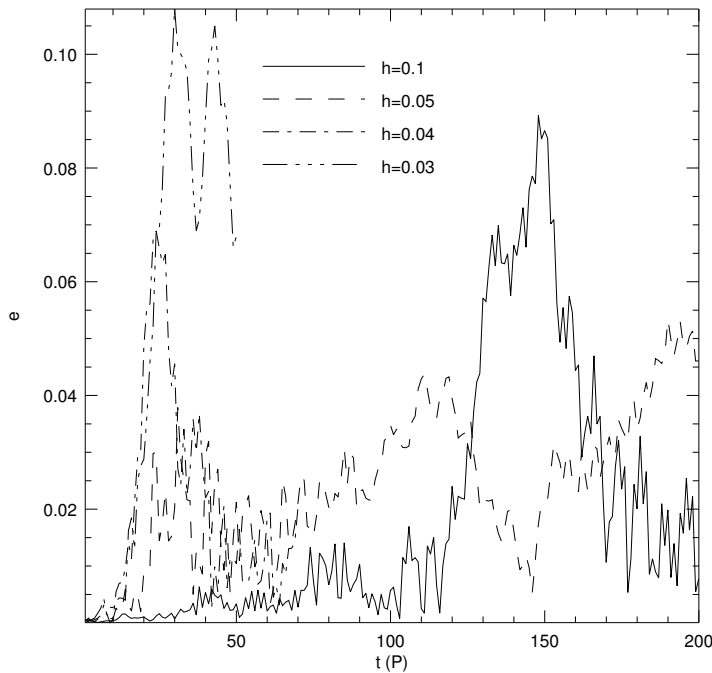


Figure 4.16: Eccentricity evolution for a $1 M_J$ planet embedded in a non-viscous disk, for different values of the pressure scale height h .

scale height for this value of h , we are forced to take the resolution twice as high, which makes the simulations eight times as expensive. For the viscous run in Fig. 4.15 we see that the eccentricity rises to a maximum of 0.035, after which it starts to decay. The decay is slow, however, and for a large number of orbits the planet is on an eccentric orbit. This is very different from the $h = 0.05$ viscous case depicted in Fig. 4.12, where e quickly drops to 10^{-4} and lower. This is because the density in the gap region decreases much faster for $h = 0.025$, which renders coorbital resonances far less effective compared to the $h = 0.05$ case.

For the inviscid run in Fig. 4.15 we see that the eccentricity is able to grow to approximately 0.09. There, the planet encounters the edge of the gap after which e decays. However, at all times e is much larger than h , oscillating around $e \approx 0.07$. Due to the deep gap the planet is able to remain in an eccentric orbit after the initial period of eccentricity growth that is present in all simulations. After that, an oscillating behavior set in where the planet periodically encounters the gap edge, followed by eccentricity damping, but e always maintains a significant value.

In Fig. 4.16 we show the eccentricity evolution for four different values of h . For $h > 0.03$ we see the initial eccentricity growth, but e always decays after that. Interestingly, after approximately 150 orbits, for $h = 0.1$ the eccentricity rises to a higher value than is ever reached by the $h = 0.05$ simulation. This is because the planet opens up a wider gap in this disk, which increases the maximum eccentricity that may be reached by the planet. However, the gap is not clean enough to sustain this eccentricity.

A similar effect can be seen for the $h = 0.03$ model: although the gap is less clean than for the $h = 0.025$ model of Fig. 4.15, the resulting eccentricity is larger. Again, this is because the gap opened by the planet is slightly wider in a disk with $h = 0.03$ compared to a disk with $h = 0.025$. We also see that the planet is able to maintain an

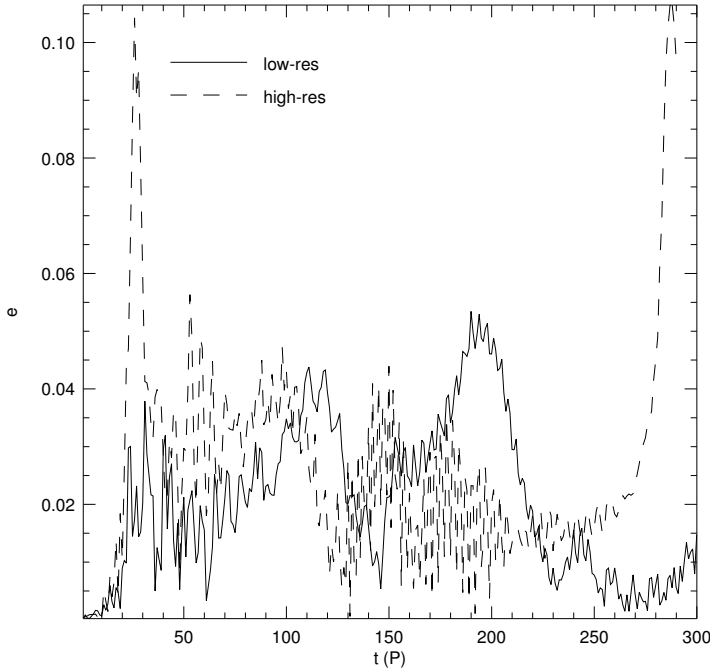


Figure 4.17: Eccentricity evolution for a $1 M_J$ planet embedded in a non-viscous disk, for two different resolutions: low (solid line, $(n_r, n_\phi) = (128, 384)$), and high (dashed line, $(n_r, n_\phi) = (256, 768)$).

eccentric orbit in the $h = 0.03$ disk. This suggests that the minimum mass for sustaining eccentricity is:

$$q_{ecc} \approx 12 q_H = 36 h^3, \quad (4.23)$$

where q_H was defined in Chapter 3. This is consistent with the $5 M_J$ planet maintaining an eccentric orbit in a $h = 0.05$ disk.

Because a clean gap is a prerequisite for eccentricity to grow, we investigate whether our results are sensitive to the numerical resolution used. Because of the irregular behavior of e in Fig. 4.12 we do not expect perfect agreement, but it is interesting to see if the global characteristics agree for different resolutions. In Fig. 4.17 we compare the evolution of e for our base resolution (solid line, see also Fig. 4.12) and a resolution that is twice as high. The first thing to note is that during the early phase of gap formation, at approximately 25 orbits, the eccentricity rises to approximately 0.1 for the high-resolution run. This is indeed due to the gap being cleared faster, because the effect is the same as for lowering h (see Fig. 4.16). Furthermore, there is a second peak in the eccentricity near $t = 290$, also with an amplitude of approximately 0.1. Clearly, the balance between eccentricity growth or damping is very delicate. The gap is only slightly deeper for the high-resolution case, but it still makes all the difference.

The second conclusion we can draw from Fig. 4.17 is that $e = 0.1$ is really an upper limit for the orbital eccentricity of a $1 M_J$ planet. As soon as the planet's radial excursions take it near the edges of the gap the eccentricity is damped again. For neither of the two resolutions the planet is able to *maintain* an eccentric orbit. This would require a thinner disk.

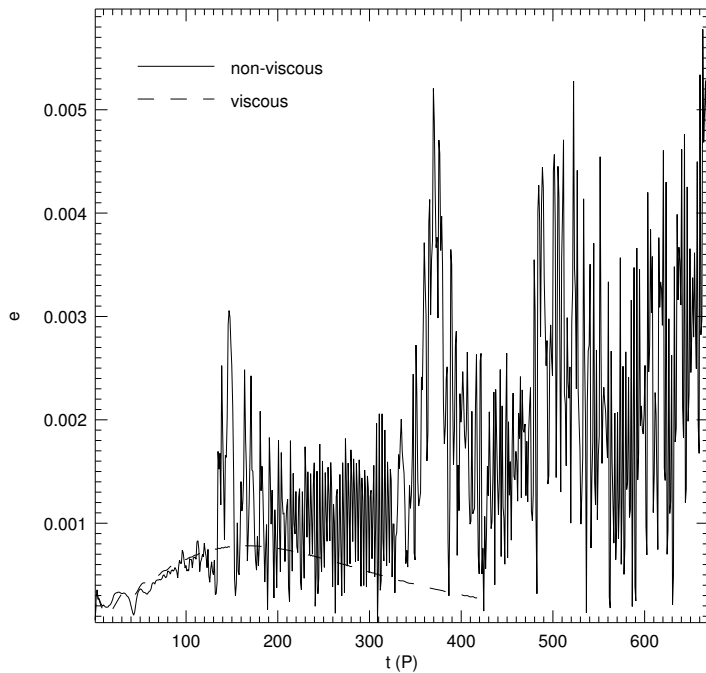


Figure 4.18: Eccentricity evolution for a $0.1 M_J$ planet embedded in a non-viscous disk (solid line) and a viscous disk, with $\alpha = 0.004$ (dashed line).

4.4.5 A planet of $0.1 M_J$

Finally, we consider a planet that is not massive enough to open up a gap in a viscous disk. In an inviscid disk, vortices appear (Koller et al. 2003; Li et al. 2005, see also Chapter 3) and it has been suggested that these may affect the eccentricity and semi-major axis evolution of the planet. Koller et al. (2003) showed that the torque behaves very irregularly once the vortices appear. In Chapter 3, we have shown that we also find vortex production for a $0.1 M_J$ planet in an inviscid disk, and in this section we investigate the influence of the vortices on the evolution of the semi-major axis and eccentricity of the planet.

As in previous sections, we start with the evolution of e , See Fig. 4.18, where we compare the results for an inviscid disk (solid line) with a viscous disk (dashed line). The viscous run shows eccentricity growth up to 170 orbits, after which it slowly decays. The maximum value of e that is reached is approximately 0.0008. Because this planet does not open up a gap in the disk, e can not grow because of the strong damping effect of coorbital Lindblad resonances.

We see that for the inviscid disk, the orbital eccentricity of the planet closely follows the viscous run until approximately 120 orbits. After that, the eccentricity evolution becomes highly irregular due to the effects of the vortices. Still, it is clear that e grows slowly during the whole simulation. This is related to the opening of the gap: while the gap is being opened, the conditions are more favorable to eccentricity growth (Sari & Goldreich 2004). After 170 orbits in the viscous disk, the shallow gap that is created by this low-mass planet has reached its steady state depth. From there on, viscous transport of angular momentum exactly balances the effect of the planet. For the inviscid disk, gap formation continues (see Chapter 3), and the eccentricity may continue

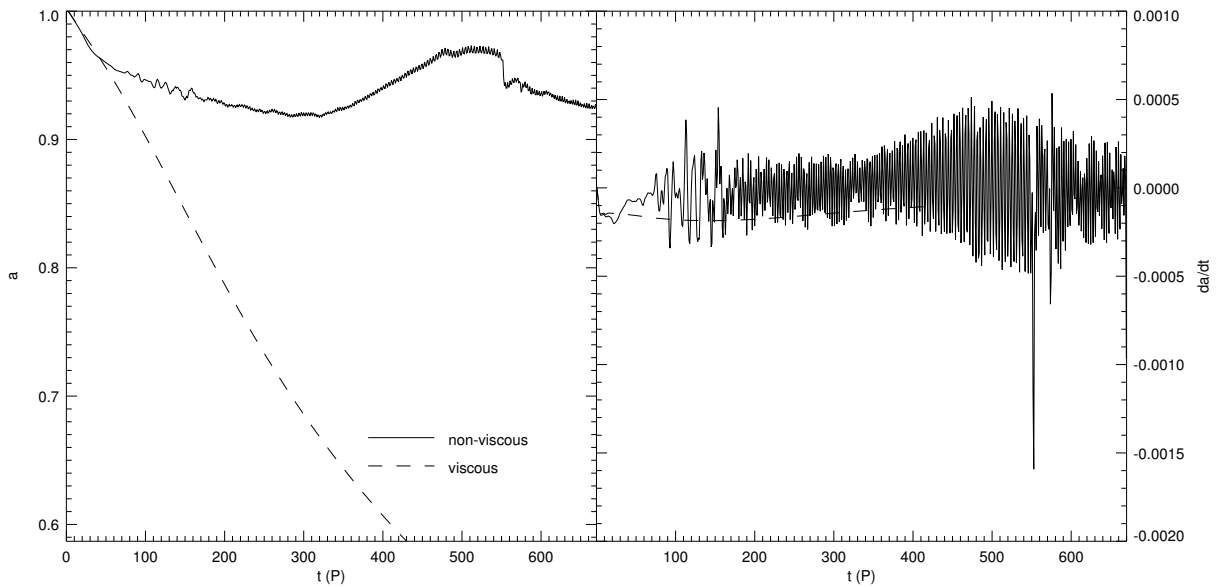


Figure 4.19: Semi-major axis evolution for a $0.1 M_J$ planet in an inviscid disk (solid line), in a viscous disk with $\alpha = 0.004$ (dashed line).

to grow. However, e only slowly increases, and it may take several thousands of orbits before a clean gap emerges. Note that in Chapter 3, we defined a gap as a region around the orbit of the planet where the density was reduced by a factor e (Euler's number, not to be confused with the eccentricity). For eccentricity evolution, the gap needs to be much deeper.

The evolution of the semi-major axis of this planet is very interesting, see Fig. 4.19. For the viscous disk, we see the regular inward migration that in this case happens to proceed very fast because of the high disk mass. It is the inviscid disk that produces the interesting results.

As soon as the vortices appear, the torque on the planet becomes highly variable with time (Koller et al. 2003; Li et al. 2005). In Fig. 4.19 we see this reflected in a highly variable migration rate. Immediately after the appearance of vortices, the planet in the inviscid disk starts to slow down its inward migration, until it comes at a full stop around 300 orbits. This phase corresponds to a local maximum in the eccentricity, see Fig. 4.18. Interestingly, after 320 orbits the planet starts to move outward, coming to a full stop again around 500 orbits. Note that the migration rate, and therefore also the torque, is not positive throughout this phase of outward migration. Also note, that during this phase where a partial gap is opened the planet is susceptible to Type III migration (Masset & Papaloizou 2003; Artymowicz 2004), which may be directed outward depending on the initial conditions. It may well be that the action of the vortices provides the seed for outward Type III migration. However, the migration rate is much too low to be called 'runaway', and therefore it seems that vortices alone are responsible for this outward migration.

We can further justify this by looking at the radial torque profile at different times, see Fig. 4.20. According to Fig. 4.19, the planet is moving inward at $t = 200$, it has

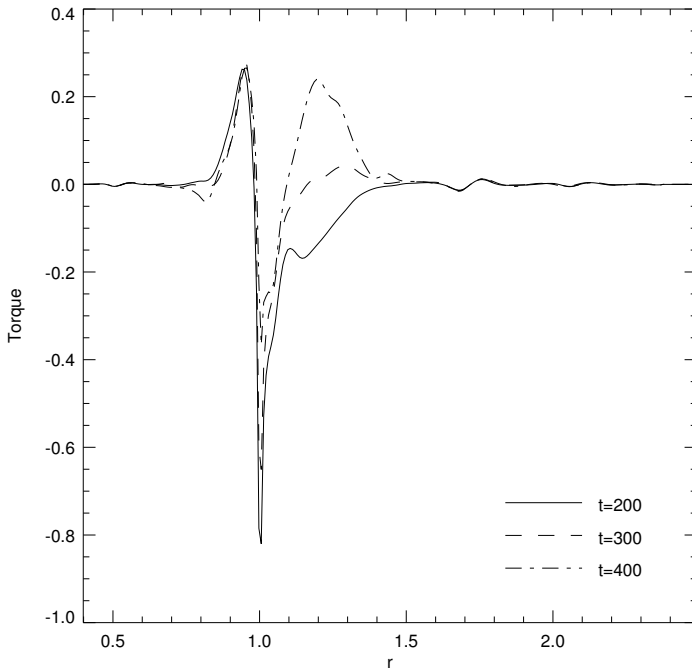


Figure 4.20: Radial torque profile for a $0.1 M_J$ planet embedded in a non-viscous disk, at three different times. At $t = 200$, the planet is moving inward (see Fig. 4.18), at $t = 300$ it has stopped migrating, and at $t = 400$ it is moving outward. The main difference in torque comes from the region near $r = 1.2$ where a large vortex is forming.

stopped migrating at $t = 300$ and it is moving outward at $t = 400$. From Fig. 4.20 it is clear that the major difference in the torque comes from the region near $r = 1.2$, which is exactly where large vortices form (Koller et al. 2003; de Val-Borro et al. 2006, ;see also Chapter 3). Therefore, the vortices play a crucial role in the angular momentum budget of the planet.

We do see a clear example of Type III inward migration after 550 orbits. There, the planet moves inward at a very high speed for a short period. Note that the radial distance traveled during this period is comparable to the half-width of the shallow gap opened by the planet. It seems that the planet is pulled out of its Type III migration by the density structure of near the inner edge of the gap it created. However, for now this is merely speculation. More work is necessary to study the effect of density structure on Type III migration to see where and when these planets are stopped.

4.5 DISCUSSION

In this Chapter we have investigated whether eccentricity growth is possible for embedded planets under the most favorable conditions. One may wonder what happens in disks that *do* have a finite viscosity and are less massive than considered here. First of all, in a less massive disk we have found that a $5 M_J$ planet still picks up eccentricity, albeit much slower than depicted in Fig. 4.7. Only when the disk becomes less massive than the planet we did not find eccentricity growth. Furthermore, we have shown that it is the exchange of eccentricity between planet and disk that governs the evolution of e . Kley & Dirksen (2006) showed that also in viscous runs the disk becomes eccentric, but on much longer time scales. It seems, therefore, that as long as the disk is

comparable in mass with the planet, a $5 M_J$ planet will pick up eccentricity.

We have found that the maximum eccentricity that can be reached by the planet is comparable to the half-width of the gap. This is because as soon as the planet becomes engulfed in the disk again, coorbital resonances quickly damp the eccentricity. Therefore, even if a $1 M_J$ planet could pick up eccentricity while embedded in a viscous disk, the maximum value of e that can be reached is about 0.1, which is still much smaller than the mean eccentricity of extrasolar planets.

The scale height H plays an important role. The lower H , the cleaner the gap that is opened, but the gap will also be less wide which limits the maximum eccentricity that can be reached. For low values of h , the gap is clean enough to sustain an eccentric planet. However, the long-term evolution of the orbit still needs to be considered. Because lower values of h require a higher resolution, these calculations are very expensive.

Vortices play an important role for intermediate-mass planets. There has been a considerable amount of work done on vortices in astrophysical disks, but it remains a very difficult subject to tackle. First of all, in order to describe a vortex correctly, high resolution is required (Johnson & Gammie 2006; Li et al. 2005), much higher than can be achieved in global disk simulations. Second, vortices that are found in two-dimensional simulations may well be unstable in three dimensions (Kerswell 2002). It is not clear, therefore, if the simulations presented here describe the effects of the vortices correctly. However, three-dimensional, high-resolution global disk models are beyond current computational resources.

4.6 SUMMARY AND CONCLUSION

We have presented a new numerical method to study orbital evolution of embedded planets. We have exploited the ability of the RODEO method to handle arbitrary spatial coordinates to design a frame that keeps the planet at a fixed location on the grid at all times, regardless of its orbital evolution. This new coordinate frame was tested with a massless eccentric planet, a low-mass planet experiencing Type I migration and eccentricity damping, and a high-mass planet undergoing Type II migration. For all migration modes we recover the analytical estimates for the migration rate.

We have found that the orbital eccentricity can grow for a $5 M_J$ planet in favorable circumstances (a massive, inviscid disk). The absence of viscosity reduces the time scale for disk eccentricity evolution as found by Kley & Dirksen (2006), and when the disk is comparable in mass to the planet we have shown that this may lead to an eccentric planetary orbit, with $e \approx 0.15$. This is still smaller than the mean eccentricity of extrasolar giant planets, $\bar{e} = 0.33$, but simulations spanning a longer time may show further growth of e .

It turns out to be extremely hard to give a $1 M_J$ planet significant eccentricity. For a viscous disk, $e \ll 10^{-3}$, while for an inviscid disks there are only short excursions to $e \approx 0.1$. The pressure scale height in the disk plays an important role. Thinner disks show eccentricity growth more readily, but at the same time the maximum eccentricity that can be reached is limited because the planetary gap is less wide in thinner disks.

For intermediate-mass planets, that are not massive enough to open up deep gaps, but are known to excite vortices in inviscid calculations (Koller et al. 2003; Li et al. 2005), we find that no significant eccentricity is produced. However, the migration behavior of this 0.1 M_J planet turns out to be very interesting. Unlike the viscous case, where the planet moves inward all the time, we find that in the inviscid case the planet stops its inward migration once the vortices appear, after which it starts to move *outward* temporarily. This is due to the formation of vortices. However, correctly describing vortex formation and evolution would require three-dimensional simulations at very high resolution, which are beyond current computational resources.

REFERENCES

- Artymowicz, P. 1993a, ApJ, 419, 166
Artymowicz, P. 1993b, ApJ, 419, 155
Artymowicz, P. 1994, ApJ, 423, 581
Artymowicz, P. 2004, in ASP Conf. Ser. 324: Debris Disks and the Formation of Planets, ed. L. Caroff, L. J. Moon, D. Backman, & E. Praton, 39
Bate, M. R., Lubow, S. H., Ogilvie, G. I., & Miller, K. A. 2003, MNRAS, 341, 213
Bryden, G., Chen, X., Lin, D. N. C., Nelson, R. P., & Papaloizou, J. C. B. 1999, ApJ, 514, 344
Chiang, E. I., Fischer, D., & Thommes, E. 2002, ApJ, 564, L105
Cresswell, P. & Nelson, R. P. 2006, A&A, 450, 833
D'Angelo, G., Henning, T., & Kley, W. 2002, A&A, 385, 647
D'Angelo, G., Kley, W., & Henning, T. 2003, ApJ, 586, 540
de Val-Borro, M., Edgar, R. G., Artymowicz, P., et al. 2006, MNRAS, 370, 529
Eulderink, F. & Mellema, G. 1995, A&AS, 110, 587
Ford, E. B., Havlickova, M., & Rasio, F. A. 2001, Icarus, 150, 303
Goldreich, P. & Sari, R. 2003, ApJ, 585, 1024
Goldreich, P. & Tremaine, S. 1979, ApJ, 233, 857
Goldreich, P. & Tremaine, S. 1980, ApJ, 241, 425
Johnson, B. M. & Gammie, C. F. 2006, ApJ, 636, 63
Kerswell, R. R. 2002, Annual Review of Fluid Mechanics, 34, 83
Kley, W. 1999, MNRAS, 303, 696
Kley, W. & Dirksen, G. 2006, A&A, 447, 369
Koller, J., Li, H., & Lin, D. N. C. 2003, ApJ, 596, L91
Li, H., Li, S., Koller, J., et al. 2005, ApJ, 624, 1003
Lin, D. N. C. & Ida, S. 1997, ApJ, 477, 781
Masset, F. S. & Papaloizou, J. C. B. 2003, ApJ, 588, 494
Nelson, A. F. & Benz, W. 2003, ApJ, 589, 556

- Nelson, R. P., Papaloizou, J. C. B., Masset, F., & Kley, W. 2000, *MNRAS*, 318, 18
- Ogilvie, G. I. & Lubow, S. H. 2003, *ApJ*, 587, 398
- Paardekooper, S.-J. & Mellema, G. 2006, *A&A*, 450, 1203
- Papaloizou, J. C. B. & Larwood, J. D. 2000, *MNRAS*, 315, 823
- Papaloizou, J. C. B., Nelson, R. P., & Masset, F. 2001, *A&A*, 366, 263
- Papaloizou, J. C. B. & Terquem, C. 1999, *ApJ*, 521, 823
- Rasio, F. A. & Ford, E. B. 1996, *Science*, 274, 954
- Sari, R. & Goldreich, P. 2004, *ApJ*, 606, L77
- Tanaka, H., Takeuchi, T., & Ward, W. R. 2002, *ApJ*, 565, 1257
- Tanaka, H. & Ward, W. R. 2004, *ApJ*, 602, 388
- Ward, W. R. 1997, *Icarus*, 126, 261
- Ward, W. R. & Hahn, J. M. 1998, *AJ*, 116, 489
- Ward, W. R. & Hahn, J. M. 2000, *Protostars and Planets IV*, 1135
- Weidenschilling, S. J. & Marzari, F. 1996, *Nature*, 384, 619

CHAPTER 5

Growing and moving low-mass planets in non-isothermal disks

Sijme-Jan Paardekooper and Garrelt Mellema

To be submitted

WE study the interaction of a low-mass planet with a protoplanetary disk with a realistic treatment of the energy balance by doing radiation-hydrodynamical simulations. We look at accretion and migration rates and compare them to isothermal studies. We use a three-dimensional version of the hydrodynamical method RODEO, together with radiative transport in the Flux-Limited Diffusion approach. The torque on the planet depends critically on the ability of the disk to cool efficiently. For densities appropriate at 5 AU in the solar nebula the torque is *positive*, indicating outward migration. It is necessary to lower the density by a factor of 2 to recover inward migration, and more than 2 orders of magnitude to recover the usual Type I migration.

5.1 INTRODUCTION

Planet formation takes place in protoplanetary disks that are commonly found around young stars (Beckwith & Sargent 1996). These disks play a critical role in structuring the forming planetary system in terms of masses and orbits, and planet-disk interaction is therefore a very important process to study in order to understand planet formation.

Planet-disk interaction affects a forming planet in three ways. First of all, the mass that the disk is able to supply to the young planet is limited, which leads to a maximum gas mass that a planet can achieve (Lubow et al. 1999; Kley 1999; D'Angelo et al. 2003b; Bate et al. 2003). This limiting mass is of the order of a few Jupiter masses (M_J). But also for planets of lower mass the disk regulates the mass accretion, which becomes especially apparent in three-dimensional numerical simulations (D'Angelo et al. 2003b).

Second, the disk is able to change the orbital radius of the planet through tidal interaction (Goldreich & Tremaine 1980). Depending on the mass of the planet, two modes of migration can be distinguished (Ward 1997): type I migration for low-mass planets that generate a linear disk response, and type II for high-mass, gap-opening planets. Recently a third type of migration was put forward, in which strong corotational torques force a very fast mode of migration (Masset & Papaloizou 2003; Artymowicz 2004). This Type III migration is very sensitive to local density gradients, in terms of migration speed and even migration direction, and therefore the structure of the gas disk determines the outcome of the migration process. This is unlike Type I and Type II migration, for which all planets move inward and only the time scale varies with disk properties.

Finally, the eccentricity of the planet's orbit may be affected by the disk. Usually, eccentricity is damped (Artymowicz 1993), but high-mass planets ($M_p > 5 M_J$) that open deep gaps may experience eccentricity growth (Papaloizou et al. 2001; Kley & Dirksen 2006). However, due to possible saturation of corotation resonances planets of $M_p \approx M_J$ may pick up significant eccentricity during the gap formation process (Sari & Goldreich 2004), although this requires a slightly eccentric orbit to start with (Goldreich & Sari 2003).

Observations of the masses and orbits of extrasolar planets provide insight in the result of planet-disk interaction. One of the most striking results that were obtained is the discovery of a new class of planets, the so-called Hot Jupiters. They are gas giant planets orbiting very close to their central star. It is unlikely that they have formed in situ (Papaloizou & Terquem 1999) and inward migration through planet-disk tidal interaction has been put forward as the explanation for their existence.

The main problem for this scenario is that the time scales for migration as obtained from analytical (Tanaka et al. 2002) and numerical (Bate et al. 2003; D'Angelo et al. 2003b) arguments are usually smaller than or comparable to the total lifetime of the disk. This means that theory essentially predicts that all planets should fall onto the central star, which poses a problem for planet formation theory. If it is already hard to form a single giant planet within the lifetime of the disk (Pollack et al. 1996), how are we going to form a huge amount of them, of which only a tiny fraction survives? Clearly a stopping mechanism is required that prevents planets from migrating all the way towards the star.

One possibility is that the planet encounters an inner hole in the disk, possibly created by the magnetic field of the central star. When there is no disk around to interact with, the planet will stop migrating. Another possibility is that the planet undergoes Type III outward migration at some point (Masset & Papaloizou 2003). Finally, direct interaction of the disk with a magnetic field may stop the planet, either by a toroidal magnetic field (Terquem 2003) or, for a low-mass planet, through magnetic turbulence induced stochastic migration (Nelson & Papaloizou 2004).

However, most numerical hydrodynamical work on planet-disk interaction lacks proper treatment of the energy balance, with only a few notable exceptions (D'Angelo et al. 2003a; Klahr & Kley 2006; Morohoshi & Tanaka 2003). The usually adopted locally isothermal equation of state assumes that all excess energy generated by compression, viscous dissipation or shocks can be radiated away efficiently, thereby keeping the temperature profile fixed. However, the ability of the disk to cool is strongly linked to the opacity, and therefore to the density.

The effects of temperature structure on planet migration in realistic disks were studied by Jang-Condell & Sasselov (2003, 2004, 2005) who used a detailed disk model including radiative transfer to calculate the torque on the planet in an analytical way. They found that temperature perturbations resulting from shadowing and illumination at the surface of the disk can decrease the migration rate by a factor of 2. Menou & Goodman (2004) also find reduced migration rates in realistic T Tauri α -disks, and they point out the importance of sudden changes in the opacity, for example near the snow line.

In this Chapter we aim at releasing the isothermal assumption in hydrodynamical simulations of planet-disk interaction. Specifically, in contrast with Klahr & Kley (2006), we focus on low-mass planets that do not open a gap in the disk. For these deeply embedded planets temperature effects are the most important. However, due to their low mass their gravitational sphere of influence is small, and one needs very high resolution locally to resolve the atmosphere of the planet. Furthermore, because radiation is the main cooling agent, we need to perform radiation-hydrodynamical simulations. This is a major leap from isothermal simulations, because we are not only adding an equation for the gas energy but also the evolution of the radiation field needs to be followed.

The plan of this Chapter is as follows. We briefly review the relevant cooling time scale in Sect. 5.2, effects of radiation in Sect. 5.3 and the condition for convection in Sect. 5.4. In Sect. 5.5 we present the adopted disk model, and in Sect. 5.6 we discuss the numerical method. In Sect. 5.7 we present the results, from simple isothermal models to the full radiation-hydrodynamical models. We give a discussion on the results in Sect. 5.8, and we conclude in Sect. 5.9.

5.2 COOLING PROPERTIES

We take the analytical opacity data from Bell & Lin (1994), which state that for low temperatures (beyond the snow line) the Rosseland mean opacity in cm^{-1} is:

$$\kappa = \kappa_0 \rho T^2, \quad (5.1)$$

where ρ is the density in g cm^{-3} , T denotes the temperature (K) and $\kappa_0 = 2.0 \cdot 10^{-4}$ is a constant. We discuss the cooling properties of the disk as a function of opacity, starting with the optically thin regime.

The time scale for the coupling between gas and radiation is given by

$$t_{\text{coupling}} = \frac{1}{\kappa c}, \quad (5.2)$$

where c is the speed of light in vacuum. When t_{coupling} is larger than the dynamical time scale t_{dyn} , which equals the orbital time scale of the planet, the gas can not transfer its internal energy to the radiation field and therefore the gas will not cool efficiently through radiation. Plugging in the opacity of Eq. (5.1), and assuming $T \approx 50$ K, we find that the density near the planet should satisfy

$$\rho > 10^{-18} \text{ g cm}^{-3}, \quad (5.3)$$

in order to cool through radiation. At the midplane of a protoplanetary disk in the planet forming region this condition is always satisfied.

In general, when a region is optically thin and Eq. (5.3) holds it can cool efficiently because all its thermally emitted photons can escape from this region. In a protoplanetary disk the scale length of interest is the disk thickness H . For planet-disk interaction specifically, most of the torque on the planet comes from material that is closer than $\sim 2H$ from the planet (Bate et al. 2003). The condition for the disk to be optically thin over one pressure scale height is given by:

$$\kappa H < 1. \quad (5.4)$$

Putting in our opacity law Eq. (5.1) we can write a condition for the density:

$$\rho < \frac{1}{\kappa_0 T^2 H}. \quad (5.5)$$

At the location of Jupiter in a typical protoplanetary disk $T \approx 50$ K and $h \equiv H/r = 0.05$, where r is the orbital distance of Jupiter. Putting in these values, we find that for the disk to be optically thin over one pressure scale height $\rho < 5.1 \cdot 10^{-13} \text{ g cm}^{-3}$, while the density at 5 AU in the Minimum Mass Solar Nebula (MMSN) is given by $\rho = 10^{-11} \text{ g cm}^{-3}$.

When a region is optically thick, it can still cool efficiently depending on the local conditions. Consider a sphere of radius H around the position of the planet. The flux through this sphere in the optically thick case can be approximated by

$$F_{\text{R}} = \frac{\sigma T^4}{\tau}, \quad (5.6)$$

where $\tau = \kappa H$ is the optical depth over the radius of the sphere and σ is the Stefan-Boltzmann constant. The internal energy density in the sphere is given by:

$$\epsilon = \frac{p}{\Gamma - 1} = \frac{\rho \frac{R}{\mu} T}{\Gamma - 1} = \frac{\tau \frac{R}{\mu}}{\kappa_0 T H (\Gamma - 1)}, \quad (5.7)$$

where p denotes gas pressure, Γ is the adiabatic exponent, R is the universal gas constant and μ is the mean molecular weight. The cooling time scale is given by the total internal energy content of the sphere divided by the total energy that flows through the surface of the sphere:

$$t_{\text{cool}} = \frac{\epsilon \frac{4}{3} \pi H^3}{F_R 4 \pi H^2} = \frac{\epsilon H}{3 F_R} = \frac{\tau^2 \frac{R}{\mu}}{3(\Gamma - 1) \kappa_0 \sigma T^5}. \quad (5.8)$$

Putting in the density and temperature appropriate for the location of Jupiter ($\rho = 10^{-11} \text{ g cm}^{-3}$, $T = 50 \text{ K}$ and $\mu = 2.4$) we find that $t_{\text{cool}} \approx 10 t_{\text{dyn}}$, where the dynamical time scale t_{dyn} equals the orbital time scale of the planet. Cooling is only efficient when $t_{\text{cool}} < t_{\text{dyn}}$, and therefore we conclude that cooling is *not* efficient for these parameters.

It is easy to show that the cooling time scale depends on the distance to the central star through:

$$t_{\text{cool}} \propto \frac{\rho^2(r) H^2(r)}{T(r)}. \quad (5.9)$$

When we assume a constant aspect ratio h , which implies that the temperature varies with radius as r^{-1} , and a power law for the density with index $-3/2$ we see that the cooling time does not depend on radius. This means that

$$\frac{t_{\text{cool}}}{t_{\text{dyn}}} \approx 10 \left(\frac{r}{5 \text{ AU}} \right)^{-\frac{3}{2}}. \quad (5.10)$$

This means that at approximately 15 AU in the MMSN $t_{\text{cool}} \approx t_{\text{dyn}}$. Inside this radius, cooling will not be efficient.

Both Eq. (5.5) and Eq. (5.8) have a strong temperature dependence, and therefore it is not possible to determine in advance if a disk with an embedded planet that changes the local temperature and density will be able to cool efficiently. However, this analysis shows that for typical densities and temperatures including proper cooling mechanisms is essential for planet-disk interaction.

Summarizing, for a fixed temperature of 50 K at 5 AU, we can distinguish four cooling regimes:

- For the lowest densities (see Eq. (5.3)) the gas can not cool through radiation.
- For somewhat higher densities, gas is able to cool through radiation but the disk is still optically thin over a distance H .
- Even higher densities make the disk optically thick over H , which means that thermally emitted photons do not immediately leave the region that provides the torque on the planet.

- For the highest densities the disk is optically thick and $t_{\text{cool}} > t_{\text{dyn}}$, which means that the disk can not cool efficiently.

Note that only the second regime resembles the isothermal limit, while the first regime is not important for low-mass planets that remain deeply embedded. In the third and the fourth regime, temperature effects may play a large role in determining the total torque onto the planet.

5.3 RADIATIVE EFFECTS

In general, radiation is not only a cooling agent but it may also dynamically change the velocity structure around the planet. The effect of radiation on the gas velocity goes through radiation pressure, which, in the isotropic case, is given by

$$P = \frac{1}{3}aT^4, \quad (5.11)$$

where a is the radiation constant. The gas pressure p is again given by the ideal gas law, and we can then write:

$$\frac{P}{p} = \frac{\frac{1}{3}aT^4}{\rho \frac{R}{\mu} T} = \frac{\mu a T^3}{3\rho R}. \quad (5.12)$$

For the typical temperature at 5 AU, $T = 50$ K, we get:

$$\frac{P}{p} = \frac{1.0 \cdot 10^{-17}}{\rho}. \quad (5.13)$$

For a typical midplane density of $\rho = 10^{-11}$ g cm⁻³ radiation pressure is negligible compared to gas pressure.

This is an important result, because it shows that near a deeply embedded planet the dynamical effects of radiation are not important. This means that the gas pressure and velocity structure will be almost the same as in the locally isothermal case. This greatly simplifies the torque analysis: in regions where the temperature rises because of gas compression or the release of potential energy the density must be lower than in the isothermal case to arrive at the same pressure. Therefore these regions will exert a lower torque onto the planet. Any asymmetry in heating will therefore show up as a torque asymmetry, which may alter the total torque balance on the planet considerably.

5.4 CONVECTION

Heat transport in a planetary envelope can occur through radiation or through convection. Convection sets in when the temperature gradient becomes too steep for radiation to transport energy towards the surface of the planet. As is well known from theory of stellar interiors, this happens when

$$\frac{\partial T}{\partial z} < \left. \frac{\partial T}{\partial z} \right|_{\text{ad}}, \quad (5.14)$$

where z is the direction towards the surface of the planet and the right hand side denotes the adiabatic temperature gradient, which can be expressed as:

$$\left. \frac{\partial T}{\partial z} \right|_{\text{ad}} = -\frac{T}{H} \frac{\Gamma}{\Gamma - 1}. \quad (5.15)$$

We can make a simple estimate of the importance of convective energy transport by approximating the actual temperature gradient in the planetary envelope as:

$$\frac{\partial T}{\partial z} \approx \frac{T_{\text{neb}} - T_{\text{c}}}{R_{\text{R}}}, \quad (5.16)$$

where T_{neb} is the temperature of the surrounding nebula, T_{c} is the central temperature of the planet and R_{R} denotes the Roche lobe of the planet. The assumption is that the planet connects to the disk at a distance given by the Roche lobe, and that the disk remains unperturbed from this distance. This is the usual assumption in one-dimensional planet formation models (Pollack et al. 1996).

When we further assume that the low-mass planets do not change to local pressure scale height in the disk, we can plug Eq. (5.15) and Eq. (5.16) into Eq. (5.14) to obtain a maximum value for the central temperature of the planet:

$$T_{\text{c}} < \left(1 + \frac{R_{\text{R}}}{H} \frac{\Gamma}{\Gamma - 1} \right) T_{\text{neb}}. \quad (5.17)$$

For a $5 M_{\oplus}$ planet embedded in a disk with aspect ratio $h = 0.05$ and adiabatic exponent $\Gamma = 1.4$ we find that $T_{\text{c}} < 2.21 T_{\text{neb}}$.

5.5 MODEL DESIGN

Our model consists of three objects: the central star, the planet and the disk. Below, we give a short description of each of these components. Throughout this Chapter, we will work in a spherical polar coordinate system (r, θ, ϕ) that co-rotates with the planet.

5.5.1 Central Star

The central star is the main source of gravity and is located in the origin of our coordinate system. This makes the system non-inertial, the principle upon which the radial velocity searches for extrasolar planets are based. However, for the low-mass planets the effect is negligible. We take the mass of the star to be $1 M_{\odot}$.

5.5.2 Planet

Our coordinate frame rotates with the angular velocity of the planet, and because we keep the planet on a fixed circular orbit it resides at a fixed location on the grid, $(r, \theta, \phi) = (r_{\text{p}}, \pi/2, \pi)$. The potential of the planet is smoothed over 2 grid cells on the

highest level of refinement, which is always much smaller than the Roche lobe of the planet (see Sect. 5.6). This way, we always resolve the potential. The planet is able to accrete matter from the disk without changing its dynamical mass. We vary the mass of the planet between 0.5 and 300 M_{\oplus} for the isothermal models, which spans the whole range from the linear regime of Type I migration to a gap-opening Jupiter-mass planet. For the radiation-hydrodynamical models we focus on a planet of 5 M_{\oplus} , which is well inside the linear regime.

5.5.3 Disk

The disk is three-dimensional, extending from $r = 0.4 r_p$ to $r = 2.5 r_p$ in the radial direction (r_p is the distance from the central star to the planet). In the azimuthal direction the computational domain is bounded by $0 \leq \phi \leq 2\pi$, while in the polar direction we go up to 2.5 pressure scale heights above the midplane of the disk: $\pi/2 - 5H/2r < \theta < \pi/2$.

Gas

The scale height H varies linearly with radius initially, with $h = H/r = 0.05$. The initial temperature profile is found from assuming hydrostatic equilibrium in the vertical direction and therefore matches the temperature profile of the isothermal simulations. The density is also a power law initially, with index $-3/2$. We vary the midplane density at the location of the planet to investigate different cooling regimes. Our nominal value is $10^{-11} \text{ g cm}^{-3}$, which is appropriate for the location of Jupiter in the Minimum Mass Solar Nebula. The initial velocities are zero in the radial and polar direction, and the Keplerian speed in the azimuthal direction, with a correction for the radial pressure gradient. The equation of state is given by the ideal gas law.

We model the disk as an ideal, inviscid fluid, and therefore its evolution is governed by the Euler equations. These can be cast in the following form:

$$\frac{\partial \mathbf{W}}{\partial t} + \frac{\partial \mathbf{F}_r}{\partial r} + \frac{\partial \mathbf{F}_\theta}{\partial \theta} + \frac{\partial \mathbf{F}_\phi}{\partial \phi} = \mathbf{S}, \quad (5.18)$$

in which \mathbf{W} is the state vector, \mathbf{F} are the fluxes in the three coordinate directions and \mathbf{S} is the source vector. The state consists of the conserved quantities:

$$\mathbf{W} = r^2 \sin \theta (\rho, \rho v_r, \rho v_\theta, \rho v_\phi, e)^T, \quad (5.19)$$

where ρ is the density, v_r is the radial velocity, v_θ and v_ϕ are the two angular velocities and e is the total energy density:

$$e = \frac{1}{2} \rho (v_r^2 + r^2 v_\theta^2 + r^2 \sin^2 \theta (v_\phi + \Omega)^2) - \rho \Phi + \frac{p}{\Gamma - 1}. \quad (5.20)$$

Here Ω is the angular velocity of the coordinate frame, Φ denotes the potential, p is the pressure and Γ is the adiabatic exponent. The three fluxes are given by:

$$\mathbf{F}_r = r^2 \sin \theta (\rho v_r, \rho v_r^2 + p, \rho v_r v_\theta, \rho v_r v_\phi, \rho v_r w)^T \quad (5.21)$$

$$\mathbf{F}_\theta = r^2 \sin \theta (\rho v_\theta, \rho v_r v_\theta, \rho v_\theta^2 + p/r^2, \rho v_\theta v_\phi, \rho v_\theta w)^T \quad (5.22)$$

$$\mathbf{F}_\phi = r^2 \sin \theta (\rho v_\phi, \rho v_r v_\phi, \rho v_\theta v_\phi, \rho v_\phi^2 + \frac{p}{r^2 \sin^2 \theta}, \rho v_\phi w)^T, \quad (5.23)$$

where w is the enthalpy of the fluid:

$$w = \frac{e + p}{\rho}. \quad (5.24)$$

The source vector \mathbf{S} is then:

$$\mathbf{S} = r^2 \sin \theta \begin{pmatrix} 0 \\ \rho r \sin^2 \theta (v_\phi + \Omega)^2 - \rho \frac{\partial \Phi}{\partial r} + \frac{2p}{r} \\ -2\rho \frac{v_r}{r} v_\theta + \sin \theta \cos \theta \rho (v_\phi + \Omega)^2 - \frac{\rho}{r^2} \frac{\partial \Phi}{\partial \theta} + \frac{\cot \theta p}{r^2} \\ -2\rho \frac{v_r}{r} (\Omega + v_\phi) - 2 \cot \theta \rho v_\theta (\Omega + v_\phi) - \frac{\rho}{r^2 \sin^2 \theta} \frac{\partial \Phi}{\partial \phi} \\ -2\rho (v_r \frac{\partial \Phi}{\partial r} + v_\theta \frac{\partial \Phi}{\partial \theta} + v_\phi \frac{\partial \Phi}{\partial \phi}) - \rho \Omega \frac{\partial \Phi}{\partial \phi} \end{pmatrix}. \quad (5.25)$$

The reason for not including an anomalous turbulent viscosity as in Bate et al. (2003) and D'Angelo et al. (2003b) is that the usual α -prescription (Shakura & Sunyaev 1973) is not a good description of the magnetic turbulence that is probably the source of viscosity (Balbus & Hawley 1990). Neglecting viscosity altogether means that our results are valid in regions of the disk where the ionization fraction is not high enough to sustain magnetic turbulence.

Radiation

Planets that do not open gaps ($M_p \ll M_J$) are deeply embedded in the disk where the material is very optically thick. It is therefore appropriate to consider radiative transfer in the diffusion limit. However, because the density drops more than an order of magnitude over a few pressure scale heights above the midplane it is necessary to deal with the optically thin regime as well.

We start by considering a medium at rest, i.e. we set the velocity of the gas to zero. In the diffusion limit there is essentially no angular information in the radiation field, which is then governed by a diffusion equation for its energy density E :

$$\frac{\partial E}{\partial t} - \nabla \cdot \frac{c}{3\kappa} \nabla E = \kappa c (B - E), \quad (5.26)$$

where c denotes the speed of light, κ is the opacity in cm^{-1} and B is the radiative source term. We consider only thermal emission from the disk, therefore

$$B = a T^4, \quad (5.27)$$

where a is the radiation constant and T is the gas temperature. In order to conserve total energy an extra source term $S_{\text{rad}} = -\kappa c (B - E)$ appears in the gas energy equation. We work with a Rosseland mean opacity that is typical for the MMSN (see Bell & Lin 1994). Initially we set $E = B$ in all simulations.

In the optically thin streaming limit the evolution of the radiation energy is given by:

$$\frac{\partial E}{\partial t} + \nabla \cdot (c E \hat{\mathbf{n}}) = \kappa c (B - E), \quad (5.28)$$

where $\hat{\mathbf{n}}$ is a unit vector in the direction of propagation of the light front. Note first of all that this is an advection equation rather than a diffusion equation, and second that there is a strong angular dependence of the radiation field. Naively applying Eq. (5.26) in the optically thin case will lead to large errors.

However, because the most important part of the disk is optically thick it is still useful to start with Eq. (5.26) but to avoid divergences in the optically thin case. Note that avoiding divergences is different from obtaining the correct solution, which would require a method based on discrete ordinates or on a Monte Carlo algorithm. Both of these methods have great difficulties with the case of a very optically thick disk.

We write Eqs. (5.26) and (5.28) in the more general form:

$$\frac{\partial E}{\partial t} + \nabla \cdot \mathbf{F}_R = \kappa c(B - E), \quad (5.29)$$

in which the radiative flux \mathbf{F}_R is given by

$$\mathbf{F}_R = -\frac{c\lambda}{\kappa} \nabla E, \quad (5.30)$$

where λ is called the flux limiter. The definition of \mathbf{F}_R in Eq. (5.30) in terms of E removes the need for solving a differential equation for \mathbf{F}_R . Closing the radiative moment equations this way is called flux-limited diffusion (Levermore & Pomraning 1981). The flux-limiter λ deals with the transition from the diffusion limit to the streaming limit. The exact functional form of λ also implicitly determines the angular dependence of the radiation field. For an overview of different forms see Kley (1989). We have used

$$\lambda = \begin{cases} \frac{2}{3 + \sqrt{9 + 10 R^2}} & \text{for } 0 \leq R \leq 2; \\ \frac{10}{10 R + 9 + \sqrt{180 R + 81}} & \text{for } R > 2, \end{cases} \quad (5.31)$$

where

$$R = \frac{1}{\kappa} \frac{|\nabla E|}{E}, \quad (5.32)$$

but the results do not depend sensitively on the adopted form of λ , mainly because of the high optical depth of the disk near the planet.

Flux-limited diffusion typically gives poor results in the streaming limit (Hayes & Norman 2003), but for our case of a deeply embedded planet it is a reliable and relatively cheap method for doing radiative transfer.

When the velocity of the gas is taken into account Eq. (5.29) needs to be extended in two ways to account for advection of radiative energy and momentum transfer between gas and radiation. The full equation for the evolution of the radiative energy then reads:

$$\frac{\partial E}{\partial t} + \nabla \cdot (\mathbf{F}_R + \mathbf{v} E + \mathbf{v} \cdot \mathcal{P}) = \kappa c(B - E) - \frac{\kappa}{c} \mathbf{v} \cdot \mathbf{F}_R, \quad (5.33)$$

where \mathcal{P} is the radiative stress tensor, given by

$$\mathcal{P} = E \mathcal{T}_{\text{Edd}}. \quad (5.34)$$

The Eddington tensor \mathcal{T}_{Edd} is calculated using

$$\mathcal{T}_{\text{Edd}} = \frac{1}{2} [(1 - f_{\text{Edd}})\mathcal{I} + (3 f_{\text{Edd}} - 1)\hat{\mathbf{n}}\hat{\mathbf{n}}], \quad (5.35)$$

where $\hat{\mathbf{n}} = \nabla E / |\nabla E|$. The Eddington factor f_{Edd} can be calculated from the streaming factor $f_s = |\mathbf{F}_R|/cE$:

$$f_{\text{Edd}} = \begin{cases} \frac{1}{3} + \frac{1}{6}f_s^2 & \text{for } 0 \leq f_s \leq 0.4; \\ \frac{5}{9}(1 - f_s)^2 + f_s^2 & \text{for } 0.4 \leq f_s \leq 1. \end{cases} \quad (5.36)$$

The extra source vector in the gas flow equations \mathbf{S}_{rad} is given by:

$$\mathbf{S}_{\text{rad}} = r^2 \sin \theta \begin{pmatrix} 0 \\ \frac{\kappa}{c} F_{R,r} \\ \frac{\kappa}{c} F_{R,\theta} \\ \frac{\kappa}{c} F_{R,\phi} \\ -\kappa c (B - E) \end{pmatrix}. \quad (5.37)$$

The total source term for the gas is given by $\mathbf{S} + \mathbf{S}_{\text{rad}}$.

5.6 NUMERICAL METHOD

We use the technique of operator splitting to evolve the hydrodynamic part and the radiative part separately every time step.

5.6.1 Hydrodynamics

We numerically solve the flow equations for the gas using a three-dimensional version of the RODEO method (Paardekooper & Mellema 2006). For isothermal simulations the necessary eigenvalues, eigenvectors and projection coefficients are simple generalizations of the two-dimensional analogs given in Paardekooper & Mellema (2006). For simulations including an energy equation, the method is equivalent to the non-relativistic version of the general relativistic method of Eulderink & Mellema (1995).

In short, RODEO evolves the Euler equations using an approximate Riemann solver (the Roe solver, see Roe 1981), together with stationary extrapolation to account for the geometrical and hydrodynamical source terms (Eq. (5.25)). The Coriolis forces are treated in an exact fashion to avoid numerical instabilities (Kley 1998; Paardekooper & Mellema 2006). The extra source terms due to interaction with the radiation field (Eq. (5.37)) are treated as external source terms and are integrated separately (see below).

Accretion onto the planet is handled in the same way as in D'Angelo et al. (2003b): every time step Δt the density near the planet is reduced by a factor $1 - f \Delta t$. The area from which we take away mass has a size r_{acc} . For all accretion results in this Chapter, we have used $f = 5/3$ and $r_{\text{acc}} = 0.1$ (see D'Angelo et al. 2002). Klahr & Kley (2006) used, in addition to runs with this accretion prescription, a procedure that conserves

total energy locally by adding the kinetic and potential energy that is accreted onto the planet to the internal energy of the gas. Because we solve for the total energy of the gas directly, our accretion prescription does conserve total energy. This means that in the accretion region the gas is heated by the accretion process.

When calculating the torque on the planet, we exclude material that resides within the Hill sphere of the planet. This was also done in Bate et al. (2003). Although material inside the Hill sphere may exert a torque on the planet, which may lead to migration reversal (D'Angelo et al. 2003b), this torque is very sensitive to numerical resolution and the details of the accretion process. Moreover, this is also the region where self-gravity should play an important role, which is not included in our models. Therefore we focus on torques due to material *outside* the Hill sphere of the planet. We anticipate that for the low-mass planets that we consider in this Chapter this will not affect our results.

5.6.2 Flux-limited diffusion

Because of the intrinsic short time scale for radiative effects, which is due to the enormously fast communication speed c compared to the sound speed, it is necessary to integrate the equation for E in an implicit way.

First of all, consider the gas coupling term. We follow the approach described in Hayes & Norman (2003). The gas is heated by the radiation field according to

$$\frac{\partial \epsilon}{\partial t} = \kappa c (E - B), \quad (5.38)$$

where $\epsilon = p/(\Gamma - 1)$ is the internal energy of the gas. Upon differencing both sides we obtain:

$$\epsilon^{n+1} - \epsilon^n = \Delta t \kappa c (E^{n+1} - B^{n+1}), \quad (5.39)$$

where X^n denotes quantity X evaluated at time n . We approximate B^{n+1} using a Taylor series expansion:

$$B^{n+1} \approx a(T^n)^3 (4T^{n+1} - 3T^n), \quad (5.40)$$

and we spell out the internal energy as

$$\epsilon^{n+1} = \frac{p^{n+1}}{\Gamma - 1} = \frac{\rho \mathcal{R} T^{n+1}}{\Gamma - 1}, \quad (5.41)$$

in which \mathcal{R} is the universal gas constant and Γ is the adiabatic exponent.

Putting Eq. (5.41) and (5.40) into Eq. (5.39) we can solve for T^{n+1} :

$$T^{n+1} = \frac{\epsilon^n + \Delta t \kappa c E^{n+1} + 3 \Delta t \kappa c B^n}{\epsilon^n + 4 \Delta t \kappa c B^n} T^n. \quad (5.42)$$

This expression is used in Eq. (5.40) to evaluate B^{n+1} . We are now in a position to difference Eq. (5.33) (for details see Hayes & Norman 2003), which gives us an algebraic

equation for $E_{i,j,k}^{n+1}$ at grid position (i, j, k) :

$$\begin{aligned} & d_{i,j,k} E_{i,j,k}^{n+1} + d_{i+1,j,k} E_{i+1,j,k}^{n+1} + d_{i,j+1,k} E_{i,j+1,k}^{n+1} + \\ & d_{i,j,k+1} E_{i,j,k+1}^{n+1} + d_{i-1,j,k} E_{i-1,j,k}^{n+1} + d_{i,j-1,k} E_{i,j-1,k}^{n+1} + \\ & d_{i,j,k-1} E_{i,j,k-1}^{n+1} = Q_{i,j,k}^n, \end{aligned} \quad (5.43)$$

for certain $d_{i,j,k}$. Note that we use only a seven point finite difference stencil. This is cheaper than taking into account all 26 neighboring cells, while we found no noticeable difference in the result.

We can write Eq. (5.43) as a linear system equation:

$$\mathcal{D} \mathbf{E}^{n+1} = \mathbf{Q}^n, \quad (5.44)$$

in which \mathcal{D} is a $N \times N$ matrix and \mathbf{E}^{n+1} and \mathbf{Q}^n are vectors with N elements. Here, N is the total number of grid points. Fortunately, this huge matrix \mathcal{D} is sparse; it has only seven non-zero entries every row. For such matrices efficient iterative linear solvers have been developed in the literature. For an overview see Barrett et al. (1994).

The most basic characteristic of a sparse linear solver is whether it is a *stationary* method or not. Stationary methods for solving Eq. (5.44) can be cast in the form:

$$\mathbf{E}_m^{n+1} = \mathcal{A} \mathbf{E}_{m-1}^{n+1} + \mathbf{C}, \quad (5.45)$$

where \mathbf{E}_m^{n+1} is the approximation to \mathbf{E}^{n+1} after m iterations. The matrix \mathcal{A} nor the vector \mathbf{C} depends on m for a stationary method. Examples are the Jacobi method, the Gauss-Seidel method and Successive Over-Relaxation (SOR), which was used for example in Klahr & Kley (2006). The main disadvantage in using SOR lies in the fact that the convergence behavior of the method depends on a relaxation parameter ω , for which the optimal value is problem-dependent.

Non-stationary methods are a more recent development, and they differ from stationary methods in that the structure of the update step changes with each iteration. A simple case is given by Eq. (5.45) with a matrix \mathcal{A} and vector \mathbf{C} that do depend on m . Examples of non-stationary methods are the Conjugate Gradient Method (CG), the Generalized Minimal Residual method (GMRES), the Quasi Minimal Residual method (QMR) and the Bi-Conjugate Gradient Stabilized method (Bi-CGStab).

The optimal method for a given problem depends on the structure of the matrix \mathcal{D} . CG, for example, is only applicable to symmetric positive definite matrices, while we know in advance that due to opacity gradients the matrix \mathcal{D} will not be symmetric. One could try CG on the matrix $\mathcal{D}^T \mathcal{D}$, where \mathcal{D}^T is the transpose of \mathcal{D} , but this is not a good idea because the condition number of $\mathcal{D}^T \mathcal{D}$ is the square of the condition number of \mathcal{D} , which would lead to very slow convergence of the method.

Another difference amongst the various methods is the memory requirement. When dealing with large matrices this can be a real bottleneck. For GMRES it can be shown that the optimal solution is reached within a finite number of iterations, but these iterations become more and more expensive because the method needs information from *all* previous steps. To avoid the enormous storage requirements one could decide to restart GMRES after a fixed number of iterations, but this introduces a free parameter

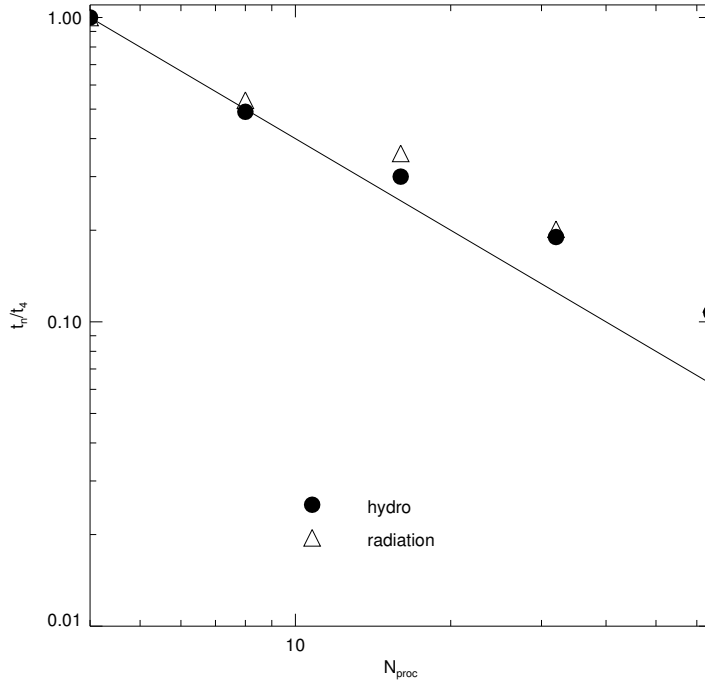


Figure 5.1: Strong scaling test for the three-dimensional radiation-hydrodynamical code, shown as the total execution time (relative to the execution time using four processors) as a function of the total number of processors. The solid line indicates perfect scaling, i.e. running on twice as many processors results in half the original execution time. Filled circles indicate the hydrodynamics part of the code; open triangles the radiation part. Note that both parts of the code scale equally well up to 64 processors.

in the method that needs to be tuned to the problem. Finally, QMR is more expensive in memory than Bi-CGStab in terms of memory because it needs more auxiliary variables. Therefore we have chosen Bi-CGStab as our method of choice.

One potential disadvantage of Bi-CGStab is that it needs four inner products every iteration. An inner product is a global quantity, and therefore it requires communication between different processors, in addition to the boundary conditions. They act as synchronization points, and therefore load-balancing is critical in this part of the numerical method. We have implemented a dynamical load-balancing module, in which during execution of the code the processors exchange part of the computational domain to optimize the domain decomposition. Note that due to the AMR it is not true that every processor should get an equal part of the computational domain, because at an AMR boundary more work is needed (i.e. interpolation of data, flux correction).

We have performed a strong scaling test on a low-resolution disk with a low-mass planet. The main grid consisted of 128 radial cells, 384 azimuthal cells and 8 meridional cells, on top of which we put 2 levels of AMR. The simulation was run on different numbers of processors (n_{proc}) for a total of 5 orbits of the planet, which comes down to approximately 7500 time steps. The resulting total execution times, relative to the case of 4 processors, is shown in Fig. 5.1. Focusing on the hydrodynamical part first (filled circles), we see that the code scales perfectly up to $n_{\text{proc}} = 8$. Due to memory requirements the simulation could not run on less than 4 processors, but the perfect scaling from 4 to 8 processors indicates that the code should scale very well from 1 to 4 processors as well.

When we increase n_{proc} beyond 8, the scaling is still very good, although not perfect. This is always the case at some point in a strong scaling test, because the amount of data that need calculation stays the same, while the amount of data that has to be

communicated increases with the number of processors. At some point increasing n_{proc} does not result in a reduction in execution time anymore. Fortunately, for up to 64 processors we still gain a significant speed-up. This gives us confidence that for the high-resolution runs (that have 8 times more computational cells in the main grid) the scaling will be good up to $8 \times 64 = 512$ processors. The simulations presented in this Chapter were run on 126 processors at the Dutch national supercomputer.

An interesting point in Fig. 5.1 is that the radiation module scales equally well as the hydrodynamics, even though the numerical methods for both parts of the physical problem differ significantly. This is an indication that for this problem only a small number of iterations is needed in the linear solver to reach convergence.

5.6.3 Boundary conditions

The planet excites waves in the disk, which subsequently propagate to the boundaries of the computational domain. To minimize reflection of outgoing waves we employ the non-reflective boundary conditions as outlined in Paardekooper & Mellema (2006) for the hydrodynamic variables. At the midplane we use reflective boundary conditions. No reflected waves were observed near the radial and upper meridional ($\theta = \pi/2 - 5h/2$) boundaries.

For the boundary conditions for the radiation energy density we take a different approach, because the initial condition for the gas temperature does not correspond to a stationary solution for E . In fact, due to the different opacity regimes at different heights above the midplane of the disk it is difficult, if not impossible, to obtain a stationary solution for E . In the case where the disk is optically thin throughout, the radiation energy density should vary as $E \propto r^{-2}$, which means that matter in equilibrium with this radiation has a temperature that varies as $T \propto r^{-1/2}$. In vertical hydrostatic equilibrium the relative scale height h is then proportional to $r^{1/4}$, while the initial condition for the gas is a constant h . However, all disk models quickly (within a few orbits of the planet) adapt to a new equilibrium corresponding to the temperature structure set by the radiation field.

Real protoplanetary disks are heated internally by viscous dissipation (in regions where magnetic turbulence operates) and externally by radiation from the central star. Irradiation effects may play a large role in structuring protoplanetary disks (Dullemond 2000; Dullemond et al. 2001), but a detailed treatment of these effects is beyond the scope of this Chapter. However, in absence of heating sources the disk cools down rapidly (see Klahr & Kley 2006), which will change the torque on embedded planets.

To account for irradiation in an approximate way we set the radiation energy density at the inner boundary to a constant value, which, for an optically thin disk, would correspond to $h = 0.05$ at the location of the planet. This way, we can compare the radiation-hydrodynamical simulations directly to their isothermal counterparts.

At the midplane we use reflective boundary conditions, while at the outer radial boundary we set the ghost cells such that $F_{R,r} \propto r^2$, which corresponds to an outflow boundary. At the $\theta = \pi/2 - 5h/2$ boundary we apply a similar procedure. This way, radiation can propagate freely off the grid.

$M_p (M_\oplus)$	Γ	α	FLD	Acc	n_{lev}	Comments
0.6	1	0.004	n	y	5	
5	1	0.004	n	y	4	
5	1	0.004	n	y	3	
5	1	0.004	n	y	2	
40	1	0.004	n	y	3	
320	1	0.004	n	y	2	
5	1.005	0	n	y	4	
5	1.01	0	n	y	4	
5	1.005	0	n	y	3	
5	1.01	0	n	y	3	
0.6	1.4	0	y	n	5	
0.6	1.4	0	y	y	5	
0.6	1.4	0	y	n	4	
0.6	1.4	0	y	y	4	
5	1.4	0	y	n	4	
5	1.4	0	y	y	4	
5	1.4	0	y	n	3	
5	1.4	0	y	y	3	
5	1.4	0	y	n	2	
5	1.4	0	y	y	2	
5	1.4	0	y	n	4	10 times lower density
5	1.4	0	y	n	4	100 times lower density
5	1.4	0	n	n	4	local model
5	1	0	n	n	4	local model

Table 5.1: Overview of model parameters. From left to right, the columns indicate: planet mass in M_\oplus , value of the adiabatic exponent ($\Gamma = 1$ means a locally isothermal equation of state), viscosity parameter α , radiation flag, accretion flag and the number of refinement levels. When n_{lev} levels of refinement are used, the local resolution within a distance of $2H$ from the planet is a factor $2^{n_{\text{lev}}}$ higher than the base resolution of $\Delta r = 0.0082 r_p$. For the local models, the indicated resolution is valid for the whole computational domain.

5.6.4 Test problems

The RODEO hydrodynamics module was tested extensively on a Cartesian grid with shock tube problems: in all coordinate directions separately as well as in two dimensions diagonally. Also a genuinely two-dimensional problem, the wind tunnel with step, was studied and the results showed that the internal Roe solver is able to deal with the complex shock structures that arise in this problem (see also Mellema et al. 1991).

The radiation module was tested with one- and two-dimensional diffusion problems with a simplified opacity law ($\kappa = \text{constant}$). See Stone et al. (1992) for a description of the diffusion tests. The numerical results were indistinguishable from the analytical solution.

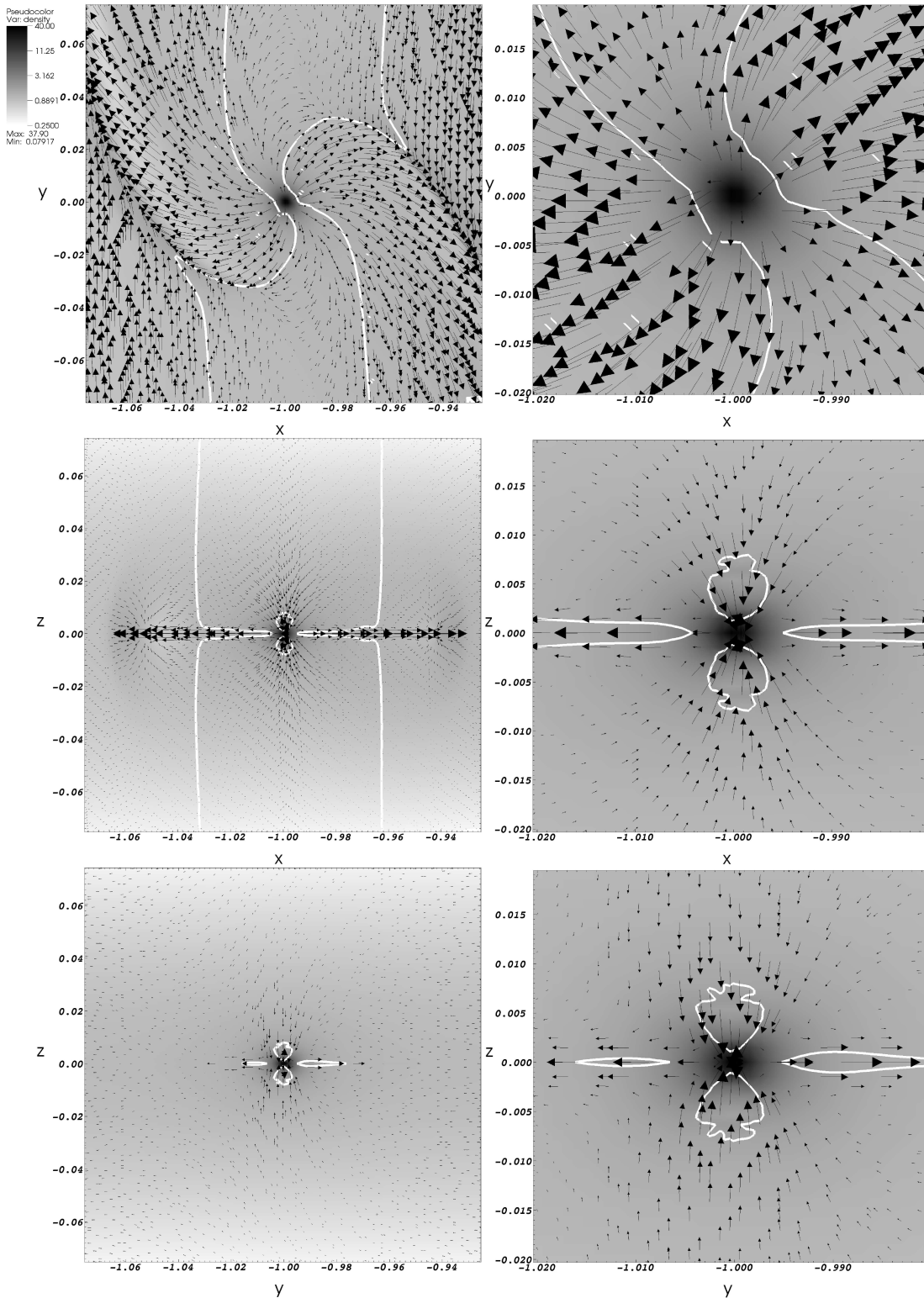


Figure 5.2: Density and velocity fields around an accreting $5 M_{\oplus}$ planet after 10 orbits. Top panels: slice through $z = 0$ ($\theta = \pi/2$), middle panels: slice through $y = 0$ ($\phi = \pi$), bottom panels: slice through $x = -1$ ($r = 1$). Inside the white contour the velocities are supersonic.

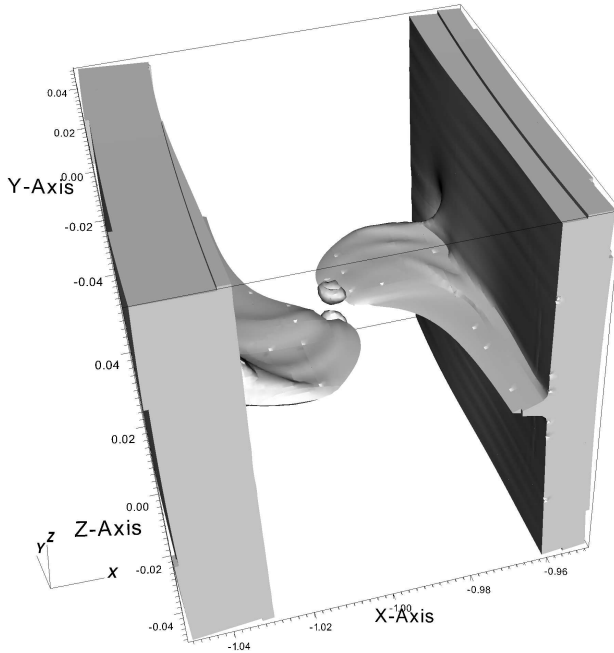


Figure 5.3: Isovolume for a Mach number of 1. Inside the solid structures the velocity relative to the planet is supersonic.

Another test for the radiation solver is an optically thin circumstellar disk. Although FLD is in principle not very well suited for optically thin problems, it should nevertheless let E diffuse towards the correct solution $E \propto r^{-2}$. Starting from the initial condition $E \propto r^{-4}$ (for $h = \text{constant}$, $T \propto r^{-1}$, therefore $E = aT^4 \propto r^{-4}$) the numerical solution agrees with $E \propto r^{-2}$ within one orbit of the planet after which it remains stable. This is an important test, because it shows that we can compare the radiation-hydrodynamical results in the optically thin limit directly to the isothermal runs.

Finally, we considered an optically thick disk with a constant opacity. In this case, the equilibrium solution is given by $E \propto r^{-1}$. Again, starting from the initial condition for constant h the numerical solution agrees with $E \propto r^{-1}$ within a few orbits of the planet, depending on the exact value of the opacity.

5.7 RESULTS

In the previous sections we have described the physical and numerical setup for the three-dimensional radiation-hydrodynamical simulations. However, we now move from the simple, 2D, viscous simulations toward the full models in two steps. The first step consists of 3D, isothermal simulations that are compared to Bate et al. (2003) and D'Angelo et al. (2003b). After that, we will include the energy equation but treat the cooling in a very simplistic way by setting the adiabatic exponent Γ close to unity. Finally, we will present the full radiation-hydrodynamical results. In Table 5.1 we give an overview of the simulations discussed in this Chapter.

5.7.1 Isothermal models

The flow structure around planets in three-dimensional isothermal disks has been described before (Bate et al. 2003; D’Angelo et al. 2003b). Therefore we limit the discussion to a few interesting remarks on the 3D-structure of the accretion flow. The disk model we use differs from the one described in Sect. 5.5 in two ways: we use a locally isothermal equation of state, and a kinematic α -type viscosity (Shakura & Sunyaev 1973) with $\alpha = 0.004$ at the location of the planet. Essentially this model is the same as in D’Angelo et al. (2003b).

In Fig. 5.2 we show density slices along the three coordinate axis for a $5 M_{\oplus}$ planet after 10 orbital periods. By this time the flow has reached a steady state (Bate et al. 2003). For a low-mass planet like this the spiral wave features in the density are not strong, but they appear nicely in the velocity field.

From the middle and bottom panels of Fig. 5.2 we see that the material accreting onto the planet originates predominantly above and below the planet. As the material enters the Hill sphere of the planet, which for this mass is $0.017 r_p$ large, it is accelerated to supersonic velocities. This was also observed by D’Angelo et al. (2003b), albeit not for a planetary mass as low as $5 M_{\oplus}$. Interesting is the equatorial outflow of mass that is apparent in Fig. 5.2. As the accreting material rains down on the planet it squeezes the envelope which forces some material to be expelled from the envelope in the equatorial plane of the disk. Even before leaving the Hill sphere of the planet this material again reaches supersonic velocities. It is important to note that no vertical hydrostatic equilibrium is established near the planet. This was also observed by D’Angelo et al. (2003b), even for non-accreting planets. The appearance of outflows does not depend on the boundary at $\theta = \pi/2$: we found the same behavior for a disk extending from $\theta = \pi/2 - 5h/2$ to $\theta = \pi/2 + 5h/2$.

In Fig. 5.3 we show the three-dimensional structure of the supersonic accretion and subsequent equatorial outflow. The solid volume represents the region where the Mach number of the flow, relative to the planet, is larger than one. For large radial distances to the planet the flow is always supersonic due to the Keplerian shear; this leads to the two large pizza boxes on both radial sides of Fig. 5.3. The supersonic accretion velocities appear as the two small spheres just above and below the planet. The equatorial outflow is quickly turned into spiral wave features by the Keplerian shear. Note that the outflow is confined to the midplane of the disk. This is illustrated further in Fig. 5.4, where we show a density slice parallel to the midplane but at a height of $0.005 r_p$. Note that this is well within the Hill sphere of the planet. Even so, the velocity structure differs dramatically from that in the midplane. Apart from the unperturbed Keplerian velocity on both sides of the planet we can also see the horseshoe orbits, as well as a rotating accretion flow close to the planet. This was also found by D’Angelo et al. (2003b).

The velocity structure inside the Hill sphere of the planet is intrinsically linked to the accretion procedure (D’Angelo et al. 2003b). However, we found that this is not true for the equatorial outflow. It is there always when the vertical accretion flow is, albeit with a different magnitude for different accretion prescriptions.

For a planet of $0.5 M_{\oplus}$ the flow within the Hill sphere remains subsonic. The density

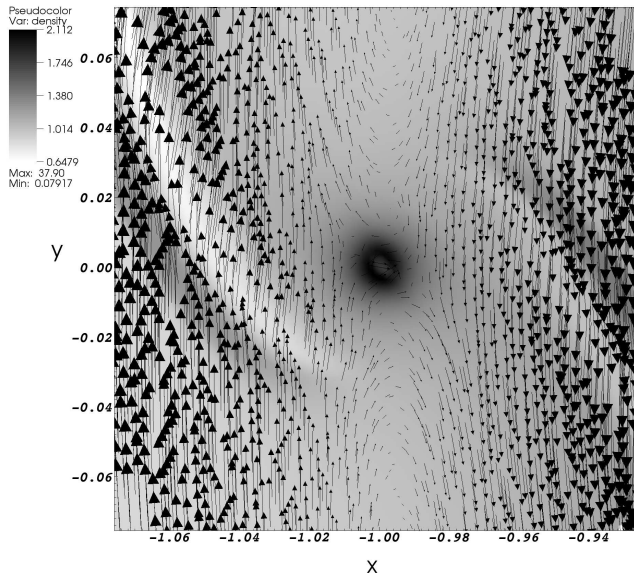


Figure 5.4: Density and velocity fields around an accreting $5 M_{\oplus}$ planet after 10 orbits. The slice is taken at a distance of $0.005 r_p$ from the midplane of the disk.

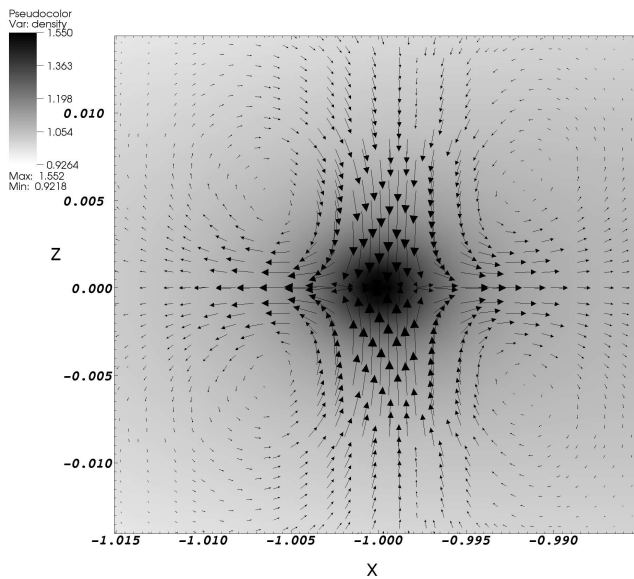


Figure 5.5: Slice through $\phi = \pi$ for a $0.5 M_{\oplus}$ planet after 10 orbits, showing density and velocity. For this low-mass planet all velocities are subsonic.

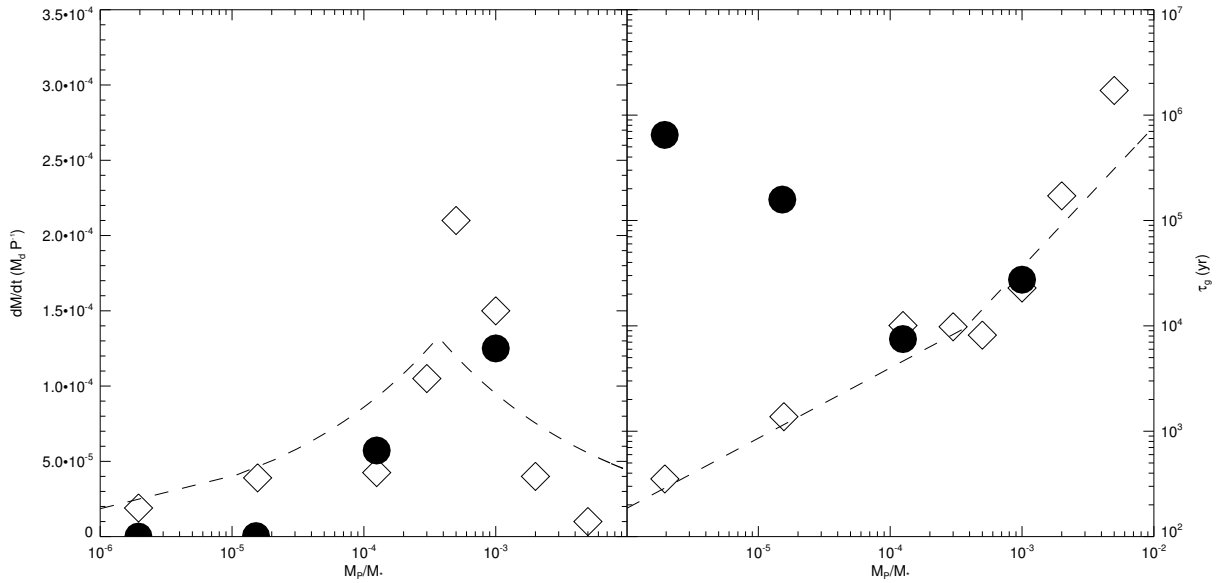


Figure 5.6: Accretion rates for two- and three-dimensional isothermal simulations. Open symbols represent the two-dimensional results from Paardekooper & Mellema (2006), filled symbols denote the three-dimensional results. Left panel: accretion rate in units of disk masses per orbit for different planetary masses. Right panel: growth time scales $\tau_g = M_p/\dot{M}_p$ in years, where we assume a disk mass of $5 M_J$.

and velocity field near the planet is shown in Fig. 5.5. Again we can see the vertical accretion flow from above and below the planet, some of which is deflected into the midplane of the disk where it may leave the Hill sphere of the planet. We can identify four circulation patterns near the edge of the Hill sphere, which is approximately $0.009 r_p$ large. Some of these patterns can also be seen in the results of D’Angelo et al. (2003b).

We will now turn to the question whether the differences in flow structure we find affect accretion and migration rates of embedded planets. In Fig. 5.6 we show the measured accretion rates as a function of planetary mass. Note that in this section we do not limit ourselves to low-mass planets in order to compare with previous numerical results (D’Angelo et al. 2003b). The two-dimensional results, shown by the open symbols, were discussed extensively in Paardekooper & Mellema (2006) and we show them here just for comparison. We have modeled four different planetary masses, spanning a range from deep in the linear regime ($M_p = 0.5 M_\oplus$) to well in the non-linear, gap-opening regime ($M_p = 1.0 M_J$).

Comparing the results of two- and three-dimensional simulations for the two planets with the highest mass, we find very good agreement. Especially for the $1 M_J$ planets this is to be expected, because the Roche lobe of this planet is larger than the scale height of the disk, which makes the two-dimensional approximation applicable. But also for the planet of $0.1 M_J$ we find good agreement, which contradicts the result of D’Angelo et al. (2003b). However, this discrepancy is small: for this planet, D’Angelo et al. (2003b) find a difference of approximately a factor of two between 2D and 3D results, while we find a difference of 1.3. It is possible that because our method is

specifically designed to handle shocks in a correct way, non-linear effects start to play a role for slightly lower planetary masses. Our results on migration rates support this suggestion (see below).

Because the Roche lobes of the low-mass planets are much smaller than the disk thickness the two-dimensional approximation breaks down. This affects migration as well as accretion, but the effect on the accretion rates is the most dramatic. When in the two-dimensional approach mass is taken away from the location of the planet, what essentially happens is that a whole column of gas is accreted onto the planet. In the full three-dimensional problem this does not happen, and therefore the accretion rates are significantly lower. For the smallest planet we consider ($M_p = 0.5 M_\oplus$) the difference amounts to more than three orders of magnitude (see the right panel of Fig. 5.6).

Qualitatively our results agree very well with the results of D'Angelo et al. (2003b). Interestingly, Bate et al. (2003) do not find an increase in growth time towards the low-mass end, but this is probably due to a lack of resolution. Our results show that in order to capture significant amounts of gas the mass of a solid core needs to be at least several Earth masses.

Migration rates also differ between 2D and 3D disks (Tanaka et al. 2002). Again, the difference is most pronounced for low-mass planets, while for planet with masses compared to Jupiter the two-dimensional approximation gives valid results. In Fig. 5.7 we show the migration time scales as a function of planetary mass. For a planet on a circular orbit, the migration time scale is related to the torque in the following way:

$$\frac{1}{\tau_m} = \frac{|\dot{r}_p|}{r_p} = \frac{2|\dot{L}|}{L} = \frac{2|\mathcal{T}|}{L}, \quad (5.46)$$

where L is the angular momentum of the planet and \mathcal{T} is the torque, which is what we measure during the simulations.

Again, for the $1 M_J$ planet the 2D result agrees very well with the 3D result, for the same reason as the accretion rates. In fact, they approach the migration rate dictated by the viscous evolution of the disk (Type II migration). On the low-mass end, we can nicely reproduce the analytical results from Tanaka et al. (2002) for Type I migration in 2D as well as in 3D. In this regime, 3D migration time scales are approximately a factor of two larger than for 2D disks.

In between the two regimes, we find that for a $0.1 M_J$ planet 2D and 3D results differ significantly, almost an order of magnitude. This is again in contradiction with D'Angelo et al. (2003b), but note that the main difference lies in the 2D results. These differences were already discussed in Paardekooper & Mellema (2006) and we will not repeat that discussion here. We only note that the results for a three-dimensional disk agree very well with D'Angelo et al. (2003b). Also, the departure from the Type I analytical result for the $0.1 M_J$ planet indicates that for this planet non-linear effects start to play a role, in accordance with the suggestion made above that these effects are also visible in the accretion rates.

Summarizing, we find excellent agreement with analytical results of torques in the low-mass regime as well as in the high-mass regime. In between, the results are not clear but D'Angelo et al. (2005) showed that this may be a general problem for this

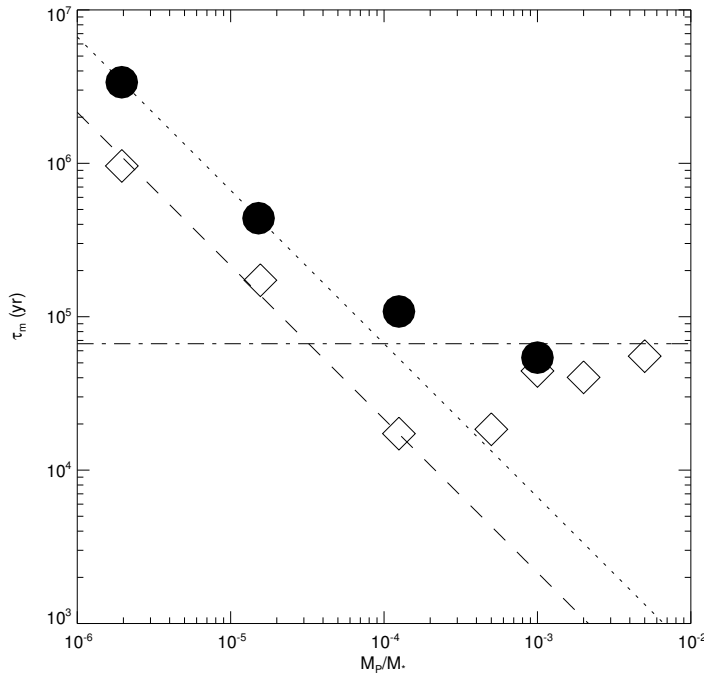


Figure 5.7: Migration time scales $\tau_m = r_p/\dot{r}_p$ for two- (open symbols) and three-dimensional (filled circles) isothermal simulations. As in Fig. 5.6 we assume a disk mass of $5 M_J$. The dotted line and the dashed line indicate the analytical results from Tanaka et al. (2002) for Type I migration in three-dimensional and two-dimensional disks, respectively. The horizontal dash-dotted line indicates migration on the viscous time scale of the disk (Type II migration).

transition regime. The measured accretion rates agree very well qualitatively with D’Angelo et al. (2003b), again with the exception of the transition regime between linear and non-linear interaction with the disk.

5.7.2 Near-Isothermal models

As a bridge between the simple, locally isothermal models of the previous section and the full radiation-hydrodynamical simulations we now consider models that do include the energy equation, but in which we treat the cooling in a simplified way. Consider the relation between internal energy and pressure for a perfect gas:

$$p = (\Gamma - 1) \epsilon, \quad (5.47)$$

which shows that the adiabatic exponent Γ is a measure of how a change in internal energy affects the gas pressure, and, given the density, therefore also the temperature of the gas. For the isothermal case, $\Gamma = 1$, pressure and internal energy evolve independently and the gas can be compressed indefinitely without changing the temperature. To simulate cooling in a very simplified way one can take a value of Γ very close to 1, which was done by Nelson & Benz (2003a,b) for the two-dimensional planet-disk problem. In Paardekooper & Mellema (2006) we commented already that this approach affects planetary accretion rates to a large extent, because even for $\Gamma = 1.001$ the planet forms a hot bubble around itself that prevents matter from entering the Roche lobe.

In Fig. 5.8 we show the density and velocity structure around a $5 M_{\oplus}$ planet after 10 orbits. This figure can be directly compared to the isothermal model depicted in Fig. 5.2. The global properties of the velocity field are similar to the isothermal case: inflow

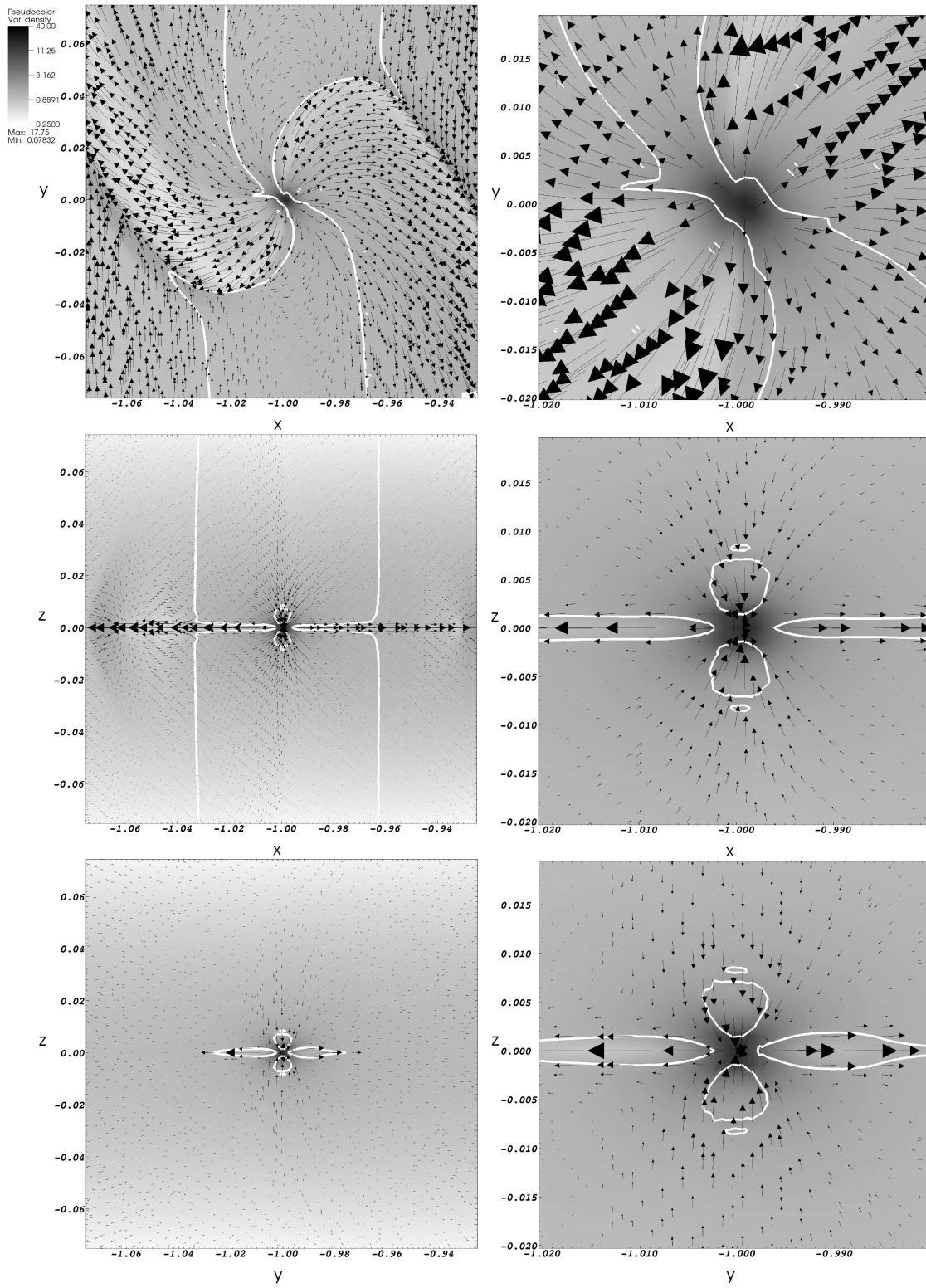


Figure 5.8: Same as Fig. 5.2, but for a nearly isothermal model with $\Gamma = 1.01$.

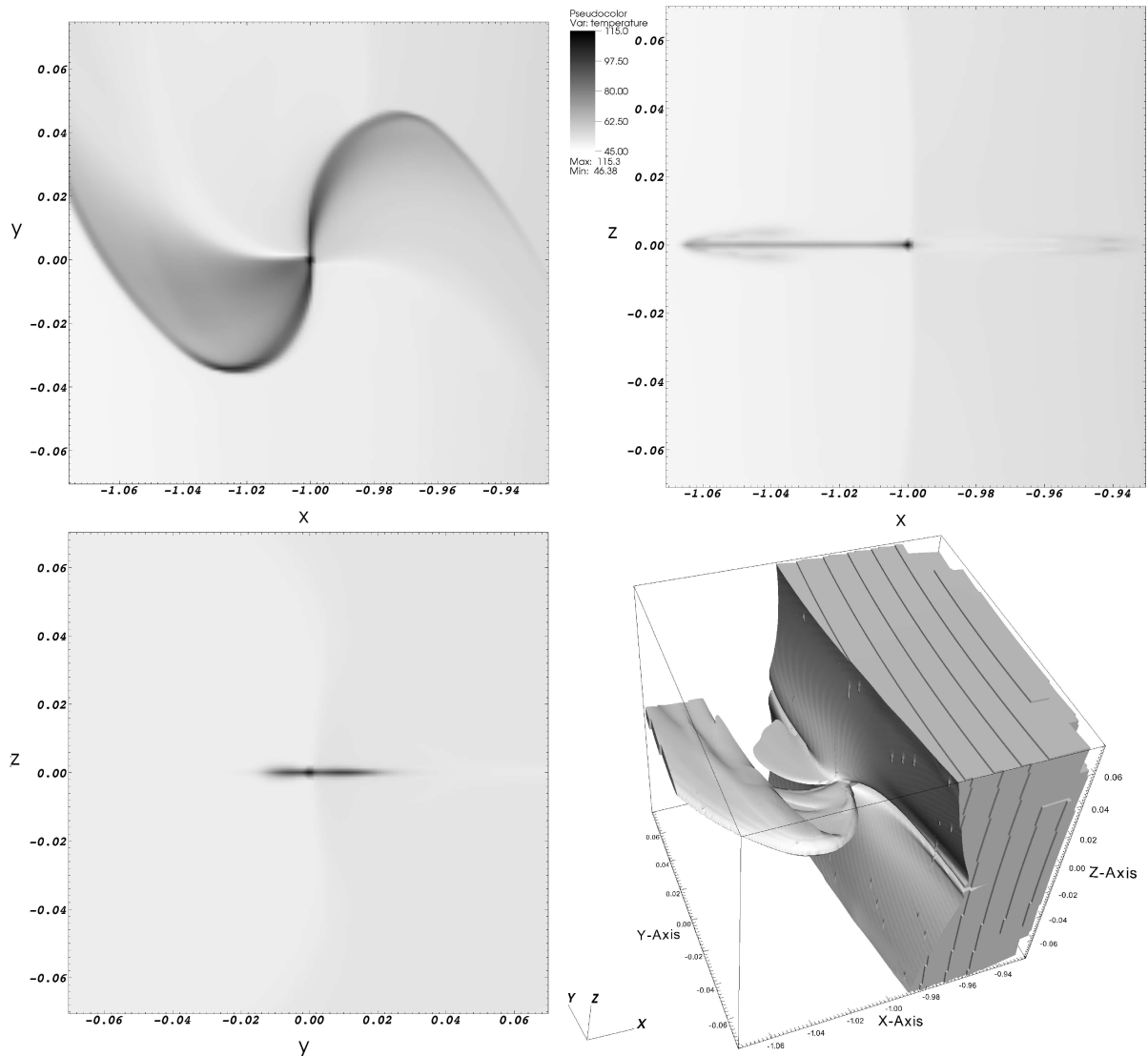


Figure 5.9: Temperature structure around a $5 M_{\oplus}$ planet after 10 orbits for $\Gamma = 1.01$. Top left panel: slice through $z = 0$ (equatorial plane). Top right panel: slice through $y = 0$ ($\phi = \pi$). Bottom left panel: slice through $x = -1$ ($r = 1$). Bottom right panel: isovolume indicating a temperature higher than the initial temperature at the location of the planet.

from above and below the planet and outflow in the midplane of the disk. Both inflow and outflow are again supersonic.

The central density is approximately 2 times lower in the nearly-isothermal model compared to the truly isothermal case. This is due to the fact that it is not only the density gradient that determines the pressure gradient, but also the temperature. This means that part of the pressure-support for the planetary envelope comes from the temperature gradient. We will see below that this lower central density affects the accretion rate onto the planet to a large extent.

Another important difference that can be seen in the top left panels of Figs. 5.2 and 5.8 is the change in outflow structure. While in the isothermal case of Fig. 5.2 both

outflow streams appear to be symmetric this is no longer the case when changes in temperature are taken into account. In the top right panel of Fig. 5.8 we see that the outflow towards positive y appears to be much more collimated along the y -axis than the outflow towards negative y , which is responsible for the asymmetry seen in the top left panel of Fig. 5.8. It is important to realize at this point that these asymmetries may suffer from resolution effects. Although in these simulations we resolve the Roche lobe by approximately 50 cells, the high-density region inside of the outflow is only resolved by 5 cells. Resolution studies show that the direction of the outflow does not depend on resolution, but the magnitude of the outflow does. This is because the central temperature and density also scale with resolution because the minimum distance to the planet does, and therefore also the depth of the potential well. The equatorial outflow therefore critically depends on the conditions near the center of the planet where the density and the temperature reach their highest values. Therefore there exists a connection between the conditions deep in the atmosphere of the planet and the planet's immediate surroundings.

In Fig. 5.9 we show the temperature structure around the same planet as in Fig. 5.8. In this model, the central temperature has risen from 50 K initially to more than 100 K. Note that it is only a very small region that acquires such a high temperature. This reflects the fact that the accreting region is only 10 % of the planet's Roche lobe. In this region, the gas is heated by the release of potential and kinetic energy of the accreted gas. The two streams of outflowing material along the y -axis are clearly visible due to their high temperature. Also the collimation of the stream in the positive y -direction is apparent in the top left panel of Fig. 5.9. The outflows remain confined to the midplane of the disk until they reach the spiral waves induced by the planet that are responsible for upward motion of gas. However, for a low-mass planet this upward motion is not strong, and from the top right panel of Fig. 5.9 we see that the hot flow does not reach high altitudes.

Another important effect can be seen in the bottom right panel of Fig. 5.9 that shows the three-dimensional temperature distribution around the planet. The solid volume indicates temperatures higher than the initial temperature at the location of the planet. The large solid structure at $x > -1$ is due to the global temperature gradient. To the left of this structure we see the effects of the planet, especially the spiral shaped hot outflow. But note that the corotational region located at $x = -1$ is also asymmetrically heated: for positive values of y the corotation region is locally heated by the planet, while this does not happen for negative y . Again, this is a consequence of the asymmetric hot outflow that originates deep inside the envelope of the planet. When the pressure remains the same, however, this temperature distribution leads to an asymmetric density distribution which will affect the total torque on the planet. Because the region *behind* the planet is heated compared with the region in front of the planet, the density will be relatively low behind the planet which leads to a torque that will be *positive* if the effect is strong enough. We will see below that for this model indeed the total torque on the planet is positive.

Before looking at the torques onto the planet we consider the measured accretion rates. In Fig. 5.10 we show the accretion rate as a function of time for three different

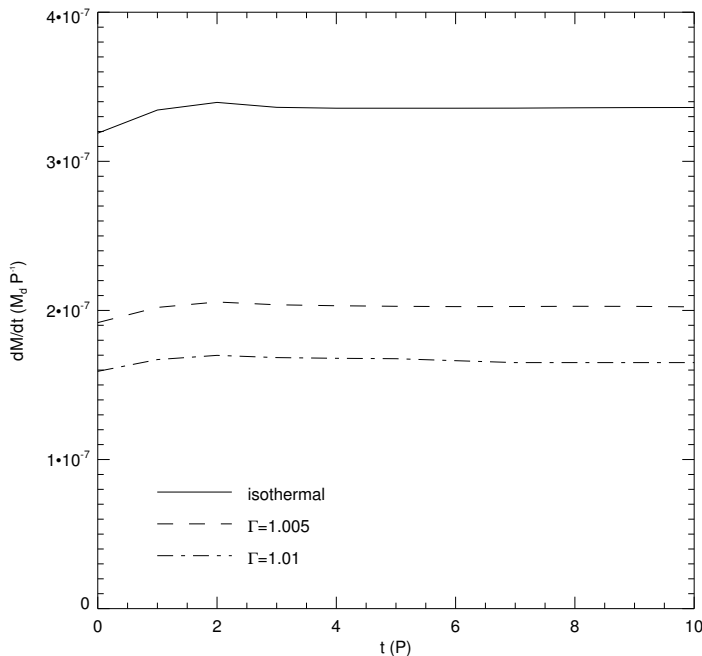


Figure 5.10: Accretion rates onto a $5 M_{\oplus}$ planet for three different equations of state.

equations of state: the isothermal result discussed in Sect. 5.7.1 together with two nearly-isothermal models. It turns out that the accretion rate depends sensitively on the central temperature. This is not surprising, because the pressure in near the center of the planet is determined mainly by the potential of the planet, which remains the same. Therefore, when the central temperature rises by a factor of 2, the central density will be a factor of 2 lower which in its turn affects the accretion rate onto the planet. From Fig. 5.9 we saw that for $\gamma = 1.01$ the central temperature indeed was a factor 2 higher than the initial temperature, while from Figs. 5.2 and 5.8 we see that the central density is lower by approximately a factor 2 for the model with $\Gamma = 1.01$ compared to the isothermal model. In Fig. 5.10 we see that this change in density is reflected in an accretion rate that is lowered again by a factor 2.

When we take Γ closer and closer to 1, we expect to retrieve the isothermal results. However, as was already mentioned in Paardekooper & Mellema (2006), even for Γ extremely close to 1 the central temperature of the planet rises significantly. In fact, due to the necessary divisions by the factor $\Gamma - 1$ (see Eulderink & Mellema 1995) one has to worry about numerical stability for $\Gamma \approx 1$. Therefore the lowest value of Γ we considered is $\Gamma = 1.005$. For this model, the central temperature rises to approximately 90 K, which is again reflected in a lower accretion rate than for the isothermal model (see Fig. 5.10).

In Fig. 5.11 we show the total torque onto the planet for the same models as in Fig. 5.10. The torques are normalized to the absolute value of the analytic result of Tanaka et al. (2002), and as was already shown in Fig. 5.7 for the isothermal model we find very good agreement with the analytical result. This can not be said of the nearly-isothermal models, however. Indeed, for both values of Γ we considered we find a *positive* torque, indicating outward migration. But not only is the direction reversed,

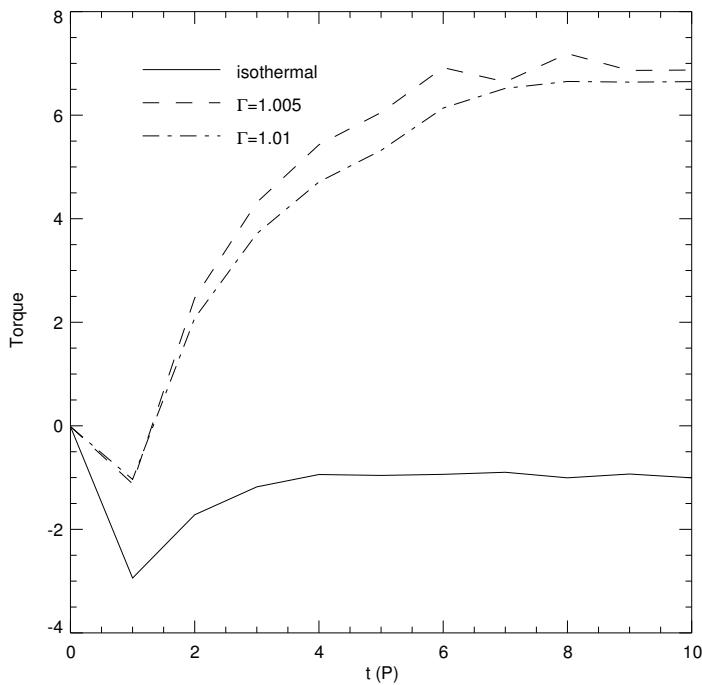


Figure 5.11: Total torque onto a $5 M_{\oplus}$ planet for three different equations of state. The torques are normalized to the absolute value of the analytical result of Tanaka et al. (2002).

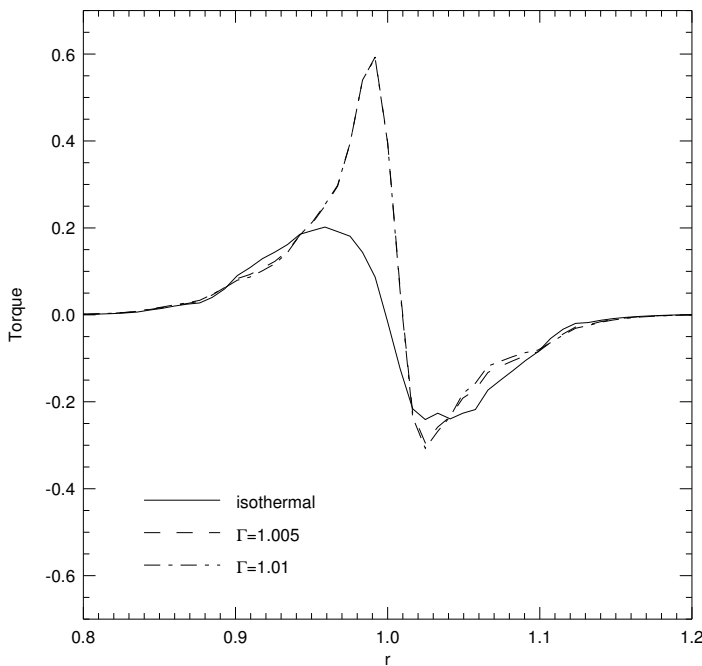


Figure 5.12: Radial torque profile for a $5 M_{\oplus}$ planet for three different equations of state. The torques are normalized in such a way that the total torque for an isothermal equation of state is equal to -1 .

also the magnitude of the torque is surprising: more than six times larger than for the isothermal case. The actual value of Γ has no influence on this result. Note that it takes a few orbits longer for the nearly-isothermal models to reach a steady state with respect to the torque, which was not the case for the accretion rates. This is probably due to the fact that the torque is modified by the equatorial outflow. This material has to come close to the planet which takes a few orbits.

It is interesting to find out where exactly this large positive contribution to the torque originates. In order to answer this question, we show in Fig. 5.12 the radial torque profile for the three different equations of state. For the isothermal case we see the usual (see Bate et al. 2003; D'Angelo et al. 2003b) contributions from the inner and the outer spiral wave, where the inner wave exerts a positive torque on the planet and the outer wave a negative torque. It is clear that even from inspection by eye that the torque due to the outer wave is slightly stronger which leads to inward migration.

The situation is totally different for nearly-isothermal models, as can be seen in Fig. 5.12. For the outer disk the changes are marginal, which is not surprising because the structure of the outer wave in Figs. 5.2 and 5.8 appears very similar. This in contrast with the inner wave, which has a much more open structure for the nearly isothermal model compared with the truly isothermal model. This changing wave structure leads to a net positive torque on the planet.

From the temperature plots in Fig. 5.9 we conclude that the outflowing material originates deep within the Roche lobe of the planet. This is an indication that accretion and migration rates of forming planets are closely linked. This was already suggested by D'Angelo et al. (2003b) for the isothermal case. However, only when the energy equation is taken into account the migration behavior changes this drastically. Although in this section we have treated cooling in a simplified way, it provides useful insight in what we may expect from the full radiation-hydrodynamical models. In the next section, we will consider a more realistic treatment of the energy balance by explicitly including radiative cooling.

5.7.3 Radiation-Hydrodynamical models

The full radiation-hydrodynamical models differ from the nearly-isothermal models in two ways: first of all, the adiabatic exponent is set to $\Gamma = 1.4$, which reduces the compressibility of the gas. Second, the FLD module calculates the energy diffusion through radiation. Therefore, the cooling properties of the gas depend on the local temperature and density. When cooling is not efficient, we expect that due to the higher value of Γ the effects seen in the nearly-isothermal models will be enhanced even more. This will certainly happen in the high density envelope of the planet, and because we saw in the previous section that temperature effects deep within the Roche lobe of the planet affect the migration behavior we may expect to see similar things in the radiation-hydrodynamical models.

In order to distinguish the effects from the accretion itself from the overall radiation-hydrodynamical behavior of the disk, we consider two cases in this section: an accreting $5 M_{\oplus}$ planet and a non-accreting planet of the same mass. The non-accreting planet

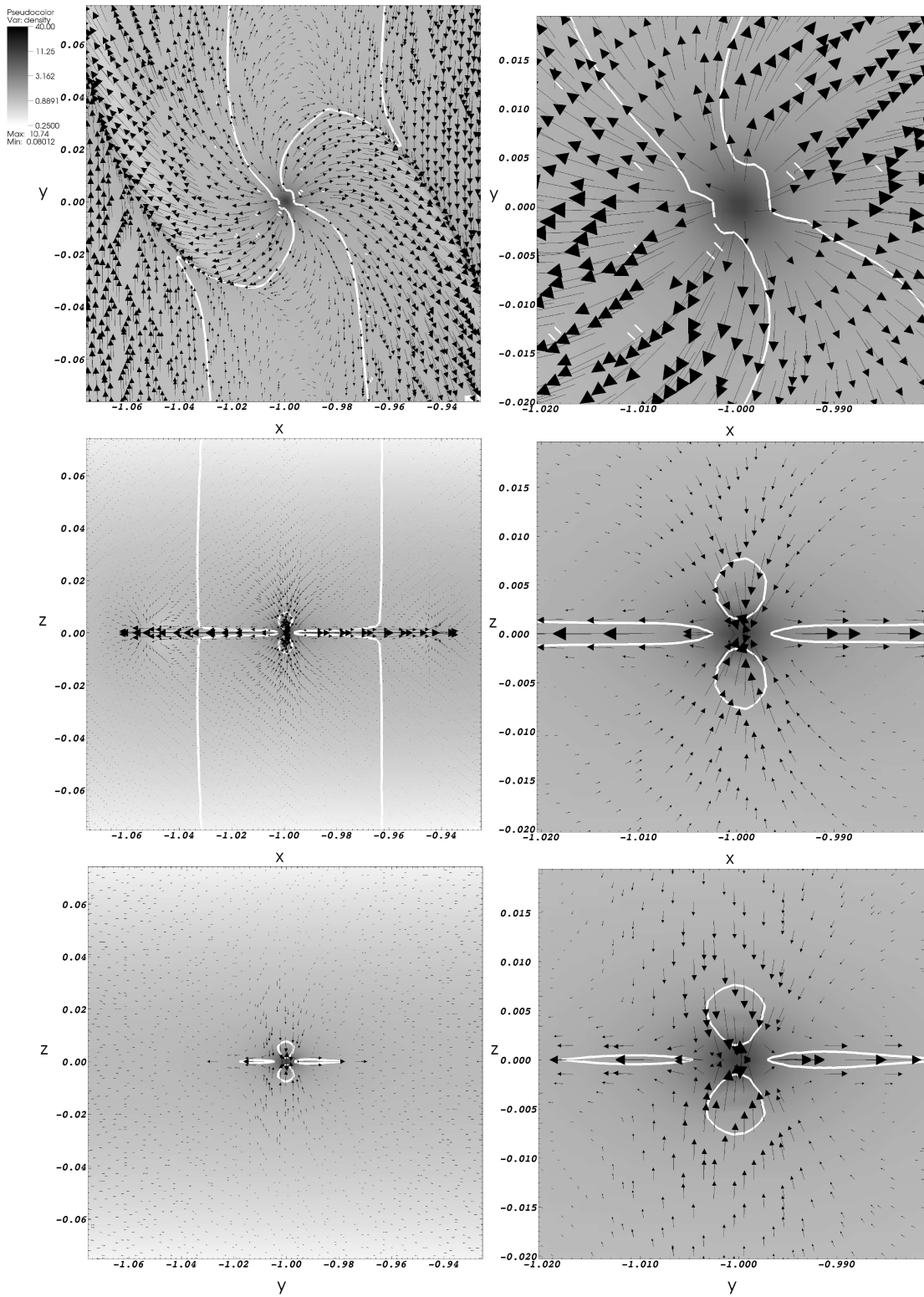


Figure 5.13: Same as Fig. 5.2, but for a non-accreting radiation-hydrodynamical model with $\rho_0 = 10^{-11} \text{ g cm}^{-3}$.

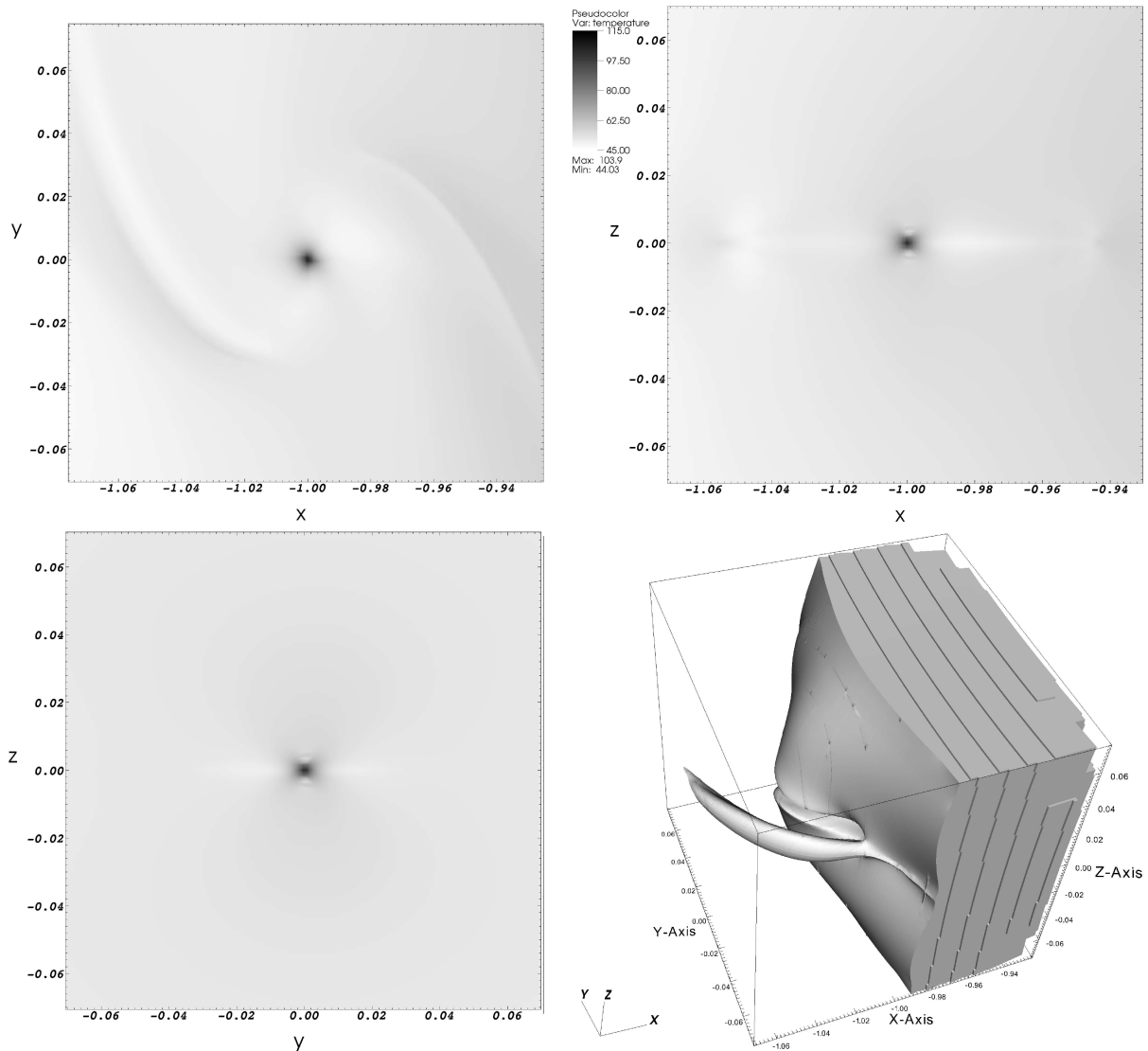


Figure 5.14: Same as Fig. 5.9, but for a non-accreting radiation-hydrodynamical model.

is allowed to build a high-density atmosphere because no mass is removed from the Roche lobe. However, as was already shown by D'Angelo et al. (2003b) for the isothermal case, even in this case the envelope does not reach a state of hydrostatic equilibrium in the vertical direction. Material still rains down into the Roche lobe from above and below the planet, some of which subsequently flows out again. Thus even in the case of a non-accreting planet there may exist a close connection between the state of the material deep within the planetary envelope and the torques due to material outside the Roche lobe.

In Fig. 5.13 we show the density and velocity structure for the non-accreting planet of $5 M_{\oplus}$. The color scale is the same as in Figs. 5.2 and 5.8, which tells us immediately that the density of the planetary envelope is very low compared to the isothermal and nearly-isothermal cases. This reflects the effect of the lower compressibility of the gas.

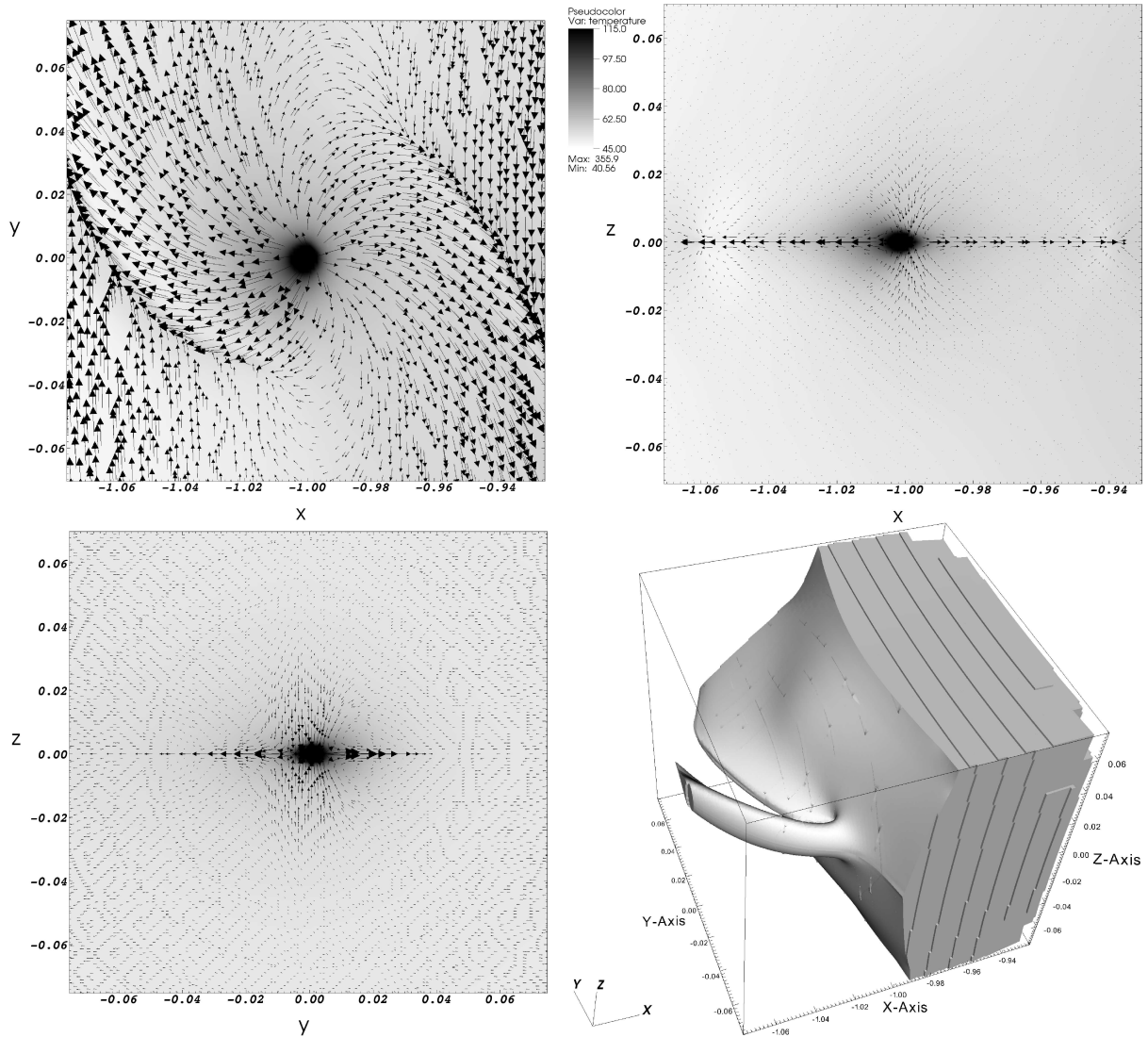


Figure 5.15: Same as Fig. 5.9, but for an accreting radiation-hydrodynamical model. Black arrows indicate the velocity field.

We will see below that this has dramatic effects on the ability of the planet to accrete gas from the disk.

Looking at the velocity field in Fig. 5.13 we see that indeed there is no hydrostatic equilibrium in the vertical direction. The same flow pattern appears as in the isothermal and nearly-isothermal cases: inflow from above and below and outflow along the equator of the planet. Inflow velocities are lower in this case because the planet does not accrete matter (D'Angelo et al. 2003b). The outflow appears much more symmetric in all directions compared to the previous nearly-isothermal case. Therefore radiative cooling restores the isothermal situation in these regions of lower density than the planetary core. However, we will see that still important differences arise in the torque on the planet.

In Fig. 5.14 we show the temperature structure around the planet, on the same

scale as in Fig. 5.9. The most important difference with the midplane temperature structure of the nearly-isothermal models is the absence of the accretion jets because in Fig. 5.14 we show a non-accreting model. The temperature at the center of the planet is also lower; about a factor of 2 higher than the initial temperature. This agrees with Eq. (5.17) for the maximum central temperature that can be reached in absence of convection. We can also identify the spiral waves in the temperature structure, because when the gas is compressed in the wave the temperature rises. In the dense midplane of the disk the gas can not radiate away this energy efficiently, and therefore the spiral waves have a higher temperature.

Inside the equatorial outflow the gas expands, and therefore cools down. This effect causes the temperature close to the hot core to be lower than the initial temperature. These regions show up as dark areas in Fig. 5.14, most notably in the top right panel.

Another difference with the nearly-isothermal models can be spotted most clearly in the bottom-left panel of Fig. 5.14. While the heat generated in the envelope of the planet remains confined to the midplane of the disk in the nearly-isothermal models (see Fig. 5.9), in the radiation-hydrodynamical models it can diffuse to higher altitudes. Because of the large opacity gradient in the vertical direction, this is the preferable direction for radiative diffusion.

In the bottom right panel of Fig. 5.14 we again, just as in Fig. 5.9, show a 3D isovolume of the temperature structure around the planet. It is clear that also the spiral wave structure in the temperature extends further in the vertical direction due to radiative heat diffusion. Also it is clear that the strong accretion jets are absent. However, what remains is the asymmetric temperature structure in the corotation region. There is a bump visible for positive y ($\phi < \phi_p$, the region behind the planet) while there is a small hole for negative y . This asymmetric corotational temperature structure affects the corotation torque.

Note that in this case the planetary envelope is unstable to convection according to Eq. (5.17): the heat generated in the accretion process can not be transported to the surface of the Hill sphere by radiation alone. Although Eq. (5.17) is of limited applicability because of the assumption that the local pressure scale height is the same as for the total disk, we can identify heat transport by fluid motion in the equatorial plane of the disk. The top left panel of Fig. 5.15 shows that the outflow velocity pattern is changed with respect to the non-accreting model: it seems that heat flows preferentially into the outer disk. However, it should be stressed that this observed asymmetry may be caused by insufficient resolution at the very center of the planetary envelope. Nevertheless, these hot outflows cause significant changes in the temperature and density distribution in the immediate surroundings of the planet and are therefore potentially important for the migration behavior of the planet. The details of the accretion process should therefore be subject of further study.

Also from Fig. 5.15 we see that the convective flow is confined to the midplane of the disk: vertical velocities in the top right and bottom left panel are all directed towards the planet. This shows that the vertical thickness of the hot bubble surrounding the planet is due to radiative heat diffusion. Its vertical extension is roughly the size of the Hill sphere of the planet.

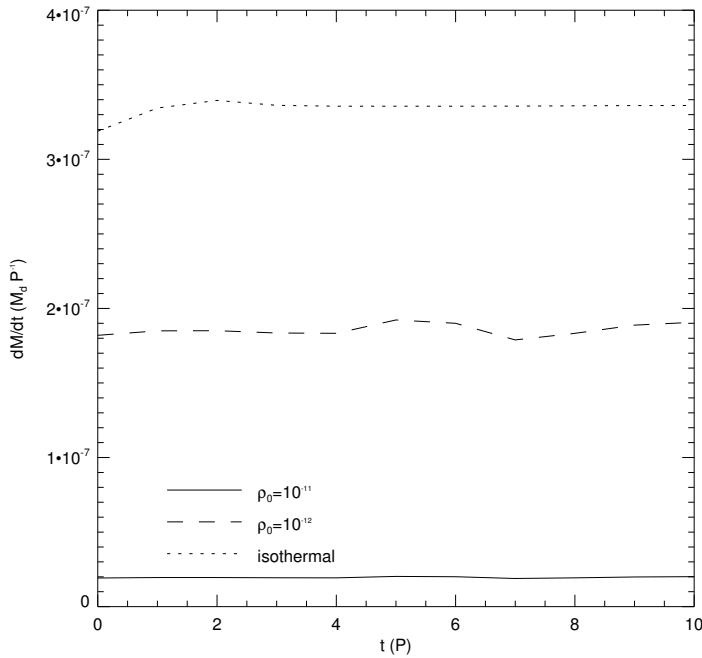


Figure 5.16: Accretion rates onto a $5 M_{\oplus}$ planet for radiation-hydrodynamical models with two different densities. For comparison, the isothermal accretion rate is also shown.

The formation of the hot bubble has dramatic consequences for the measured accretion rate onto the planet. In Fig. 5.16 we show the accretion rate as a function of time for the isothermal case (dotted line) and two radiation-hydrodynamical models with two different initial values for the density at the location of the planet. The solid line indicates an initial density of $\rho_0 = 10^{-11} \text{ g cm}^{-3}$ which is our nominal value. For this density we measure an accretion rate that is more than an order of magnitude lower than for the locally isothermal equation of state. The hot bubble surrounding the planet severely limits the gas flow towards the planet. Because this bubble is created by the accretion process itself, accretion is a self-limited process in this case.

For a lower density the cooling efficiency increases. In fact, according to Eq. (5.10) the cooling time is proportional to the square of the density. For a model with a ten times lower density (dashed line in Fig. 5.16) we measure an accretion rate that is almost ten times higher than for our nominal model. This accretion rate is comparable to the results for nearly-isothermal models (see Fig. 5.10). Lowering the density even more did not change the accretion rate significantly. This also agrees with the nearly-isothermal models, where we saw that even for Γ as low as 1.005 the accretion rate remained far from the isothermal result. This can be understood in terms of the high central density required to achieve the isothermal accretion rate. From Fig. 5.2 we see that the central density is more than a factor 37 higher than the initial density. It is very hard to cool such a high-density envelope efficiently, especially when accretion-generated heat is considered as well.

In Fig. 5.17 we show the growth time scales for the isothermal results (see also Fig. 5.6) with the radiation-hydrodynamical results added as open triangles. The changes with respect to the isothermal models are not as dramatic as the changes from moving from 2D simulations to 3D simulations, but still it represents another order of magni-

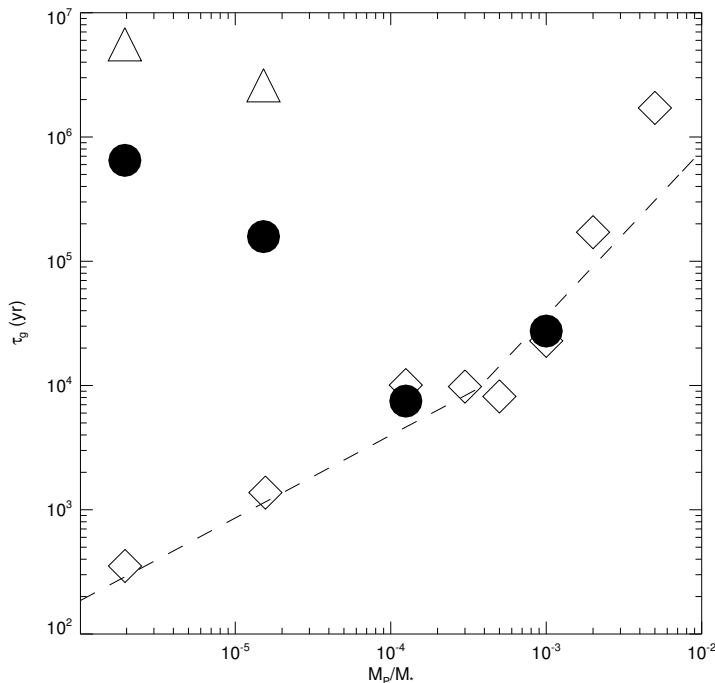


Figure 5.17: Same as the right panel of Fig. 5.6, with the radiation-hydrodynamical results (with our nominal initial density of $\rho_0 = 10^{-11} \text{ g cm}^{-3}$) included as open triangles.

tude slower accretion. Also from Fig. 5.17 we see that the effect is slightly less strong for a planet of $0.5 M_{\oplus}$. This is because the potential for this planet is less deep, but the decrease in accretion rate is still significant even for this very small planet.

We now turn to the question of planetary migration within the radiation hydrodynamical models. From the nearly-isothermal models we know that even the migration direction is very sensitive to temperature variations, and we expect that because for our nominal density cooling is not efficient we should recover at least some of the features of the nearly-isothermal models.

In Fig. 5.18 we show the total torque acting on the planet as a function of time, for three different radiation-hydrodynamical models. All torques reach a constant value within 10 dynamical time scales, even though the cooling time for the high-density case is somewhat longer. We checked that the torques did not change over several cooling times. Again, as was the case for the nearly-isothermal models, the torque needs some more time to reach a steady value than in the isothermal case.

For our nominal, non-accreting model we observe that the total torque is again positive, indicating outward migration. Its magnitude is comparable to the ordinary Type I torque as calculated by Tanaka et al. (2002), and this is much lower than the magnitude of the torque in the accreting, nearly isothermal models. It turns out that this is due to the accretion flow. Indeed, for our accreting radiation-hydrodynamical model (dashed line in Fig. 5.18) the magnitude of the torque increases by a factor of 3 compared to the non-accreting case. It is the asymmetric, hot outflow that is responsible for a large part of the positive torque in the accreting model. Radiative heat diffusion tends to lower the magnitude of the torque, because the flow is spread out more evenly around the planet. This effect is not strong, however.

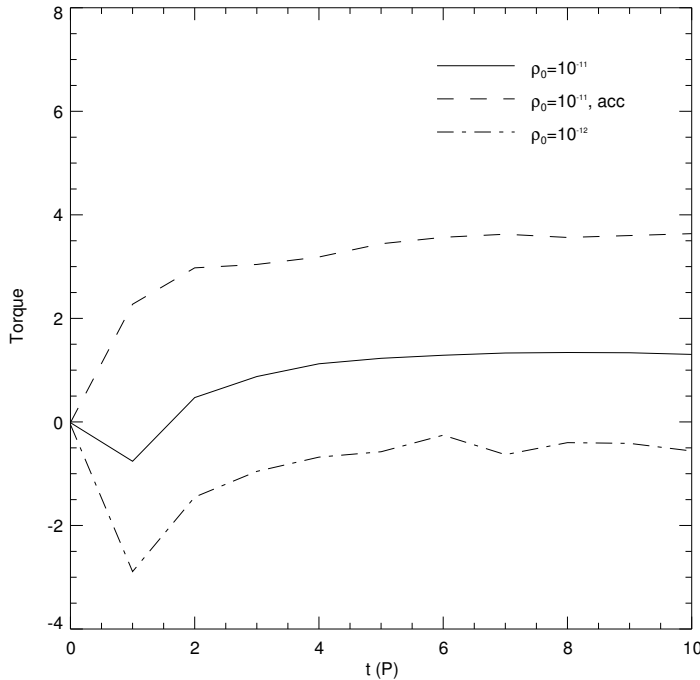


Figure 5.18: Total torque onto a $5 M_{\oplus}$ planet for three different radiation hydrodynamical models. The torques are normalized to the absolute value of the analytical result of Tanaka et al. (2002).

When we lower the density the magnitude of the torque decreases until at some point it becomes negative. This is because the cooling time decreases with decreasing density, and therefore the disk is more and more able to cool towards its initial temperature. From Fig. 5.18 we see that for a 10 times lower density the total torque is negative, with a magnitude that is approximately a factor 2 lower than the analytical Type I torque from Tanaka et al. (2002). As we reduce the density even more the torque approaches the analytical result even more, but the scatter around the equilibrium value increases. This is due to the fact that for such densities the disk becomes very optically thin, which makes the problem less well suited to treat in the diffusion approximation.

For accreting models, we do not reach the Type I result, however. The results on accretion indicated already that even for very low densities there is still a very hot bubble formed around the planet, and the subsequent hot outflow comes to dominate the torque, which we found to remain positive even for the case of a 10 times lower density. This is again an indication that accretion and migration of embedded planets are closely linked. In order to make progress, the detailed process of accretion requires further study.

Nevertheless, even for our non-accreting model we find a torque that is positive, which means that the hot accretion flow is not the whole story. It is interesting to see where in the disk this positive torque arises. In Fig. 5.19 we show the torque on the planet as a function of radius. The low-density case (dash-dotted line), giving rise to a negative torque in Fig. 5.18, agrees very well with the isothermal model (see Fig. 5.12). For our nominal density (indicated by the dashed line in Fig. 5.19) we see that the magnitudes of the torques due to the inner and the outer spiral wave are lower

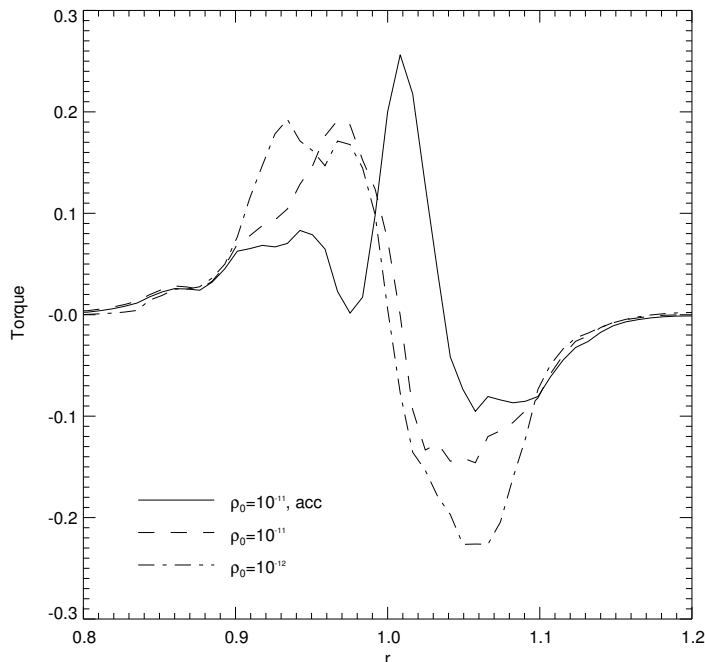


Figure 5.19: Radial torque profile for a $5 M_{\oplus}$ planet for three different radiation-hydrodynamical models. The torques are normalized in such a way that the total torque for an isothermal equation of state is equal to -1 .

than for the low-density case. This is due to compressional heating in the waves, as can be seen in the top left panel of Fig. 5.14. Because of the higher temperature, the same pressure distribution as in the isothermal case requires the density to be lower in the waves, and therefore the torque is less strong.

However, it turns out that the total torque due to the spiral waves is still negative. This means that it is the corotation region that determines the sign of the torque and therefore the direction of migration. In the next section, we will further specify where and how this torque arises using local, adiabatic simulations.

Before we do that, we take a brief look at the accreting radiation-hydrodynamical model in Fig. 5.19. The whole numerical set-up was the same as for our nominal density model in Fig. 5.19, only now accretion was turned on. All differences between the solid line and the dashed line in Fig. 5.19 arise from the accretion process. Note that the sphere of influence of the accretion flow has a radius of approximately $0.1 r_p$, or $2 H$. The outflow of energy released by accretion heats the spiral waves even more, and consequently the torques decrease in magnitude. On top of that, the asymmetric hot bubble seen in Fig. 5.15 itself exerts a large positive torque onto the planet, which can be identified as the large peak in the torque around $r = 1$ in Fig. 5.19. This peak is less strong than in the nearly-isothermal case (see Fig. 5.12) because the heat generated by accretion is diffused by radiation over a much larger volume.

5.7.4 Local, adiabatic models

In this section we take a step back and look at local, adiabatic simulations. That is, we keep $\Gamma = 1.4$ but we switch off the radiative transport, and we further reduce the com-

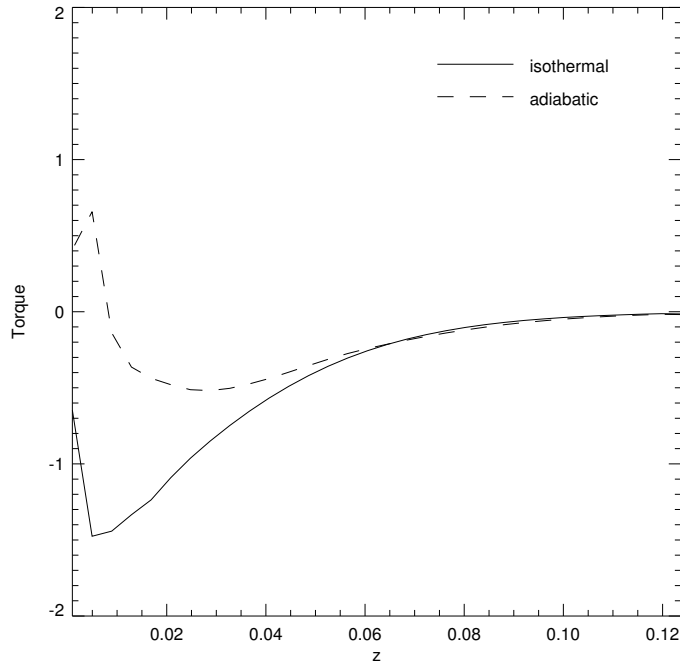


Figure 5.20: Vertical torque profile for a $5 M_{\oplus}$ planet for a local isothermal model (solid line) and a local adiabatic model (dashed line).

putational effort by simulating only a small part of the disk of 5 initial pressure scale heights around the planet. This volume is large enough to capture the basic features of the flow, because the effects of the low-mass planets we consider on the disk remain fairly local. We made sure that the global resolution in these local models matches the highest local resolution of the previously described models.

In these simplified simulations the gas is still heated by compression and gravitational effects, while radiative cooling is absent. This way, these simulations would apply to a very dense region where the cooling time scale is much larger than the dynamical time scale everywhere, also in the upper layers of the disk. Although unrealistic for real protoplanetary disks, these simulations allow us to pin down where the positive torque in a non-accreting model arises while not being hindered by the cooling effects of radiation. These cooling effects will partially wash out the effects of compression, and while the total torque is still positive, its origin is much harder to find.

From Fig. 5.19 we concluded that the largest contribution to the positive torque comes from the corotation region. In Fig. 5.20, we show the torque as a function of distance to the midplane for an isothermal local model and an adiabatic local model. For the isothermal model, we see that the torque is negative throughout the simulated part of the disk. Because this is a local simulation, the total torque may not be the Type I torque because we exclude all material that is farther than $5 H$ from the planet. However, for now we are only interested in the differences between the isothermal and the adiabatic models. It is clear that both models agree on the torque for material that is higher than approximately one pressure scale height from the midplane. Closer to the midplane, the adiabatic torque becomes less and negative until it finally reaches positive values around a height of approximately $z = 0.01 r_p$ from the midplane. As

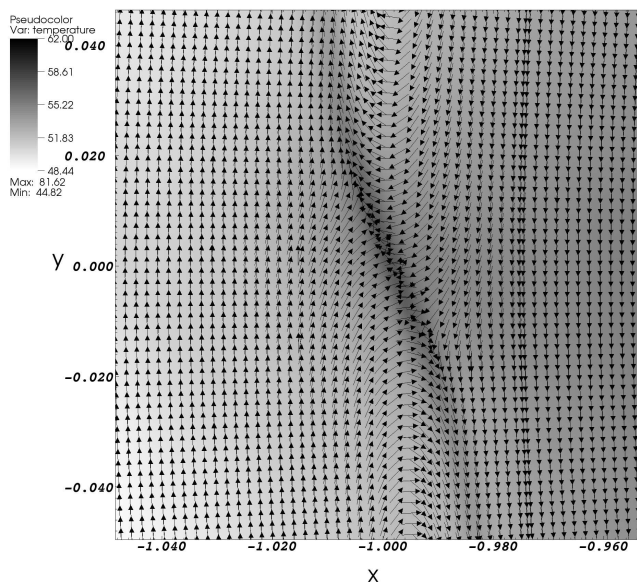


Figure 5.21: Temperature and velocity around a $5 M_{\oplus}$ planet after 5 orbits for a local, adiabatic model. Shown is a slice through $z = 0.02 r_p$.

was mentioned before, the Hill sphere of this $5 M_{\oplus}$ planet is approximately $0.017 r_p$ large, so the heating effects on the torque start well outside the Hill sphere of the planet.

In Fig. 5.21 we show the temperature structure at a distance of $0.02 r_p$ from the midplane of the disk. This is just outside the Hill sphere of the planet, but from Fig. 5.20 we see that at this height the effects of inefficient cooling are clearly present. In Fig. 5.21 we see that the disk is heated at the corotation radius, where the largest part of the positive torque is generated.

The velocity vectors in Fig. 5.21 show the familiar horseshoe orbits that were also seen in Fig. 5.4. We see that the heating of the disk occurs where the horseshoe streamlines clash into each other and the gas is subsequently compressed. Part of this heat is advected along the separatrix which marks the edge of the horseshoe region. It is this heating that causes the large positive torque on the planet because it is not symmetric with respect to the planet.

This is illustrated in Fig. 5.22, where we show a slice through $r = r_p$. The two warm gas columns stretching out in the vertical direction are due to the horseshoe-heating. The planetary envelope is heated as well, and we see that the equatorial outflow is able to cool the gas substantially by expansion. It is immediately clear that the two vertical warm gas columns do not reside at $y = 0$ (or, equivalently, $\phi = \pi$). Instead, due to the slightly sub-Keplerian orbital velocity of the gas they are located *behind* the planet. Inside these warm columns the density is lower and therefore the negative torque due to this material decreases in magnitude. From Fig. 5.22 we see that this heating occurs through the whole vertical extent of the disk between $z = -H$ and $z = H$. From Fig. 5.20 we see that around $|z| = 0.01 r_p$ this effect is large enough to change the sign of the torque. However, because this occurs within the Hill sphere of the planet it is

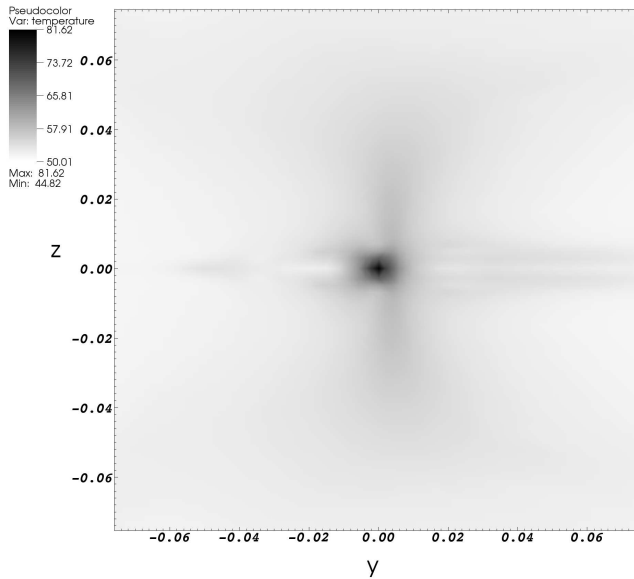


Figure 5.22: Temperature structure around a $5 M_{\oplus}$ planet after 5 orbits for a local, adiabatic model. Shown is a slice through $r = r_p$.

much more difficult to visualize at $|z| = 0.01 r_p$ than it was for Fig. 5.21 because of the additional heating of gas within the Hill sphere.

5.8 DISCUSSION

Our results on gas accretion onto low-mass protoplanets suggest that mass flow into the Hill sphere depends critically on the temperature profile of the planetary envelope. In isothermal simulations, pressure gradients correspond to density gradients alone, and therefore a pressure-supported isothermal envelope will have a very high central density. This leads to the relatively high accretion rates in isothermal models. When the energy balance is taken into account, part of the pressure gradient that is needed to sustain the envelope is carried by a gradient in temperature and therefore the corresponding density profile will be less peaked, and therefore the measured accretion rate will go down. Moreover, the energy released in the accretion process raises the central temperature even further, slowing down the mass flow even more. This way, accretion is a self-limiting process, and the subsequent accretion rate is more than an order of magnitude below the isothermal result.

Because the release of accretion energy plays such a significant role in accretion, migration and observations of protoplanetary envelopes (Klahr & Kley 2006) it is important to consider the validity of this accretion recipe. Although at first sight it seems a good idea to conserve total energy and momentum during accretion, it is not entirely clear if this is indeed the case. The momentum carried by the accreted matter, for example, might be transferred to the planet itself, which may induce rotation of the

protoplanetary core.

As an example for an alternative to energy-conserving accretion, consider an accretion recipe that conserves entropy. Because at constant entropy the pressure is related to the density as:

$$p = K \rho^\Gamma, \quad (5.48)$$

we can, using the ideal gas law, immediately write down that

$$T = C \rho^{\Gamma-1}, \quad (5.49)$$

for some constant C . This means that taking away mass from the grid actually *cools* the accretion region. In this case the assumption is that the accretion energy is transferred to the planetary core. Note that in using an isothermal equation of state, taking away mass from the grid amounts to conservation of entropy as well. Because accretion plays such a major role in non-isothermal planet-disk interaction, obviously in the growth of the planet but also in the migration behavior, more work on the details of the accretion process is necessary.

But even for non-accreting planet, a hydrostatic envelope is never reached (see also D'Angelo et al. 2003b). Mass constantly flows in and out of the Roche lobe, and it is not yet clear what role these outflows play in planet-disk interaction. In our simulations we have found that the outflow is predominantly equatorial, irrespective of whether the planet is accreting mass or not. The depth of the potential well does influence the outflow, however, because it is driven by the high pressure region at the location of the planet. We found that this outflow did not alter the torque balance in the isothermal limit, but because the gas expands rapidly inside the outflow it affects the temperature in the midplane and it may therefore be of importance in non-isothermal disks.

The most interesting result from this study is the observed reversal of migration direction with respect to isothermal disks. We have tried to isolate the origin of the positive torque arising in adiabatic simulations, and we have found that gas heating in the region where the horseshoe orbits make their U-turn is the dominant effect. We have interpreted the asymmetry of the horseshoe region to be due to the sub-Keplerian velocity of the gas. It is also present in isothermal simulations, for accreting as well as for non-accreting planets. Though the topology of the horseshoe-region is very sensitive to pressure gradients near the U-turn, the pressure gradients induced by the planetary envelope does not seem to play an important role. For a full discussion on the dependence of the corotation torque on disk properties see Masset (2001, 2002).

Corotation torques tend to saturate when the viscous diffusion time scale across the librating region is longer than the libration time scale (Ogilvie & Lubow 2003). In our inviscid models, saturation should occur, but a much larger time range is needed to see the effect. The computational costs of radiation-hydrodynamical simulations are too large to achieve this, however. Global adiabatic models may provide more insight in this matter.

In our models where we solve the energy equation we have focused on a $5 M_\oplus$ planet. One run involved a $0.5 M_\oplus$ accreting planet that also moved outward, but more study is necessary to establish the trend. The width of the horseshoe region decreases for lower planetary masses, and therefore also the compression in the region where

the horseshoe orbits meet. For a certain planetary mass, the Lindblad torques will take over again, forcing inward migration, albeit at reduced rate due to the compression of the spiral density waves. Moving towards higher-mass planets the corotation torque will increase, but as long as we stay in the linear regime so will the Lindblad torques, and until we establish the scaling of the positive corotation torque with planetary mass it is not clear what the total torque will do.

When the planet gets massive enough to substantially change the density in its direct environment, the situation changes. Due to the lower density near the orbit of the planet the positive corotation torques decrease in strength because the cooling efficiency increases. Note that the cooling time is proportional to the density squared as long as the disk remains optically thick. Therefore the outward migration induced by corotational heating will quickly lose strength when the planet opens up a gap. For gap-opening planets, this mechanism does not operate because the disk near the planet can cool efficiently (density reductions of two orders of magnitude were measured in 2D simulations).

This new migration behavior of low-mass planets raises a few interesting issues. First of all, because the direction of migration depends on the density, there exists a certain radius R_0 with density $\rho(R_0)$ where the total torque is zero. Inside R_0 , cooling is not efficient and planets move outward. Outside R_0 , planets move inward through ordinary Type I migration. Therefore all low-mass planets near R_0 in the disk will slowly approach R_0 . In a simple power-law disk there is only one R_0 , which, in the Minimum Mass Solar Nebula is located around 10-15 AU. When the density structure becomes more complicated (for example due to the presence of a gap-opening planet) there may be several locations in the disk where the total torque is zero.

As the low-mass planets approach R_0 , planet-planet interactions will eventually come to dominate. When this happens depends on the magnitude of the torque in that region. Interesting effects were observed for differentially migrating low-mass planets by Cresswell & Nelson (2006). The planets may lock into mean-motion resonances or be scattered out of the system.

As the disk evolves it slowly loses mass. Therefore, in a simple power-law disk, R_0 will shift inwards slowly. Once a planet has reached R_0 either by outward or inward migration, it will slowly migrate inward due to the dispersal of the disk. Therefore the migration time scale for low-mass planets becomes directly coupled to the disk life time. While in the isothermal Type I migration scenario migration may proceed on any time scale depending on the disk mass, when the energy budget is taken into account this is no longer the case. Low-mass planet migration will proceed at time scales comparable to the disk life time, which is equal to the viscous time scale of Type II migration. Therefore, this scenario of corotational heating provides a solution to the problem of fast-migrating cores.

In using Eq. (5.1) in calculating the cooling time we have assumed that the planet resides beyond the snow line. Interesting things may happen in regions where the opacity suddenly changes, as was pointed out by Menou & Goodman (2004). Also, grain growth affects the opacity to a great extent. A disk in which all particles have grown to cm-size will be optically thin, and therefore the mechanism of corotational

heating will not apply. However, such efficient growth of particles is not consistent with observations of protoplanetary disks (Dullemond & Dominik 2005) and therefore some sort of replenishment of small grains is needed.

Another important effect that will have to be included is irradiation from the central star. Although the disk is not severely perturbed by the low-mass planets considered in this Chapter, it is desirable to treat the heating of the disk in a self-consistent way. However, detailed models including irradiation from the central source are computationally very expensive and therefore hard to implement in a dynamical model.

5.9 SUMMARY AND CONCLUSIONS

In this Chapter we have presented the first global radiation-hydrodynamical simulations of the interaction between low-mass planets and protoplanetary disks. Specifically, we looked at accretion and migration rates in the mass regime of linear disk response.

We have found that accretion and migration rates depend sensitively on the ability of the disk to radiate away energy generated by compression in the various flow regions around the planet. Compression deep within the planetary envelope leads to a decrease in accretion rate onto the planet of more than an order of magnitude. Compression within the tidal waves generated by the planet leads to a decreased Lindblad torque, which makes the planet move inward but at a slower rate than predicted by analytical models for isothermal Type I migration. Compression in the horseshoe region, finally, leads to a large positive corotation torque that is able to change the direction of migration.

All these effects depend critically on the cooling properties of the disk. For a density appropriate for the Minimum Mass Solar Nebula at 5 AU we find outward migration, while a ten times lower density gives rise to inward migration. Lowering the density even more we are able to reproduce the analytical Type I torque. This means that inward Type I migration is restricted to the outer parts of protoplanetary disks, or to older disks that have a lower density.

Because low-mass planet migration is driven by the decrease of density in the disk, it proceeds on the viscous time scale, just as Type II migration for gap-opening planets. This means that corotational heating is able to solve the problem of protoplanetary cores that move inward too fast to form giant planets. All planets within the region where the cooling time scale is much larger than the dynamical time scale will experience outward migration.

Future studies should be aimed at finding the most appropriate recipe to simulate gas accretion onto the planet, and at including irradiation from the central star.

ACKNOWLEDGMENTS

SP thanks Yuri Levin, Mordecai-Marc MacLow and Peter Woitke for useful discussions. We thank Willem Vermin for his assistance at the Dutch National Supercomputer. This

work was sponsored by the National Computing Foundation (NCF) for the use of supercomputer facilities, with financial support from the Netherlands Organization for Scientific Research (NWO).

REFERENCES

- Artymowicz, P. 1993, *ApJ*, 419, 166
- Artymowicz, P. 2004, in *ASP Conf. Ser. 324: Debris Disks and the Formation of Planets*, 39
- Balbus, S. A. & Hawley, J. F. 1990, *BAAS*, 22, 1209
- Barrett, R., Berry, M., Chan, T. F., et al. 1994, *Templates for the Solution of Linear Systems: Building Blocks for Iterative Methods* (Philadelphia, PA: SIAM)
- Bate, M. R., Lubow, S. H., Ogilvie, G. I., & Miller, K. A. 2003, *MNRAS*, 341, 213
- Beckwith, S. V. W. & Sargent, A. I. 1996, *Nature*, 383, 139
- Bell, K. R. & Lin, D. N. C. 1994, *ApJ*, 427, 987
- Cresswell, P. & Nelson, R. P. 2006, *A&A*, 450, 833
- D'Angelo, G., Bate, M. R., & Lubow, S. H. 2005, *MNRAS*, 358, 316
- D'Angelo, G., Henning, T., & Kley, W. 2002, *A&A*, 385, 647
- D'Angelo, G., Henning, T., & Kley, W. 2003a, *ApJ*, 599, 548
- D'Angelo, G., Kley, W., & Henning, T. 2003b, *ApJ*, 586, 540
- Dullemond, C. P. 2000, *A&A*, 361, L17
- Dullemond, C. P. & Dominik, C. 2005, *A&A*, 434, 971
- Dullemond, C. P., Dominik, C., & Natta, A. 2001, *ApJ*, 560, 957
- Eulderink, F. & Mellema, G. 1995, *A&AS*, 110, 587
- Goldreich, P. & Sari, R. 2003, *ApJ*, 585, 1024
- Goldreich, P. & Tremaine, S. 1980, *ApJ*, 241, 425
- Hayes, J. C. & Norman, M. L. 2003, *ApJS*, 147, 197
- Jang-Condell, H. & Sasselov, D. D. 2003, *ApJ*, 593, 1116
- Jang-Condell, H. & Sasselov, D. D. 2004, *ApJ*, 608, 497
- Jang-Condell, H. & Sasselov, D. D. 2005, *ApJ*, 619, 1123
- Klahr, H. & Kley, W. 2006, *A&A*, 445, 747
- Kley, W. 1989, *A&A*, 208, 98
- Kley, W. 1998, *A&A*, 338, L37
- Kley, W. 1999, *MNRAS*, 303, 696
- Kley, W. & Dirksen, G. 2006, *A&A*, 447, 369
- Levermore, C. D. & Pomraning, G. C. 1981, *ApJ*, 248, 321
- Lubow, S. H., Seibert, M., & Artymowicz, P. 1999, *ApJ*, 526, 1001
- Masset, F. S. 2001, *ApJ*, 558, 453

- Masset, F. S. 2002, *A&A*, 387, 605
- Masset, F. S. & Papaloizou, J. C. B. 2003, *ApJ*, 588, 494
- Mellema, G., Eulderink, F., & Icke, V. 1991, *A&A*, 252, 718
- Menou, K. & Goodman, J. 2004, *ApJ*, 606, 520
- Morohoshi, K. & Tanaka, H. 2003, *MNRAS*, 346, 915
- Nelson, A. F. & Benz, W. 2003a, *ApJ*, 589, 556
- Nelson, A. F. & Benz, W. 2003b, *ApJ*, 589, 578
- Nelson, R. P. & Papaloizou, J. C. B. 2004, *MNRAS*, 350, 849
- Ogilvie, G. I. & Lubow, S. H. 2003, *ApJ*, 587, 398
- Paardekooper, S.-J. & Mellema, G. 2006, *A&A*, 450, 1203
- Papaloizou, J. C. B., Nelson, R. P., & Masset, F. 2001, *A&A*, 366, 263
- Papaloizou, J. C. B. & Terquem, C. 1999, *ApJ*, 521, 823
- Pollack, J. B., Hubickyj, O., Bodenheimer, P., et al. 1996, *Icarus*, 124, 62
- Roe, P. L. 1981, *J. Comp. Phys*, 43, 357
- Sari, R. & Goldreich, P. 2004, *ApJ*, 606, L77
- Shakura, N. I. & Sunyaev, R. A. 1973, *A&A*, 24, 337
- Stone, J. M., Mihalas, D., & Norman, M. L. 1992, *ApJS*, 80, 819
- Tanaka, H., Takeuchi, T., & Ward, W. R. 2002, *ApJ*, 565, 1257
- Terquem, C. E. J. M. L. J. 2003, *MNRAS*, 341, 1157
- Ward, W. R. 1997, *Icarus*, 126, 261

CHAPTER 6

Planets opening dust gaps in gas disks

Sijme-Jan Paardekooper and Garrelt Mellema

Astronomy & Astrophysics 2004, 425, L9

Astronomy & Astrophysics 2006, 453, 1129

IN this Chapter we study the dynamics of gas and dust in a protoplanetary disk in the presence of embedded planets. We investigate the conditions for dust-gap formation in terms of particle size and planetary mass. We also monitor the amount of dust that is accreted by the planet relative to the amount of gas, which is an important parameter in determining the enrichment of solids in giant planets compared to the solid content of the central star. We use a new two-fluid hydrodynamics code to solve the flow equations for both gas and dust. For the gas, we use a Godunov-type scheme with an approximate Riemann solver (the Roe solver). The dust is treated as a pressureless fluid by essentially the same numerical method as is used for the gas. We find that it only takes a planet of 0.05 Jupiter masses to open up a gap in a disk with a significant population of mm-sized particles. Dust particles larger than $150 \mu\text{m}$ participate in gap formation. We also find that the formation of the gap severely slows down dust accretion compared to that in the gas. Therefore, it is not possible to enrich a newly formed giant planet in solids, if these solids are contained in particles with sizes from $150 \mu\text{m}$ to approximately 10 cm.

6.1 INTRODUCTION

Dust plays a major role in planet formation, theoretically as well as observationally. First of all, terrestrial planets consist mainly of solid material. They are giant agglomerates of interstellar dust particles, and therefore the behavior of these small particles is important during the first stages of planet formation. Whether they grow to kilometer-sized bodies by slow coagulation or through the gravitational instability of a thin dust layer in the midplane of the disk (Goldreich & Ward 1973) is still an open question. A mixture of equal amounts of gas and dust is subject to streaming instabilities (Youdin & Goodman 2005), and it is not clear whether the resulting turbulent structure will prohibit gravitational instabilities or enhance them (Johansen et al. 2006b). To answer this question, multi-component simulations are needed in which gas and dust are able to evolve separately.

Secondly, giant planets can be formed either by gas accretion onto a solid core (Pollack et al. 1996) or by direct gravitational fragmentation of the disk (Boss 1997). In the core accretion model, dust growth is of critical importance to build up a massive core before the gas disk dissipates. The gravitational instability model does not rely on the existence of such a core, but still, accretion of dust in a later stage will determine the enrichment in solids with respect to the solar nebula, which is an important observational constraint (Guillot et al. 2004).

Finally, dust is the major source of continuum radiation in the disk. Therefore, infra-red and sub-millimeter emissions mainly indicate the density and temperature of the dust disk. The relation of the dust to the density of the gas disk can be quite complicated if the disk has a non-trivial structure, especially if the dust particles are only marginally coupled to the gas.

It is therefore very important to study dust dynamics in gas disks. Axisymmetric disks can be handled analytically, and various authors have studied dust migration in these disks (Weidenschilling 1977; Takeuchi & Lin 2002). Particles move both inward and outward under the influence of gas drag, depending on their distance from the midplane, but the average migration is inward (Takeuchi & Lin 2002). Haghhighipour & Boss (2003) studied dust migration in a non-uniform axisymmetric nebula, and Takeuchi & Artymowicz (2001) investigated the effect of a sharp disk edge on dust migration. The overall conclusion is that the structure of the gas disk can have a significant effect on the dust distribution, and that the distribution of gas and dust can differ substantially.

When the gas distribution becomes more complicated, one has to rely on numerical simulations. Suttner & Yorke (2001) studied dust evolution during the initial collapse of the nebula with a two-dimensional multi-fluid hydrodynamics code to obtain the large-scale dust distribution. Johansen & Klahr (2005) studied the effect of MHD turbulence on the dust distribution. These multi-fluid calculations are computationally very expensive, requiring more than twice the computing time for ordinary gas-dynamical simulations, even if one solves for only a single dust particle size.

To compare dust observations with gas-dynamical simulations, but at the same time avoid the large computational effort of these multi-fluid calculations, one can assume a fixed dust-to-gas ratio and solve only for the gas dynamics only. The effects

of an embedded planet on a gaseous disk have been studied numerically before by multiple authors (e.g. Kley 1999; Nelson et al. 2000; Lubow et al. 1999; D'Angelo et al. 2002). Wolf et al. (2002) used these results to simulate observations of gaps in protoplanetary disks. Their calculations are valid only for the smallest particles that couple extremely well to the gas.

However, in a protoplanetary disk where grain growth is very important (see, for example, Dullemond & Dominik 2005), a significant fraction of the dust population is large enough to be only marginally coupled to the gas. Paardekooper & Mellema (2004) showed that including the full gas and dust dynamics leads to a dramatic evolution of the dust component in the disk. Planets not massive enough to open up a gap in the gas disk do so in the dust disk, which should make the orbit of even $0.05 M_J$ planets visible to ALMA (the Atacama Large Millimeter Array).

In this Chapter we study dust flow in gas disks around embedded planets, with more attention to detail than in Paardekooper & Mellema (2004). In Sect. 6.2, we review the equations governing dust flow and gas-dust interaction. Section 6.3 is devoted to the numerical method, and we discuss the initial and boundary conditions in Sect. 6.4. In Sect. 6.5, we present the results. Section 6.6 is reserved for a short discussion, and we conclude in Sect. 6.7.

6.2 BASIC EQUATIONS

Protoplanetary disks are fairly thin, i.e. the vertical thickness H is small compared with the distance r from the center of the disk. Typically we use $H/r = h = 0.05$. It is therefore convenient to average the equations of motion vertically and to work with vertically averaged quantities only.

The governing equations are then solved in a cylindrical coordinate frame (r, ϕ) , centered on the central star and corotating with the embedded planet that has a Keplerian angular velocity Ω .

6.2.1 Gas

The equations that control the gas evolution are described in detail in Paardekooper & Mellema (2006). We do not solve the energy equation, but instead use an isothermal equation of state:

$$P = c_s^2 \Sigma_g, \quad (6.1)$$

where Σ_g is the surface density of the gas and P is the vertically averaged pressure.

The isothermal sound speed c_s is, in hydrostatic equilibrium, directly related to the disk thickness:

$$c_s = h v_K, \quad (6.2)$$

where v_K is the Keplerian velocity.

We use a constant kinematic viscosity ν , which is set by assuming an α -parameter (Shakura & Sunyaev 1973) of 0.004 at the location of the planet:

$$\nu = \alpha c_s H|_{r=1}. \quad (6.3)$$

6.2.2 Dust

We treat the dust as a pressureless fluid; its evolution is governed by conservation of mass and, in absence of external sources, conservation of radial and angular momentum. These can be written in the following compact form:

$$\frac{\partial \mathbf{W}}{\partial t} + \frac{\partial \mathbf{F}}{\partial r} + \frac{\partial \mathbf{G}}{\partial \phi} = \mathbf{S}, \quad (6.4)$$

where \mathbf{W} is called the state vector and where \mathbf{F} and \mathbf{G} are the fluxes in the radial and azimuthal direction, respectively. \mathbf{S} is called the source term.

The components of the state, fluxes, and source-term vectors can be written in the following form:

$$\mathbf{W} = r(\Sigma, \Sigma v_r, \Sigma v_\phi) \quad (6.5)$$

$$\mathbf{F} = r(\Sigma v_r, \Sigma v_r^2, \Sigma v_r v_\phi) \quad (6.6)$$

$$\mathbf{G} = r(\Sigma v_\phi, \Sigma v_r v_\phi, \Sigma v_\phi^2) \quad (6.7)$$

$$\mathbf{S} = \begin{pmatrix} 0 \\ \Sigma r^2 (v_\phi + \Omega)^2 - \Sigma r \frac{\partial \Phi}{\partial r} + r f_{d,r} \\ -2\Sigma v_r (\Omega + v_\phi) - \frac{\Sigma}{r} \frac{\partial \Phi}{\partial \phi} + r f_{d,\phi} \end{pmatrix}. \quad (6.8)$$

Here, Σ denotes the dust surface density, v_r and v_ϕ the radial and angular velocity, respectively, Ω the angular velocity of the coordinate frame (corotating with the planet), and Φ the gravitational potential of the central star and the planet. The gravitational potential of the planet is softened over a fraction 0.2 of the Roche lobe of the planet. The potential also contains terms due to the non-inertial nature of the coordinate system. The drag forces are incorporated through $f_{d,r}$ and $f_{d,\phi}$.

The major difference between the equations for the gas and the dust is the absence of pressure in the latter. In this sense, the dust fluid behaves like a gas that is always moving with supersonic velocity. This implies that near shock waves, where the gas goes from sonic to supersonic flow and where large density and velocity gradients are present, dust and gas behave in very different ways.

The basic building block for Godunov-type hydrodynamic solvers is the Riemann problem, consisting of two stationary states separated by a discontinuity. If we consider the two states as belonging to neighboring grid cells, with the discontinuity at the interface between the cells, the analytic solution of the Riemann problem can be used to define an interface flux between the cells. Popular schemes of this type are the Piecewise Parabolic Method (PPM, Woodward & Colella 1984) and the Roe solver (Roe 1981).

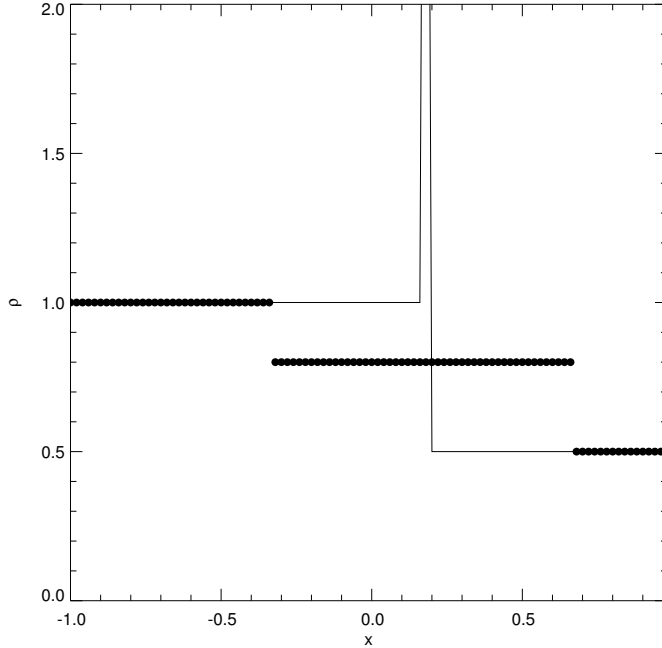


Figure 6.1: Solution to the Riemann problem with initial conditions $\rho_L = 1.0$, $\rho_R = 0.5$, $u_L = 0.5$, and $u_R = 0.25$. The solid line represents the dust density and the dots represent the gas density, both at $t = 0.5$. For the gas, the speed of sound was set to 1.0.

For pressureless fluids, the solution to the Riemann problem differs significantly from the case with pressure. Figure 6.1 shows the analytic solutions for the gas (dots) as well as the dust density (solid line), with initial conditions $\rho_L = 1.0$, $\rho_R = 0.5$, $u_L = 0.5$, and $u_R = 0.25$. The gas solution consists of two waves moving at speeds $\hat{u} - c_s$ and $\hat{u} + c_s$, where

$$\hat{u} = \frac{\sqrt{\rho_L} u_L + \sqrt{\rho_R} u_R}{\sqrt{\rho_L} + \sqrt{\rho_R}}. \quad (6.9)$$

If we now let $c_s \rightarrow 0$ to obtain a pressureless fluid, the separation between the waves becomes smaller and smaller, until they overlap at $c_s = 0$. The overlapping waves create a delta-function singularity that moves with velocity \hat{u} (e.g. Leveque 2004). The singularity arises because Eq. (6.4) is only *weakly* hyperbolic, in contrast with the gas hydrodynamical equations, which are *strictly* hyperbolic.

Figure 6.1 deals with the case $u_L > u_R$. When $u_L < u_R$, the solution consists of the two states moving away from each other with a vacuum in between. Note that for both cases, the flux is well defined everywhere but at the position of the delta function.

The solution to the Riemann problem not only forms the basis for our numerical method (see Sect. 6.3), but from Fig. 6.1 it is also clear that gas and dust react very differently to *physical* shocks, which may lead to gas-dust separation when shock waves are present in the computational domain.

6.2.3 Gas-dust interaction

The interaction between the gas fluid and the dust fluid occurs only through the drag forces. The nature of the drag force depends on the size of the particles with respect

to the mean free path of the gas molecules. We consider only spherical particles with radius s . Because the main constituent of the gas is molecular hydrogen, for the mean free path we can write:

$$\lambda = \frac{m_{\text{H}_2}}{\pi \rho_{\text{g}} r_{\text{H}_2}^2}. \quad (6.10)$$

When the particle size is small, compared to λ , we are in the Epstein regime, whereas $s \gg \lambda$ corresponds to the Stokes regime. For particles that move subsonically through the gas, the transition occurs around $\lambda/s = 4/9$. For typical midplane densities, particles larger than approximately 50 cm move in the Stokes regime. In this Chapter we will focus on particles smaller than ~ 1 cm, and therefore we can safely use the Epstein drag law.

In the Epstein regime, when the relative velocity of gas and dust is much smaller than the local sound speed, the drag force is written as:

$$\mathbf{f}_{\text{d}} = -\Sigma \frac{\Omega_{\text{K}}}{T_{\text{s}}} \Delta \mathbf{v}, \quad (6.11)$$

where Ω_{K} is the Keplerian angular velocity, $\Delta \mathbf{v}$ is the velocity difference between gas and dust, and T_{s} is the dimensionless stopping time (Takeuchi & Lin 2002):

$$T_{\text{s}} = \sqrt{\frac{\pi}{8}} \frac{\rho_{\text{p}} s v_{\text{K}}}{\rho_{\text{g}} r c_{\text{s}}}. \quad (6.12)$$

Here, ρ_{p} is the particle internal density, s is the radius of the particle, and c_{s} is the sound speed. We have used $\rho_{\text{p}} = 1.25 \text{ g cm}^{-3}$, and the isothermal sound speed is given by Eq. (6.2). The gas density ρ_{g} is found by using $\rho_{\text{g}} = \Sigma_{\text{g}}/2H$.

For particles that move very supersonically through the gas, the drag force becomes:

$$\mathbf{f}_{\text{d}} = -\Sigma \frac{3}{4} \sqrt{\frac{\pi}{8}} \frac{\Omega_{\text{K}}}{T_{\text{s}}} \frac{|\Delta \mathbf{v}|}{c_{\text{s}}} \Delta \mathbf{v}. \quad (6.13)$$

A standard way to connect the supersonic to the subsonic regime is (Kwok 1975):

$$\mathbf{f}_{\text{d}} = -\Sigma \frac{\Omega_{\text{K}}}{T_{\text{s}}} \sqrt{1 + \frac{9\pi}{128} \frac{|\Delta \mathbf{v}|^2}{c_{\text{s}}^2}} \Delta \mathbf{v}. \quad (6.14)$$

See Woitke & Helling (2003) for the general case.

Only very massive planets of approximately $1 M_{\text{J}}$ are able to accelerate the larger particles to velocities that are comparable to the speed of sound. For the low-mass planets considered in Paardekooper & Mellema (2004), the subsonic version of the drag force proved to be sufficient.

Particles with $T_{\text{s}} \ll 1$ are well-coupled to the gas, and the radial drift velocity can be written as (Takeuchi & Lin 2002):

$$v_{r,\text{drift}} = -\eta T_{\text{s}} v_{\text{K}}, \quad (6.15)$$

where η is the ratio of the gas pressure gradient to the stellar gravity in the radial direction:

$$\eta = -h^2 \frac{\partial \log P}{\partial \log r} = h^2 \left(1 - \frac{\partial \log \Sigma_{\text{g}}}{\partial \log r} \right). \quad (6.16)$$

The direction in which the dust moves with respect to the gas is determined by the sign of η , and in general the pressure gradient is negative, making η positive, which leads to an inward migration of the dust particles. However, if there is a large positive density gradient ($\partial \log \Sigma_g / \partial \log r > 1$, see Eq. (6.16)), as there is near the outer edge of a density gap, the dust particles can move outward. On the other hand, if there is an extra large negative density gradient, as is the case near the inner edge of a density gap, the dust moves inward with higher velocity.

Thus, we expect that near the gap edges, the larger particles decouple from the gas, altering the dust-to-gas ratio in that region. Furthermore, the drag forces may not be large enough to prevent gas-dust separation by shocks. Both processes should play a role in the dust dynamics near the embedded planet.

6.3 NUMERICAL METHOD

6.3.1 Gas and dust advection

For the evolution of the gas component, we use the RODEO method described by Paardekooper & Mellema (2006). It is a second-order Eulerian hydrodynamics code, which uses an approximate Riemann solver (Roe 1981). It derives from a general relativistic method (Eulderink & Mellema 1995), and it is especially suitable to treat non-Cartesian, non-inertial coordinate systems. A module for Adaptive Mesh Refinement (AMR) can be used to obtain high resolution near the planet.

For the dust, we use the method outlined in Leveque (2004), which has the advantage of being similar to the method used for the gas. Below, we only consider the radial direction. The azimuthal direction is handled in the same way.

For every cell interface, we consider the Riemann problem defined by a left state \mathbf{W}_L and a right state \mathbf{W}_R with corresponding fluxes. When $v_{r,L} < 0 < v_{r,R}$, the solution to the Riemann problem gives us a vacuum state at the cell interface, so we set the interface flux $\mathbf{F}_{\text{int}} = \mathbf{0}$. Otherwise, we compute the shock speed \hat{v} from Eq. (6.9), and compute the interface flux according to

$$\mathbf{F}_{\text{int}} = \begin{cases} \mathbf{F}_L & \text{if } \hat{v} > 0; \\ (\mathbf{F}_L + \mathbf{F}_R)/2 & \text{if } \hat{v} = 0; \\ \mathbf{F}_R & \text{if } \hat{v} < 0. \end{cases} \quad (6.17)$$

In the first and the last case, the cell interface is respectively left and right of the delta shock, allowing for an easy definition of the interface flux. When $\hat{v} = 0$, however, the delta shock is exactly at the cell interface. We then choose to distribute this shock equally over both cells.

To put this in the language of Paardekooper & Mellema (2006), we write $\mathbf{F} = \mathcal{A}\mathbf{W}$, where the matrix \mathcal{A} is given by:

$$\mathcal{A} = \begin{pmatrix} v_r & 0 & 0 \\ 0 & v_r & 0 \\ 0 & 0 & v_r \end{pmatrix}. \quad (6.18)$$

The eigenvalues of this matrix are:

$$\lambda_1 = \lambda_2 = \lambda_3 = v_r. \quad (6.19)$$

The corresponding eigenvectors read:

$$\begin{aligned} \mathbf{e}_1 &= (1, 0, 0) \\ \mathbf{e}_2 &= (0, 1, 0) \\ \mathbf{e}_3 &= (0, 0, 1). \end{aligned} \quad (6.20)$$

A vector $\mathbf{\Delta} \equiv (\Delta_\rho, \Delta_r, \Delta_\phi)$ can be projected on these eigenvectors using the following projection coefficients, found by solving the system $\mathcal{C}\mathbf{b} = \mathbf{\Delta}$, where \mathcal{C} is the matrix with the eigenvectors:

$$\begin{aligned} b_1 &= \Delta_\rho \\ b_2 &= \Delta_r \\ b_3 &= \Delta_\phi. \end{aligned} \quad (6.21)$$

To approximate the matrix \mathcal{A} at an interface of two grid cells, we use Roe-averages. If we then project the flux difference across the interface we are considering onto the eigenvectors of \mathcal{A} :

$$\mathbf{F}_R - \mathbf{F}_L = \sum b_k \mathbf{e}_k, \quad (6.22)$$

we can then define the first order interface flux just as it was defined in the gas case:

$$\mathbf{F}_{\text{int}} = \frac{1}{2}(\mathbf{F}_L + \mathbf{F}_R) - \frac{1}{2} \sum \sigma_k b_k \mathbf{e}_k, \quad (6.23)$$

where $\sigma_k = \text{sign}(\lambda_k)$. When $\lambda_k = 0$, we take $\sigma_k = 0$. It is easy to show that this version of the interface flux corresponds exactly with Eq. (6.17). Having the interface flux in this form, we can immediately write down a second-order interface flux that is again analogous to the gas case:

$$\mathbf{F}_{\text{int}} = \frac{1}{2}(\mathbf{F}_L + \mathbf{F}_R) - \frac{1}{2} \sum (\sigma_k a_k - (\sigma_k - \nu_k) \psi_k) \lambda_k \mathbf{e}_k, \quad (6.24)$$

where $\nu_k = \lambda_k \Delta t / \Delta r$ and ψ is the flux limiter. We have used the same limiter as in Paardekooper & Mellema (2006) for both gas and dust in all simulations.

6.3.2 Accretion

We model accretion onto the planet by taking mass away from the grid at the location of the planet. There are two parameters governing the amount of mass taken away at each time step: the accretion area and the accretion rate. We take the accretion area to be a circle with a radius equal to a tenth of the Roche lobe of the planet, and the accretion rate to be such that the time scale for emptying this region is equal to three fifths of the orbital time scale of the planet. The same parameters were used in D'Angelo et al. (2002) and Paardekooper & Mellema (2006).

6.3.3 Source terms

All the source terms except the drag forces are integrated using stationary extrapolation (Paardekooper & Mellema 2006). The combination of exact extrapolation for the angular momentum and approximate extrapolation for the other geometrical source terms was shown to give reliable results for single-fluid calculations of the planet-disk problem. Because these results were not affected by increasing the resolution, we can conclude that using this treatment of the source terms is accurate enough. However, when other forces besides gravity are included, it is not guaranteed that a stationary solution exists. Simis et al. (2001) found that the source terms arising in two-fluid calculations are best integrated analytically. Therefore, the drag forces are incorporated separately using an ordinary differential equation:

$$\frac{d}{dt}(\Sigma \mathbf{v}) = \mathbf{f}_d. \quad (6.25)$$

During this step, we keep the dust and gas density fixed. Using Eq. (6.14), we can write an ordinary differential equation for the velocity difference between gas and dust:

$$\frac{d}{dt}(\Delta \mathbf{v}) = -\alpha \sqrt{1 + \beta \Delta \mathbf{v}^2} \Delta \mathbf{v}, \quad (6.26)$$

where $\alpha = \frac{\Omega_K}{T_s}$ and $\beta = \frac{9\pi}{128c_s^2}$. This equation can be integrated analytically to give

$$\Delta \mathbf{v}(t) = \frac{2\Delta \mathbf{v}_0 \exp(-\alpha t)}{1 + \sqrt{1 + \beta \Delta \mathbf{v}_0^2} - \frac{\beta \Delta \mathbf{v}_0^2 \exp(-2\alpha t)}{1 + \sqrt{1 + \beta \Delta \mathbf{v}_0^2}}}. \quad (6.27)$$

Note that when $\beta = 0$, we recover the ordinary exponential decay of the velocity difference. Using conservation of total momentum:

$$\Sigma \mathbf{v} + \Sigma_g \mathbf{v}_g = \text{constant}, \quad (6.28)$$

we can solve for the evolution of the velocities of gas and dust separately, while keeping the total momentum conserved exactly.

6.3.4 Test problem

Gasdynamical codes are often tested against a simple Riemann problem (Sod 1978), also known as the shock tube. In this section, we test the method for dust advection against the Riemann problem shown in Fig. 6.1, using a 100-zone grid. We also study the effect of the interaction between gas and dust. The initial dust-to-gas mass ratio is 1. The simulations were run until $t = 0.5$, which took approximately 50 time steps.

In Fig. 6.2, we show the results for three different stopping times: $T_s = \infty$ (left panels), $T_s = 0.5$ (middle panels), and $T_s = 0.05$ (right panels). We see that for the case of no interaction, we reproduce the result of Fig. 6.1 for gas and dust. The delta shock is smeared over approximately 4 computational cells, but it moves at the correct speed.

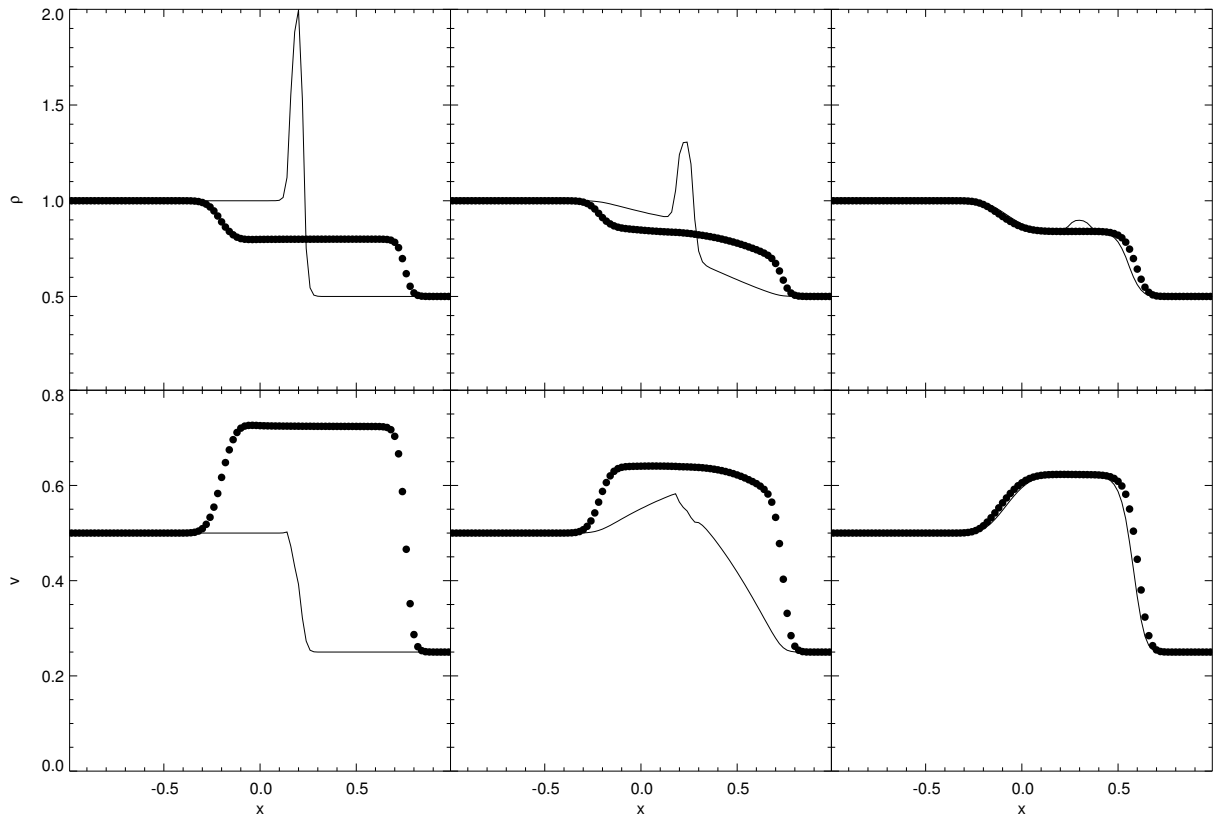


Figure 6.2: Numerical results for the Riemann problem of Fig. 6.1 for gas (dots) and dust (solid line). The top row shows the density, the bottom row the velocity. Left panels: no gas-dust interaction. Middle panels: $T_s = 0.5$. Right panels: $T_s = 0.05$.

Note that because the velocity is less than the sound speed everywhere, the waves in the gas are not shock waves, but are simply sound waves.

For the middle panels, the stopping time is comparable to the sound-crossing time and the dust velocity increases towards the gas velocity, while by conservation of momentum, the gas velocity decreases with respect to the left panels. The velocities approach each other the fastest at the position of the delta shock which has decreased in amplitude because the gas and dust densities also approach each other.

When we decrease the stopping time by a factor of ten, the densities and velocities of gas and dust are almost equal everywhere. In the right panels of Fig. 6.2, there is only a small bump left of the delta shock, and the gas has lost enough momentum to the dust to visibly slow down the sound waves. Note that this only happens because the gas and dust densities were equal initially. For an interstellar dust-to-gas ratio of 1 : 100, the gas is not affected by the dust.

6.3.5 Limits

The approach presented here cannot be used in all circumstances. To begin with, the continuum form for the equations of motion is only valid if two requirements are met.

First, there need to be enough particles in the volume under consideration (in our case, one grid cell) to work with average states. Second, there need to be enough interparticle collisions to make such an average state meaningful. For a dust fluid, both criteria are only fulfilled if the particles are well-coupled to the gas (Garaud et al. 2004). In other words, we can only work with particles for which $T_s \ll 1$ everywhere in the computational domain. For larger dust boulders, a particle-based method is more appropriate (Johansen et al. 2006a; Fromang & Nelson 2005).

On the other hand, when the stopping time is very small, the source terms due to gas-dust friction become stiff. Even though we integrate these source terms in an implicit way, which makes the method *stable* for these small particles, it does not necessarily give us the correct answer. This is because the gas source terms due to pressure are dealt with in the advection step, and pressure is precisely what causes gas-dust separation. Therefore, even for $T_s = 0$, the dust would numerically slowly drift inward, while according to Eq. (6.15), its radial velocity should be zero. The range in T_s that we can consider is therefore also bounded from below. The time scale for the advection (the hydrodynamical time step, determined by the Courant-Friedrichs-Lewy (CFL) condition) should not be much larger than the time scale for gas-dust coupling. Combining the two limits, we can conclude that we can only consider particles for which the stopping time satisfies:

$$\Omega_K \Delta t \approx T_s \ll 1. \quad (6.29)$$

In practice, for the gas densities considered here (see Sect. 6.4), Eq. (6.29) limits the particle size from below at approximately $150 \mu\text{m}$ and from above at approximately 1 cm . In all our simulations we checked that lowering the time step Δt did not influence the results.

It is important to realize that Eq. (6.29) should hold true everywhere on the grid. When the gas density changes significantly, for example due to the formation of a gap, the stopping time can vary by orders of magnitude. The condition $T_s \ll 1$ for gap-opening planets makes the simulations very expensive. To do the calculations in a reasonable amount of time, we restrict our parameter space to non-gap-opening planets. Note, however, that gap-opening planets also pose problems for particle-based methods because very many particles are needed to achieve enough resolution inside the gap.

The two-dimensional nature of these simulations also puts conditions on the size of the parameter space we can consider. When the Roche lobe of the planet is smaller than the disk thickness, three-dimensional effects come into play, lowering accretion and migration rates for example, (D'Angelo et al. 2003). However, global three-dimensional multi-fluid calculations are beyond current computational resources. Furthermore, because of dust settling, the dust disk will be much thinner than the gas disk, depending on the particle size. The two-dimensional approach will therefore cause fewer discrepancies in the dust distribution. Still, one has to be very careful when interpreting results for planets with $M < 0.1 M_J$.

6.4 INITIAL AND BOUNDARY CONDITIONS

The standard numerical resolution we use is $(n_r, n_\phi) = (128, 384)$. This way, the cells close to the planet are of equal size in the radial and in the azimuthal directions. We do not resolve the Roche lobe using a low resolution like this, but this resolution is sufficient to capture the long-term global evolution of the disk. For the runs with dust accretion, we used 4 levels of AMR to achieve a resolution that is 16 times higher near the planet.

As mentioned before, we use an aspect ratio of $h = 0.05$, and the initial gas surface density distribution is constant, with $\Sigma_g = 34 \text{ g cm}^{-2}$. This surface density is appropriate for a disk with $0.01 M_\odot$ within 100 AU at approximately 7 AU, between the location of Jupiter and Saturn in the solar system, or at 13 AU in the Minimum Mass Solar Nebula. Note, however, that the fundamental parameter is the stopping time, and our results can therefore be scaled to disks of arbitrary mass by adopting a different grain size for a given T_s .

The initial dust-to-gas ratio is 0.01. Our distance unit is the radius of the planet's orbit, and in this unit the inner boundary is at $r = 0.4$ and the outer boundary at $r = 2.5$.

It is easy to see that for a constant surface density the stopping time is also constant:

$$T_s = 0.0461 \left(\frac{s}{\text{cm}} \right), \quad (6.30)$$

where the size of the particles s is given in cm.

The gas rotates with a slightly sub-Keplerian velocity due to the radial pressure gradient (note that even when there is no density gradient, there is a pressure gradient caused by the gradient in the sound speed). The dust rotates exactly with the Keplerian velocity, initially. All radial velocities are taken to be zero.

The constant kinematic viscosity is set so that $\alpha = 0.004$ at $r = 1$ in all models. For the disk described above, the critical planet mass for gap opening is about 1 Jupiter mass ($1 M_J$) (Bryden et al. 1999). We varied the mass of the planet between $0.001 M_J$ and $1.0 M_J$.

The boundary conditions are the same as in Paardekooper & Mellema (2006), deriving from Godon (1996). They are specifically designed to be non-reflecting, so that all waves generated in the simulated region leave the computational domain without influencing the interior.

6.5 RESULTS

6.5.1 Axisymmetric disk

To begin with, we consider a disk without a planet. The analytic solution for the drift velocity is given in Eq. (6.15). Figure 6.3 shows this analytic solution for particles of 1 mm, as well as the numerical solution after 10 orbits of the gas at $r = 1$. The analytical

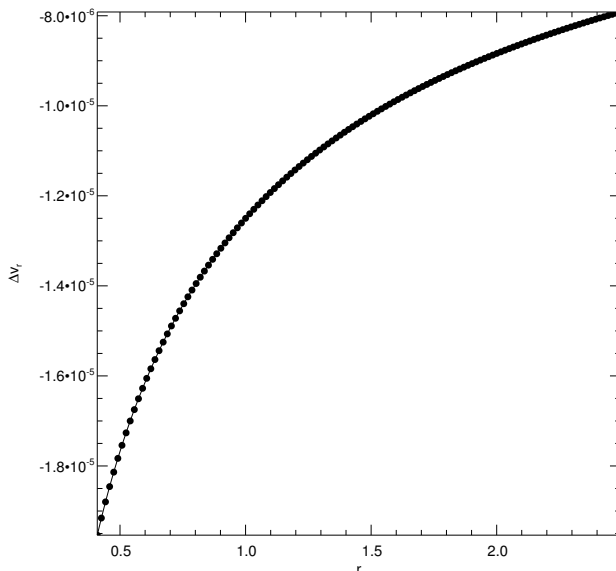


Figure 6.3: Relative radial velocity of gas and dust (1 mm) in a disk without a planet. The dots represent the numerical solution, and the solid line represents Eq. (6.15)

solution is indistinguishable from the numerical result, showing that the method handles the large source terms arising due to the small T_s very well. The angular velocity of the dust is always equal to the angular velocity of the gas. The Coriolis force starts to play a role only when the relative radial velocity becomes very large.

6.5.2 Dust response to a spiral wave

An embedded planet perturbs the gas disk by launching spiral density waves. In this section, we investigate the dust response to such a single wave. In Fig. 6.4, we show a close-up on part of the spiral pattern generated by the planet. The velocity arrows indicate the relative velocity of gas and dust. In the upper right direction, the density and velocity of the gas are close to their initial values, and in this region, the dust drifts slowly inward, according to Eq. (6.15). In the lower left part of the figure the dust particles drift inward again, but at a higher speed, due to the lower gas density. At the location of the spiral wave, gas density and velocity are such that the dust always moves towards the center of the wave. This is not surprising in view of Eq. (6.16), which states that in an axisymmetric disk, dust particles will always move towards the highest pressure. Note that even in this perturbed disk, the angular velocities of gas and dust are still almost equal: the particles move only radially through the gas. Therefore, the dust response to a spiral wave is the same as the response to an axisymmetric density wave, but stretched in the radial direction. The effect of a density wave, as shown in Fig. 6.4, remains very local and is of minor importance for the global disk evolution.

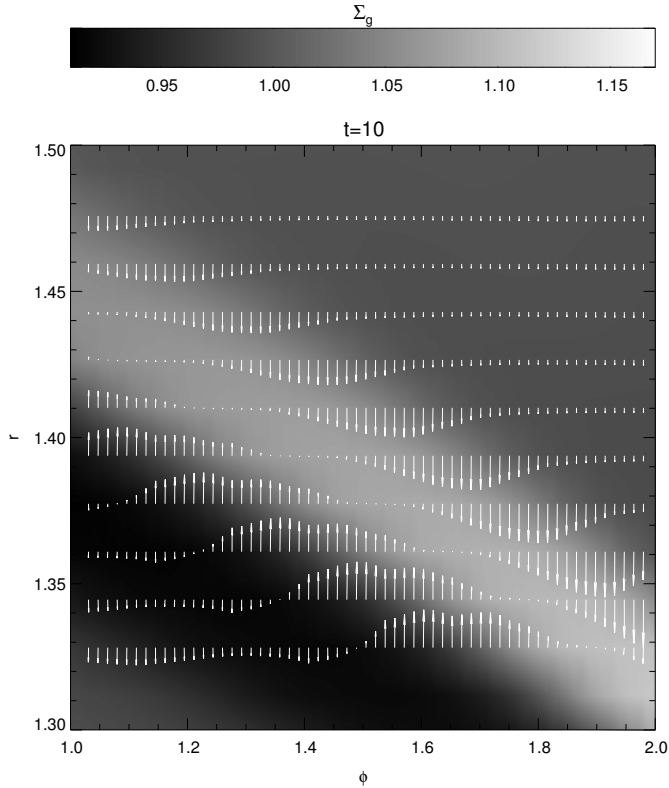


Figure 6.4: Close-up on a spiral density wave, with relative velocity arrows superimposed. Outside of the spiral wave, the dust drift is directed inward, according to Eq. (6.15). Close to the spiral, the particles move towards the center of the wave. For 5 mm dust particles, as shown here, the maximum relative velocity is $2.6 \cdot 10^{-6}$, in units of the orbital velocity of the planet.

6.5.3 Global disk evolution

Paardekooper & Mellema (2004) showed that planets of $\sim 0.1 M_J$ are able to decouple the evolution of the gas disk and the dust disk. More specifically, they showed that the dust particles tend to move away from the orbit of the planet, creating a deep annular gap. Furthermore, the final dust disk appeared to be structured near mean motion resonances. In this section, we further explain the mechanism for structuring the disk.

First of all, Fig. 6.5 shows a radial density cut through a disk perturbed by a $0.1 M_J$ planet after 500 orbits. Again, as in Paardekooper & Mellema (2004), we see a clear gap and a density enhancement at the position of the 2:1 mean motion resonance.

Note that since $T_s \ll 1$, the dust particles are never influenced by the planet directly at the radii of the indicated resonances, they only react to the gas density and velocity. The mechanism for structuring the dust disk is therefore intrinsically different from ordinary resonance capture, which is the usual explanation for the existence of the Plutino's in the Kuiper belt (Luu & Jewitt 2002).

In Fig. 6.6, we plot the radial acceleration of dust particles, excluding the drag force:

$$a = r(v_\phi + \Omega)^2 - \frac{\partial \Phi}{\partial r}. \quad (6.31)$$

Figure 6.6 shows the azimuthally averaged a , with a close-up on the outer region of the disk. The first thing to note is that the dust is always accelerated inward, except for

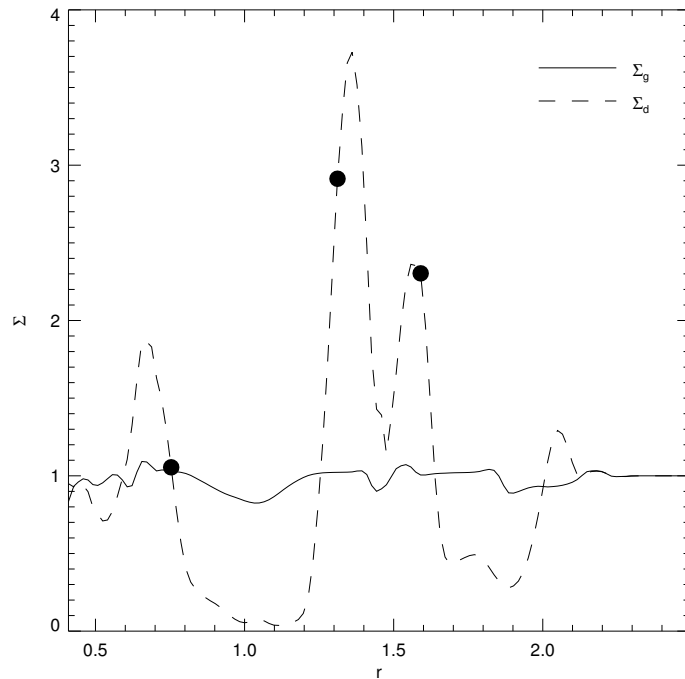


Figure 6.5: Surface density of gas and dust ($s = 0.1$ cm) after 500 orbits of a $0.1 M_J$ planet at $\phi = 0$ (opposite to the planet). The dust density is multiplied by 100. The dots indicate the positions of the 2:3, the 3:2, and the 2:1 resonances.

the region around $r = 1.1$. Inside the planet's orbit, the acceleration is very negative, indicating that the dust will quickly move toward the inner boundary.

The large inward and outward accelerations near $r = 0.9$ and $r = 1.1$, respectively, are due to the inner and outer edges of the density dip carved in the gas. The pressure gradient at the outer edge is large enough to push the dust outward. The densest ring outside the planet's orbit forms where a switches sign at $r = 1.3$. Particles approach this location in the disk from both smaller and larger radii, which leads to a strong dust accumulation.

The close-up in Fig. 6.6 indicates the outer 2:1 mean motion resonance, which shows up as a bump in the radial acceleration at $r = 1.6$. Note that a is still negative near the resonance, so the dust keeps moving inward. However, near the resonance, the dust particles are decelerated, and therefore the dust piles up at that location. From Fig. 6.5, we can also see that the density peaks just outside the gap are close to, but not exactly located at the position of the 3:2 and the 2:3 resonance, showing that the mechanism by which they are formed is different. In contrast to the region close to the shallow gas gap, there is no apparent pressure gradient near the 2:1 resonance to structure the dust disk. Nonetheless, the resonance does show up in the acceleration in Fig. 6.6, and it is therefore the velocity field rather than the density of the gas that makes the dust move into the 2:1 resonance.

The adopted initial gas surface density is correct for a distance of 13 AU in the Minimum Mass Solar Nebula (MMSN). For this location of the planet, the initial dust mass between $r = 1.2$ and $r = 1.5$ is $5.4 M_\oplus$. After 500 orbits of the planet, the dust mass in this region has grown to $10.9 M_\oplus$, an enhancement of more than a factor of 2 (see Fig. 6.5). This may have serious implications for building planetesimals

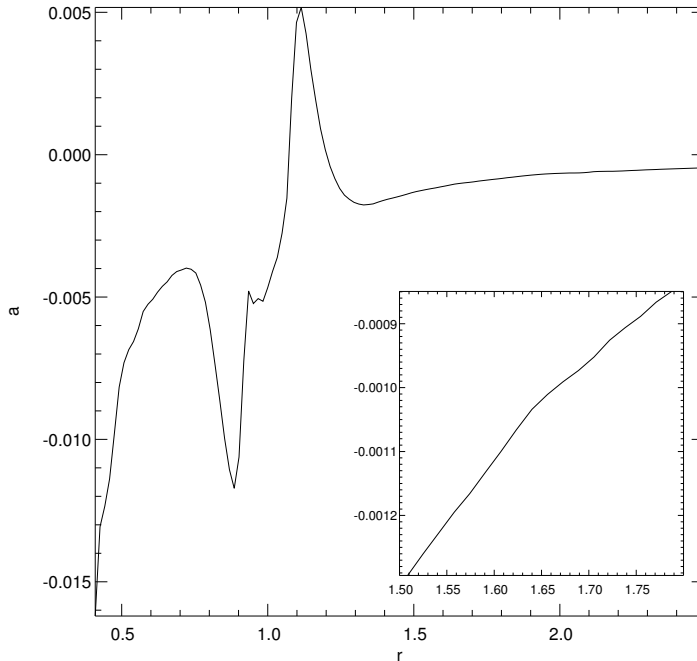


Figure 6.6: Azimuthally averaged radial acceleration a of dust particles after 100 orbits of a $0.1 M_J$ planet. The close-up shows a in the outer region of the disk. The 2:1 mean motion resonance is visible as a small bump in a .

(boulders with sizes larger than 10 centimeters) in this region.

We have not included dust diffusion in our models. Turbulent transport of small dust grains is not yet fully understood, but it can be described by diffusion for the smallest particles (Johansen & Klahr 2005). To see what effect diffusion has on dust-gap formation, we gave the dust fluid the same turbulent diffusion coefficient as the gas, and included the viscous force terms in the dust source update. It turned out that dust diffusion affects the dust density distribution only at the 1 % level, indicating that this is not an important process. However, the largest particles we consider may be subject to vortex trapping in turbulent eddies (Johansen & Klahr 2005), and for these particles, the diffusion approach may not be entirely valid.

6.5.4 Dependence on particle size

We have seen that particles of 1 mm decouple from the gas due to the disk perturbation induced by a small planet. As we examine smaller and smaller particles, we expect a certain minimum particle size for this decoupling to occur because smaller particles couple better to the gas. We can make a simple estimate for this s_{\min} by looking at the region in the disk near $r = 1.1$, where the dust experiences the largest positive acceleration a_{\max} . According to Fig. 6.6, $a_{\max} = 0.005$. The radial gas velocity in a standard accretion disk is

$$v_{r,g} = -\frac{3\nu}{2r}. \quad (6.32)$$

The gas radial velocity in a disk with a planet is similar. Balancing the outward acceleration with the radial drag force gives an equilibrium velocity difference between gas

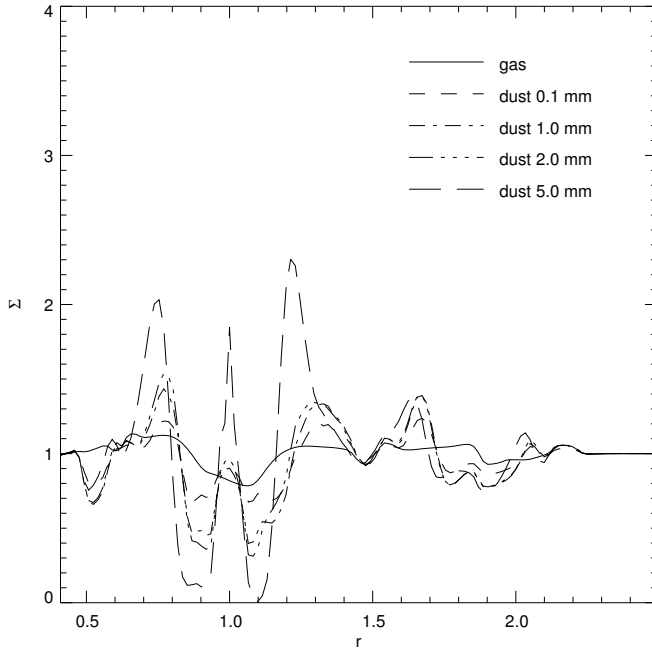


Figure 6.7: Radial density cut opposite to the planet for four different particle sizes after 100 orbits of a 0.1 M_J planet. The dust densities are multiplied by 100.

and dust of

$$\Delta v_r = a_{\max} \frac{T_s}{\Omega_K}. \quad (6.33)$$

When this velocity difference is larger than the radial gas velocity, dust particles can be accelerated outward around $r = 1.1$, creating a low density gap and a high density ring. The minimum stopping time for this to occur is

$$T_{s,\min} = \frac{3\Omega_K \nu}{2r a_{\max}}. \quad (6.34)$$

For our disk parameters, this implies a minimum particle size of approximately 500 μm . Note, however, that although smaller particles will not be pushed outward, they will travel inward at a different speed near the edge of the gas dip. As in the case for the 2:1 resonance, where in spite of the acceleration being negative everywhere a dust ring still arises, these particles will eventually create a gap, but on a much longer time scale.

Figure 6.7 shows the radial dust density for four different particle sizes after 100 orbits. First of all, it is clear that the larger particles react even more dramatically on the planet. The three bumps at $r = 0.7$, $r = 1.3$, and at corotation all grow very fast with increasing particle size. After 400 orbits, the dust-to-gas ratio of 5 mm particles at $r = 1.3$ is enhanced by more than an order of magnitude. The width of the dust gap does not depend on the size of the particles.

The outer disk ($r > 1.1$) reaches a quasi-static state after approximately 100 orbits. From then on the only evolution is in the further growth of existing features. The inner disk is slowly cleared, however, but on a time scale that is set by the unperturbed

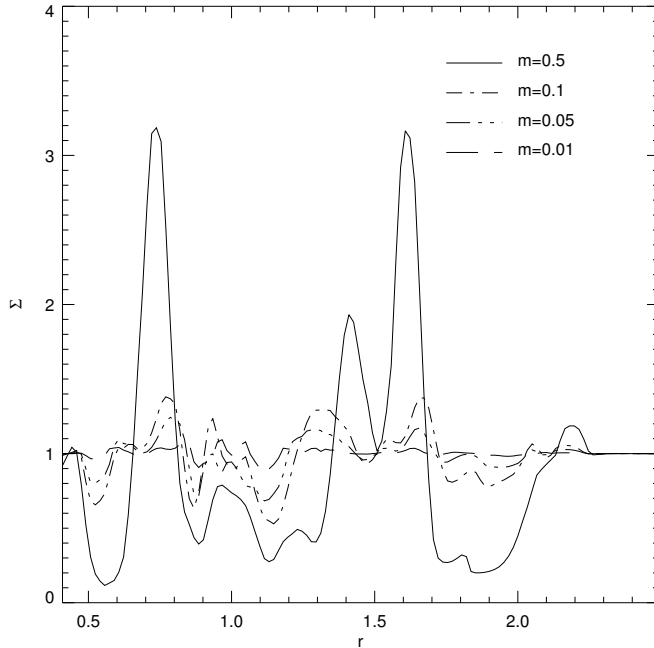


Figure 6.8: Radial density cut opposite to the planet for four different planetary masses after 100 orbits and for a particle size of 1 mm. The dust densities are multiplied by 100, and the planetary masses are in units of M_J

motion of gas and dust. If we take Eq. (6.32) for the velocity of the gas and Eq. (6.15) for the relative velocity, we can write the following for the dust velocity:

$$v_r = - \left(\frac{3}{2} \alpha + T_s \right) h^2 v_K. \quad (6.35)$$

This gives a time scale for clearing the region inside $r = 1$ of approximately 50000 orbits.

Looking at the distribution of 0.1 mm particles in Fig. 6.7, we see that even these well-coupled particles start to create a clearing in the inner disk. However, since this planet is not strong enough to keep all the dust outside of $r = 1.3$, the inner disk is still fed from outside. Particles larger than $500 \mu\text{m}$ are able to create a fast gap for this planet. This agrees with the estimate of Eq. (6.34). Based on Fig. 6.7, we estimate that particles larger than $150 \mu\text{m}$ will open up a dust gap within 500 orbits.

6.5.5 Dependence on planetary mass

Smaller planets do not dramatically perturb the disk, so we expect that a minimum planetary mass for dust-gap opening also exists. In this section, we consider only 1 mm particles.

Figure 6.8 shows the radial dust distributions for four different planetary masses. The smallest planet is not able to produce a density dip near its orbit, so the gas density is equal to 1 everywhere except in the spiral waves. From Fig. 6.8, we conclude that a planet of $0.05 M_J$ is the lowest-mass planet that is able to create a gap, albeit on a longer time scale than for more massive planets.

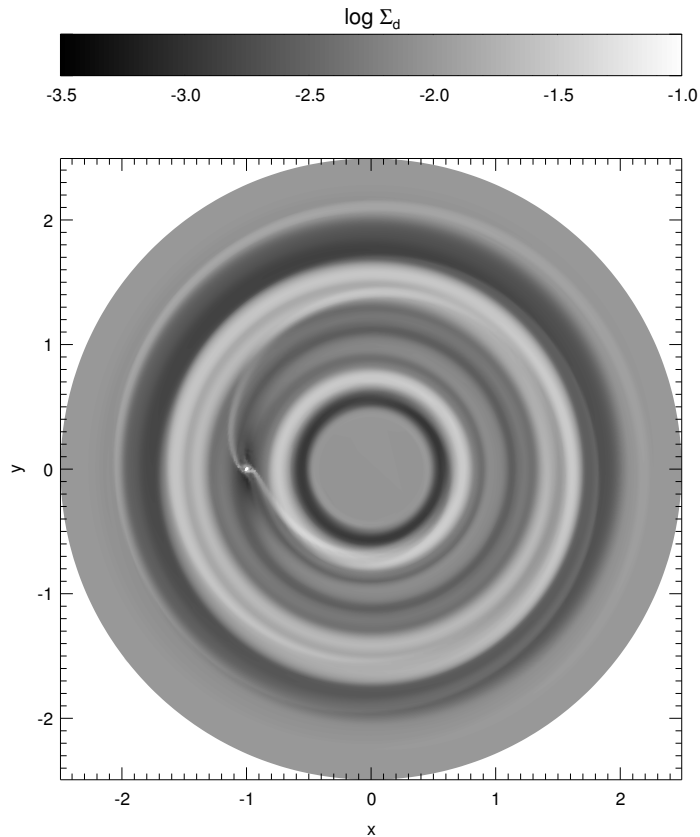


Figure 6.9: Surface density of 1 mm dust particles after 100 orbits of a 0.5 M_J planet.

The highest mass planet in Fig. 6.8 is on the edge of creating a gap in the gas disk. As a result of the lower gas density, the stopping time for particles near the orbit of the planet is relatively large, which allows for the strong evolution near $r = 1$. The time scale for dust-gap formation for this planet is about half the time scale for gas-gap formation, which is approximately 100 planetary orbits. Also, due to the strong spiral waves, the 2:1 mean motion resonance plays a major role; the resonance is able to suck material up from both sides, leading to a less pronounced peak near $r = 1.4$ and to an empty region around $r = 1.8$. Figure 6.9 shows the dust surface density for this planet. Note that the resonance-induced gaps at $r = 0.55$ and $r = 1.8$ are as deep as the gap near the planet's orbit. Observationally, it may be difficult to distinguish a single-planet system like this from one with multiple planets.

Because of the conditions discussed in Sect. 6.3.5, a 0.5 M_J planet is the maximum planetary mass we can accurately model with a two-fluid calculation. However, based on the relation between the radial acceleration a and the resulting dust distribution (compare Figs. 6.5 and 6.6), we can still make a few remarks concerning higher-mass planets.

First of all, we expect similar things to happen for a 1 M_J planet as for a 0.5 M_J planet, only in a more extreme form. Secondly, we noted in Sect. 6.5.3 that the dust ring just outside the gap forms where a changes sign from positive to negative. In Fig. 6.10, we show a together with the gas surface density Σ for a 1 M_J planet. The gas gap

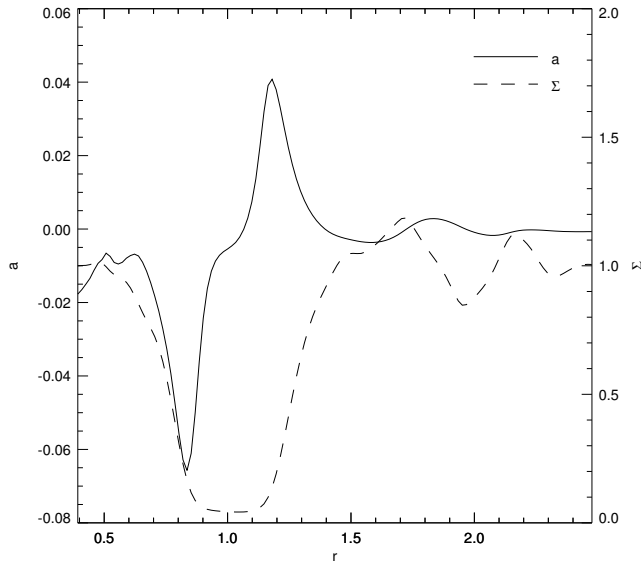


Figure 6.10: Azimuthal averages of the radial acceleration a (solid line) and gas surface density Σ (dashed line, shown for $0.4 \leq r \leq 1.8$) for a $1 M_J$ planet after 400 orbits.

clearly stands out, and we see that a changes sign at the outer edge of the gap around $r = 1.4$. A dust ring at that location would coincide with the outer edge of the gas gap. Therefore, a possible dust gap would have the same width as the gap in the gas disk.

Also from Fig. 6.10, we see that a is structured up to $r \approx 2.5$, which is larger than for the $0.1 M_J$ planet (see Fig. 6.6). For a planet at Neptune's orbit (semi-major axis 30 AU), the resonant structure in the dust disk can therefore extend to at least 75 AU.

6.5.6 Flow within the Roche lobe

The flow of dust deep within the Roche lobe (R_R) of the planet is relatively simple. Due to the strong pressure gradient in the direction of the planet, the relative velocity of the dust particles is always directed towards the planet. In other words, if we take a cylindrical coordinate frame (s, θ) centered on the planet, then $\Delta v_s = v_{s,d} - v_{s,g}$ is always negative.

In Fig. 6.11, we show this relative velocity as a function of distance to a $0.1 M_J$ planet for 1 mm particles. The first thing to note is that the relative velocity changes sign very close to the planet. That is because this was a run with gas and dust accretion, and therefore most of the gas inside $0.1 R_R$ was removed (see Paardekooper & Mellema (2006) for the accretion procedure), leading to a reversed pressure gradient locally. Outside the accretion area, dust moves slowly towards the planet with respect to the gas. The spread in velocities stems from the fact that the gas density distribution around the planet is not symmetric with respect to the planet (D'Angelo et al. 2002).

If we take the average relative velocity in the Roche lobe as $4.0 \cdot 10^{-4}$ in units of the Kepler velocity at the location of the planet, then we get a time scale to clear the Roche lobe of dust of less than 100 orbits for particles of 1 mm. This is an important time scale for accretion, as we will see in the next section.

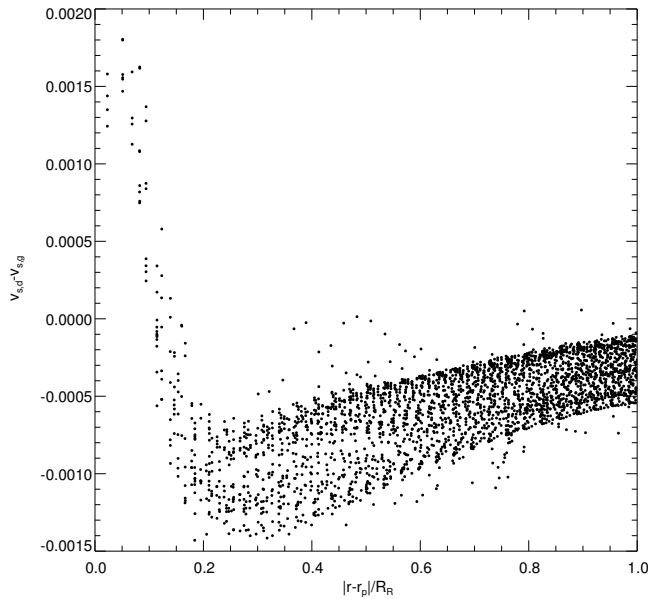


Figure 6.11: Scatter plot of the relative velocity in the direction of a $0.1 M_J$ planet. The distance to the planet is in units of the Roche lobe R_R , and the unit of relative velocity is the Kepler velocity at the position of the planet. The size of the dust particles in this simulation is 2 mm.

6.5.7 Gas and dust accretion

We now turn to the interesting problem of dust accretion. The accretion of dust particles compared to the gas is important for the final enrichment of gaseous giant planets. When the dust accretion rate is higher than 0.01 (the initial dust-to-gas ratio) times the gas accretion, the planet will get enriched in solids, and when the dust accretion is lower than 0.01 the gas-dust mixture that is accreted onto the planet is relatively gas-rich. In the discussion below, we multiply the dust content of the disk by 100, so that gas and dust accretion can be directly compared.

The mass range we can consider is limited because for $M_p < 0.1 M_J$, three dimensional effects start to play an important role (D'Angelo et al. 2003), while planets larger than approximately $0.5 M_J$ open up a deep gas gap in the disk, which we cannot treat in the fluid approach. Therefore, to elucidate the basic principles that govern dust accretion and to provide a starting point for future, more detailed simulations, we only consider a $0.1 M_J$ planet.

In the left panel of Fig. 6.12, we show the accreted mass of gas and dust in units of gas and dust disk masses as a function of time. The accretion of gas (solid line) was extensively discussed in Paardekooper & Mellema (2006) and is shown here only for comparison. After approximately 200 orbits, it reaches a constant value of $1.5 \cdot 10^{-4}$ gas disk masses per orbit.

The accretion rates for dust particles of different sizes show a different behavior. In the first few orbits, relatively more dust is accreted than gas, which means that the dust mass that is accreted is larger than 0.01 times the gas mass that is accreted. This is the stage where the immediate surroundings of the Roche lobe are cleared of dust, due to the strong pressure gradients in the planetary atmosphere. Later, the competing process of dust-gap formation sets in, and consequently, dust accretion slows down. In the end, for all particle sizes, relatively more gas is accreted than dust, which means

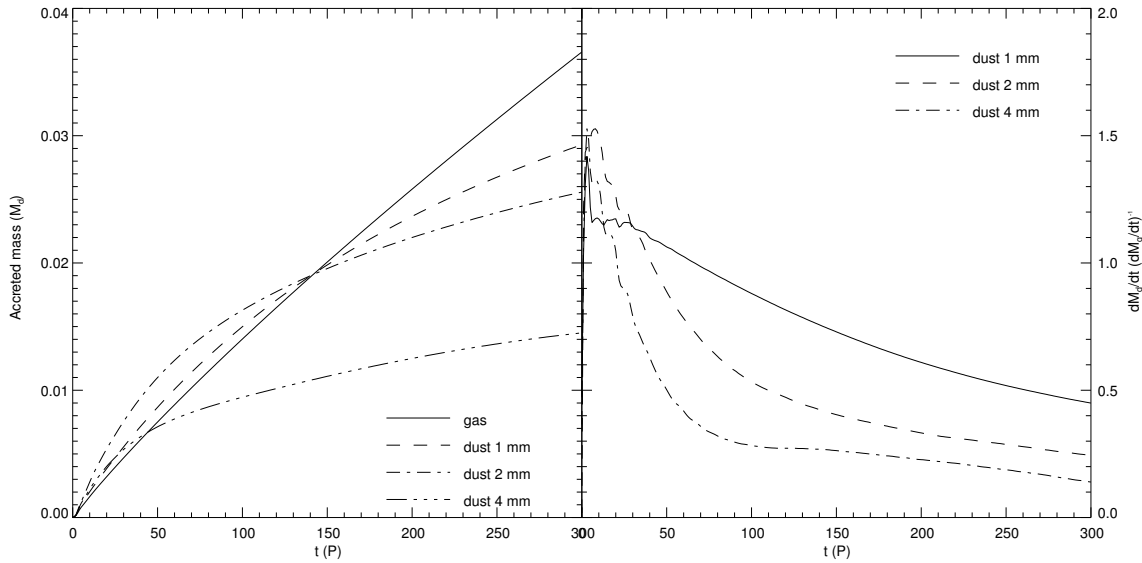


Figure 6.12: Accretion of gas and dust onto a $0.1 M_J$ planet. Left panel: gas and dust mass accreted on the planet. Right panel: relative accretion rate of dust with respect to the gas. For both panels, the dust mass is multiplied by 100 to compare it with the gas.

that the planet will not be enriched in solids of these particular sizes.

The right panel of Fig. 6.12 shows the ratio of accretion rates for the different particle sizes to the gas accretion rate. We see that initially the accretion rate of dust is higher than 0.01 times the accretion rate of the gas or all particle sizes, corresponding to the Roche lobe clearing mentioned before. If we look at the accretion rate of 1 mm particles, after the first sharp peak, the accretion rate stays almost constant for 30 orbits, after which the process of gap formation sets in, and the accretion rate slowly declines. After 300 orbits, the accretion rate for the dust is less than half the accretion rate of the gas, and it is still declining.

For the larger particles, we see a larger initial accretion rate because these more weakly coupled dust particles move up the strong pressure gradient near the planet more easily. However, for larger particles, gap formation sets in earlier, as well, and it will eventually win. A particle size of 2 mm results in the largest accreted mass of dust in this first stage of accretion. For 4 mm particles, gap formation sets in before the planet can accrete a significant amount of surrounding dust. However, in the long run, more small than large particles will have been accreted, as can be seen from the left panel of Fig. 6.12.

The planet clears the outer part of the gap of 4 mm particles in approximately 100 orbits (see Fig. 6.7). At this point, the accretion rate curve levels off at a value of $0.2 \dot{M}_{\text{gas}}$, but around 150 orbits, it starts to decrease again. Accretion around this time comes from the dense ring at $r = 1$, which will slowly diffuse into the inner disk. After it is gone, dust accretion will be negligible compared to gas accretion.

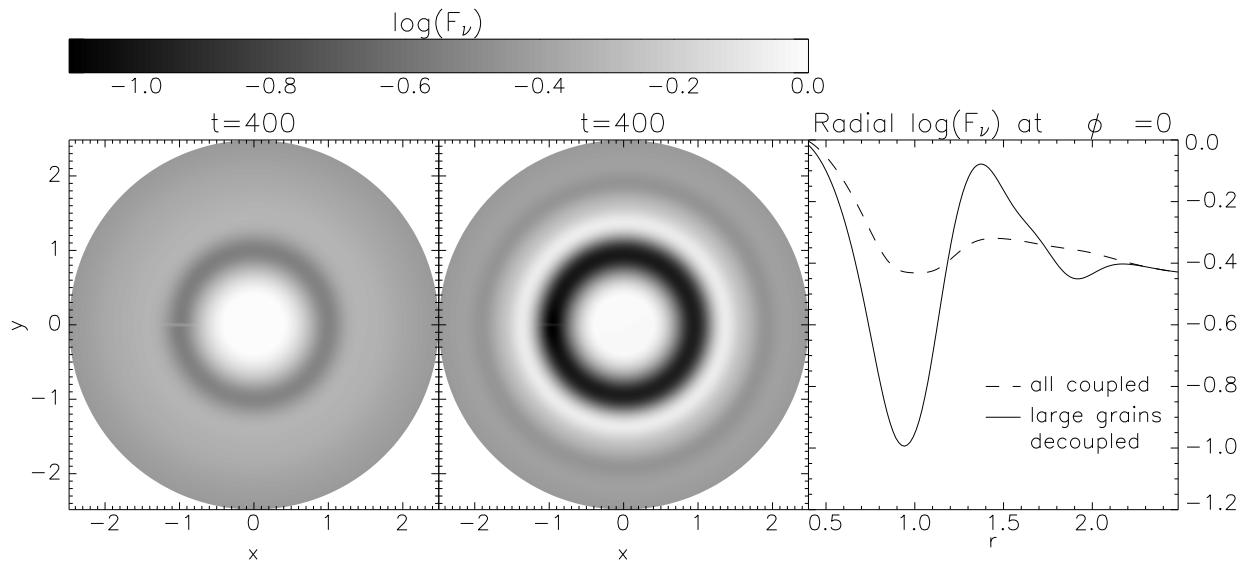


Figure 6.13: Logarithm of flux densities at 1 mm, normalized by the maximum and convolved with a Gaussian of FWHM 2.5 AU, corresponding to a resolution of 12 mas at 140 pc. Left panel: all particles follow the gas exactly (static dust evolution). Middle panel: particles larger than the critical size decouple from the gas (dynamic dust evolution). Right panel: the corresponding radial flux densities.

6.5.8 Simulated observations

To investigate the observational effects of the gas-dust decoupling we simulate an image taken at a wavelength of 1 mm. The disk is optically thin at this wavelength, and we put the planet at 5.2 AU. Calculations with different particle sizes showed that the minimum grain size for gap formation is approximately 0.15 mm (see Sect. 6.5.4), with a very sharp transition. We therefore assume that all particles larger than this critical size create a gap, and smaller particles follow the gas exactly. To estimate the relative amount of mass in these two families of particles we take an MRN size distribution (Mathis et al. 1977), in which the number density of particles is a power law in s with exponent -3.5 . For a maximum particle size of 5 mm most mass is in particles larger than our critical size, and as a conservative assumption we take an equal amount of mass in the particles smaller than 0.15 mm and in the larger particles. But since the opacity at 1 mm is dominated by particles with $s \approx 1$ mm (Miyake & Nakagawa 1993), the emission will be dominated by the larger particles. We used the size-dependent opacity data from Miyake & Nakagawa (1993) to calculate the flux densities. In Fig. 6.13 the resulting flux densities are shown, convolved with a Gaussian of FWHM 2.5 AU, which corresponds to an angular resolution of 12 mas at 140 pc (the Taurus star forming region). This resolution is comparable to the maximum resolution of 10 mas that ALMA will achieve. In the left panel of Fig. 6.13 we computed the flux under the assumption that all particles move with the gas, as was done for example by Wolf et al. (2002). There is a little dip visible due to the decrease in density in the gas, but only when we include the density distribution of Fig. 6.5 for the larger particles a clear gap

emerges (middle panel of Fig. 6.13). The right panel of Fig. 6.13 shows the radial dependence of the flux density. From this panel we can see that the contrast between the inside of the gap and the gap edges is enhanced from almost a factor of two (dashed line) to more than an order of magnitude (solid line). So the impact of the dynamics of the larger particles on the appearance of a low-mass planet in a disk is considerable.

6.6 DISCUSSION

Dust gaps opened by low-mass planets have some interesting observational and theoretical consequences. In Sect. 6.5.8 we showed that the Atacama Large Millimeter Array (ALMA) will provide the resolution to observe these gaps in protoplanetary disks at the distance of the Taurus starforming region. Observationally, the relatively large particles we consider are only important at mm-wavelengths. To create gaps and inner holes in disks that can be detected at infra-red wavelengths, more massive planets are needed to remove the smallest particles.

Next, we will explore some more possible consequences for planet formation. Before we can make any quantitative statements about the importance of the limited size range we consider in this Chapter, we need to determine what fraction of the total dust mass these particles represent. If we look at the size distribution from Fig. 7 of Dullemond & Dominik (2005) we see a bimodal distribution (dust and planetesimals), with a transition around particles of 10 cm. It is interesting to note that for typical midplane densities, a size of 10 cm gives rise to $T_s \approx 1$ (see Eq. (6.30)), which is the upper limit for which the fluid approach is valid. Boulders larger than 10 cm are not influenced by the gas as much as the smaller particles, and therefore will not participate in gap formation due to pressure gradients, while particles smaller than 150 μm are too well-coupled to the gas to form a gap (see Sect. 6.5.4). From Fig. 7 of Dullemond & Dominik (2005), we estimate that half of the total mass of particles smaller than 10 cm is in particles larger than 150 μm . Furthermore, about 30 % of the total dust mass is in particles with sizes between 150 μm and 10 cm.

The above estimate implies that the inner disk is denied 30 % of the amount of solids it would receive from the outer disk without the presence of the planet. If (terrestrial) planets are still being formed in the inner disk, it may slow down this process considerably.

Dust piles up outside the planet's orbit (see Fig. 6.5). In Sect. 6.5.3, we mentioned that after 500 orbits of the planet, the amount of dust had already doubled. Because the planet acts as a barrier for particles moving inward, more and more dust will stream into the resonance from the outer disk. It is interesting to note that this is in the region where the Kuiper Belt resides with respect to Neptune. This large amount of dust may well have influenced planetesimal formation in that region.

If an already-formed giant planet is present in the inner disk, this planet is also denied 30 % of the amount of solids it would be able to accrete without the presence of the outer planet. One could imagine that in the present configuration of our Solar System, with three dust-gap-opening planets outside 5.2 AU, the amount of solid material accreted by Jupiter would be dramatically small, even without the mechanism

outlined in Sect. 6.5.7.

Depending on the dust size distribution in the disk, the low relative accretion rates for mm-sized particles found in Sect. 6.5.7 will have a significant effect on the final composition of the planet. Our results show that the accretion rates for these particles are, on the long run, more than an order of magnitude lower than the gas accretion rate. This will significantly affect the final enrichment in solids for giant planets, even more so if a dust-gap-opening planet exists in the outer disk.

In other words, if, as is standard in planet-formation models, one considers gas accretion and the accretion of planetesimals separately, the gas that is accreted is relatively *poor* in solids (by a factor of 2) compared to the solar value. This process works against the usual enrichment scenarios for the giant planets (Gautier et al. 2001a,b; Owen et al. 1999). However, as was mentioned before, we cannot make firm statements about planets of higher mass. More definitive conclusions about dust accretion onto giant planets require further study.

Dust growth may also play an important role in structuring the disk. When the growth time scale τ_g is long compared to the dust gap formation time scale, what effectively happens is that particles will be removed from the dust gap as soon as they become large enough. This means that the gap will also be cleared of the smallest particles on a time scale τ_g . However, the process of dust growth in disks is not understood well enough to make any quantitative statements about it.

It is important to realize that the dust-gap-formation process basically only needs a shallow gas dip formed by an embedded planet. As long as more complicated disk models including magnetic fields and radiative transfer do not change this gas structure, the basic picture outlined in this Chapter will not change. Three-dimensional effects may be important, however, because gas and dust behave differently in the vertical direction: dust particles will settle to the midplane, while the gas forms a pressure-supported structure. Angular momentum transport, and therefore also gap formation, is reduced in three-dimensional models, compared to vertically integrated models, but because of settling effects, the dust will mainly interact with gas near the midplane where the planetary potential is strongest. It is not clear how these competing processes will affect our results; three-dimensional, multi-fluid simulations are needed to answer that question.

6.7 SUMMARY AND CONCLUSIONS

In this Chapter, we have elaborated on the findings of Paardekooper & Mellema (2004), who showed that intermediate mass planets are able to open dust gaps in gas disks. We have shown how the formation of the gap depends on particle size and planetary mass, indicating that particles larger than $150 \mu\text{m}$ and planets larger than $0.05 M_J$ are needed to open a gap in a typical protoplanetary disk. Planets larger than $0.5 M_J$ clear a gas gap around their orbit, increasing the stopping time T_s locally by 2 orders of magnitude, leaving the dust inside the gap largely decoupled from the gas. If the planet clears a gas gap, the dust gap will be of equal width.

Within the Roche lobe of the planet, the pressure gradient is such that solids will

quickly move to the center of the planetary atmosphere, allowing for a very high dust accretion rate. However, this enhancement is more than counterbalanced by the local depletion of dust due to the formation of the dust gap. In the end, much more gas can be accreted compared to solids. This may have serious consequences for the enrichment of giant planets.

ACKNOWLEDGMENTS

S.P. and G.M. acknowledge financial support from the European Research Training Network “The Origin of Planetary Systems” (PLANETS, contract number HPRN-CT-2002-00308) at Leiden Observatory. G.M.’s work in Leiden is made possible through support from the Royal Netherlands Academy of Arts and Sciences.

REFERENCES

- Boss, A. P. 1997, *Science*, 276, 1836
- Bryden, G., Chen, X., Lin, D. N. C., Nelson, R. P., & Papaloizou, J. C. B. 1999, *ApJ*, 514, 344
- D’Angelo, G., Henning, T., & Kley, W. 2002, *A&A*, 385, 647
- D’Angelo, G., Kley, W., & Henning, T. 2003, *ApJ*, 586, 540
- Dullemond, C. P. & Dominik, C. 2005, *A&A*, 434, 971
- Eulderink, F. & Mellema, G. 1995, *A&AS*, 110, 587
- Fromang, S. & Nelson, R. P. 2005, *MNRAS*, 364, L81
- Garaud, P., Barrière-Fouchet, L., & Lin, D. N. C. 2004, *ApJ*, 603, 292
- Gautier, D., Hersant, F., Mousis, O., & Lunine, J. I. 2001a, *ApJ*, 550, L227
- Gautier, D., Hersant, F., Mousis, O., & Lunine, J. I. 2001b, *ApJ*, 559, L183
- Godon, P. 1996, *MNRAS*, 282, 1107
- Goldreich, P. & Ward, W. R. 1973, *ApJ*, 183, 1051
- Guillot, T., Stevenson, D. J., Hubbard, W. B., & Saumon, D. 2004, *The interior of Jupiter (Jupiter. The Planet, Satellites and Magnetosphere)*, 35–57
- Haghighipour, N. & Boss, A. P. 2003, *ApJ*, 598, 1301
- Johansen, A., Henning, T., & Klahr, H. 2006a, *ApJ*, 643, 1219
- Johansen, A. & Klahr, H. 2005, *ApJ*, 634, 1353
- Johansen, A., Klahr, H., & Henning, T. 2006b, *ApJ*, 636, 1121
- Kley, W. 1999, *MNRAS*, 303, 696
- Kwok, S. 1975, *ApJ*, 198, 583
- Leveque, R. J. 2004, *Journal of Hyperbolic Differential Equations*, 1, 315
- Lubow, S. H., Seibert, M., & Artymowicz, P. 1999, *ApJ*, 526, 1001
- Luu, J. X. & Jewitt, D. C. 2002, *ARA&A*, 40, 63

- Mathis, J. S., Rimpl, W., & Nordsieck, K. H. 1977, *ApJ*, 217, 425
- Miyake, K. & Nakagawa, Y. 1993, *Icarus*, 106, 20
- Nelson, R. P., Papaloizou, J. C. B., Masset, F., & Kley, W. 2000, *MNRAS*, 318, 18
- Owen, T., Mahaffy, P., Niemann, H. B., et al. 1999, *Nature*, 402, 269
- Paardekooper, S.-J. & Mellema, G. 2004, *A&A*, 425, L9
- Paardekooper, S.-J. & Mellema, G. 2006, *A&A*, 450, 1203
- Pollack, J. B., Hubickyj, O., Bodenheimer, P., et al. 1996, *Icarus*, 124, 62
- Roe, P. L. 1981, *J. Comp. Phys*, 43, 357
- Shakura, N. I. & Sunyaev, R. A. 1973, *A&A*, 24, 337
- Simis, Y. J. W., Icke, V., & Dominik, C. 2001, *A&A*, 371, 205
- Sod, G. A. 1978, *J. Comp. Phys*, 27, 1
- Suttner, G. & Yorke, H. W. 2001, *ApJ*, 551, 461
- Takeuchi, T. & Artymowicz, P. 2001, *ApJ*, 557, 990
- Takeuchi, T. & Lin, D. N. C. 2002, *ApJ*, 581, 1344
- Weidenschilling, S. J. 1977, *MNRAS*, 180, 57
- Woitke, P. & Helling, C. 2003, *A&A*, 399, 297
- Wolf, S., Gueth, F., Henning, T., & Kley, W. 2002, *ApJ*, 566, L97
- Woodward, P. & Colella, P. 1984, *Journal of Computational Physics*, 54, 115
- Youdin, A. N. & Goodman, J. 2005, *ApJ*, 620, 459

CHAPTER 7

Dust accretion onto high-mass planets

Sijme-Jan Paardekooper

To be submitted

WE study the accretion of dust particles of various sizes onto embedded massive gas giant planets, where we take into account the structure of the gas disk due to the presence of the planet. The accretion rate of solids is important for the structure of giant planets: it determines the growth rate of the solid core that may be present as well as their final enrichment in solids. We use the RODEO hydrodynamics solver to solve the flow equations for the gas, together with a particle approach for the dust. The solver for the particles' equations of motion is implicit with respect to the drag force, which allows us to treat the whole dust size spectrum. We find that dust accretion is limited to the smallest particle sizes. The largest particles get trapped in outer mean-motion resonances with the planet, while particles of intermediate size are pushed away from the orbit of the planet by the density structure in the gas disk. Only particles smaller than approximately $s_{\max} = 10 \mu\text{m}$ may accrete on a planet with the mass of Jupiter. For a ten times less massive planet $s_{\max} = 100 \mu\text{m}$. The strongly reduced accretion of dust makes it very hard to enrich a newly formed giant planet in solids.

7.1 INTRODUCTION

Planets form in circumstellar disks consisting of gas and dust. Initially, gas and solids are well-mixed with a dust-to-gas ratio of 1:100, which is similar to the interstellar value, and the dust particles will be as small as interstellar grains ($\sim 1 \mu\text{m}$). However, due to the pressure structure of the disk the dust particles start to move with respect to the gas: the vertical component of the stellar gravity makes the particles rain down onto the midplane of the disk, while the radial pressure gradient of the gas pushes the particles inward (Weidenschilling 1977).

The magnitude of the velocity difference between gas and dust depends on the particle size: small particles couple well to the gas and move slower than the larger particles. These size-dependent velocities in the radial and vertical direction, together with Brownian motion and turbulence, will lead to collisions between the dust particles of various sizes. Assuming that impact velocities are low the particles stick together upon colliding, after which they continue as one large particle. This leads to a rapid depletion of small grains (Dullemond & Dominik 2005).

However, sticking probabilities are still unclear, especially for larger particles. Experimental results (Blum & Muench 1993; Blum & Wurm 2000) suggest that unless the relative velocities of particles are very low collisions lead to bouncing or even shattering of the particles. Another problem arises once the particles grow to sizes of approximately one meter, because then the time scale for drag-induced radial migration becomes as short as 100 yrs for particles at 1 AU (Weidenschilling 1977). These problems led to a renewed interest in planetesimal formation through gravitational instability (Goldreich & Ward 1973; Youdin & Shu 2002; Garaud et al. 2004).

Once the planetesimals reach sizes of roughly 1 km the aforementioned problems cease to exist. These bodies couple not well enough to the gas to experience fast radial migration, and their gravitational influence is aiding their growth. An important consequence of gravity-aided growth is that the heavier bodies will grow fastest, which leads to a phase of oligarchic growth where a few large bodies dominate the dynamics of the system (Kokubo & Ida 1998, 2000, 2002). This is an important epoch in planet formation, because it covers the phase from planetesimals to planets of masses comparable to Mercury or Mars in the inner regions of the solar system, while in the outer regions the full-grown cores of giant planets may have been formed (Chambers 2006). In the core accretion model (Pollack et al. 1996) of giant planet formation these cores of several M_{\oplus} attract significant amounts of gas from the nebula which results in the end in the birth of a gas giant planet.

The alternative for the core accretion model is the gravitational instability scenario, in which a massive disk becomes gravitational unstable and fragments into giant planets (Boss 1997; Mayer et al. 2004). However, whether a disk can become unstable depends sensitively on the cooling time scale (Pickett et al. 2000, 2003) and it is not yet clear if realistic protoplanetary disks will be subject to gravitational instabilities. Furthermore, the fragments produced in numerical simulations have masses around 10 Jupiter masses (M_J), which is rather high compared to the giant planets found in extra-solar planet surveys.

One of the key differences between the two scenarios is the presence of a solid core.

Unfortunately, the existence of solid cores in gas giant planets is still subject of debate. Models of the internal structure of Jupiter (Guillot et al. 2004) can not constrain the core mass from below due to uncertainties in the equation of state near the center of the planet. However, the same models do suggest that Jupiter is enriched in solids with respect to the Sun. If Jupiter was formed by means of gravitational instability it would have had to accrete these solids in a later stage.

Accretion of solids also determines the luminosity of forming planets, which is important for future observations of protoplanetary disks. On their way to the core the accreted planetesimals deposit their energy in the gaseous envelope, which radiates away part of this energy into space. This accretion rate plays a major role in the dynamics of forming giant planets (Pollack et al. 1996).

It is therefore important to understand the process of accretion of solids onto forming planets. Greenberg et al. (1978) studied accretion onto solid cores, and the effect of gas drag was investigated by Weidenschilling & Davis (1985), who found that inward moving planetesimals will be captured in Mean Motion Resonances (MMRs). Only if the gas drag is strong enough (i.e. the planetesimals are small enough) they will make it to the surface of the planet. At first sight one might think that this slows down planetesimal accretion severely, but since their eccentricity is pumped up in the resonances collisions become much more frequent and the small debris resulting of catastrophic collisions subsequently accrete onto the planet (Weidenschilling & Davis 1985). However, Kary et al. (1993) showed that even particles small enough to move through all resonances do not always reach the surface of the planet. Instead, they are transferred into inferior orbits and they continue to move towards the central star.

These studies including gas drag assumed a uniform gas disk, but hydrodynamical simulations of planets embedded in a gaseous disk show that planets more massive than $0.1 M_J$ start to restructure their environment (e.g. D'Angelo et al. 2002, 2003). Eventually a deep gap forms in the disk for the most massive planets $M_p \geq M_J$ (Lin & Papaloizou 1993; Bryden et al. 1999). The pressure gradients associated with these gaps dramatically change the behavior of dust particles, which may lead to a dust gap while there is no gas gap (Paardekooper & Mellema 2004), and also to a substantially reduced accretion rate of solids (Paardekooper & Mellema 2006a). However, the latter study was limited in particle size and planet mass due to the fluid nature of the simulated dust component. In this Chapter we use a particle-based method to study dust accretion onto high-mass planets for arbitrary particle sizes. We focus on planets with masses large enough to affect their direct environment, $M_p \geq 0.1 M_J$. This also allows us to do two-dimensional simulations, since the measured gas accretion rates for these planets in 2D are similar to the 3D values (D'Angelo et al. 2003).

We start in Sect. 7.2 by reviewing the governing equations of motion, including the adopted gas drag law. In Sect. 7.3 we describe the numerical method used to integrate the equations of motion, and Sect. 7.4 is devoted to the disk model. In Sect. 7.5 we describe the results of the simulations, which we briefly discuss in Sect. 7.6. We conclude in Sect. 7.7.

7.2 EQUATIONS OF MOTION

Throughout we will work in a cylindrical coordinate frame (r, ϕ) with the central star in the origin. Because of the presence of a planet this is not an inertial frame, of which good use has been made in finding extrasolar planets, but we have to correct for this in the potential. The planet's orbit is circular, and the coordinate frame corotates with the planet at angular velocity Ω_p . Our unit of distance is the orbital radius of the planet, which is then located at $(r, \phi) = (1, \pi)$ throughout the simulation. The mass of the planet only enters the problem as a fraction of the stellar mass $q = M_p/M_*$. When quoting explicit planetary masses (relative to the mass of Jupiter, M_J) we assume that the central star has a mass of $1 M_\odot$. Then $1 M_J$ corresponds to $q = 10^{-3}$.

7.2.1 Gas

The evolution of the gas component of the disk is governed by the Euler equations, which for this specific case are described in detail in Paardekooper & Mellema (2006b). We do not solve the energy equation, but we use a locally isothermal equation of state:

$$p = c_s^2 \Sigma_g \quad (7.1)$$

where Σ_g is the surface density of the gas, p is the vertically integrated pressure, and the isothermal sound speed c_s is directly related to the disk thickness H :

$$c_s = H \Omega_K = h v_K \quad (7.2)$$

where Ω_K is the Keplerian angular velocity, $h = H/r$ and $v_K = r\Omega_K$. The gas has a kinematic viscosity ν , which we take to be constant throughout the computational domain. We neglect the self-gravity of the gas.

7.2.2 Dust Particles

The equations of motion for a dust particle read:

$$\frac{dv}{dt} = \frac{L^2}{r^3} - \frac{\partial \Phi}{\partial r} + f_r \quad (7.3)$$

$$\frac{dL}{dt} = -\frac{\partial \Phi}{\partial \phi} + f_\phi \quad (7.4)$$

where v denotes radial velocity, L is the specific angular momentum, Φ is the gravitational potential and \mathbf{f} is the drag force, which we specify below. The potential contains contributions from the central star, the planet and indirect terms due to the acceleration of the coordinate frame. We do not consider self-gravity for the dust particles.

7.2.3 Drag Force

The nature of the friction between gas and dust depends on the size of the dust particles relative to the mean free path of the gas molecules. This is expressed by the Knudsen number:

$$Kn = \frac{\lambda}{2s} \quad (7.5)$$

where λ is the mean free path of the gas molecules and s is the size of the dust particles under consideration. When $Kn \gg 1$ we are in the Epstein regime of free molecular flow, and the drag force is given by (Schaaf 1963):

$$\mathbf{F}_{\text{eps}} = -\pi s^2 \rho_g |\Delta \mathbf{v}| \Delta \mathbf{v} \left[\left(1 + \frac{1}{m^2} - \frac{1}{4m^4} \right) \text{erf}(m) + \left(\frac{1}{m} + \frac{1}{2m^3} \right) \frac{e^{-m^2}}{\sqrt{\pi}} \right] \quad (7.6)$$

where ρ_g is the gas density, $\Delta \mathbf{v}$ is the velocity of the dust particle relative to the gas, and m is the relative Mach number of the flow: $m = |\Delta \mathbf{v}|/c_s$. Equation (7.6) has the following asymptotic behavior:

$$\mathbf{F}_{\text{eps}} = \begin{cases} -\frac{\sqrt{128\pi}}{3} s^2 \rho_g c_s \Delta \mathbf{v} & \text{if } |\Delta \mathbf{v}| \ll c_s; \\ -\pi s^2 \rho_g |\Delta \mathbf{v}| \Delta \mathbf{v} & \text{if } |\Delta \mathbf{v}| \gg c_s. \end{cases} \quad (7.7)$$

Because Eq. (7.6) is difficult to implement numerically we interpolate between these limits in order to obtain the drag force for arbitrary velocities (Kwok 1975):

$$\mathbf{F}_{\text{eps}} = -\frac{\sqrt{128\pi}}{3} s^2 \rho_g c_s f_D \Delta \mathbf{v} \quad (7.8)$$

where

$$f_D = \sqrt{1 + \frac{9\pi}{128} m^2} \quad (7.9)$$

When $Kn \ll 1$ the drag force is given by Stokes friction:

$$\mathbf{F}_{\text{sto}} = -6\pi s k_D \mu_{\text{kin}} \Delta \mathbf{v} \quad (7.10)$$

where μ_{kin} is the kinematic viscosity of the gas, which we write as:

$$\mu_{\text{kin}} = \frac{1}{3} \rho_g v_{\text{th}} \lambda \quad (7.11)$$

where $v_{\text{th}} = \sqrt{8/\pi} c_s$ is the mean thermal velocity of the gas. Note that μ_{kin} , and therefore also \mathbf{F}_{sto} , is independent of the ambient gas density. This in contrast with \mathbf{F}_{eps} , for which a higher gas density leads to a larger force of friction.

In Eq. (7.10) the drag coefficient k_D depends on the Reynolds number Re as follows:

$$k_D = \begin{cases} 1 + 0.15 Re^{0.687} & \text{if } Re \leq 500; \\ 3.96 \cdot 10^{-6} Re^{2.4} & \text{if } 500 < Re \leq 1500; \\ 0.11 Re & \text{if } Re > 1500. \end{cases} \quad (7.12)$$

where

$$Re = \frac{2s\rho_g|\Delta\mathbf{v}|}{\mu_{\text{kin}}} = 3\sqrt{\frac{\pi}{8}} \frac{m}{Kn} \quad (7.13)$$

For flows of intermediate Knudsen number reliable expressions for the drag force are not readily available, so we just interpolate (see Woitke & Helling 2003):

$$\mathbf{F} = \left(\frac{3Kn}{3Kn+1}\right)^2 \mathbf{F}_{\text{eps}} + \left(\frac{1}{3Kn+1}\right)^2 \mathbf{F}_{\text{sto}} \quad (7.14)$$

Using Eqs. (7.8), (7.10) and (7.11) we can rewrite the total drag force as:

$$\mathbf{F} = -\sqrt{128\pi} \frac{3Kn f_D + k_D}{(3Kn+1)^2} s^2 \rho_g c_s Kn \Delta\mathbf{v} \quad (7.15)$$

Upon dividing by the mass of the dust particle, $\frac{4}{3}\pi s^3 \rho_p$, where ρ_p is the internal density of a dust particle, we can write for the force per unit mass:

$$\mathbf{f} = -\frac{\Omega_K}{T_s} \Delta\mathbf{v} \quad (7.16)$$

where Ω_K is the Keplerian angular velocity and T_s is the dimensionless stopping time:

$$T_s = \sqrt{\frac{\pi}{8}} \frac{(3Kn+1)^2}{9Kn^2 f_D + 3Kn k_D} \frac{s}{r} \frac{\rho_p}{\rho_g} \frac{v_K}{c_s} \quad (7.17)$$

Note that in the limit $|\Delta\mathbf{v}| \ll c_s$, $Re \ll 1$ Eq. (7.16) is linear in the relative velocity of the particle, which has great advantages for numerically solving the equations of motion (see Sect. 7.3).

7.3 NUMERICAL METHOD

7.3.1 Gas

We solve the flow equations for the gas using the RODEO method (Paardekooper & Mellema 2006b). This method was extensively tested on the planet-disk problem, and also used in two-fluid mode in Paardekooper & Mellema (2004). It makes use of an approximate Riemann solver, together with stationary extrapolation (Eulerink & Mellema 1995) to integrate the source terms. See Paardekooper & Mellema (2006b) for details.

7.3.2 Dust

The dust component of astrophysical fluids can in principal be described as being a continuous fluid or as a collection of particles. Both approaches have their advantages and disadvantages. The major advantage for the fluid approach is that the flow is

accurately described even in regions of very low dust density. In the particle approach these regions would be severely depleted of particles, and therefore the local resolution would be relatively poor. In the context of embedded planets, the opening of a dust gap in a gas disk (Paardekooper & Mellema 2004) should preferably be modeled using a dust fluid.

However, the fluid approach is not valid in all circumstances (Garaud et al. 2004). First of all, one fluid element (one grid cell) should contain enough dust particles to define a density, and to work with averaged velocities. Second, there should be enough interparticle collisions to make such an average meaningful. In a gas-dominated disk this means that the particles should couple reasonably well to the gas. In view of both these limitations of the fluid approach the larger particles of the dust size distribution can not accurately be modeled as a fluid. The critical size depends on the gas density and the shape of the particles, but for dust grains larger than approximately 10 μm the fluid approach breaks down at 5 AU in the Minimum Mass Solar Nebula. If locally the gas density is lowered severely, for example by a gap-opening planet, this maximum size goes down correspondingly.

Therefore in cases of low gas density the particle approach seems to be the better option, although one has to make sure that enough particles reside inside the gap in order to obtain accurate results. In this study we focus on high-mass planets that open up gas gaps in the disk, and therefore we chose for the particle approach.

In order to integrate the equations of motion numerically we used a standard second order symplectic integrator (leapfrog), in which alternately positions and velocities are updated. During a position update, velocities are assumed to be constant and vice versa:

$$\frac{d\mathbf{r}}{dt} = \mathbf{v}, \quad \mathbf{v} \text{ constant} \quad (7.18)$$

$$\frac{d\mathbf{v}}{dt} = \mathbf{a}(\mathbf{r}, \mathbf{v}), \quad \mathbf{r} \text{ constant} \quad (7.19)$$

where \mathbf{a} denotes the acceleration of the particle.

The position update is trivial. For the radial velocity update we need to solve

$$\frac{dv}{dt} = \frac{L^2}{r^3} - \frac{\partial\Phi}{\partial r} - \frac{\Omega_K}{T_s} \Delta v \quad (7.20)$$

Because we keep the gas velocity constant, the same differential equation applies to Δv . In order to make the integration scheme suited in the regime $T_s \ll 1$ we treat the drag term implicitly. Formally this can only be done in the limit $f_D, k_D = 1$ (subsonic and laminar regime). However, because supersonic drift velocities as well as high Reynolds numbers only occur when $T_s \gg 1$ this is not a problem, because then the effects of gas drag are small and there is no need to treat the drag force implicitly.

Upon differencing Eq. (7.20) we obtain:

$$\frac{\Delta v - \Delta v_0}{\delta t} = \frac{L^2}{r^3} - \frac{\partial\Phi}{\partial r} - \frac{\Omega_K}{T_s} \Delta v \quad (7.21)$$

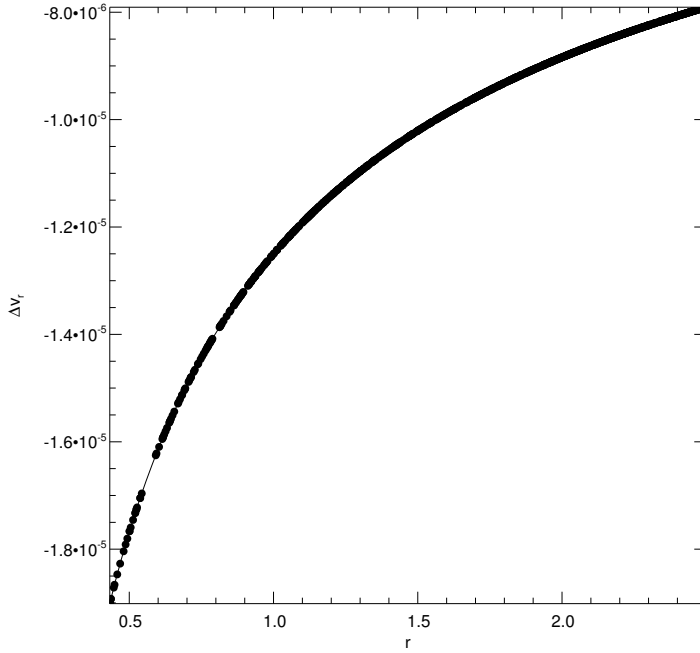


Figure 7.1: Radial velocity difference between gas and dust particles with $T_s = 0.005$.

which has the solution

$$\Delta v = \frac{\Delta v_0 + \delta t \left(\frac{L^2}{r^3} - \frac{\partial \Phi}{\partial r} \right)}{1 + \frac{\Omega_K \delta t}{T_s}} \quad (7.22)$$

A similar equation can be derived for the angular momentum equation. These equations are used to update the radial and angular velocities of the dust particles.

The method was tested in two limiting cases: $T_s = \infty$ and $T_s \ll 1$. When there is no coupling to the gas ($T_s = \infty$) the problem reduces to the restricted three-body problem, which has the Jacobi constant as an integral of motion:

$$J = E - \boldsymbol{\Omega}_p \cdot \mathbf{L} \quad (7.23)$$

where E is the total energy of the particle under consideration. We reduced the magnitude of the time step for the particle integration with respect to the hydrodynamical time step until J was conserved to 1 part in 10^6 after 100 orbits of the planet.

In an axisymmetric disk without a planet, the radial drift velocity is given by (Takeuchi & Lin 2002):

$$\Delta v = -\eta \left(T_s^{-1} + T_s \right) v_K \quad (7.24)$$

where η is the ratio of the gas pressure gradient to the stellar gravity. For uniform gas surface density, together with the temperature profile dictated by Eq. (7.2), $\eta = h^2$. We compare this analytical result with the numerical solution for $T_s = 0.005$ in Fig. 7.1, and it turns out that they are indistinguishable. This shows that our implicit integration scheme for the drag force works correctly.

We model dust accretion onto the planet by taking away all particles within one

half of the Roche lobe R_R of the planet:

$$R_R = \left(\frac{q}{3}\right)^{\frac{1}{3}} \quad (7.25)$$

where q is the ratio of the masses of the planet and the central star. The actual solid core is much smaller than this, so we do not measure the number of impacts onto this core directly. However, the high-mass planets that we consider in this Chapter are able to capture a dense gaseous envelope that is able to efficiently direct particles towards the center of the planet (see also Paardekooper & Mellema 2006a). We do not take away gas from the computational domain, as has been done before to mimic gas accretion (Lubow et al. 1999; D'Angelo et al. 2002; Paardekooper & Mellema 2006b). The process of accretion only influences the density structure close to the planet, and therefore this does not influence the results on dust accretion.

7.4 INITIAL AND BOUNDARY CONDITIONS

The gas disk model is the same as in Paardekooper & Mellema (2004). The surface density of gas and dust particles is uniform initially, and we take the gas disk thickness to be $H = 0.05 r$, so $h = 0.05$, which is the canonical value for simulations of planet-disk interaction. In order to compensate for the radial pressure gradient dictated by Eq. (7.1) the gas orbits at a slightly sub-Keplerian angular velocity, while the dust particles are on exact Keplerian orbits initially. We take all initial radial velocities of gas and dust to be zero. The gas has an anomalous viscosity ν that is parametrized by the usual α -prescription (Shakura & Sunyaev 1973):

$$\nu = \alpha c_s H \quad (7.26)$$

We adopt $\alpha = 0.004$ at the location of the planet.

In order to calculate the stopping time in Eq. (7.17) we need a value for the gas density. We fix the initial density to be $10^{-11} \text{ g cm}^{-3}$ at $r = 1$, which is appropriate for the location of Jupiter in the Minimum Mass Solar Nebula. From the gas density we can calculate the mean free path of gas molecules:

$$\lambda = \frac{m_{\text{H}_2}}{\pi \rho_g r_{\text{H}_2}^2} \quad (7.27)$$

where m_{H_2} and r_{H_2} are the mass and radius of an H_2 molecule, respectively. The internal particle density ρ_p is 1.25 g cm^{-3} . Using these parameters, we can calculate T_s as a function of particle size s (but note that T_s also depends on $|\Delta \mathbf{v}|$ through the factors f_D and k_D).

The dust density does not enter the equations of motion as long as it remains much smaller than the gas density. If not, the gas is affected by the drag force from the dust particles. We assume that initially the dust-to-gas ratio is equal to 1:100, and that we therefore can ignore the feedback on the gas. We vary the number of dust particles N typically from 5000 to 10^6 .

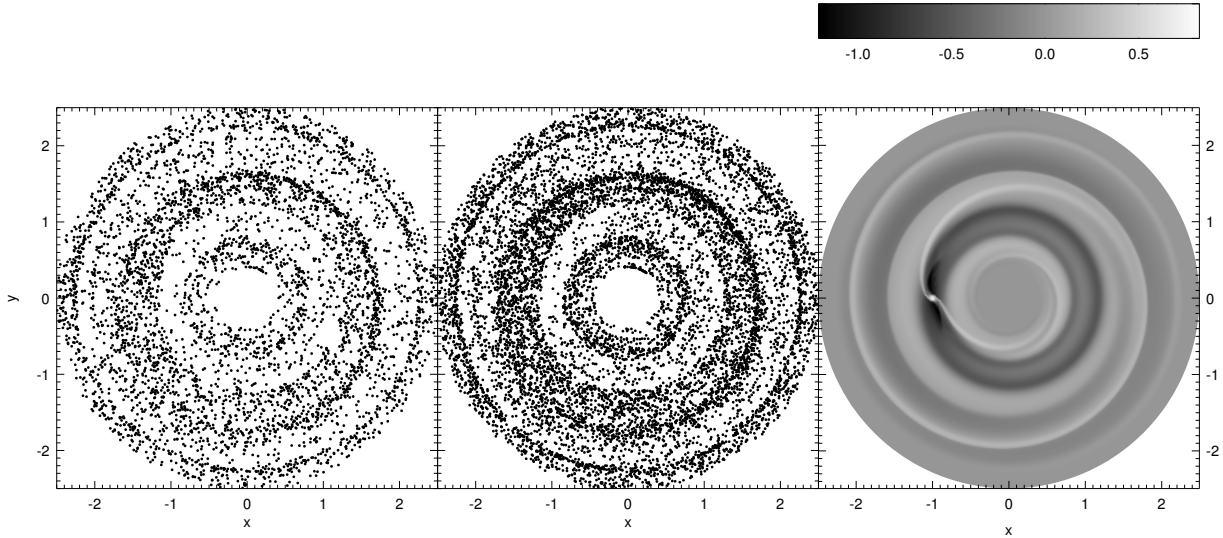


Figure 7.2: Density structure after 50 orbits of a $1 M_J$ planet around a solar mass star. Left panel: particle distribution ($T_s = 0$), $N = 5000$. Middle panel: particle distribution ($T_s = 0$), $N = 10000$. Right panel: logarithm of the gas surface density.

The computational domain extends from $r = 0.4$ to $r = 2.5$ in the radial direction, and from $\phi = 0$ to $\phi = 2\pi$ in azimuth. This domain is covered by a uniform grid consisting of 128 radial and 384 azimuthal cells which is used to evolve the gas component of the disk.

We take the boundary conditions for the gas to be non-reflecting (Godon 1996; Paardekooper & Mellema 2006b), in order to keep the waves generated by the planet from reflecting back into the computational domain. When a dust particle moves off the computational domain we remove it from the simulation.

7.5 RESULTS

We have performed simulations with different particle sizes in order to sample the parameter space in stopping time ranging from the limit of perfect coupling $T_s = 0$ to the limit of no coupling $T_s = \infty$. The former limit offers an opportunity to compare the measured accretion rates to the gas accretion, so we will start by discussing perfectly coupled particles.

7.5.1 Perfect coupling

First of all we discuss the case for $T_s \ll \Omega_K \Delta t$, where Δt is the magnitude of the time step as required for the integration of the Euler equations. For such a small value of the stopping time the dust particles are forced to move with the gas velocity, and the dust-to-gas ratio remains the same everywhere. In particular, gas and dust accretion rates should be equal as well, when we correct for the factor 100 in the dust-to-gas

ratio.

Gas accretion onto embedded planets has been studied before using different numerical approaches (Lubow et al. 1999; D'Angelo et al. 2002; Paardekooper & Mellema 2006b), and they were found to agree reasonably well with each other. There is no strong dependence on the details of the accretion procedure (differences remain within $\sim 40\%$), except for intermediate mass planets for which the Roche lobe is approximately equal to the disk scale height. For these planets, accretion depends strongly on the conditions inside the Roche lobe and the measured accretion rates differ up to a factor of 2. Therefore we focus on a $1 M_J$ planet, for which a well-defined gas accretion rate has been measured of $\dot{M} = 10^{-4}$ disk masses per orbit; a value that we would like to reproduce for the perfectly coupled dust particles. Typically this value was reached within 200 orbits of the planet.

We have varied the number of particles in the simulation from 5000 to 10^5 . Note that in order to accurately measure an accretion rate the number of particles that is accreted onto the planet every orbit should be larger than one. For an accretion rate of 10^{-4} disk masses per orbit the total number of particles in the simulation N therefore needs to be larger than 10^4 . For a smaller value of N we need to rebin the accreted particles into larger time intervals. The loss of time resolution is of no importance for the final accretion rate because it does not vary rapidly after ~ 50 orbits.

In Fig. 7.2 we show the particle distribution for a simulation of a $1 M_J$ planet after 50 orbits. In the gas density (right panel) we see the gap that is developing, as well as the prominent spiral waves excited by the planet. For a run with 10000 particles (middle panel) we can clearly see the gap and also the spiral waves in regions where the particle density is high enough. However, in the gap region near the planet, where in the gas density we see the origin of the spiral waves, nothing is to be seen in the particle density. This is because the spatial resolution in a particle simulation critically depends on the particle density. In regions of low density, as in the case of a disk gap, the resolution is correspondingly low and the spiral waves are not visible. This is of no concern for the outcome of these simulations, however, because the dust density has no dynamical effect. If the density was used for example in calculating the number of collisions between these particles, which in turn would create smaller dust grains, resolution effects would play an important role. The same would be true if the dust density becomes high enough that the gas feels its drag. The only thing we need to worry about for these simulations is that we accrete enough particles per time step (see above).

Even if we lower the number of particles N to 5000 there is still density structure visible (left panel of Fig. 7.2). The outer edge of the gap is less sharp than in the case of $N = 10000$, but all features in the density can still be identified.

Also, if we look at the accretion rates for different values of N in Fig. 7.3 the results look promising, as expected. After 200 orbits, the amount of disk mass that was accreted for the various number of simulated particles differs less than 15%. Even more, the final accretion rates agree very well, yielding a mean value of $\dot{M} = 9.5 \cdot 10^{-5}$ disk masses per orbit, in close agreement with the value that came out of gasdynamical simulations. The total mass that is accreted as well as the slightly lower accretion rates

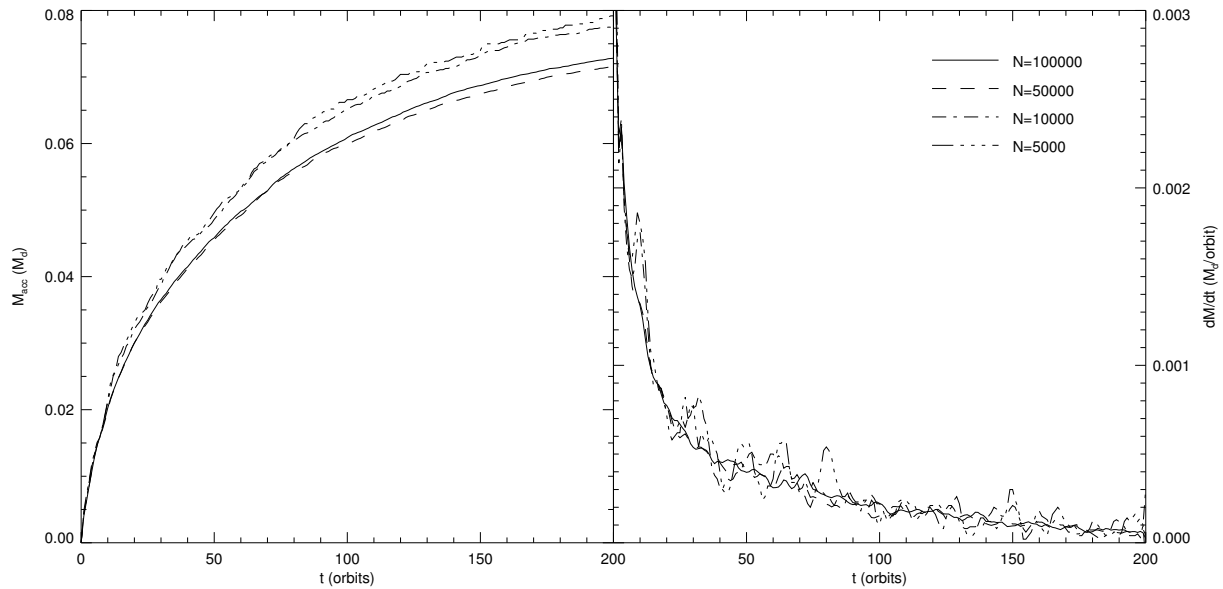


Figure 7.3: Accretion of perfectly coupled particles onto a $1 M_J$ planet for four different amounts of particles. Left panel: accreted dust mass in units of the total dust mass in the disk. Right panel: corresponding accretion rates, in disk masses per orbit.

can be attributed to the large imposed accretion inside the Roche lobe. While for the gas case one usually takes out a small *fraction* of the density away from the accretion region every time step, for our particle simulations we remove *all* particles from the inner half of the Roche lobe. Such a high imposed accretion rate tends to decrease the total amount of mass that is accreted (see Fig. 7 of Paardekooper & Mellema 2006b).

We conclude that we are able to reproduce the gas accretion rates in the limit of perfectly coupled particles, and that we only need a relatively small amount of particles to achieve this.

7.5.2 No coupling

When we increase the size of the particles the stopping time increases as well. We can distinguish three regimes:

- $T_s \ll 1$: the motion of the particles is dominated by gas drag. However, significant gas-dust separation may occur in the presence of planets on time scales of approximately $\Omega_K^{-1} T_s^{-1}$ (see Paardekooper & Mellema 2004).
- $T_s \gg 1$: particle motion is dominated by gravitational interaction with the star and the planet, with the gas drag as a small perturbation.
- $T_s \approx 1$: the orbital time scale for a particle is comparable to the time scale for gas drag. Depending on the gas density, there may be region in which either gas drag or gravity will dominate.

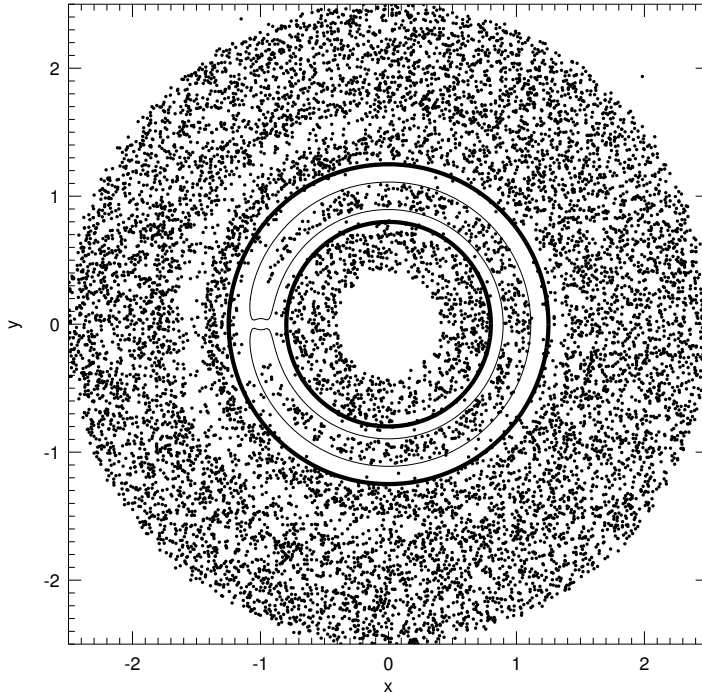


Figure 7.4: Particle distribution ($N = 10000$) for $T_s = \infty$ after 500 orbits of a $1 M_J$ planet. Thick contours mark the boundary of the accretion region of the planet. The thin contour gives the corresponding zero-velocity curve.

In this section we will focus on the limit of no coupling to the gas. For these particles the problem is equivalent to the restricted three-body problem, and therefore we can gain some insight by examining the integral of motion of the problem, J (see Eq. (7.23)). In particular, the motion of a particle is confined to a region bound by so-called zero-velocity curves, which can be obtained by solving Eq. (7.23) for a given value of $J = J_0$ and all velocities equal to zero. Particles with a starting value $J = J_0$ will never cross the zero-velocity curve associated with J_0 . This means that the region in the disk from which the planet may accrete particles is also bounded, and once this feeding zone is empty accretion will stop.

In Fig. 7.4 we show the particle distribution after 500 orbits of the planet for $T_s = \infty$ and $N = 10000$. The region close to the planet is almost empty, and two annular empty rings appear at approximately $r = 1$ and $r = 0.9$. Particles in these rings travel on horseshoe orbits and suffer close encounters with the planet, which leads to accretion of these particles. Material that orbits further away from the planet ($r > 1.1$ and $r < 0.9$) can not reach the planet because of the constraint set by the Jacobi integral. The thick contours mark the radii at which particles may *just* make it to the planet, which is shown by the zero-velocity curve (thin contour) corresponding to the Jacobi constant at the location of the thick contour. For particles orbiting outside the region $0.9 \leq r \leq 1.1$ their zero-velocity curve prevents them from reaching the planet.

The thick contours trace the outer edges of the feeding zone reasonably well, and almost all particles initially located just inside this feeding zone are accreted by the planet. However, particles closer to $r = 1$ do not suffer close encounters with the planet: they move on stable tadpole orbits and will not be accreted. In the solar system similar objects can be found around the orbit of Jupiter: the Trojan asteroids. The end

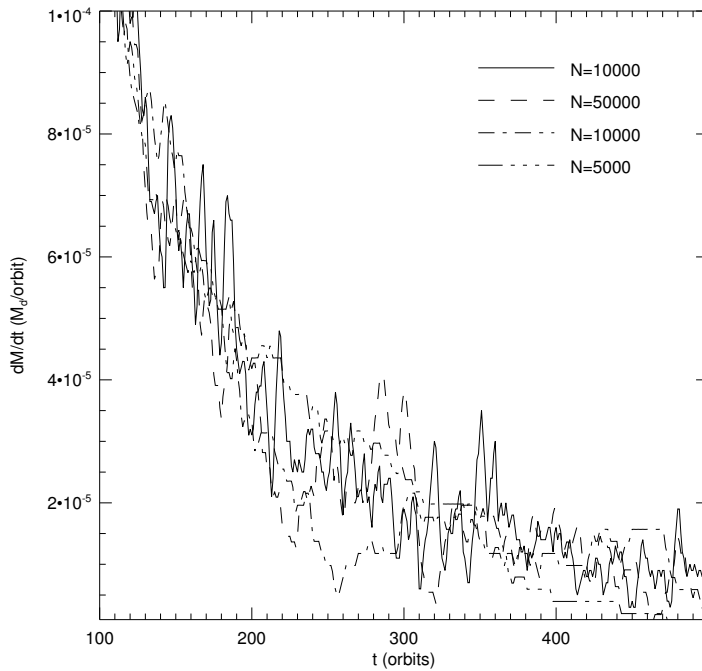


Figure 7.5: Accretion of uncoupled particles onto a $1 M_J$ planet for four different amounts of particles.

result of the simulation is a particle distribution with two empty “rails” at a radial distance of 0.1 from the planet, together with a non-empty corotation region. The empty semi-circle outside the orbit of the planet is due to resonant perturbations of the 2:1 outer mean motion resonance.

In Fig. 7.5 we show the accretion rate up to 500 orbits for the same simulation, for four different values of N . Before $t = 100$ (not shown in the figure) the accretion rate is very high, and the planet accretes roughly 10 % of the total disk during that time. However, after approximately 120 orbits the accretion rate drops below the gas accretion rate (10^{-4} disk masses per orbit) and it continues to decline for the whole simulation time. After 500 orbits the particle accretion rate is an order of magnitude below the gas accretion rate, which makes further dust accretion negligible.

All particles were started on circular orbits until now, while mutual gravitational interactions between larger boulders leads to eccentricity excitation (Greenzweig & Lisauer 1990, 1992). The eccentricity of the particles’ orbits determines the width of the accretion zone, and therefore the total mass that may be accreted. However, because the feeding zone is still bounded the accretion rate will still tend to zero after a certain amount of time. This is illustrated in Fig. 7.6, where we show the accretion rates for three different initial eccentricity distributions. All eccentricities in the specified range were uniformly distributed amongst the particles. It is clear that from approximately 130 orbits the accretion rate is the same for all initial eccentricities, which is the same time scale as for the clearing of the feeding zone (see above). Therefore a non-zero initial eccentricity for the planetesimals enlarges the accretion zone, and therefore increases the total amount of mass that can be accreted (see the left panel of Fig. 7.6), but it does not affect the time scale on which the feeding zone is cleared.

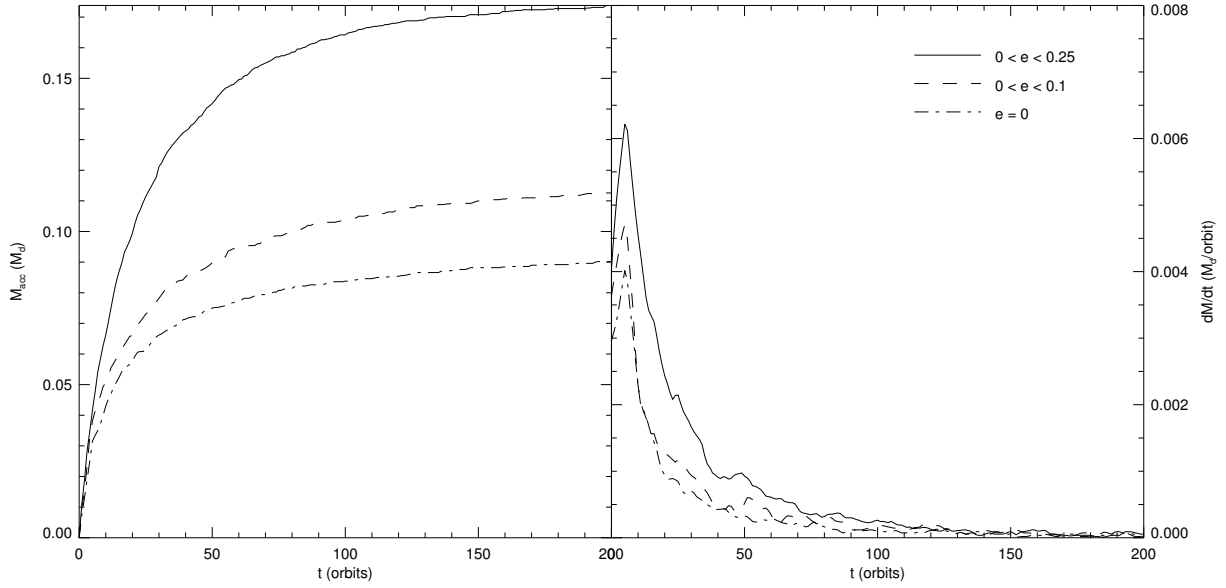


Figure 7.6: Accretion of uncoupled particles ($N = 5000$) onto a $1 M_J$ planet for three different initial eccentricity distributions. Left panel: accreted dust mass in units of the total dust mass in the disk. Right panel: corresponding accretion rates, in disk masses per orbit.

7.5.3 Steady gas disk

Clearly, the feeding zone needs to be replenished one way or the other in order for accretion to continue. In this section, we explore the possibility that gas drag may prevent the feeding zone from getting empty. We do this by keeping the gas disk steady, in order to separate the effects on accretion of a non-uniform gas disk from effects due to pure dust dynamics. Also this gives us an opportunity to compare with previous work by Kary et al. (1993).

Based on Eq. (7.24) one might expect that dust accretion would always be stronger than gas accretion. Because the mass that flows inward through a circle with radius r equals:

$$\dot{M} = -2\pi r \Sigma v_r \quad (7.28)$$

the ratio of gas and dust accretion rates would be given by:

$$\frac{\dot{M}_d}{\dot{M}_g} = \frac{2\pi r \Sigma_d v_{r,d}}{2\pi r \Sigma_g v_{r,g}} = d \left(1 + \frac{\Delta v}{v_{r,g}} \right) \quad (7.29)$$

where d is the dust-to-gas ratio and Δv is given by Eq. (7.24). In an unperturbed disk with constant surface density and kinematic viscosity ν the radial velocity of the gas is equal to $v_{r,g} = -\frac{3\nu}{2r}$, and therefore we have:

$$\frac{\Delta v}{v_{r,g}} = \frac{h^2 (T_s^{-1} + T_s) v_K}{\frac{3}{2}\alpha c_s h} = \frac{2 (T_s^{-1} + T_s)}{3\alpha} \quad (7.30)$$

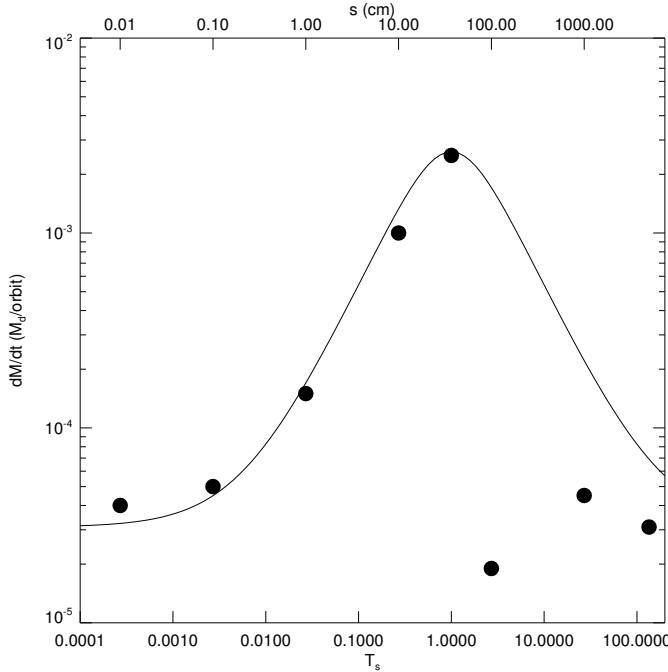


Figure 7.7: Accretion of particles onto a $1 M_J$ planet. The solid line gives the accretion rate of dust particles predicted by Eq. (7.24). All runs included 5000 particles.

When all dust grains have the same stopping time T_s the gas-dust mixture that is accreted by the planet has an effective dust-to-gas ratio of

$$d^* = d \left(1 + \frac{2(T_s^{-1} + T_s)}{3\alpha} \right) \quad (7.31)$$

Using $\alpha = 0.004$, already for $T_s = 0.001$ the planet would get enriched in solids by more than 15 %.

However, the planet may not be able to grab all the material that is passing by (Kary et al. 1993) which leads to lower dust accretion rates. Gas, however, may be accreted at a *higher* rate than predicted by Eq. (7.28) (see Lubow et al. 1999; Lubow & D'Angelo 2006). It is therefore not clear, even in an unperturbed gas disk, how dust accretion compares to gas accretion.

In Fig. 7.7 we show the dust accretion rates of dust particles onto a $1 M_J$ planet as a function of particle size. Note that we do not take into account effects of the particle size distribution in the disk: the accretion rates shown would be valid if *all* particles in the disk would have a single size. The solid line gives the accretion rate predicted by Eq. (7.28) with the radial velocity of Eq. (7.24). Towards the lowest values of s (and therefore the lowest values of T_s) it approaches the value of the gas accretion. Note, however, that this is not the *measured* gas accretion rate, which is higher due to the high accretion efficiency of the planet (Lubow et al. 1999).

Particles $T_s \ll 1$ have a small radial velocity, and they can essentially all be captured by the planet. This results in Fig. 7.7 in accretion rates close to the predicted value for the smallest particles. When T_s increases towards 1, the radial velocity of the dust particles increases, but at the same time it is easier for the planet to accrete them because

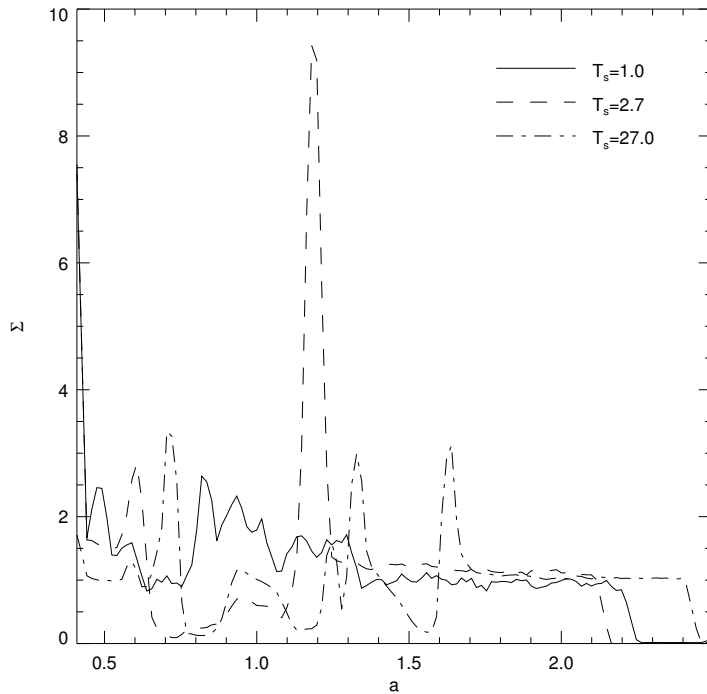


Figure 7.8: Particle surface density after 50 orbits of a $1 M_J$ planet and three different values for T_s .

they suffer no strong gas friction. Therefore essentially all particles with $T_s < 1$ can be accreted by the planet.

For larger particles a dramatic change in accretion rate occurs. Increasing the size of the particles by less than a factor of three leads to a reduction of accretion by almost two orders of magnitude. The reason for this low accretion rate lies in the mechanism of resonance trapping (Weidenschilling & Davis 1985), where inward moving particles are captured in mean motion resonances (MMRs). The drag force that moves the particles inward is exactly balanced by resonant perturbations which are directed away from the planet. This is illustrated in Fig. 7.8, where we show azimuthally averaged particle surface density as a function of particle semi-major axis a . Because the eccentricities remain below 0.1 (see Fig. 7.9), a almost coincides with r .

The solid line in Fig. 7.8 corresponds to the particles size responsible for the peak of the accretion rate in Fig. 7.7, $s = 37.0$. There is a lot of structure near the position of the planet, but no gap is forming and there is no structure in the outer disk. Note that the surface density goes to zero at $a \approx 2.25$ because of the movement of the particles towards the central star. In the inner disk a small feature is visible at $a = 0.48$, which we can attribute to the 1 : 3 MMR. Note, however, that these structures in the *inner* disk are not stable: resonant perturbations as well as gas drag both push the particles inward.

When we increase the particle size by less than a factor of three (dashed line in Fig. 7.8) the situation is remarkably different. Near $a = 1$ an annular gap starts to form, together with a strong overdensity at $a = 1.2$, which is close to the 4:3 mean motion resonance ($a \approx 1.21$). Apart from this large peak there is no structure in the outer disk. The inner disk shows a feature near the 1:2 MMR at $a = 0.63$.

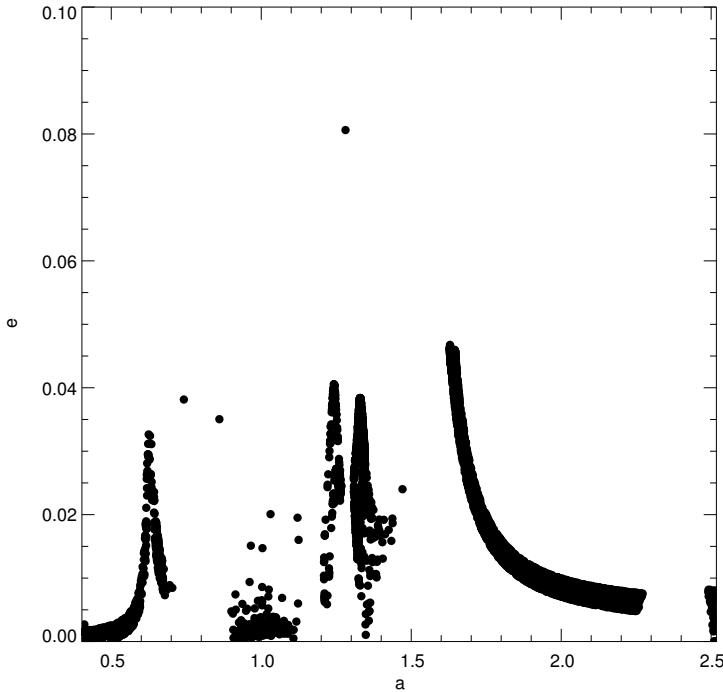


Figure 7.9: Particle semi-major axis versus eccentricity after 200 orbits of a $1 M_J$ planet and $s = 1000$ cm ($T_s \approx 27.0$).

Increasing the particle size by another factor of 10 again changes the picture (dash-dotted line in Fig. 7.8). Now the feature at $a = 1.2$ has disappeared and instead we can see a peak near the 2:1 MMR at $a = 1.6$, together with a feature at $a = 1.3$, which corresponds to the 3:2 MMR. In the inner disk the 2:3 MMR is excited at $a = 0.76$.

It is clear from Fig. 7.8 that resonance trapping occurs when $T_s > 1$, and that weaker-coupled particles may occupy lower-order resonances. Close to a resonance the eccentricity of a particle is excited. In Fig. 7.9 we show the eccentricity e of the particles' orbits for the $T_s = 27.0$ case from Fig. 7.8. At the location of the 2:1 MMR e is excited to a maximum of approximately 0.05, which is consistent with the analytical result of Weidenschilling & Davis (1985) who showed that the equilibrium eccentricity for a particle in a $(j + 1) : j$ MMR is approximately given by $\bar{e} = 0.07/\sqrt{j + 1}$.

Resonance trapping occurs because resonant perturbations tend to change the semi-major axis of the particle's orbit in such a way that it moves away from the planet. For outer resonances, this means that this effect opposes the drag-induced inward migration. Inner resonances can never trap particles in a stable way, unless the drag force is directed outward. This may happen when a strong gas density gradient is present, possibly at the outer edge of a gas gap in the disk.

The strength of a resonance $(j + 1) : j$ depends on the mass planet-to-star mass ratio q as well as on the order of the resonance j . Higher order resonances, which are located closer to the planet, are stronger and they can stop inward moving particles more easily. Therefore the location at which a particle is stopped by resonant perturbations depends on the particle size s . This is clear from Fig. 7.8, where particles with $T_s = 27.0$ ($s = 1000$ cm) become trapped in the $j = 1$ resonance, while particles with $T_s = 2.7$ ($s = 100$ cm) move all the way to the $j = 3$ resonance. Weidenschilling &

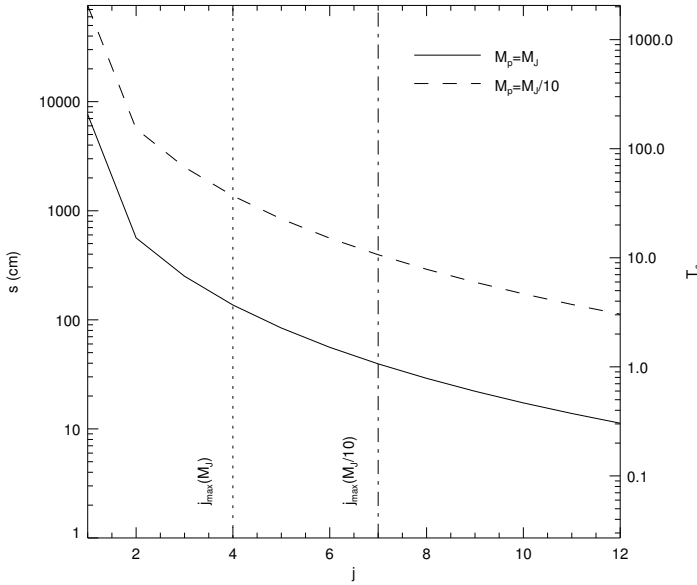


Figure 7.10: Minimum particle size that can be trapped in the j^{th} resonance, for a $1 M_J$ planet and a $0.1 M_J$ planet. The vertical lines mark the onset of chaotic orbits for high j .

Davis (1985) derived a minimum size for a particle that is able to move through the j^{th} resonance:

$$s_{\min} = \frac{\rho_g h r_p}{3 \rho_p q C(j) j^{3/2}} \quad (7.32)$$

where $C(j)$ is an increasing function of j . For particles smaller than s_{\min} the drag force is stronger than the resonant perturbations and the particles are able to move inward through the resonance. Because s_{\min} becomes smaller for higher values of j they may get trapped in a resonance closer to the planet.

For higher values of j , successive resonances are more closely spaced and their overlap may lead to chaotic behavior (Wisdom 1980). The distance at which this happens is approximately (Duncan et al. 1989):

$$|r - r_p| \approx 1.5 q^{2/7} \quad (7.33)$$

For a planet of $1 M_J$ this means that particles cannot be trapped closer than $|r - r_p| = 0.2$. It is interesting to note that this is also approximately equal to the width of the gas gap that is opened by a planet of the same mass (see Bryden et al. 1999; Paardekooper & Mellema 2006b).

In Fig. 7.10 we show s_{\min} as a function of j for a $1 M_J$ planet and a $0.1 M_J$ planet. Also shown are the maximum values of j for which no chaotic orbits exist (from Eq. (7.33)). Focusing on the $1 M_J$ planet we see that only particles smaller than approximately 100 cm are able to travel through the $j = 4$ resonance, beyond which no stable trapping exists because of Eq. (7.33). In terms of accretion onto the planet this means that only particles smaller than 100 cm are sufficiently coupled to the gas to make it all the way to the surface of the planet. From Fig. 7.7 we see that indeed the large jump in accretion rate happens around $s = 100$ cm. Our numerical result for s_{\min} agrees within a factor of 2 with Eq. (7.32).

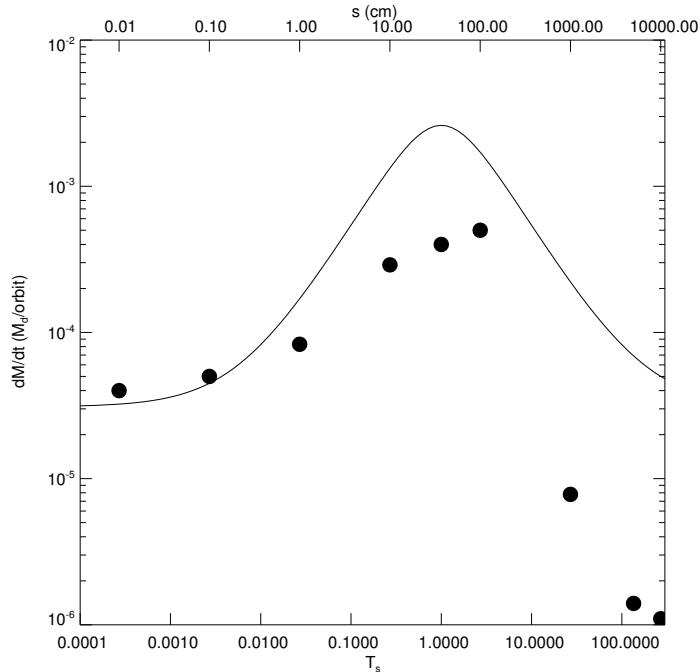


Figure 7.11: Accretion of particles onto a $0.1 M_J$ planet. The solid line gives the accretion rate of dust particles predicted by Eq. (7.24).

From Fig. 7.7 it is clear that essentially *all* particles that make it through the resonances are eventually accreted by the planet. This is not true in general (Kary et al. 1993), and especially for low-mass planets a significant fraction of particles that cross the orbit of the planet are transferred to the inner disk rather than to be accreted onto the planet. This is illustrated for the case of $q = 10^{-4}$ in Fig. 7.11. Moving from the smallest towards the largest particles (from left to right in Fig. 7.11) we see three classes of particles:

- I. Particles with $s < 1$ cm are very strongly coupled to the gas, which makes their radial velocity low enough for them to always reach the planet.
- II. Particles with $s > 1000$ cm are again trapped in exterior resonances, and the accretion rate is therefore very low.
- III. In between, there is a steady flow of particles onto the planet but there is a significant fraction of particles that misses the planet.

The transition from Class III to Class II happens again approximately at the size predicted by Eq. (7.32) (see also Fig. 7.10). The deviation from the accretion rate given by Eq. (7.24) for Class III particles seems to increase with s , except for the largest Class III particle at $s = 100$, which has a relatively high accretion rate.

From Figs. 7.7 and 7.11 we conclude that particles that are trapped in exterior resonances are excluded from accretion onto the planet. Only particles smaller than s_{\min} may reach the planet, where s_{\min} is approximately given by Eq. (7.32). Particles with for which $1 \text{ cm} \leq s \leq s_{\min}$ potentially have a higher accretion rate than the gas.

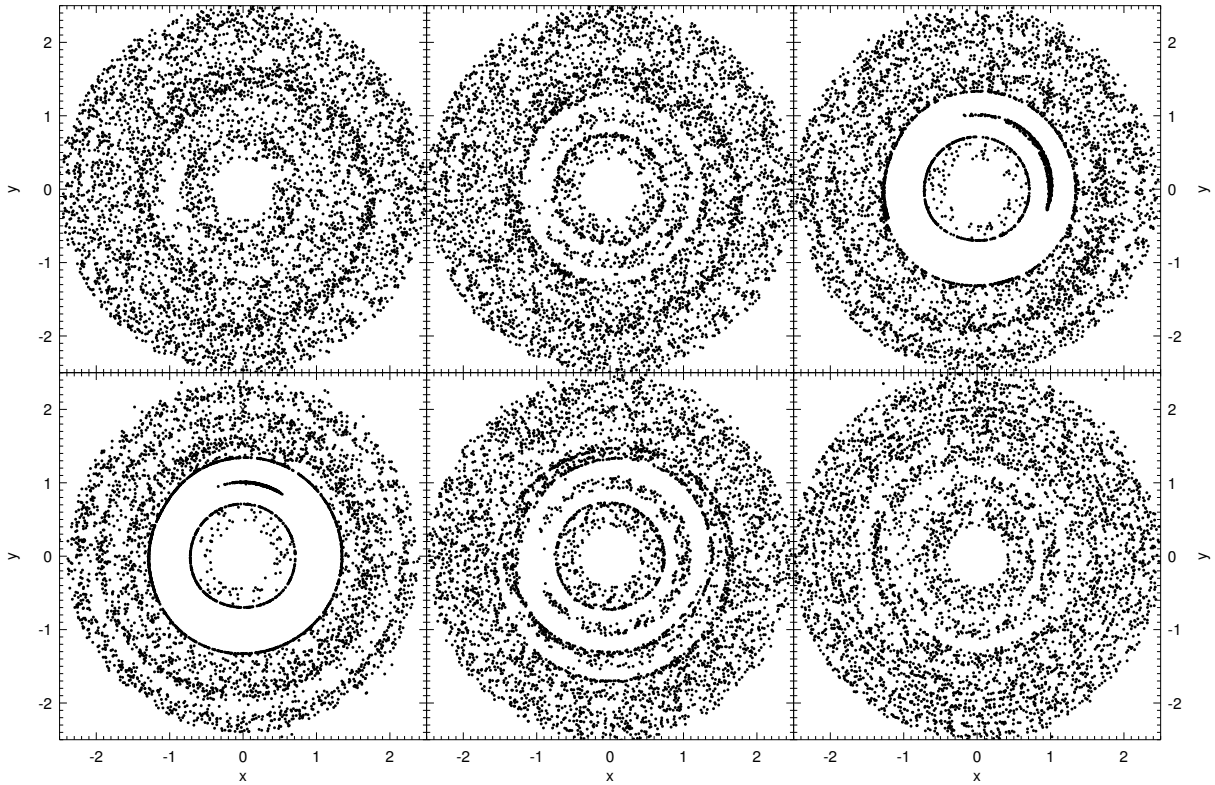


Figure 7.12: Particle distribution after 20 orbits of a $1 M_J$ planet for 6 different particle sizes. Top row, from left to right: $s = 0$ (perfect coupling, $T_s = 0$), $s = 1.0$ cm ($T_s = 0.027$) and $s = 10.0$ cm ($T_s = 0.27$). Bottom row, from left to right: $s = 37.0$ cm ($T_s = 1.0$), $s = 1000.0$ cm ($T_s = 27.0$) and $s = \infty$ (no coupling, $T_s = \infty$).

7.5.4 Evolving gas disk

However, when planets get massive enough to attract significant amounts of gas and dust they also start to reshape the surrounding disk. Planets as massive as Jupiter open up a deep gas gap in the disk, but already Neptune-class planets restructure the gas disk in such a way that a *dust* gap emerges, even though there is no gap in the gas (Paardekooper & Mellema 2004). It was also shown that this leads to a dramatic decline in dust accretion (Paardekooper & Mellema 2006a) for particles larger than 0.1 cm. In this section we want to study the general case of dust accretion onto high-mass planets.

We start by inspecting the particle distribution after 20 orbits of a $1 M_J$ planet in Fig. 7.12. From the upper left panel to the lower right panel the stopping time increases from $T_s = 0$ (perfectly coupled particles, see Sect. 7.5.1) to $T_s = \infty$ (uncoupled particles, see Sect. 7.5.2). After 20 orbits the planet did not get a chance to open up a gap in the gas yet, as is clear from the upper left panel. The uncoupled particles in the lower right panel also do not clear a whole gap, but instead two empty "rails" (see also Fig. 7.4).

For particles with $T_s = 0.027$ (upper-middle panel in Fig. 7.12) we see that the pressure gradients at the edges of the forming gap are pushing the particles away from

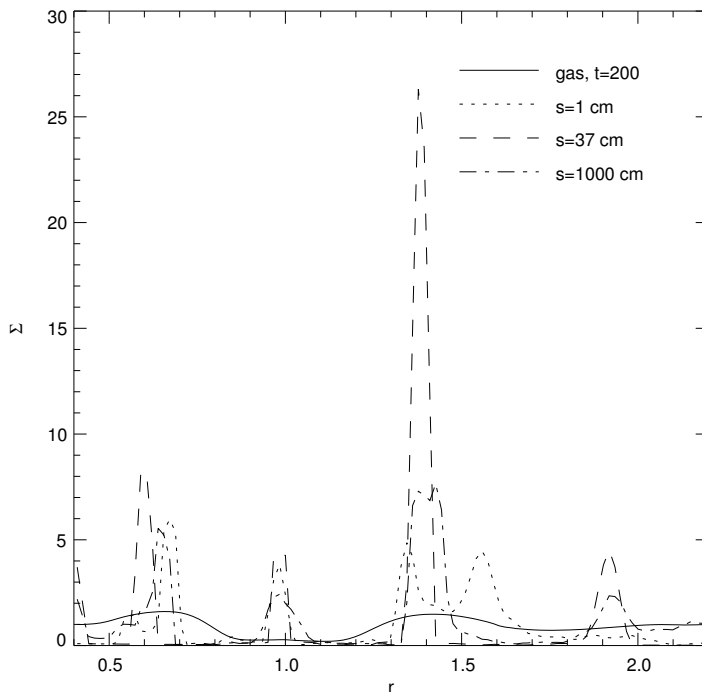


Figure 7.13: Azimuthally averaged surface density of gas and dust after 100 orbits of a $1 M_J$ planet for three different particle sizes.

the planet's orbit, as was also observed in Paardekooper & Mellema (2004) for a ten times less massive planet. Because of the high mass of the planet in Fig. 7.12, and the corresponding large pressure gradients, the effect takes place on much shorter time scales. Note also that because of the forming gap the gas density is already significantly lower near the orbit of the planet, and consequently the particles couple not as well to the gas as at the start of the simulation. This, together with the larger pressure gradients at the gap edges accounts for the fast evolution of the dust component of 1 cm.

When the stopping time approaches 1 the drift velocity of the particles becomes so large that already after 20 orbits of the planet an almost empty gap has formed (upper right and lower left panel of Fig. 7.12). The particles accumulate at the gap edges and at corotation. The latter because when a gas gap is forming the density at $r = 1$ is always larger than at $|r - 1| = 0.1$ (see Kley 1999; Paardekooper & Mellema 2006b), and the corresponding pressure gradient pushes the dust particles towards $r = 1$. However, when the gas gap is sufficiently clean (which happens after approximately 100 orbits) this pressure gradient disappears and the particles near $r = 1$ will be dragged inward.

When $T_s > 1$ (lower middle panel in Fig. 7.12) we see again that the pressure gradient associated with the edges of the gas gap stimulate the formation of the two empty "rails" compared to the case of no coupling. The first signs of resonant capture can be seen as a dark eccentric ring outside the planet's orbit. Because these particles do not couple well to the gas it becomes progressively harder to clean the corotation region while the gas gap is forming. Particles larger than 1000 cm are not removed from the corotation region before the gas gap is complete, which makes the horseshoe-shaped feature at $r = 1$ almost permanent just as in the case of no coupling.

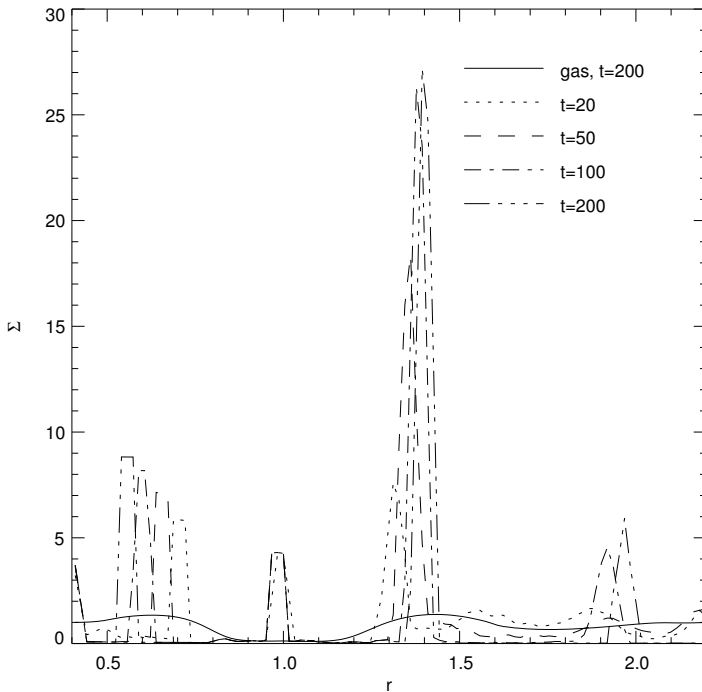


Figure 7.14: Particle surface density ($s = 37$ cm) around a $1 M_J$ planet at different times.

At later times, resonant trapping comes to dominate the density structure of the largest particles. In Fig. 7.13 we show the azimuthally averaged surface density after 100 orbits of the planet for the gas and for three different particle sizes. The first thing that catches the eye is the large peak in the density of particles with $s = 37$ cm. The gas density (solid line in Fig. 7.13) reveals that the pressure gradients around the peak all point *away* from $r = 1.4$. This makes this location an efficient dust trap for basically all material originally located at $1.1 < r < 1.8$. Locally the surface density is increased with a factor of 25.

The smaller particles (1 cm) move slower with respect to the gas than the 37 cm particles. As a result two peaks can be seen near $r = 1.4$: one from outward moving particles coming from $r \approx 1$ and one from inward moving particles coming from $r > 1.7$. The large particles of 1000 cm also show a double-peaked feature. Note that the density gradient near the 2:1 MMR at $r = 1.6$ is such that the particles are dragged inward more efficiently than in the case of the steady gas disk. Therefore while Fig. 7.10 predicts that the 1000 cm particles should be captured in the 2:1 MMR they are able to move all the way to $r \approx 1.4$.

In Fig. 7.14 we show the time evolution of the surface density of particles of 37 cm. Four distinct features can be distinguished at $r \approx 0.6$, $r \approx 1$, $r \approx 1.4$ and $r \approx 1.9$, which are all due to the density structure in the disk. We have already mentioned the large peak near $r = 1.4$, which builds up largely from the inside within 100 orbits. Note that the peak slowly moves outward but stops near $r = 1.4$, because it has arrived at a pressure maximum.

For the peak near the inner edge of the gas gap at $r = 0.6$ the situation is slightly different. Again, the peak is moving slowly but this time the density gradient inside

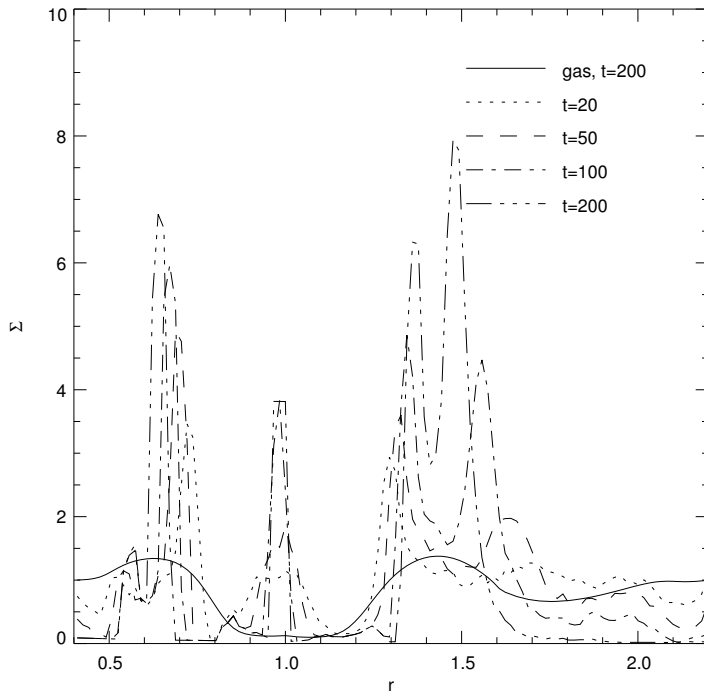


Figure 7.15: Particle surface density ($s = 1$ cm) around a $1 M_J$ planet at different times.

$r = 0.6$ is not strong enough to stop the particles completely. The peak slows down, but continues steadily towards the inner boundary and in the end it will move off the grid.

The peak at corotation is steady. Because the gas density has dropped approximately 2 orders of magnitude, the effective stopping time at $r = 1$ has increased from 1.0 to 100.0. This means that it will take several hundreds of orbits more to remove this feature. Finally, a small outward moving feature can be seen associated with the density gradient near $r = 1.9$. Note that resonant trapping is not important for particles of $s = 37$ cm, which agrees with Fig. 7.7. However, the density gradients induced by the planet are so large that even particles of 1000 cm are not captured in the 2:1 MMR.

The behavior of particles of 1 cm is shown in Fig. 7.15. First thing to note is the absence of the density feature near $r = 1.9$, which is due to the stronger gas drag that makes the particles follow the inward viscous motion of the gas. Near $r = 1.4$ we can clearly see the two density peaks originating from both sides of the gas density maximum slowly moving towards each other. In contrast with the 37 cm particles from Fig. 7.14 the outer peak is the strongest, which is due to the lacking feature near $r = 1.9$. Particles of 37 cm originally located at $r = 1.8$ move outward, while their 1 cm counterparts move inward and contribute to the inward moving peak near $r = 1.4$.

From Fig. 7.12 we conclude that the particles that had the largest accretion rate in Fig. 7.7 actually create the cleanest dust gaps. Already after 20 orbits the feeding zone is almost empty, and this has severe implications for the accretion rates. In fact, for all particles that open dust gaps the accretion rate equals zero after a finite amount of time.

This is illustrated in Fig. 7.16, where we show the accretion rate for four different

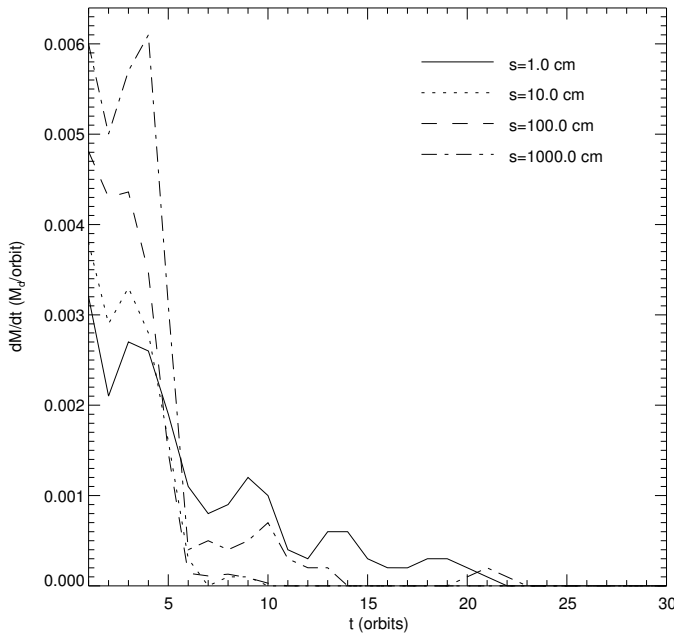


Figure 7.16: Accretion of particles onto a $1 M_J$ planet and an evolving gas disk for four different particle sizes. After 30 orbits, all accretion rates stay exactly zero.

particle sizes. After only 30 orbits, all accretion rates stay exactly zero. Note that this is unlike all previous models: for perfectly coupled particles as well as uncoupled particles there was still residual accretion after 200 orbits (see Fig. 7.5). This shows how powerful pressure structure in the disk is when it comes to moving dust particles.

The time scale at which accretion stops depends on the stopping time. The shortest time scales correspond to particles of 10 and 100 cm, which have an initial stopping time of $T_s \approx 1$. Smaller particles as well as larger particles have a smaller drift velocity (see Eq. (7.24)) and therefore it takes longer for them to clear the dust gap. Eventually, for the smallest particle sizes we expect to recover the gas accretion rate, while for the largest particle sizes we expect some residual accretion.

The accretion rate during the first 5 orbits of the planet grows monotonically with particle size. Particles of 1 cm accrete approximately as fast as perfectly coupled particles in this stage (see Fig. 7.3). Our resolution close to the planet is not high enough to see the Roche lobe clearing stage as was observed in Paardekooper & Mellema (2006a) using an adaptive mesh. Larger particles accrete faster, and the particles of 1000 cm have an even higher accretion rate than uncoupled particles (see Fig. 7.6). The turnover occurs around $T_s = 1$, which marks the transition from gas drag dominated dynamics ($T_s < 1$) and gravity dominated dynamics ($T_s > 1$). During this stage, when the planet has not opened up a gas gap yet, gas drag is able to speed up accretion as long as we are in the gravity dominated regime. However, when the initial stopping time $T_s < 1$ gas drag really takes over and forces the particles to accrete at the same rate as the gas.

In Fig. 7.17 we show the accretion rate after 200 orbits of a $1 M_J$ planet for various particle sizes. Again we see that the accretion rate is identically zero for a large range of sizes, while at both ends of the figure we approach the accretion rates of the limiting cases of perfectly coupled particles (left) and uncoupled particles (right). The dust accretion rates almost never become steady, unless they are identically zero or in

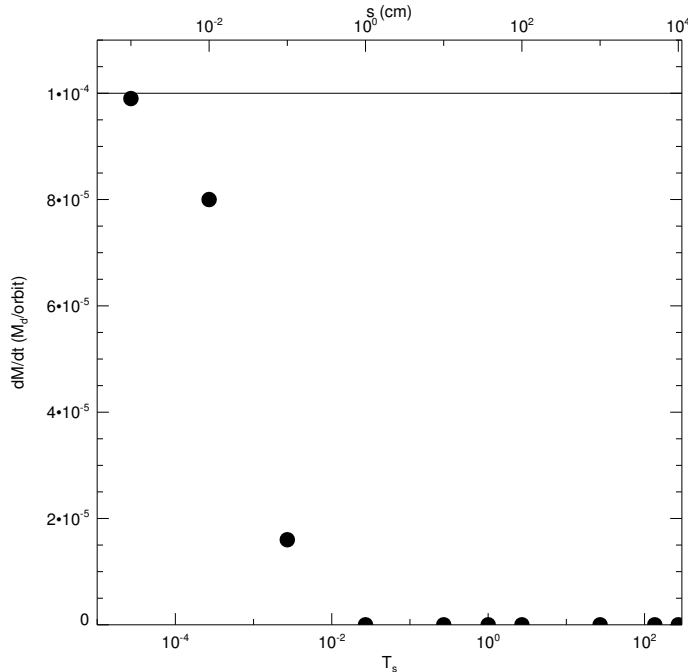


Figure 7.17: Accretion of particles onto a $1 M_J$ planet and an evolving gas disk. The solid line gives the gas accretion rate. All runs included 5000 particles.

the limiting case of perfectly coupled particles (cf. Figs. 7.3 and 7.5). The radial distribution of the smallest particles evolves on a time scale proportional to T_s^{-1} , which becomes prohibitively long when $T_s \ll 1$. Therefore we chose a conservative approach to take the accretion rate after 200 orbits, when the gas accretion has settled to a steady state, as the final accretion rate for a given particle size, even though the particle accretion rate is still declining.

The transition from no accretion to gas accretion begins around $s = 0.001$ cm, or equivalently $T_s = 0.000027$. This means that the total accretion flow onto the planet is severely depleted in particles larger than $10 \mu\text{m}$. Even more, dust accretion never exceeds gas accretion, which makes it very difficult to enrich a giant planet in solids.

A ten times less massive planet of $0.1 M_J$ does not open up a gas gap, and therefore the planet-induced pressure gradients in the disk are less strong. However, Paardekooper & Mellema (2006a) showed that even for such a small planet dust accretion severely slows down. Figure 7.18 shows the dust accretion rates for various particle sizes. Again, we see accretion rates that are identically zero for $s > 1.0$ cm, but the transition from gas accretion rates to zero accretion is shifted to larger s with respect to the planet of $1 M_J$. We find that particles larger than $100 \mu\text{m}$ have significantly low dust accretion rates compared to the gas, which agrees with the result of Paardekooper & Mellema (2006a). Also for this low-mass planet it is very hard to get enriched in solids.

More massive planets than Jupiter open up wider and deeper gaps, but the gap edges do not get much steeper. Therefore the minimum particle size that is able to move across the outer gap edge to be accreted by the planet is the same as for the $1 M_J$ planet. The width gas gap as well as the dust gap increases, though, which brings the density peak at the outer gap edge close to the 2:1 MMR. This could lead to interaction

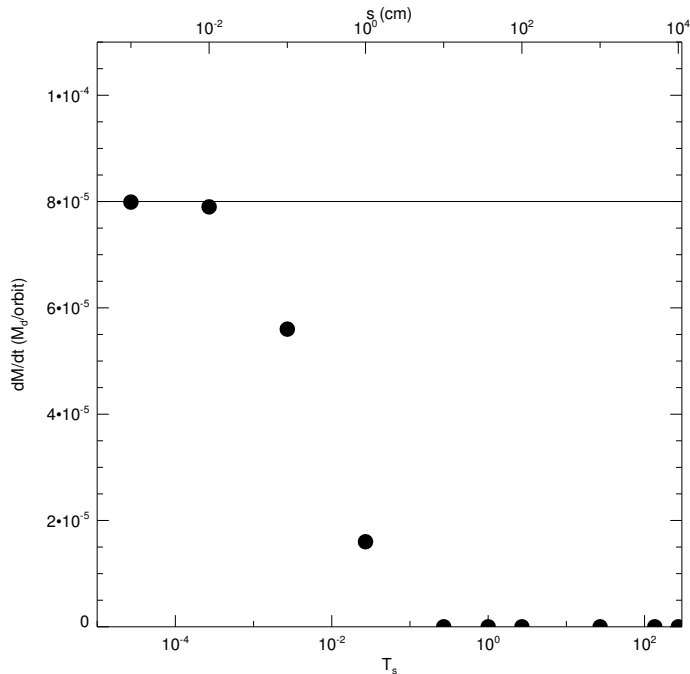


Figure 7.18: Accretion of particles onto a $0.1 M_J$ planet and an evolving gas disk. The solid line gives the gas accretion rate. All runs included 5000 particles.

between large bodies trapped in the 2:1 MMR and smaller bodies trapped at the gap edge.

7.6 DISCUSSION

When Weidenschilling & Davis (1985) discovered that orbital resonances are effective dust traps, they argued that this would not stop dust accretion completely. The increase in eccentricity near the resonance would promote collisions between planetesimals, and the resulting debris would be small enough to move through the resonances towards the planet. Kary et al. (1993) showed that this is not the whole story: particles small enough to make it through the orbital resonances have a significant chance of being transferred to interior orbits rather than being accreted onto the planet. We have demonstrated that there is yet another barrier for smaller dust particles when the planet is massive enough to induce significant pressure gradients in the disk, which is already the case for a planet of $15 M_\oplus$ (Paardekooper & Mellema 2006a).

According to Fig. 7.10, when a planetesimal breaks up into 100 cm sized boulders in a catastrophic collision, these can subsequently be accreted by a $1 M_J$ planet. However, inspection of Fig. 7.17 reveals that 100 cm boulders are stopped at the outer gap edge, and they need to be grinded down to 10-100 μm before they can reach the planet. Moreover, it becomes progressively harder to break smaller particles because they are better coupled to the gas and their relative velocities are low. This means that the accretion flow onto the planet will be severely depleted in solids. The same holds for a $0.1 M_J$ planet, although somewhat larger particles may enter the accretion flow (see Fig. 7.18).

This has severe consequences for the final composition of the planet. According to Pollack et al. (1996), a $1 M_J$ planet at 5.2 AU approximately spends the final 500,000 years of its formation accreting the major part of its massive gaseous envelope. Before that happened, the planet had already reached a mass of $0.1 M_J$, which makes it vulnerable to dust gap formation. Therefore the major part of the mass accreted by the planet is relatively dust-poor compared to the interstellar value, which is of importance for the final composition of the planet. When Jupiter starts accreting gas when its solid core as well as the gaseous envelope both have a mass of $10 M_\oplus$ the difference in solid content between dust-rich gas accretion and dust-poor gas accretion can be as large as 33 %.

Patterson (1987), in contrast with the suggestion by Weidenschilling & Davis (1985), suggested that the accumulation of bodies in orbital resonances may lead to enhanced growth of planetesimals. Especially for a planet on an eccentric orbit, for which the eccentricities of the planetesimals in low-order resonances stay rather low. In either case, the size distribution of trapped particles may be very dynamical, because growth as well as destruction is enhanced with respect to the rest of the nebula. This makes it hard to predict the outcome of resonance trapping with respect to the resulting size distribution.

Another interesting question is what the change in opacity does to the accretion flow. Dust is the major source of continuum radiation in the disk, and if the dust content is very low the gas may not be able to cool efficiently through radiation. This may severely slow down gas accretion. The magnitude of the opacity drop depends on how many of the smallest dust particles enter the accretion flow, which in turn depends on the details of the collisions of the larger bodies.

We have focused on planets of relatively high mass, in order for the two-dimensional approach to be valid. For planets more massive than $0.1 M_J$ the gas accretion rates in two and three dimensional simulations agree reasonably well (D'Angelo et al. 2003), and because the dust particles are probably confined to an even thinner layer we believe that three-dimensional effects will be of minor importance. Also the results presented here do not depend on the density structure within the Roche lobe of the planet.

Turbulence in circumstellar disks is probably of magnetic origin (Balbus & Hawley 1990). If strong enough, it may prevent the formation of a deep gap but for reasonable disk parameters the gap formation paradigm is not changed (Papaloizou et al. 2004). Note that the only thing that is needed to trigger dust gap formation is the existence of planet-induced pressure gradients, and therefore as long as the turbulent disk structure does not overcome gap formation the mechanism presented here will operate to reduce dust accretion onto high-mass planets.

The effect of a nonzero eccentricity of the planet's orbit on resonance trapping was studied by Patterson (1987) and Kary & Lissauer (1995). The effect on the gas disk, in particular the formation of a gap, is not different from case of a circular orbit (Papaloizou et al. 2001). Moreover, eccentricity growth of embedded planets is associated with deep annular gaps (Artymowicz 1992; Lin & Papaloizou 1993; Goldreich & Sari 2003; Sari & Goldreich 2004; Kley & Dirksen 2006). Therefore it is likely that dust ac-

cretion onto eccentric planets also suffers from the planet-induced pressure gradients in the disk.

7.7 SUMMARY AND CONCLUSION

In this Chapter we have studied the accretion rates of solid particles of different sizes onto high-mass planets using a new particle-based method for the integration of the equations of motion of the dust component. We have shown that we can reproduce the gas accretion rates as found in hydrodynamical simulations in the limit of perfectly coupled particles. In the limit of no coupling to the gas, the planet is able to clear its feeding zone in approximately 100 orbits, regardless of the initial eccentricity distribution of the particles. In order for accretion to proceed it is necessary to continuously replenish the feeding zone.

For a non-evolving gas disk three different classes of particles can be distinguished: the smallest particles couple very well to the gas and they accrete at the same rate as the gas, the largest particles get trapped in exterior resonances with the planet, and only particles with intermediate sizes ($1 \text{ cm} \leq s \leq s_{\text{min}}$) accrete onto the planet at a higher rate than the gas.

When the gas is allowed to evolve dynamically it turns out that the planet-induced pressure gradients due to the formation of an annular surface density depression play a major role in the movement of dust particles towards the planet. Only the particles that couple very well to the gas are able to move across the outer edge of the density depression, which limits the size of particles that can be accreted by a $1 M_{\text{J}}$ planet to $s \leq 10 \mu\text{m}$. For planets of lower mass somewhat larger particles may be accreted, but even for a $0.1 M_{\text{J}}$ planet $s \leq 100 \mu\text{m}$. The lack of accreting large bodies may have important consequences for growing planets in disks, especially with regard to their enrichment in solids. If a large mass fraction of the solid component of the disk resides in particles larger than $10 \mu\text{m}$ then it is not possible to enrich the planet.

REFERENCES

- Artymowicz, P. 1992, *PASP*, 104, 769
Balbus, S. A. & Hawley, J. F. 1990, *BAAS*, 22, 1209
Blum, J. & Muench, M. 1993, *Icarus*, 106, 151
Blum, J. & Wurm, G. 2000, *Icarus*, 143, 138
Boss, A. P. 1997, *Science*, 276, 1836
Bryden, G., Chen, X., Lin, D. N. C., Nelson, R. P., & Papaloizou, J. C. B. 1999, *ApJ*, 514, 344
Chambers, J. 2006, *Icarus*, 180, 496
D'Angelo, G., Henning, T., & Kley, W. 2002, *A&A*, 385, 647
D'Angelo, G., Kley, W., & Henning, T. 2003, *ApJ*, 586, 540
Dullemond, C. P. & Dominik, C. 2005, *A&A*, 434, 971

- Duncan, M., Quinn, T., & Tremaine, S. 1989, *Icarus*, 82, 402
- Eulderink, F. & Mellema, G. 1995, *A&AS*, 110, 587
- Garaud, P., Barrière-Fouchet, L., & Lin, D. N. C. 2004, *ApJ*, 603, 292
- Godon, P. 1996, *MNRAS*, 282, 1107
- Goldreich, P. & Sari, R. 2003, *ApJ*, 585, 1024
- Goldreich, P. & Ward, W. R. 1973, *ApJ*, 183, 1051
- Greenberg, R., Hartmann, W. K., Chapman, C. R., & Wacker, J. F. 1978, *Icarus*, 35, 1
- Greenzweig, Y. & Lissauer, J. J. 1990, *Icarus*, 87, 40
- Greenzweig, Y. & Lissauer, J. J. 1992, *Icarus*, 100, 440
- Guillot, T., Stevenson, D. J., Hubbard, W. B., & Saumon, D. 2004, *The interior of Jupiter (Jupiter. The Planet, Satellites and Magnetosphere)*, 35–57
- Kary, D. M. & Lissauer, J. J. 1995, *Icarus*, 117, 1
- Kary, D. M., Lissauer, J. J., & Greenzweig, Y. 1993, *Icarus*, 106, 288
- Kley, W. 1999, *MNRAS*, 303, 696
- Kley, W. & Dirksen, G. 2006, *A&A*, 447, 369
- Kokubo, E. & Ida, S. 1998, *Icarus*, 131, 171
- Kokubo, E. & Ida, S. 2000, *Icarus*, 143, 15
- Kokubo, E. & Ida, S. 2002, *ApJ*, 581, 666
- Kwok, S. 1975, *ApJ*, 198, 583
- Lin, D. N. C. & Papaloizou, J. C. B. 1993, in *Protostars and Planets III*, 749–835
- Lubow, S. H. & D’Angelo, G. 2006, *ApJ*, 641, 526
- Lubow, S. H., Seibert, M., & Artymowicz, P. 1999, *ApJ*, 526, 1001
- Mayer, L., Quinn, T., Wadsley, J., & Stadel, J. 2004, *ApJ*, 609, 1045
- Paardekooper, S.-J. & Mellema, G. 2004, *A&A*, 425, L9
- Paardekooper, S.-J. & Mellema, G. 2006a, *A&A*, 453, 1129
- Paardekooper, S.-J. & Mellema, G. 2006b, *A&A*, 450, 1203
- Papaloizou, J. C. B., Nelson, R. P., & Masset, F. 2001, *A&A*, 366, 263
- Papaloizou, J. C. B., Nelson, R. P., & Snellgrove, M. D. 2004, *MNRAS*, 350, 829
- Patterson, C. W. 1987, *Icarus*, 70, 319
- Pickett, B. K., Cassen, P., Durisen, R. H., & Link, R. 2000, *ApJ*, 529, 1034
- Pickett, B. K., Mejía, A. C., Durisen, R. H., et al. 2003, *ApJ*, 590, 1060
- Pollack, J. B., Hubickyj, O., Bodenheimer, P., et al. 1996, *Icarus*, 124, 62
- Sari, R. & Goldreich, P. 2004, *ApJ*, 606, L77
- Schaaf, S. A. 1963, *Handbuch der Physik* (Berlin : Springer Verlag)
- Shakura, N. I. & Sunyaev, R. A. 1973, *A&A*, 24, 337
- Takeuchi, T. & Lin, D. N. C. 2002, *ApJ*, 581, 1344

-
- Weidenschilling, S. J. 1977, *MNRAS*, 180, 57
Weidenschilling, S. J. & Davis, D. R. 1985, *Icarus*, 62, 16
Wisdom, J. 1980, *AJ*, 85, 1122
Woitke, P. & Helling, C. 2003, *A&A*, 399, 297
Youdin, A. N. & Shu, F. H. 2002, *ApJ*, 580, 494

CHAPTER 8

Planetary signatures in transitional circumstellar disks

Sijme-Jan Paardekooper and Siard van Boven

To be submitted

WE study the effects of radiation pressure and a dust-to-gas ratio d close to unity on the appearance of a low-mass planet orbiting in a circumstellar disk. We compare the resulting dust surface density with the inferred density structure around HD 141569 A. The model disk consists of gas and dust. We use the RODEO hydrodynamics code to evolve the gas. We treat the dust as a second, pressureless fluid. Drag forces between gas and dust are integrated analytically, and radiation pressure on the dust grains is taken into account. When d approaches unity, strong streaming instabilities develop. The result of these instabilities is a turbulent density structure of gas and dust, even in the absence of a planet. Gap formation occurs more readily in these disks compared to gas-rich protoplanetary disks. Radiation pressure provides an outward flux of gas and dust that works against gap formation, but as long as the ratio of radiation pressure force to the stellar gravity β is smaller than unity shallow gaps in gas and dust can be maintained. When $\beta = 0.1$, the non-axisymmetric signature of the planet can propagate much further outward than in protoplanetary disks. We show that a planet on a circular orbit with radius 100 AU produces a dust density structure that is remarkably similar to what is observed in HD 141569 A.

8.1 INTRODUCTION

The interaction between a massive planet and a gaseous disk is a critical ingredient in planet formation theory. The disk regulates the amount of mass that may flow onto the planet (Kley 1999; D'Angelo et al. 2002; Bate et al. 2003; D'Angelo et al. 2003; Paardekooper & Mellema 2006b), and tidal torques in the disk trigger inward planet migration (Goldreich & Tremaine 1980; Ward 1997). This migration is the most probable explanation for the existence of Hot Jupiters very close to their central star.

Planet-disk interaction also plays an important role for observations of protoplanetary disks. Planets with masses comparable to Jupiter open up a deep annular gap in the disk (Lin & Papaloizou 1993) that may be imaged with future instruments (Wolf et al. 2002). These observations will provide the first direct look into the process of planet formation. Models of the spectral energy distribution of stars with disks suggest that gaps in disks are a common phenomenon (see for example Calvet et al. 2002)

Paardekooper & Mellema (2004) showed that the criteria for gap formation are different for a gas-dust disk than for a disk containing gas alone. Pressure gradients near the edges of small density depressions along the orbits of low-mass planets are able to structure the dust disk in a way that especially the larger grains of the dust population will form a deep dust gap even though there is no gap in the gas. This is important for observations of protoplanetary disks because what observations probe is mostly thermal emission from dust grains, not the gas.

As protoplanetary disks evolve their gas content decreases. At the very early evolutionary stages the dust-to-gas ratio d probably has the interstellar value of 1 : 100. For older disks like those around β -Pic or Vega d is of the order unity or larger. These older disks also have a different chemical structure than their younger counterparts (Kamp & van Zadelhoff 2001; Jonkheid et al. 2006). Some of these older disks are observationally interesting because they are nearby and can be resolved, showing a lot of structure. One of the most beautiful examples is the disk around HD 141569 A, whose complex morphology has been imaged by various groups (Augereau et al. 1999; Weinberger et al. 1999; Mouillet et al. 2001; Boccaletti et al. 2003; Clampin et al. 2003).

In Fig. 8.1, we show an HST image taken by Mouillet et al. (2001) of the HD 141569 A disk in scattered light. The shape of the dust disk is described in detail in Augereau & Papaloizou (2004), and we repeat only the most important features here:

- the disk contains two bright rings, located at 200 and 325 AU from the star
- in between the rings, there exists a dark gap that is relatively wide compared to the rings
- inside 150 AU, the disk seems to be clear of dust

Furthermore, the rings display azimuthal asymmetry, which is indicative of the presence of companions rather than dust-gas interaction (Takeuchi & Artymowicz 2001).

In Fig. 8.2 we show the deprojected dust surface density, taken from Clampin et al. (2003). The asymmetry of the rings is clearly visible, and the outer ring turns out to have a tightly wound spiral structure. But also the inner ring shows substantial substructure, and it seems to be composed of two separate arcs.

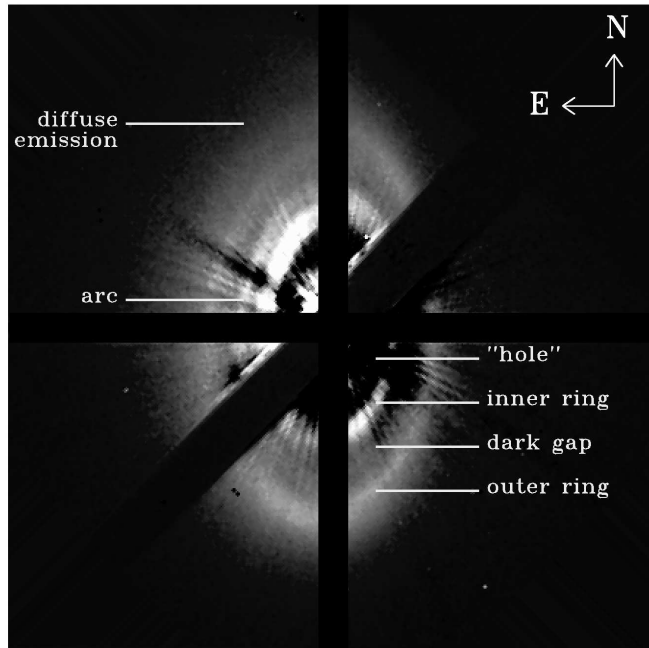


Figure 8.1: HST/STIS visible image (585 nm) of the disk around HD 141569 A, adopted from Augereau & Papaloizou (2004). The image was taken by Mouillet et al. (2001). The two companion stars are located to the north-west, outside of the image.

The origin of the structures seen in the HD 141569 A disk has been the subject of numerous studies. Augereau & Papaloizou (2004) investigated the impact of two possibly bound companion stars to HD 141569 A on the dust disk morphology, and could explain the outer spiral very nicely. However, the inner ring remained unexplained. Quillen et al. (2005) consider the effect of bound companions (stars or planets) on the gas, and they too get a reasonable fit for the outer features of the disk, albeit with a different orbit for the companion. Wyatt (2005) considers the effect of planets on very wide orbits on the secular evolution of the dust disk. Spiral features similar to those observed in HD 141569 A pop up, but the presence of a planet at a distance of more than 100 AU needs to be explained.

All these models treat exactly one component of the disk: Augereau & Papaloizou (2004) and Wyatt (2005) considered collisionless particles, accounting for the structure of a planetesimal disk, while Quillen et al. (2005) looked only at the gas. In reality, the HD 141569 A disk consists of planetesimals as well as remnant gas, together with a population of small scattering particles that produce the scattered light. Because the latter are subject to radiation pressure and gas drag, the distribution of planetesimals may be different from the distribution of small particles. Furthermore, because of the low gas content of the disk even the smallest dust particles may only be marginally coupled to the gas, and gas and dust also do not necessarily follow the same distribution. A realistic model for the disk around HD 141569 A should contain all three components.

Ardila et al. (2005) considered such models. They explored the effect of a parabolic flyby of the companion stars of HD 141569 A on a disk consisting of gas, dust and planetesimals. They found reasonable agreement with the morphology depicted in

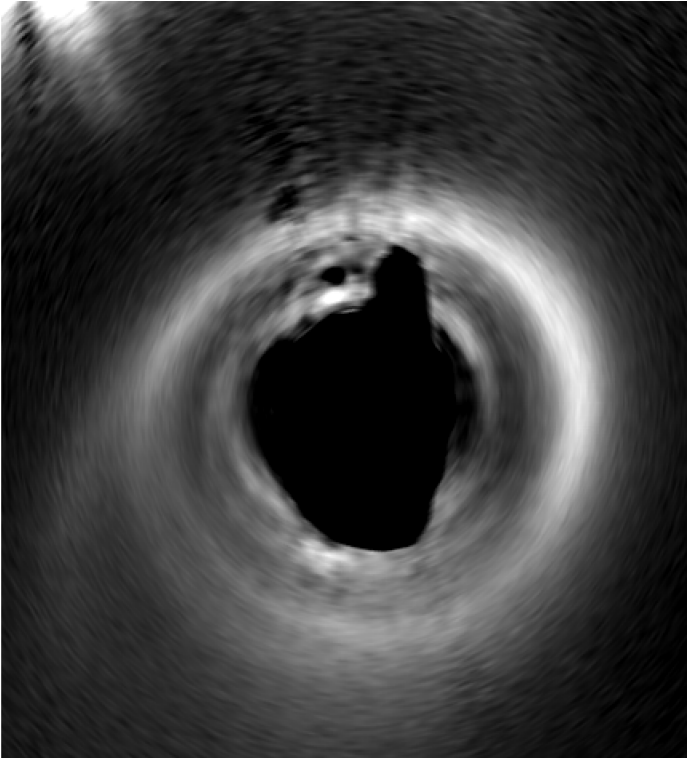


Figure 8.2: Dust surface density derived from HST/ACS images after deprojection, correction for stellar flux dilution and anisotropic scattering. North is to the left, and the line of sight is directed towards the bottom of the figure. Adopted from Clampin et al. (2003).

Fig. 8.2. However, in their simulations dust particles were added a posteriori, while they may have dynamical importance because the gas mass in the disk is comparable to the dust mass. This means that gas and dust compete on dominating the dynamics. In protoplanetary disks, where $d \approx 0.01$, the dynamics are governed by the gas, and the dust reacts primarily on the gas (Paardekooper & Mellema 2006a). In older disks, where both gas and dust are present in comparable amounts, the outcome is not clear.

It is hard to determine the gas mass in these disks directly, and therefore d remains an uncertain parameter. In this Chapter, we present results on gas and dust dynamics in disks where $d \approx 1$. This way, we probe a different part of parameter space than considered in Chapter 6. We focus on the interaction of a massive planet with such a disk, and we compare the flow morphology with the results presented in Chapter 6. Although we compare our results with the dust distribution around HD 141569 A, the main emphasis is on general mechanisms rather than on this specific object.

The plan of this Chapter is as follows: in Sect. 8.2 we briefly explain the physics that goes into the models, in Sect. 8.3 we discuss the numerical method, and in Sect. 8.4 we show the results. We give a short discussion of the results in Sect. 8.5 and we conclude in Sect. 8.6.

8.2 PHYSICAL BACKGROUND

8.2.1 Coupling of gas and dust

In this section we discuss the physics of gas and dust in circumstellar disks. Depending on the gas-to-dust ratio in the disk, different physical processes will be important.

We consider only two-dimensional disks, in a coordinate frame (r, ϕ) centered on the primary star. Ignoring the third dimension is valid as long as the relative scale height $h = H/r \ll 1$, where H is the pressure scale height in the disk. If the disk is isothermal and in hydrostatic equilibrium in the vertical direction, H is related to the temperature through the isothermal sound speed:

$$c_s = \frac{P}{\Sigma_g} = H \Omega_K \quad (8.1)$$

where P and Σ_g are the vertically integrated gas pressure and surface density, respectively, and Ω_K is the Kepler angular velocity. In our numerical simulations, we only consider a locally isothermal equation of state.

Gas and dust are coupled through drag forces. The functional form of the drag force depends on the size of the dust particles under consideration and on the amount of gas (Woitke & Helling 2003). In this work we focus on the small-particle limit, for which the Epstein drag law gives the drag force acting on the dust:

$$\mathbf{f}_{\text{drag,d}} = -\Sigma_d \frac{\Omega_K}{T_s} \sqrt{1 + \frac{9\Delta\mathbf{v}^2}{128 c_s^2}} \Delta\mathbf{v} \quad (8.2)$$

where Σ_d is the surface density of dust, $\Delta\mathbf{v}$ is the relative velocity of gas and dust, and T_s is the non-dimensional stopping time (Takeuchi & Lin 2002):

$$T_s = \sqrt{\frac{\pi}{8}} \frac{\rho_p s v_K}{\rho_g r c_s} \quad (8.3)$$

Here, ρ_p is the dust particle internal density, s is the radius of the particle, ρ_g is the gas density and c_s is the sound speed. The stopping time is a measure of the strength of gas-dust coupling. When $T_s \ll 1$ this coupling is very strong and gas and dust will always move at approximately the same velocity. This situation occurs for high gas densities or small particles. Conservation of momentum requires that a similar force acts on the gas.

Because of the dependence of T_s on the gas density, the stopping time is not constant during a simulation. On the contrary, it can vary strongly in space and time. When quoting values of the stopping time for the various models, we always quote the value of T_s for the *initial* gas density.

In addition to the drag force, dust particles are also subject to radiation pressure. The force due to radiation is conveniently expressed as a fraction β of the gravitational force:

$$\mathbf{f}_{\text{rad,d}} = \Sigma_d \beta \frac{GM_\odot}{r^2} \hat{\mathbf{r}} \quad (8.4)$$

The fraction β is a function of particle size (Takeuchi & Artymowicz 2001). A dust particle located at $r = r_0$ and rotating with the Keplerian angular velocity $\Omega_K(r_0)$ will, due to radiation pressure, try to orbit at a lower angular velocity:

$$\Omega(r) = \sqrt{1 - \beta} \Omega_K(r). \quad (8.5)$$

Conservation of angular momentum requires that for the new velocity Ω :

$$r_0^2 \Omega_K = r^2 \Omega(r), \quad (8.6)$$

which, together with Eq. (8.5), implies that the dust particle will move outward to a new radius, given by:

$$r = \frac{r_0}{\sqrt{1 - \beta}} > r_0. \quad (8.7)$$

When $\beta > 1$, no new equilibrium angular velocity can be found (see Eq. (8.5)), and the particle will be blown out of the system. However, interesting effects may occur already for $\beta < 1$; for example, when

$$|\Omega - \Omega_K| = \left(1 - \sqrt{1 - \beta}\right) \Omega_K > h \Omega_K, \quad (8.8)$$

the equilibrium angular velocity of the dust is supersonic with respect to the local Keplerian velocity. For the standard value $h = 0.05$, we find that $\beta > 0.1$ is enough to make this happen. These particles are still gravitationally bound to the system, but their dynamics are very different from the $\beta = 0$ case.

8.2.2 Protoplanetary disks

Protoplanetary disks as found around young stars (Beckwith & Sargent 1996) are dominated by gas. Initially the dust-to-gas ratio d in these disks equals the interstellar value of 1 : 100, but as the dust starts to settle towards the midplane this pristine ratio will increase considerably locally. Whether this leads to the unstable situation of equal amounts of gas and dust near the midplane is still a matter of debate (Garaud et al. 2004; Youdin & Goodman 2005; Youdin & Shu 2002).

As long as $d \ll 1$ the gas does not feel the drag from the dust, and we can take the gas to move independently from the dust. This was done for example in Paardekooper & Mellema (2004) to study the appearance of low-mass planets in protoplanetary disks.

Also, due to the large amounts of gas and dust in protoplanetary disks, radiation from the central star does not penetrate into the disk, except in the uppermost layers. Therefore it is safe to leave out radiation pressure when dealing with young protoplanetary disks.

These two simplifications make it easier to understand the behavior of dust in these disks. Due to a radial pressure gradient the gas does not move exactly at the Keplerian velocity, and when $T_s \ll 1$ the dust is forced to orbit at the same angular velocity. This leads to radial migration of dust particles:

$$v_{r,\text{drift}} = -\eta T_s v_K \quad (8.9)$$

where η is the ratio of the gas pressure gradient to the stellar gravity in the radial direction:

$$\eta = -h^2 \frac{\partial \log P}{\partial \log r} = h^2 \left(1 - \frac{\partial \log \Sigma_g}{\partial \log r} \right). \quad (8.10)$$

When a planet orbiting in the disk creates large pressure gradients near its orbit, this migration can significantly change the dust distribution with respect to the gas (Paardekooper & Mellema 2004).

8.2.3 Debris disks

When disks grow older they start to lose their gas, eventually leaving a gas-free circumstellar dust disk. Because small particles are blown away by radiation pressure on dynamical time scales, it is assumed that dust is constantly replenished by collisions in an unobserved planetesimal distribution (Backman & Paresce 1993).

The observed structures in these disks can be due to for example recent planet formation (Kenyon & Bromley 2004) or interaction with bound companions (Ozernoy et al. 2000; Augereau & Papaloizou 2004).

8.2.4 Transitional disks

In between the two extremes of a gas-rich disk and a gas-free disk there exists a class of objects called transitional disks, one of which is HD 141569 A. These disks may have lost most, but not all, of their gas content, and the residual gas may play an important role in the dynamics of these systems. For example, it can provide a braking mechanism against the acceleration of dust particles by radiation pressure. However, because the dust-to-gas ratio d is close to unity in these systems, the situation is much less clear than for gas-dominated protoplanetary disks. Dust particles may indeed transfer momentum to the gas, but contrary to the situation in protoplanetary disks this transferred momentum may be comparable in magnitude to the original momentum of the gas, which changes the gas motion considerably. Another difference with debris disks is that the dust is still original, not second generation "debris".

Another important consequence of the reduced gas content in these disks is that for the same value of the stopping time T_s the corresponding particle size is much smaller in transitional disks compared to protoplanetary disks. This is interesting, because the two-fluid approach we use puts constraints on the stopping time and therefore on the particle size we can model (Garaud et al. 2004; Paardekooper & Mellema 2006a). While in typical protoplanetary disks, the two-fluid approach works best when particles have sizes of $100 \mu\text{m}$; when the density in a transitional disk is 100 times lower we are able to model micron-sized particles. These particles carry most of the opacity at infra-red wavelengths, and are the main source of scattered light that we observe in these disks.

The new physics that needs to be included in the models compared to that in Chapter 6 consists of radiation pressure and incorporating the effect of momentum transfer of dust on gas.

8.3 NUMERICAL METHOD

Our numerical method consists of two distinct modules: gas and small dust particles. Below, we consider each module separately.

We use the RODEO method to simulate the gas disk (Paardekooper & Mellema 2006b). It uses an approximate Riemann solver (the Roe solver) to deal with advection, and stationary extrapolation (Eulderink & Mellema 1995) to integrate the source terms. RODEO has been successfully applied to study planet-disk interaction (Paardekooper & Mellema 2006b), and was compared extensively against other codes (de Val-Borro et al. 2006). The drag force is integrated analytically (see Simis et al. 2001, and Chapter 6).

We treat the dust as a pressureless fluid, which is valid as long as $T_s \ll 1$ (Garaud et al. 2004). Because of the dependence of T_s on gas density and particle size, the particle size we can simulate is limited (Paardekooper & Mellema 2006a). However, the results of Chapter 7 suggest that the behavior of larger particles is reasonably described by extrapolation of the behavior of small particles. The resulting two-fluid code (gas and dust) was tested and applied to planets orbiting in protoplanetary disks in Paardekooper & Mellema (2006a).

The inclusion of radiation pressure and momentum transfer from dust to gas comes down to integrating extra source terms. We focus on particles for which $\beta < 1$, and therefore we can include radiation pressure by considering a reduced stellar gravitational force onto the dust particles:

$$F_{\text{grav},*,\text{dust}} = (1 - \beta) F_{\text{grav},*}. \quad (8.11)$$

This way, we can incorporate radiation pressure into the stationary extrapolation of the source terms (see Chapter 2).

The velocity of a dust particle subject to drag forces only evolves according to

$$\frac{d\mathbf{v}_d}{dt} = -\frac{\Omega_K}{T_s} \sqrt{1 + \frac{9\Delta\mathbf{v}^2}{128c_s^2}} \Delta\mathbf{v}, \quad (8.12)$$

see also Chapter 6. This drag law is valid for all drift velocities, as long we remain in the Epstein regime.

Conservation of momentum requires that

$$\rho_d \frac{d\mathbf{v}_d}{dt} + \rho_g \frac{d\mathbf{v}_g}{dt} = 0, \quad (8.13)$$

which can be rewritten as

$$-\frac{d\mathbf{v}_g}{dt} = d \frac{d\mathbf{v}_d}{dt}. \quad (8.14)$$

Combining this with Eq. (8.12), we find that

$$\frac{d\Delta\mathbf{v}}{dt} = -(1 + d) \frac{\Omega_K}{T_s} \sqrt{1 + \frac{9\Delta\mathbf{v}^2}{128c_s^2}} \Delta\mathbf{v}, \quad (8.15)$$

which differs from Eq. (6.26) in the factor $(1 + d)$. For $d \ll 1$, as was considered in Chapter 6, this factor can be neglected, but it is needed in simulations where the gas density equals the dust density. As in Chapter 6, the analytical solution to Eq. (8.15) for $\Delta\mathbf{v}(t)$ is used to update the velocities of gas and dust. To do this, we rewrite the total momentum as

$$M = \rho_d \mathbf{v}_d + \rho_g (\mathbf{v}_g + \mathbf{v}_d - \mathbf{v}_d) = \rho_d \mathbf{v}_d - \rho_g \Delta\mathbf{v} + \rho_g \mathbf{v}_d, \quad (8.16)$$

from which follows:

$$\mathbf{v}_d = \frac{\frac{M}{\rho_g} + \Delta\mathbf{v}}{1 + d}. \quad (8.17)$$

From conservation of momentum we find the gas velocity to be

$$\mathbf{v}_g = \frac{\frac{M}{\rho_g} - d\Delta\mathbf{v}}{1 + d}. \quad (8.18)$$

These last two equations are used to update gas and dust velocities.

8.3.1 Initial and boundary conditions

We start with a disk of uniform surface density, with $h = 0.05$. In all simulations and all plots we rescale the initial gas density to unity; its exact value in cgs units depends on the adopted stopping time through Eq. (8.3). All radial velocities are set to zero. The equilibrium orbital velocity is different for gas and dust, because both fluids feel a reduced gravitational force: for the gas this is due to the radial pressure gradient, and for the dust it is due to radiation pressure. A mixture of gas and dust will rotate at a velocity that is in between the equilibrium velocity for the dust and the gas equilibrium velocity, given by:

$$\Omega_g = \Omega_K \sqrt{1 - \eta}. \quad (8.19)$$

The equilibrium velocity for the dust is

$$\Omega_d = \Omega_K \sqrt{1 - \beta}. \quad (8.20)$$

In fact, for a given value of d , the equilibrium velocity for the gas-dust mixture is:

$$\Omega_{\text{eq}} = \frac{\Omega_g + d\Omega_d}{1 + d}, \quad (8.21)$$

which we take as our initial condition for both gas and dust.

We parametrize the turbulent viscosity ν using the α -prescription (Shakura & Sunyaev 1973):

$$\nu = \alpha c_s H, \quad (8.22)$$

where we take $\alpha = 0.004$ for all simulations.

We focus on a planet of $q \equiv M_p/M_* = 10^{-4}$, which is equivalent to a 0.1 Jupiter mass (M_J) planet around a Solar mass star. Merín et al. (2004) derive a mass of $2 M_\odot$ for

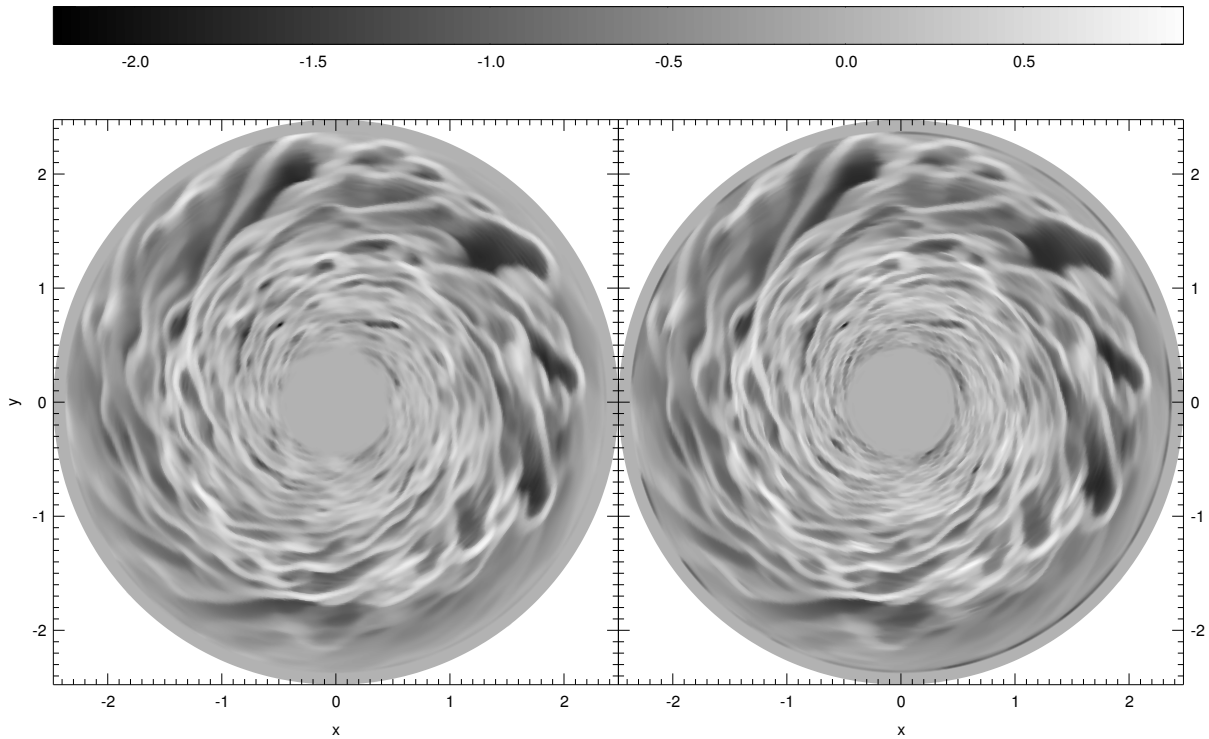


Figure 8.3: Logarithm of the gas surface density (left panel) and dust surface density (right panel) after 20 orbits at $r = 1$, relative to the initial (constant) surface densities. The initial gas-to-dust ratio was unity, and $T_s = 0.01$.

HD 141569 A, which makes the mass of this planet $0.2 M_J$, or $65 M_\oplus$. The planet remains on a fixed circular orbit throughout the simulation. We rescale the radial coordinate to make $r_p = 1$. This way, our results can be scaled to any circular planet orbit.

As boundary conditions we use the non-reflective boundaries of Godon (1996), see also Chapter 2.

8.4 RESULTS

In this section we present the results of our two-fluid simulations on transitional disks. We start with disks without planets, to illustrate the effects of streaming instabilities. Next, we show how these instabilities modify gap formation in the gas and in the dust. Finally, we consider the effect of radiation pressure and compare our dust surface density to what is observed in HD 141569 A (see Fig. 8.2).

8.4.1 Streaming instabilities

It is well-known that gas-dust mixtures are unstable to streaming instabilities when $d \approx 1$. However, most analytical and numerical work has focused on the problem of an unstable thin dust layer, embedded in a gas disk, that may or may not become

gravitational unstable and form planetesimals (e.g. Goldreich & Ward 1973; Sekiya 1998; Youdin & Shu 2002; Johansen et al. 2006). Youdin & Goodman (2005) found that streaming instabilities are a rather general phenomenon when two fluids are coupled by aerodynamic drag. Growth rates of unstable modes become comparable to the dynamical time scale around $d \approx 1$. In this section, we show that indeed we find streaming instabilities in our two-fluid calculations.

In Fig. 8.3 we show the density of gas and dust after 20 Keplerian orbits at $r = 1$. Initially, d was equal to unity throughout the disk, and we used a stopping time of

$$T_s = 0.01 \frac{\Sigma_{g,0}}{\Sigma_g}. \quad (8.23)$$

It is clear that the smooth disk has developed strong filamentary structures, while d stays close to 1. This is because the drift time scale is much longer than the growth time scale of the unstable modes. The density inside the filaments can be a factor of 10 higher than the initial density, for both gas and dust.

It is interesting to look in more detail what exactly the numerical source of the disturbances is. Because the disk is axisymmetric initially, one may expect that it stays axisymmetric during the simulation, because, in absence of azimuthal source terms, the numerical ϕ -sweeps do not change the state, while the r -sweeps are independent of ϕ . In the end, it is the finite precision of the calculations that provides the seeds of the instability. The exact source can be found in the definition of the first-order interface flux between two computational cells:

$$\mathbf{F}_{\text{int}} = \frac{1}{2} ((1 + \sigma)\mathbf{F}_L + (1 - \sigma)\mathbf{F}_R), \quad (8.24)$$

where σ is the sign of the eigenvalue λ of the Roe matrix (see Chapter 6 for details). When $\sigma > 0$, all information comes from the left and the interface flux is equal to the flux just left of the interface. When $\sigma < 0$, the dust flows from right to left and the interface flux is equal to the flux just right of the interface. The crucial question is what happens when $\lambda \approx 0$, in particular when it becomes comparable to the machine precision. Then, as we go around in azimuth, sometimes $\lambda > 0$ and sometimes $\lambda < 0$, while the state is still axisymmetric to machine precision. Therefore some cells pick F_L as interface flux, and some pick F_R . But when at the same time F_L is very different from F_R axisymmetry is broken, even when taking into account finite machine precision. This provides the numerical seeds for the instability to grow.

Youdin & Goodman (2005) considered the simplified case of incompressible gas and one-dimensional perturbations, and they found no linear secular instability for in-plane motions (as we consider here). Our results show that in the case of compressible gas and possible non-linear, two-dimensional waves there are indeed unstable modes. Although it seems likely that these instabilities have the same origin as those described in Youdin & Goodman (2005), it remains to be investigated what the exact relation is between the instabilities we find and those of Youdin & Goodman (2005). However, we can easily point out some similarities and differences in the dependence on d and T_s .

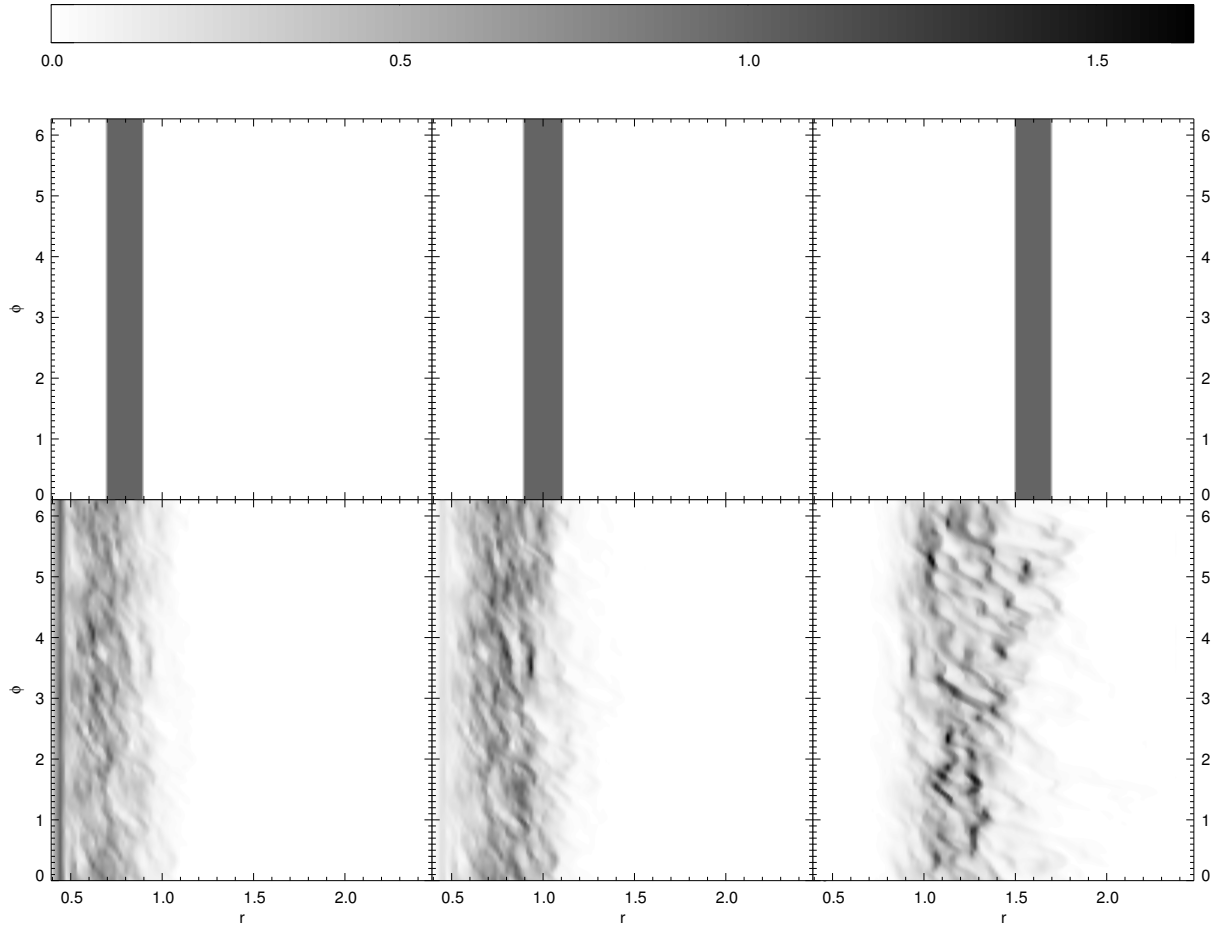


Figure 8.4: Dust tracer density at $t = 0$ (top panels) and $t = 20$ (bottom panels), where t measures the number of orbits that have passed at $r = 1$. The stopping time $T_s = 0.01$.

The growth rate of the instability as found by Youdin & Goodman (2005) depends in a complicated way on d around $d \approx 1$. Time scales comparable to the dynamical time scale for $T_s \ll 1$ are only possible for $d > 1$, but d needs to be only slightly larger than unity for the growth time scale to decrease significantly. Therefore any disturbance that increases d beyond unity (such as, for example, the effect of the varying dust drift velocity with r) would make the mixture susceptible to streaming instabilities. We have verified that indeed when $d < 1$ everywhere, no unstable modes develop on dynamical time scales. A run with $d = 0.1$ showed no signs of streaming instabilities up to 100 orbits at $r = 1$, while momentum transfer from dust to gas should be significant. On the other hand, a run with $d = 10$ proved to be unstable within 10 dynamical time scales. So indeed, as was found by Youdin & Goodman (2005), streaming instabilities require $d > 1$.

The two-fluid approach requires $T_s < 1$, and the numerical simulations require $T_s > \Delta t \Omega_K$ (see also Chapter 6), and therefore we can only provide a limited study of the dependence of the growth rate of the unstable modes on T_s . However, qualitatively we find the same behavior as in Youdin & Goodman (2005): the instability grows faster

with decreasing T_s . A more detailed comparison is beyond the scope of this Chapter.

We can investigate the effect of the turbulence generated by streaming instabilities by using tracer fluids. These fluids are passively advected along with the dust (or the gas, for a gas tracer) and therefore provide information on where a specific dust fluid particle originates from. We set up three narrow annular rings of tracer fluids, and investigated how the ring as a whole moves (inward or outward, and at what speed), and whether the turbulence causes the ring to spread significantly.

In Fig. 8.4, we show the initial dust tracer density (top panels), together with the dust tracer density after 20 orbits at $r = 1$ (bottom panels), for which the gas and dust densities are shown in Fig. 8.3. Initially, the three rings of tracer fluid were located at $r = 0.6$, $r = 1.0$ and $r = 1.6$, and had widths of 0.2. As can be seen from the bottom panels of Fig. 8.4, the turbulence induced by the streaming instabilities causes significant mixing and diffusion in the fluid.

It turns out that the overall movement of the dust rings is inward. This is not surprising, because due to the pressure gradient in the gas disk dust particles drift inward. However, the speed at which the rings move *is* surprising. According to Eq. (8.9), in a constant gas surface density disk the dust migration time scale would be approximately 10000 dynamical time scales, while we see significant dust migration already after 20 dynamical time scales. This migration is induced by the streaming instabilities, because a run with $d = 0.1$ showed no signs of migration after 20 orbits, in agreement with Eq. (8.9). The physical reason for this fast migration is that due to the turbulence the gas density is decreased significantly locally, as can be seen from Fig. 8.3. This causes T_s to increase by two orders of magnitude locally, and this is enough to account for the fast migration.

The turbulence induced by the streaming instabilities also causes significant spreading of the tracer rings. The material that was located initially between $r = 1.5$ and $r = 1.7$ is, after 20 dynamical time scales, spread over a region between $r = 0.8$ and $r = 1.8$. Note that in fact some material has moved *out*, opposite to the overall movement of the ring. The inner rings also spread significantly, but they are halted by the inner boundary.

In Fig. 8.5 we compare the dust tracer fluid densities for two different stopping times. The upper panels are the same as the lower panels in Fig. 8.4, and the lower panels in Fig. 8.5 show the results for $T_s = 0.001$, a ten times smaller stopping time. We see that the overall inward motion as well as the radial spreading of the rings decrease for a smaller value of T_s . The main reason for this is that for a given gas density, the drift velocity for the better-coupled particles will be lower. It is of minor importance that the streaming instabilities set in a couple of orbits later for $T_s = 0.001$.

It is important to realize that there is no radiation pressure in these models, so the effect of these instabilities may be of minor importance in optically thin transitional disks. However, when radiation from the central star is blocked in the inner parts of the disk, or when the disk is still optically thick, they provide an efficient mechanism for radial mixing of both gas and dust.

Another important regime in which these streaming instabilities may be important is when, in an earlier stage of disk evolution, dust settles into a thin layer around the

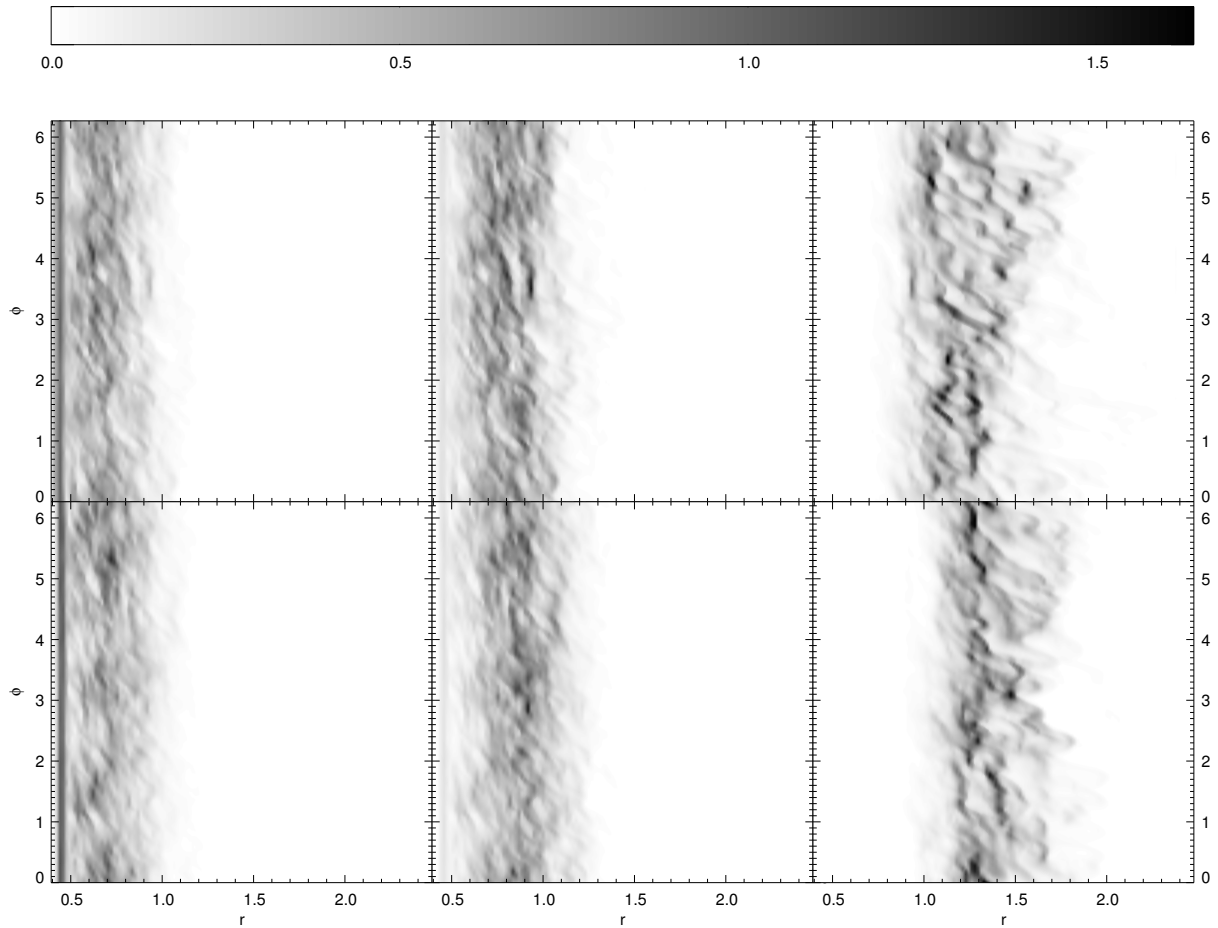


Figure 8.5: Dust tracer density at $t = 20$ for $T_s = 0.01$ (top panels) and $T_s = 0.001$ (bottom panels).

midplane of the disk, increasing the dust-to-gas ratio locally. Our results show that, when d becomes larger than unity, turbulence sets in. Because the dust density can increase by approximately an order of magnitude locally, this may trigger gravitational instabilities that lead to planetesimal formation. See Johansen et al. (2006) for a similar argument.

8.4.2 Planetary gaps

We now turn to the question in what way streaming instabilities, or, more general, the back-reaction of the gas on the dust, affect the density structure near the planet. Paardekooper & Mellema (2004) showed that a $0.1 M_J$ planet is able to carve a dust gap in a gas disk, while no gap is formed in the gas disk. However, in those simulations $d \approx 0.01$, and momentum transfer from dust to gas could be safely ignored. In this section, we consider the same $0.1 M_J$ planet, but now in a disk where the dust-to-gas ratio is unity, initially.

In Fig. 8.6 we compare two simulations with $M_p = 0.1 M_J$ and $T_s = 0.001$ after 100

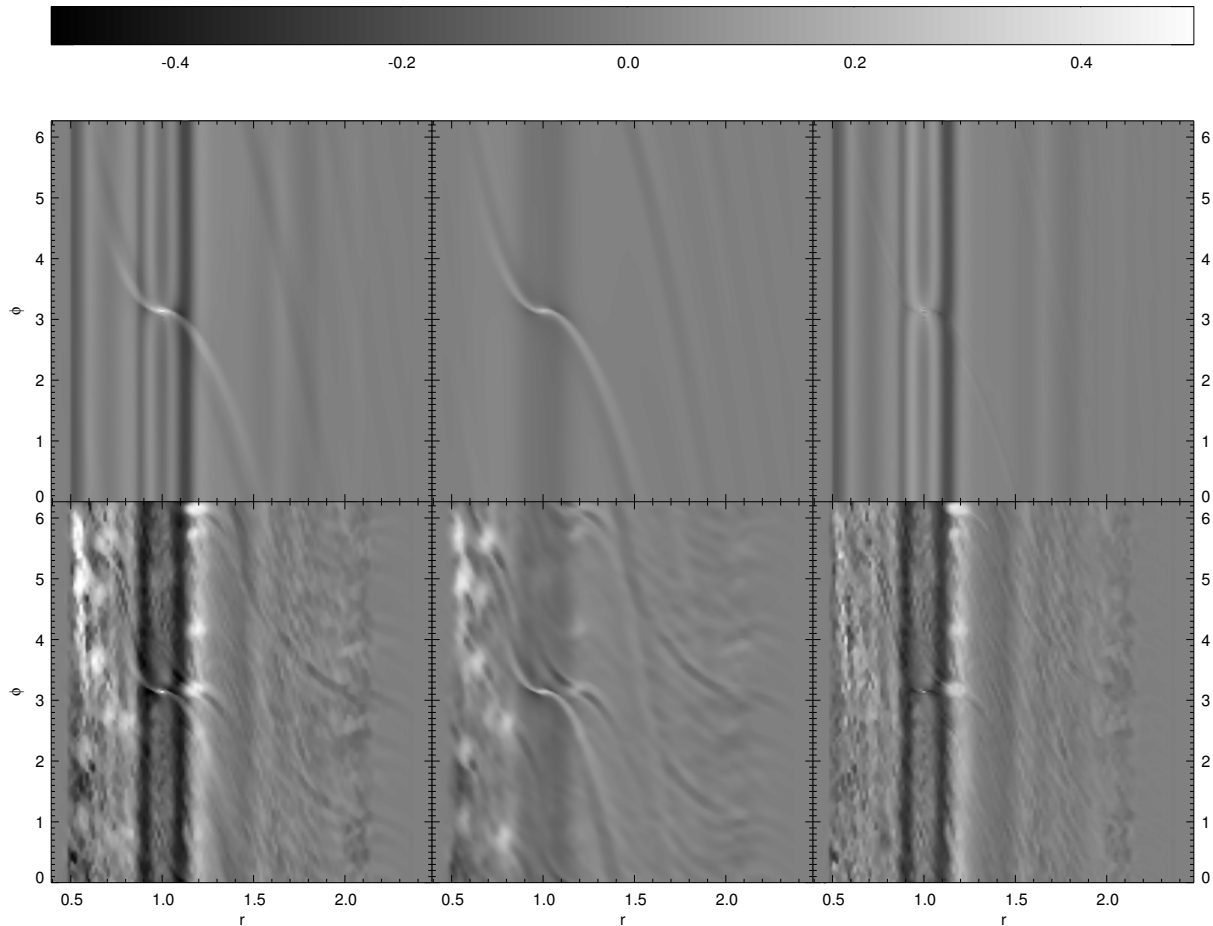


Figure 8.6: Logarithm of the gas and dust density around a $q = 10^{-4}$ planet after 100 orbits for $T_s = 0.001$. Top panels: $d = 0.01$ initially. For clarity the dust density is multiplied by 100 to compare with the $d = 1$ simulation. Bottom panels: $d = 1$ initially. Left panels: dust density. Middle panels: gas density. Right panels: d .

orbits. The top panels show, from left to right, dust density, gas density and dust-to-gas ratio for a model with $d = 0.01$ initially, while the bottom panels show the same quantities but now for a model in which $d = 1$. Note that in the top panels the dust density was multiplied by 100 to be able to compare the two simulations.

The first thing to note is that we see again turbulent structures throughout the disk, created by the streaming instabilities. In the inner disk, vortex-shaped structures are seen in both gas and dust, while near the outer edge of the shallow gap opened up by the planet the turbulent structures appear much stronger in the dust than in the gas. The reason for this is that the dust-to-gas ratio will tend to be larger near the outer edge of the dip than near the inner edge (see Chapter 6). For larger values of d , the fluid mixture is less stable (Youdin & Goodman 2005) and therefore the instabilities grow faster. When d is much larger than unity, the structures will be more apparent in the dust than in the gas.

It is also clear from Fig. 8.6 that the shallow planetary density gap is deeper for

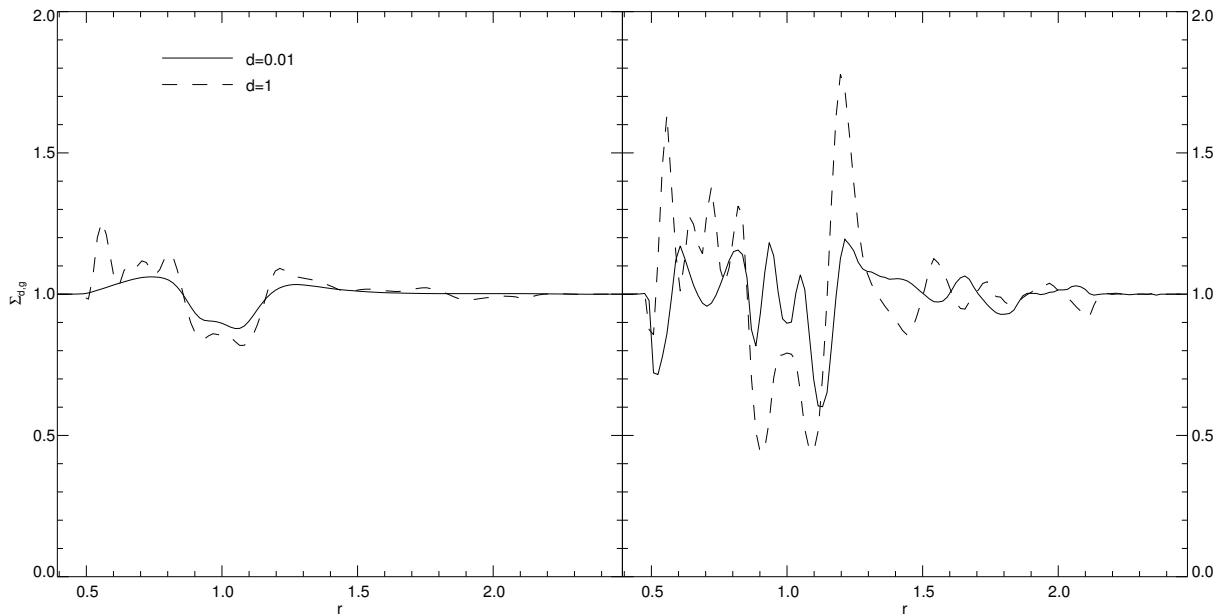


Figure 8.7: Azimuthally averaged gas (left panel) and dust (right panel) surface densities after 100 orbits of a $0.1 M_J$ planet with $T_s = 0.001$. The solid lines indicate a model where $d = 0.01$, initially (the final dust density was multiplied by 100 to compare with the $d = 1$ case), and the dashed lines indicate a $d = 1$ model.

$d = 1$ than for $d = 0.01$. This is further illustrated in Fig. 8.7, where we show the azimuthally averaged surface densities of gas (left panel) and dust (right panel) for both values of d . Both in the gas and the dust the dip is deeper for $d = 1$. This is because there is a positive feedback in the gap formation process. The dust particles will try to open a dust gap, as outlined in Chapter 6. Because now also the gas is subject to drag forces, it is dragged along with the dust to a certain extent. This lowers the gas density in the gap region, which makes the dust particles less well coupled to the gas, and therefore they start to clear the gap a little faster. This, in turn, leads to faster gas gap formation, and the net result is that a deeper gap forms in both gas and dust. However, because d is decreasing in the gap region, eventually the gas will not feel the drag from the dust anymore and then we recover the situation described in Chapter 6. Therefore, no real gas gap will form, and the net effect is that the dust gap will form faster than when $d = 0.01$.

This may have some important observational consequences. First of all, because the gas density is much lower than in protoplanetary disks, particles for which $T_s \in [0.001, 0.01]$ have sizes of micrometers in a transitional disk instead of millimeters for a protoplanetary disk. Because dust gap formation is similar, this opens up a way for low-mass planets to carve out dust gaps that are observable in optical scattered light. Furthermore, because dust gap formation proceeds faster than in a protoplanetary disk, even planets somewhat less massive than considered in Chapter 6 may open

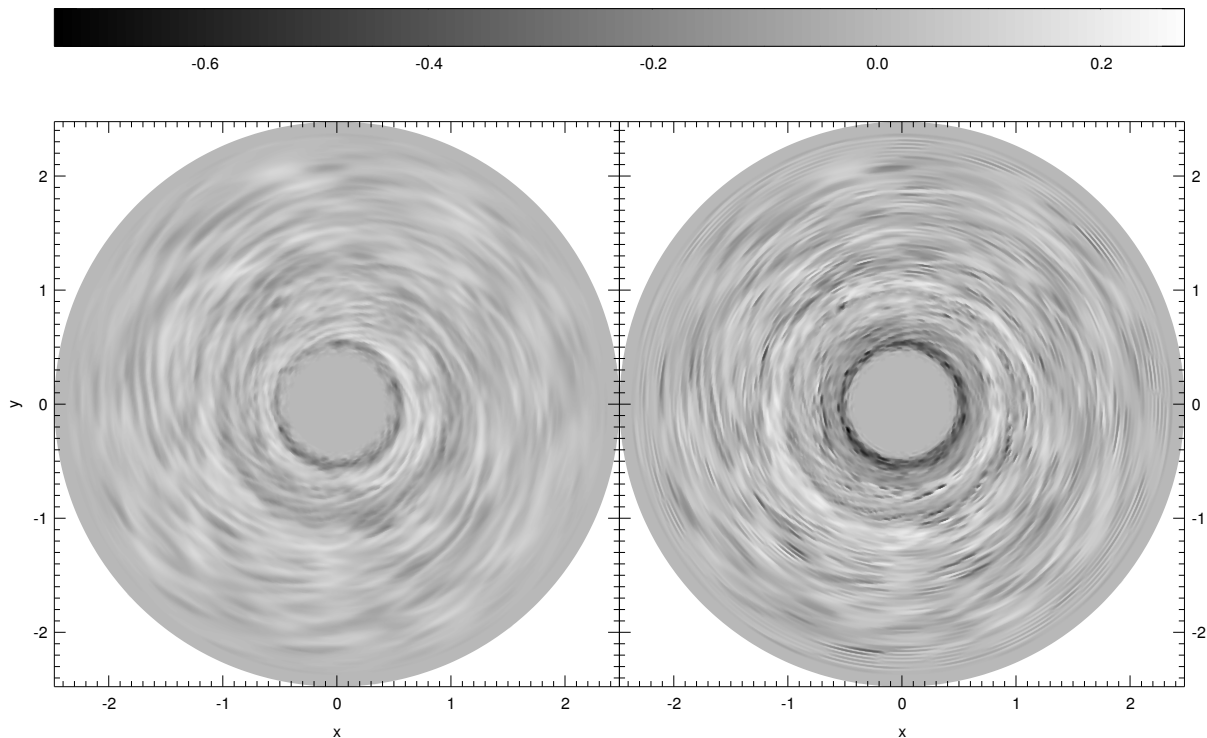


Figure 8.8: Same as Fig. 8.3, but for $\beta = 0.1$.

up dust gaps. However, this only holds for disks in which radiation pressure is not important. In the next section, we will investigate the effect of radiation pressure on gap formation.

8.4.3 Radiation pressure

In absence of a population of planetesimals generating dust, we can only consider particles for which $\beta < 1$. However, even when $\beta < 1$ radiation pressure changes the dynamics of both gas and dust significantly. In general, the dust particles are forced by the gas to rotate *faster* than their equilibrium angular velocity, which leads to outward dust migration. The opposing effect of radial pressure gradients causing inward migration of solids is not strong enough because $\eta \approx h^2 \ll \beta$ for typical values of h and β . Note that gas drag is needed for $\beta < 1$ to induce outward dust migration, while for $\beta > 1$ the particles are blown out of the system by radiation pressure alone.

First we consider a disk without a planet, and we set $d = 1$ and $\beta = 0.1$ to investigate the effect of radiation pressure on the streaming instabilities. Because radiation pressure tries to decouple gas and dust, relative velocities between the two fluids will increase compared to the case with $\beta = 0$, and therefore we expect to see an even stronger growth of streaming instabilities. However, it turns out that although the growth rate of the instabilities is indeed larger, radiation pressure has a stabilizing effect on the resulting turbulent structure (see Fig. 8.8). Compared to Fig. 8.3 the density of both gas and dust appear smoother when we include radiation pressure. The main

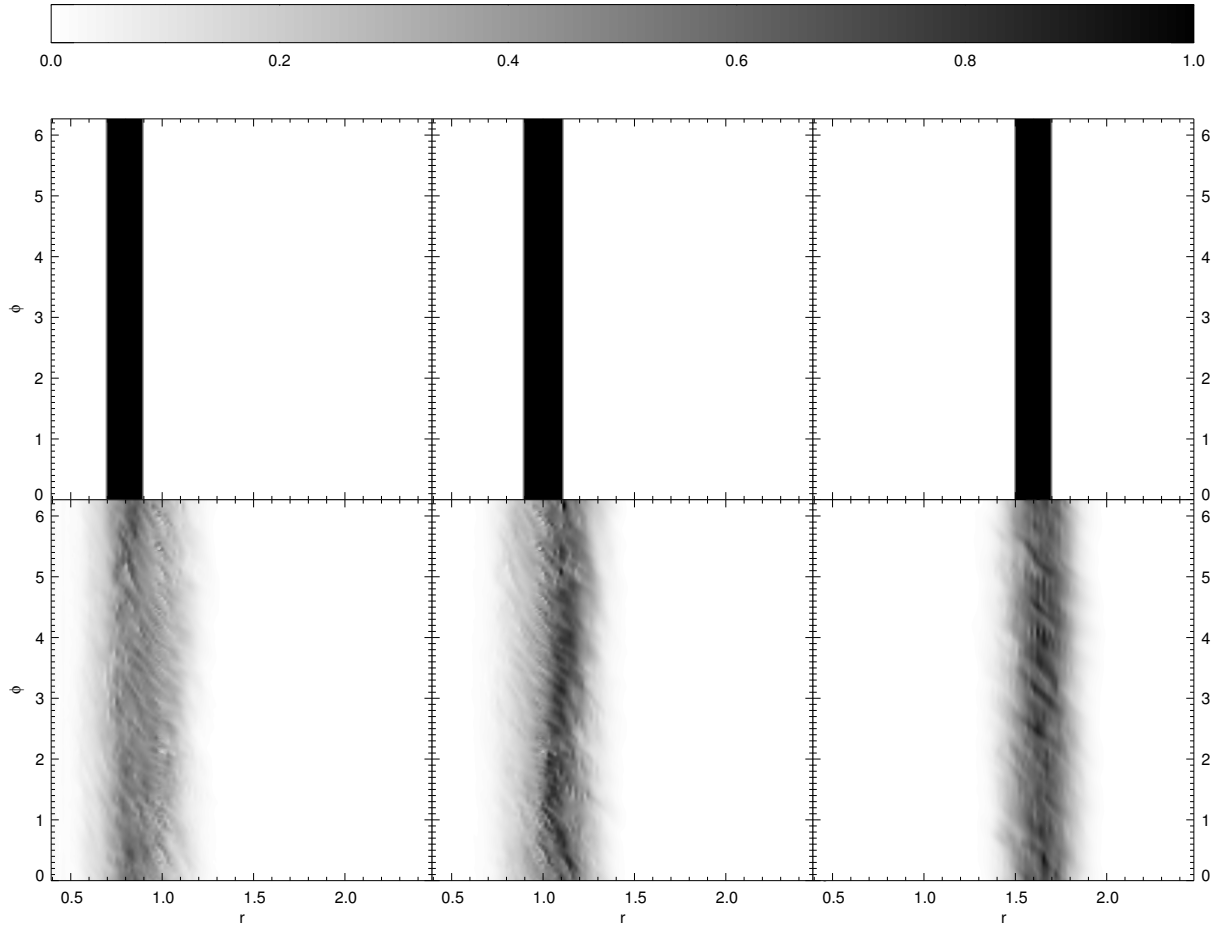


Figure 8.9: Same as Fig. 8.4, but with $\beta = 0.1$ after 30 orbits at $r = 1$.

reason for this can be seen in Fig. 8.8. Because of the outward motion of dust, a region with $d < 1$ develops in the inner region of the disk, which is much more stable against streaming instabilities. This stable region is able to suppress the streaming instabilities in the outer disk to some extent. Comparing Figs. 8.8 and 8.3 we see that the disk in Fig. 8.8 looks similar to the inner part of the disk in Fig. 8.3. This inner part also has an interior buffer zone that suppresses streaming instabilities: the boundary cells. Both these buffer zones have a stabilizing effect on the fluid mixture.

From the dust tracer fluids it is also clear that the dust moves outward, see Fig. 8.9. Compared to Fig. 8.4, where $\beta = 0$, the rings stay relatively compact. This is because of the different turbulent structure when $\beta \neq 0$.

The effects of radiation pressure on (dust) gap formation are illustrated in Fig. 8.10, where we show the azimuthally averaged surface densities of gas (left panel) and dust (right panel) after 100 orbits of a $0.1 M_J$ planet for different values of β , all with $T_s = 0.001$ and $d = 1$, initially. The $\beta = 0$ case was also shown in Fig. 8.7. Already for $\beta = 0.01$ we see significant differences, in the gas as well as in the dust. This is not surprising, because wherever $\beta > |\eta|$ radiation pressure dominates over gas pressure. This means that already for $\beta = 0.01$ radiation pressure is the dominant force every-

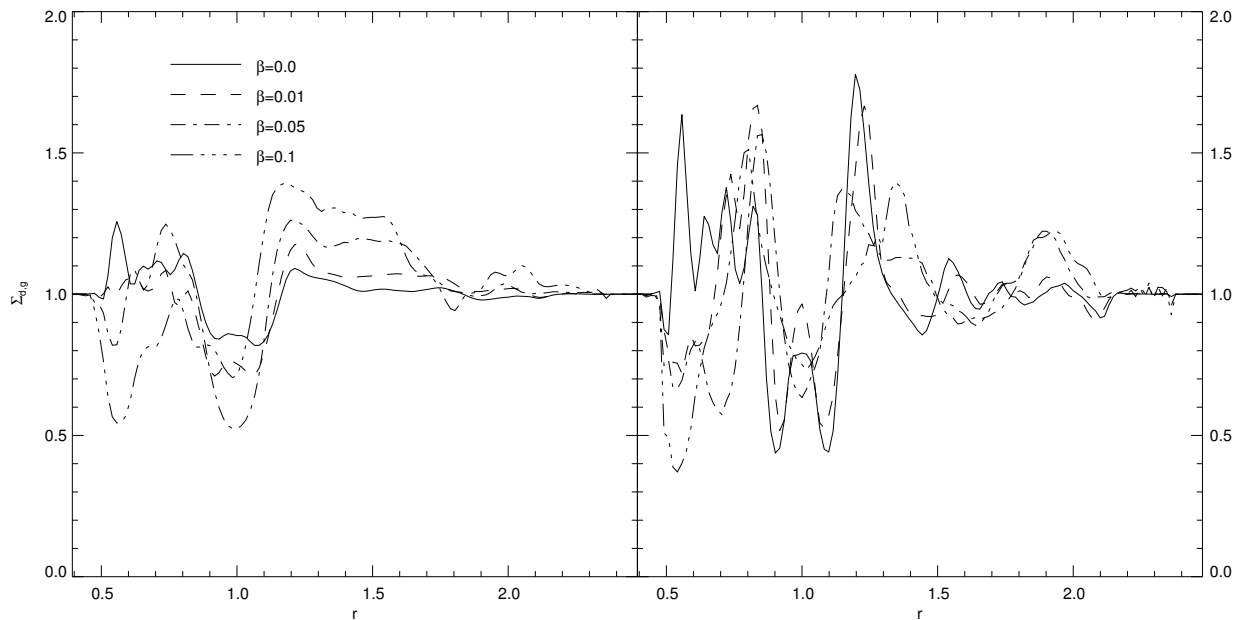


Figure 8.10: Azimuthally averaged gas (left panel) and dust (right panel) surface densities after 100 orbits of a $0.1 M_J$ planet with $T_s = 0.001$. Different line styles denote models with different values of β .

where in the disk except where the gas pressure gradients due to the planet are very strong, such as near the edges of the shallow gap or near the Roche lobe of the planet.

There are two competing processes operating in the dust gap. Radiation pressure tries to fill the gap from the inside, while the reduced gas density in the gap region promotes dust gap formation. We see that already for $\beta = 0.01$ radiation pressure starts to win, even though some of the gas is dragged along with the dust, which accounts for the deeper gas gap compared to the $\beta = 0$ case. The gas that is dragged outward is deposited in the outer disk, raising the gas density beyond $r = 1.1$. In the inner disk a region with $d < 1$ starts to emerge around $r = 0.6$, because dust is blown outward by radiation pressure while the inner boundary is closed. Also the gas density is reduced, albeit more slowly than the dust density.

For $\beta = 0.05$ (the dash-dotted line in Fig. 8.10) we see these trends continue. The dust gap gets less deep, while the gas gap gets deeper. For this value of β the gas gap is even slightly deeper than the dust gap. Even more gas is dragged towards the outer disk, and now also the gas is getting depleted around $r = 0.6$. The shallow gas and dust gaps are very smooth compared to the models with smaller values of β . This is reminiscent of the fact that the edges of the gas dip, which are responsible for the “W” shaped dust gap in the $\beta = 0$ model, are no longer dominant over radiation pressure. For larger values of β , gas and dust move almost freely from the inner disk to the outer disk, only slightly hindered by the planet.

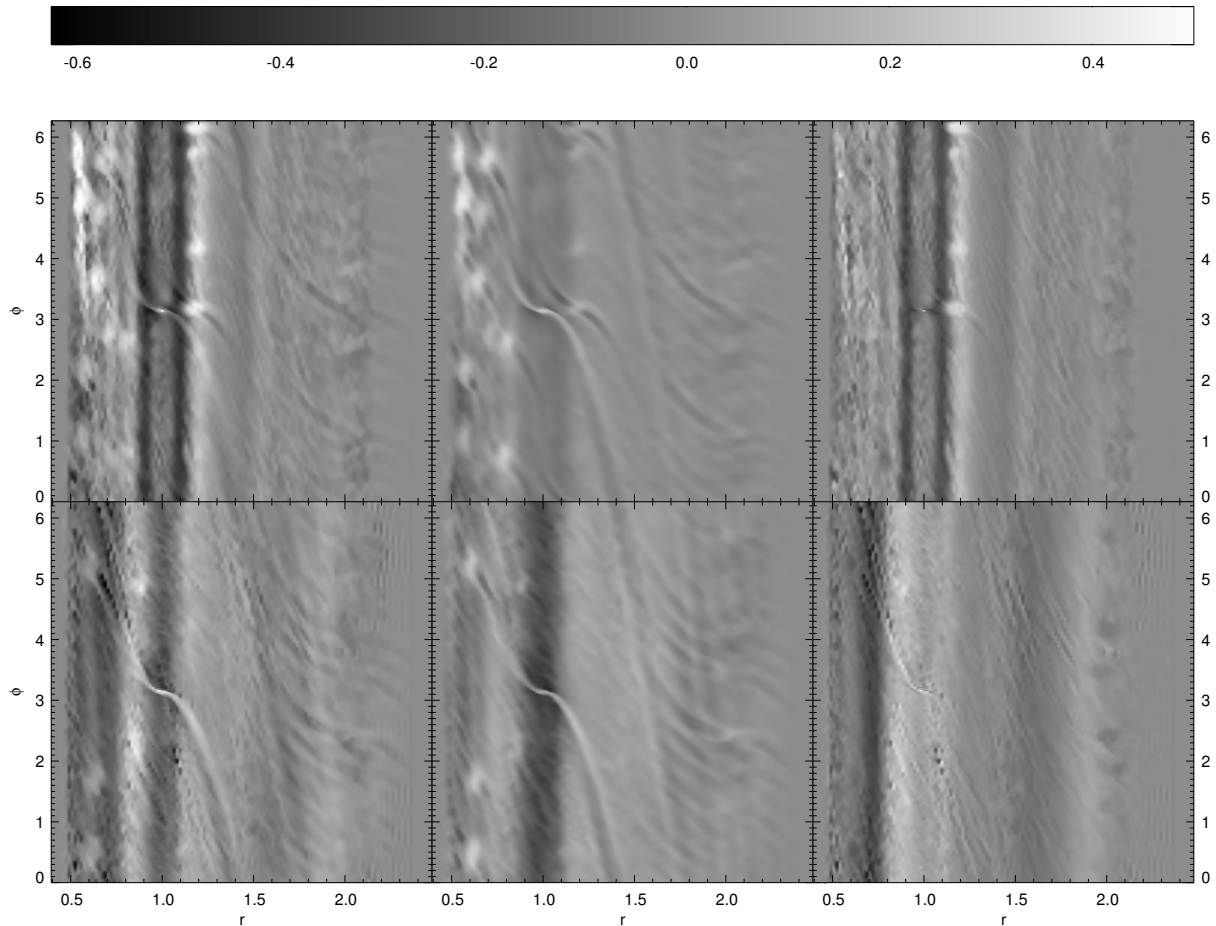


Figure 8.11: Logarithm of the gas and dust density around a $0.1 M_J$ planet after 100 orbits for $T_s = 0.001$ and $d = 1$ initially. Top panels: $\beta = 0$, see also Fig. 8.6. Bottom panels: $\beta = 0.05$. Left panels: dust density. Middle panels: gas density. Right panels: d .

In Fig. 8.11 we compare the two-dimensional dust and gas distributions for $\beta = 0$ and $\beta = 0.05$. The depletion of dust in the inner disk is clear from the lower left panel, while comparison of the two left panels shows that the dust gap is narrower and less deep for $\beta = 0.05$ compared to $\beta = 0$. This can also be seen from Fig. 8.10. From the middle panels we see that the gas gap is deeper but also a little narrower in the $\beta = 0.05$ model. The streaming instabilities are much less strong in the lower panels, which is partly due to the lower dust-to-gas ratio in the inner disk, and to the stabilizing effect of radiation pressure in general (as was the case in Fig. 8.8 compared to Fig. 8.3).

For the largest value of β considered here, $\beta = 0.1$, the inner gas disk gets severely depleted (see Fig. 8.10). There is still a peak in the density near the original inner edge of the shallow gap, and this is responsible for the dust peak near $r = 0.8$. As time proceeds, the inner disk will be cleared of gas, leaving a large inner planetary gas gap. However, eventually all gas will be blown away from the disk by indirect radiation pressure. For the dust disk, due to the peak in gas density near $r = 0.8$, there exists a well-defined shallow gap in the density distribution.

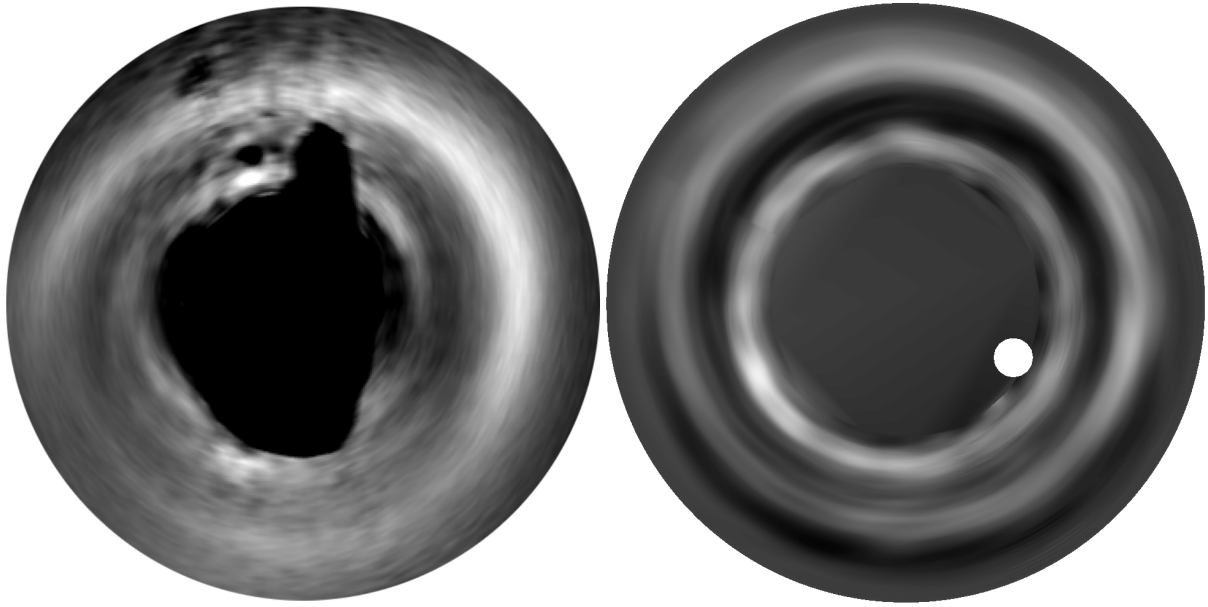


Figure 8.12: Comparison of the dust surface density around HD 141569 A (left panel) and the dust surface density produced by a 0.1 M_J planet in a disk with $\beta = 0.1$, $T_s = 0.001$, and $d = 1$, initially (right panel). The position of the planet is indicated by the white circle.

When β becomes comparable to unity, the radial speed of dust particles becomes comparable to the local Keplerian velocity. Therefore, non-axisymmetric features are much less readily broken by the Keplerian shear. Already for $\beta = 0.1$ we find large-scale asymmetry in the dust flow. See the right panel of Fig. 8.12, where we show the dust surface density from our model after 100 planetary orbits with $M_p = 0.1 M_J$, $T_s = 0.001$, $\beta = 0.1$ and $d = 1$, initially. The image was smoothed over a distance of $0.16 r_p$ to compare with the inferred surface density of HD 141569 A.

The axisymmetry of the dust flow is broken at the location of the planet, but because of the relatively large value of β this non-axisymmetry is not sheared away immediately, as is the case for $\beta \ll 1$ (leading to the axisymmetric outer dust ring in Chapter 6). Instead, the outer ring, located near $r = 2$, shows asymmetry in azimuth. The inner ring shows a ‘hot spot’ where the planetary spiral wave meets the outer edge of the dust gap. The location of the planet is indicated by the white circle.

In Fig. 8.12 we also show for comparison the result of the simulation with the dust surface density from Clampin et al. (2003) for HD 141569 A. Although the agreement is not perfect, it is important to realize that large scale asymmetric structures *can* be produced by a planet on a circular orbit. Further tuning of the parameters may yield a much better fit.

8.5 DISCUSSION

The dynamics of dust particles subject to gas drag and radiation pressure are governed by two parameters: T_s and β . Both are related to the grain size and shape. The stopping time, for example, is proportional to the ratio of the mass of the grain and its surface area; for spherical grains this ratio is proportional to the radius of the grains, see Eq. (8.3). Values for β can be calculated using Mie theory for different grain sizes and shapes (see Artymowicz 1988). A realistic model should therefore include the full dust size spectrum, from sub-micron sized interstellar dust grains to a planetesimal distribution. The enormous size of this parameter space makes such a model computationally very expensive. In this Chapter, we have covered the fraction of this space that can be modeled in the two-fluid approach without a population of dust-generating planetesimals.

Because the gas mass in transitional disks is about a factor of 100 lower than in protoplanetary disks (which accounts for a dust-to-gas ratio of unity), the two-fluid approach is limited to micron-sized particles, rather than millimeter-sized particles for protoplanetary disks (see Chapter 6). Calculations of β around HD 141569 A for different grain sizes show that $\beta < 1$ for particles larger than approximately $2 \mu\text{m}$. Therefore, our simulations trace self-consistently the population of micron-sized dust grains. Augereau & Papaloizou (2004) show that this is comparable to the minimum grain size in the disk of HD 141569 A, but it seems that there is also a population of dust particles for which $\beta > 1$. A more realistic model for HD 141569 A should therefore include dust-creating planetesimals. Their reaction on the possibly bound companions of HD 141569 A can also explain the large spiral in the disk (Augereau & Papaloizou 2004).

We have considered only planets on circular orbits. It turns out that the structures in the dust disk induced by the planet are predominantly axisymmetric for $\beta \ll 1$. This was also found in Chapter 6, and this conclusion does not change when $d \rightarrow 1$ and $\beta > 0$, except for the small turbulent structures. An eccentric planet (or companion star) will be required to produce strong non-axisymmetric features as seen in HD 141569 A. When β approaches unity, however, it turns out that non-axisymmetric features emerge even for a planet on a circular orbit.

If a planet is indeed perturbing the disk around HD 141569 A, the semi-major axis of its orbit would be approximately 100 AU. This is a little less extreme than the planets considered by Wyatt (2005), but still an explanation is lacking as how to move a planet to such a large distance (or form it there). However, since we are not aiming in this Chapter at providing a detailed model of HD 141569 A, but rather at describing the general phenomena that occur when planets orbit inside a transitional circumstellar disk, we leave more detailed modeling to future work. It is encouraging, though, that Fig. 8.12 shows that a single object produces the outer ring as well as the inner ring structures, while the eccentric bound companion considered by Augereau & Papaloizou (2004) only explains the *outer* spiral.

8.6 SUMMARY AND CONCLUSIONS

In this Chapter, we have presented the results of two-fluid calculations of a planet embedded in a transitional circumstellar disk. Compared to more massive protoplanetary disks, their transitional cousins can have approximately equal amounts of gas and dust, while, because these disks are optically thin to stellar radiation, radiation pressure plays an important role. We have examined the effects of radiation pressure and a dust-to-gas ratio d of unity on the signature of embedded planets.

When d becomes larger than unity, the disk is subject to streaming instabilities, as was predicted by Youdin & Goodman (2005). These instabilities lead to a turbulent structure of the disk, with density variations of two orders of magnitude. Radiation pressure has a stabilizing effect.

Gap formation proceeds more readily in disks with $d = 1$ compared to the protoplanetary disks considered in Chapter 6. This is because the gas is dragged along with the dust, lowering the gas density in the gap region. This makes the particles less well-coupled to the gas in the gap region, which promotes dust gap formation.

For $\beta > 0.05$ radiation pressure starts to dominate the dynamics. Gas and dust are blown from the inner disk to the outer disk by radiation pressure, and although the perturbations induced by the planet still lead to shallow gaps in the dust and in the gas, the structure is significantly different.

When β becomes comparable to unity, radial velocities of gas and dust become large enough to reduce the shearing capabilities of the disk. Non-axisymmetric density structures induced by the planet survive at much larger radii than for a disk where $\beta \ll 1$. We have shown that a low-mass planet on a circular orbit perturbs a disk of gas and dust with $T_s = 0.001$, $\beta = 0.1$ and $d = 1$, initially, in a similar fashion as the structures seen in the disk around HD 141569 A. However, more detailed modeling of the population of particles with $\beta > 1$ is needed to reach more definite conclusions, together with modeling the unseen population of planetesimals.

ACKNOWLEDGMENTS

We thank J. C. Augereau for useful discussions.

REFERENCES

- Ardila, D. R., Lubow, S. H., Golimowski, D. A., et al. 2005, *ApJ*, 627, 986
Artymowicz, P. 1988, *ApJ*, 335, L79
Augereau, J. C., Lagrange, A. M., Mouillet, D., & Ménard, F. 1999, *A&A*, 350, L51
Augereau, J. C. & Papaloizou, J. C. B. 2004, *A&A*, 414, 1153
Backman, D. E. & Paresce, F. 1993, in *Protostars and Planets III*, 1253–1304
Bate, M. R., Lubow, S. H., Ogilvie, G. I., & Miller, K. A. 2003, *MNRAS*, 341, 213
Beckwith, S. V. W. & Sargent, A. I. 1996, *Nature*, 383, 139

- Boccaletti, A., Augereau, J.-C., Marchis, F., & Hahn, J. 2003, *ApJ*, 585, 494
- Calvet, N., D'Alessio, P., Hartmann, L., et al. 2002, *ApJ*, 568, 1008
- Clampin, M., Krist, J. E., Ardila, D. R., et al. 2003, *AJ*, 126, 385
- D'Angelo, G., Henning, T., & Kley, W. 2002, *A&A*, 385, 647
- D'Angelo, G., Kley, W., & Henning, T. 2003, *ApJ*, 586, 540
- de Val-Borro, M., Edgar, R. G., Artymowicz, P., et al. 2006, *MNRAS*, 370, 529
- Eulderink, F. & Mellema, G. 1995, *A&AS*, 110, 587
- Garaud, P., Barrière-Fouchet, L., & Lin, D. N. C. 2004, *ApJ*, 603, 292
- Godon, P. 1996, *MNRAS*, 282, 1107
- Goldreich, P. & Tremaine, S. 1980, *ApJ*, 241, 425
- Goldreich, P. & Ward, W. R. 1973, *ApJ*, 183, 1051
- Johansen, A., Klahr, H., & Henning, T. 2006, *ApJ*, 636, 1121
- Jonkheid, B., Kamp, I., Augereau, J. C., & van Dishoeck, E. F. 2006, *A&A*, 453, 163
- Kamp, I. & van Zadelhoff, G.-J. 2001, *A&A*, 373, 641
- Kenyon, S. J. & Bromley, B. C. 2004, *AJ*, 127, 513
- Kley, W. 1999, *MNRAS*, 303, 696
- Lin, D. N. C. & Papaloizou, J. C. B. 1993, in *Protostars and Planets III*, 749–835
- Merín, B., Montesinos, B., Eiroa, C., et al. 2004, *A&A*, 419, 301
- Mouillet, D., Lagrange, A. M., Augereau, J. C., & Ménard, F. 2001, *A&A*, 372, L61
- Ozernoy, L. M., Gorkavyi, N. N., Mather, J. C., & Taidakova, T. A. 2000, *ApJ*, 537, L147
- Paardekooper, S.-J. & Mellema, G. 2004, *A&A*, 425, L9
- Paardekooper, S.-J. & Mellema, G. 2006a, *A&A*, 453, 1129
- Paardekooper, S.-J. & Mellema, G. 2006b, *A&A*, 450, 1203
- Quillen, A. C., Varnière, P., Minchev, I., & Frank, A. 2005, *AJ*, 129, 2481
- Sekiya, M. 1998, *Icarus*, 133, 298
- Shakura, N. I. & Sunyaev, R. A. 1973, *A&A*, 24, 337
- Simis, Y. J. W., Icke, V., & Dominik, C. 2001, *A&A*, 371, 205
- Takeuchi, T. & Artymowicz, P. 2001, *ApJ*, 557, 990
- Takeuchi, T. & Lin, D. N. C. 2002, *ApJ*, 581, 1344
- Ward, W. R. 1997, *Icarus*, 126, 261
- Weinberger, A. J., Becklin, E. E., Schneider, G., et al. 1999, *ApJ*, 525, L53
- Woitke, P. & Helling, C. 2003, *A&A*, 399, 297
- Wolf, S., Gueth, F., Henning, T., & Kley, W. 2002, *ApJ*, 566, L97
- Wyatt, M. C. 2005, *A&A*, 440, 937
- Youdin, A. N. & Goodman, J. 2005, *ApJ*, 620, 459
- Youdin, A. N. & Shu, F. H. 2002, *ApJ*, 580, 494

Bibliography

REFEREED PAPERS

A comparative study of disc-planet interaction

de Val-Borro, M., Edgar, R. G., Artymowicz, P., Cieliegi, P., Cresswell, P., D'Angelo, G., Delgado-Donate, E. J., Dirksen, G., Fromang, S., Gawryszczak, A., Klahr, H., Kley, W., Lyra, W., Masset, F., Mellema, G., Nelson, R. P., **Paardekooper, S. -J.**, Peplinski, A., Pierens, A., Plewa, T., Rice, K., Schäfer, C., Speith, R.

2006, Monthly Notices of the Royal Astronomical Society, Volume 370, pp. 529-558

Dust Flow in Gas Disks in the presence of embedded Planets

Paardekooper, S. -J., Mellema, G.

2006, Astronomy & Astrophysics, Volume 453, pp. 1129-1140

RODEO: a new method for planet-disk interaction

Paardekooper, S. -J., Mellema, G.

2006, Astronomy & Astrophysics, Volume 450, pp. 1203-1220

Planets opening dust gaps in gas disks

Paardekooper, S. -J., Mellema, G.

2004, Astronomy & Astrophysics, Volume 425, pp. L9-L12

New type of brightness variations of the colliding wind WO4 + O5((f)) binary WR 30a

Paardekooper, S. -J., van der Hucht, K. A., van Genderen, A. M., Brogt, E., Gieles, M., Meijerink, R.

2004, Astronomy & Astrophysics, Volume 404, pp. 29-32

On the variability of the visual binary WR86. WC7 with a β -Cephei companion

Paardekooper, S. -J., Veen, P. M., van Genderen, A. M., van der Hucht, K. A.

2002, Astronomy & Astrophysics, Volume 384, pp. 1012-1022

CONFERENCE PROCEEDINGS

Planets in Disks: A New Method for Hydrodynamic Disk Simulations

Paardekooper, S. -J., Mellema, G.

2004, appeared in the proceedings of the Paris conference "Extrasolar Planets: Today and Tomorrow", June 30-July 4, 2003

Groeiende en Bewegende Planeten in Schijven

DE geschiedenis van de Aarde en haar bewoners is het terrein van verschillende disciplines in de wetenschap. De geschiedenis van de mensheid wordt bestudeerd door historici, terwijl de oorsprong van het leven het terrein is van de biologie. Geologen bestuderen de geschiedenis van de Aarde, en sterrenkundigen houden zich bezig met de geschiedenis van het Heelal. Planeetvorming, waar dit proefschrift over handelt, bevindt zich op de grens tussen sterrenkunde en geologie. Over het algemeen zijn de vroegste stadia van planeetvorming het terrein van de sterrenkunde, terwijl de geologie begint als er daadwerkelijk een planeet is. Er is echter een groot gebied van overlap. Dit proefschrift benadert planeetvorming van de sterrenkundige kant, en we proberen te beantwoorden hoe een zojuist ontstane planeet zijn omgeving vervormt, en hoe de planeet door zijn omgeving verder wordt beïnvloed. In deze samenvatting zullen we eerst de termen "planeet" en "omgeving" preciezer definiëren.

PLANETEN

Het is opmerkelijk hoe vaag de definitie van "planeet" is. De naam komt uit het Grieks en betekent "zwerfer", wat refereert aan het feit dat ze ten opzichte van de "vaste" sterrenhemel bewegen gedurende het jaar. Nu zijn er veel meer hemelverschijnselen die hetzelfde doen: van kometen tot vliegtuigen, beide overduidelijk geen planeten. De huidige officiële definitie van een planeet luidt: een lichaam met een aanzienlijke massa dat rond een ster cirkelt en geen energie als gevolg van kernfusie produceert. Dat laatste onderscheidt een planeet van een ster. Het probleem zit natuurlijk in het woord "aanzienlijk". Hoe zwaar moet een lichaam zijn om "planeet" te mogen heten?

Het Zonnestelsel

Als we beginnen bij de Zon, dan is het eerste lichaam dat we vinden Mercurius, duidelijk een planeet, hoewel hij bijna 20 keer zo licht is als de Aarde. Mercurius bevindt zich ongeveer 2.5 keer dichterbij de Zon dan de Aarde. Door zijn geringe massa heeft Mercurius geen atmosfeer.

Iets verder van de Zon vinden we Venus, het tweelingzusje van de Aarde. Venus

is slechts een klein beetje lichter dan de Aarde, en staat slechts een klein beetje dicht bij de Zon, maar toch zijn er gigantische verschillen in weersomstandigheden aan het oppervlak. De atmosfeer van Venus zit vol druppels zwavelzuur, en deze wolken zijn zo dik dat het oppervlak van Venus nooit zichtbaar is vanuit de ruimte. Het enorme broeikas effect zorgt voor extreem hoge temperaturen: gemiddeld zo'n 480 °C. Een zeer vijandige omgeving dus.

Op een gemiddelde afstand van 1 Astronomische Eenheid (ongeveer 150 000 000 km) van de Zon bevindt zich de Aarde. De Aarde weegt zo'n $6 \cdot 10^{24}$ kg (een 6 met 24 nullen). De Aarde is bij ons wel bekend, en kan dienen als vergelijkingsmateriaal voor andere planeten.

Anderhalf keer verder van de Zon vinden we Mars, de rode planeet. Tien keer zo licht als de Aarde, maar nog steeds zeker een planeet. Pas voorbij Mars vinden we de eerste voorbeelden van lichamen die te licht zijn bevonden om zich "planeet" te mogen noemen: de asteroïdengordel. Dit is een ring van rotsblokken van variabele grootte, tot ongeveer 1000 km. Er zijn er inmiddels ruim 300 000 bekend, en intuïtief is het duidelijk dat dit geen planeten zijn. Door hun geringe dichtheid komen ze qua massa ook niet in de buurt van Mercurius, dus tot zo ver geen probleem.

Alle planeten die we tot nu toe hebben genoemd hebben één ding gemeen: er is een oppervlak waar je op zou kunnen staan. Op Venus moet je eerst door een dik wolkendek heen, maar de massa van deze atmosfeer is veel kleiner dan de massa van de planeet. Voor Jupiter, de eerstvolgende planeet die we voorbij de asteroïdengordel tegenkomen, is het precies andersom: Jupiter is bijna een en al atmosfeer. Het is niet eens duidelijk of er ergens diep van binnen wel een vaste kern is. In ieder geval is Jupiter zo'n 300 keer zo zwaar als de Aarde, waarbij meer dan 90% van die massa in de atmosfeer zit.

Jupiter behoort duidelijk tot een andere klasse van planeten dan Mercurius, Venus, de Aarde en Mars. Voor deze laatste groep zijn verschillende namen in omloop: rotsplaneten, Aarde-achtige planeten, in het Engels "terrestrial planets". Jupiter behoort tot de zogenaamde gasreuzen: planeten die vooral grote bollen van gas zijn, mogelijk met een kleine, vaste kern. Ook Saturnus behoort tot die groep, alsmede Uranus en Neptunus. Vanwege de lage temperaturen rond deze laatste twee (door hun grote afstand tot de Zon: Neptunus staat meer dan 30 keer verder van de Zon dan de Aarde) worden ze ook wel ijsreuzen genoemd.

Tot zo ver is de structuur van het zonnestelsel redelijk eenvoudig: we hebben een binnenste ring van rotsplaneten, dan de asteroïdengordel, en nog verder vinden we de gasreuzen. Voorbij Neptunus komen we in het schemergebied van de ijsdwergen, ook wel de Kuiper gordel genoemd. De Kuiper gordel bestaat uit vele rotsblokken, net als de asteroïdengordel, maar helaas hebben sommigen van deze ijsdwergen een redelijk grote massa. Het beste voorbeeld is Pluto, oorspronkelijk gepresenteerd als de negende planeet, voordat de Kuiper gordel werd ontdekt. Toen bleek dat Pluto slechts één van de velen was, rezen de eerste twijfels, maar Pluto was nog steeds verreweg het grootste object in de Kuiper gordel: een reus onder de ijsdwergen. Met de ontdekking van Sedna en Quaoar, ijsdwergen die in grootte vergelijkbaar zijn met Pluto, is de planeetstatus van Pluto verder onder druk komen te staan.

Gezien de structuur van het zonnestelsel ligt het nu het meest voor de hand om Pluto als een ijsdwerf te classificeren, en niet als de negende planeet. We hebben dan vier rotsplaneten, de astroïdengordel, vier gasreuzen en tenslotte ijsdwerfen. Nog verder van de Zon verwijderd vinden we de Oortwolk; een bolvormige wolk van blokken van steen en ijs nog verder weg dan de Kuiper-gordel. Deze wolk is de bron van een bepaalde klasse kometen, maar speelt verder geen rol in dit proefschrift.

Exoplaneten

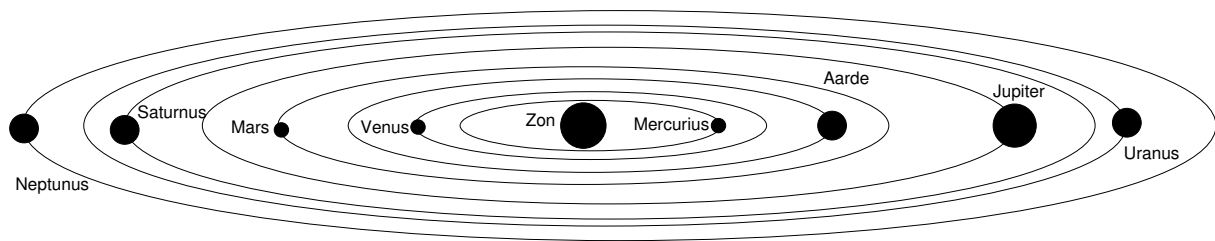
Het is alweer ruim tien jaar geleden dat de eerste planeet buiten ons eigen Zonnestelsel werd gevonden. Net als vrijwel alle andere inmiddels ontdekte exoplaneten is de planeet rond de ster 51 Pegasi niet gevonden door directe waarneming, dat wil zeggen: er werd geen lichtstraal van het oppervlak van de planeet gezien voordat men wist dat hij er was. De reden hiervoor is dat een ster zo ongelooflijk veel helderder is dan een planeet dat deze gewoon overstraald wordt door de ster. Gelukkig is er een truc: de ster trekt aan de planeet om hem in zijn baan te houden (zwaartekracht), maar op dezelfde manier trekt de planeet ook aan de ster. Samen roteren ze om het massa-middelpunt. Zoals we bij een film van een kogelslingeraar, waarbij we de kogel weg-retoucheren, toch kunnen zien aan de beweging van de slingeraar dat hij iets zwaars rondslingert, kunnen we ook aan de beweging van de ster zien dat er een zware planeet omheen draait. Deze methode werkt natuurlijk het beste als de planeet erg zwaar is, en er zijn tot nu toe slechts gasreuzen zoals Jupiter mee gevonden. Toch hebben deze waarnemingen tot vele verrassingen geleid.

Er bleken vele planetenstelsels te bestaan rond sterren zoals de Zon. Sommigen lijken op die van ons, maar velen zijn heel anders van opbouw. Er is een hele nieuwe klasse van planeten ontdekt: de "Hete Jupiters". Dit zijn gasreuzen zoals Jupiter die op extreem kleine afstand van de ster staan: enkelen wel 100 keer dichterbij hun ster dan de Aarde van de Zon staat. Een andere verrassing was de hoge gemiddelde eccentriciteit van de planeetbanen: terwijl in ons Zonnestelsel alle gasreuzen een bijna cirkelvormige baan beschrijven, blijkt de gemiddelde eccentriciteit voor exoplaneten zo'n 7 keer hoger te zijn dan die van Jupiter. Exoplaneten draaien in ellipsen rond hun ster.

Tot 1995 kenden we alleen ons eigen Zonnestelsel wat planeten betreft, en de hele theorie over hoe planeten ontstaan was er dan ook op gericht om slechts dit ene voorbeeld van een planetenstelsel dat we zo goed kennen te verklaren. Men moet roeien met de riemen die beschikbaar zijn, tenslotte. De verrassingen die werden ontdekt gedurende de speurtocht naar exoplaneten hebben de wereld behoorlijk op zijn kop gezet.

SCHIJVEN

De structuur van het zonnestelsel is erg plat: alle planeten draaien rond in hetzelfde vlak (zie Fig. 1). Dat dit geen toeval is, werd al vermoed in de 18^e eeuw, waarin Laplace



Figuur 1: Schematisch overzicht van de planeten in het Zonnestelsel (niet op schaal).

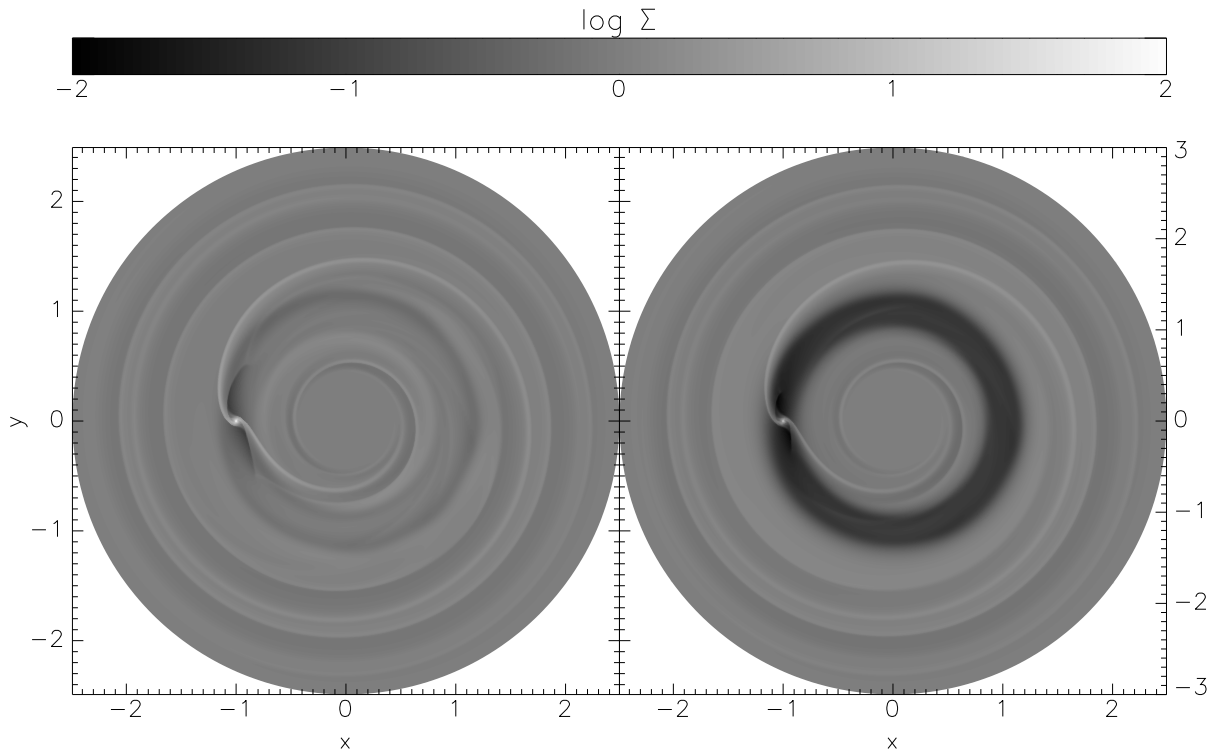
(1796) voorstelde dat planeten gevormd zijn in een platte wolk van gas en stof. Tegenwoordig kunnen we deze schijven ook daadwerkelijk zien rond jonge sterren, terwijl de vorming van zulke schijven ook theoretisch zeer aannemelijk is, wat suggereert dat planeetvorming plaatsvindt in platte schijven van gas en stof.

Protoplanetaire schijven zijn interessante objecten. Er bestaat een delicaat evenwicht tussen de zwaartekracht van de centrale ster, die alle materie naar binnen wil trekken, en de rotatie van de schijf, die alle materie naar buiten wil slingeren. Omdat de zwaartekracht naar buiten toe afneemt, neemt ook de rotatie naar buiten af: hoe verder weg van de ster, hoe langzamer de materie beweegt. Dit is dus een heel ander geval dan de *starre* rotatie van bijvoorbeeld een frisbee of een CD: een protoplanetaire schijf roteert *differentieel*. Dit leidt tot interessante fenomenen.

Stel: je draait in een ruimteschip mee in de schijf rond een jonge ster. Je draaisnelheid is precies goed om zwaartekracht en middelpuntvliedende kracht in evenwicht te houden, en de afstand tussen jou en de ster blijft gelijk. Plotseling merk je dat er iemand anders, in zijn eigen ruimteschip, voor je vliegt, in dezelfde baan. Omdat ook je voorligger een evenwicht bewaart tussen de twee krachten, zijn jullie snelheden gelijk en verandert de afstand tussen beide ruimteschepen niet. Je besluit je voorligger in te halen. Wat te doen?

Op de snelweg was het eenvoudig geweest: het gaspedaal indrukken en links er voorbij. In de schijf rond een ster gaat het er anders aan toe. Als je versnelt, neemt je rotatiesnelheid toe. Dit verstoort het evenwicht tussen de zwaartekracht en de middelpuntvliedende kracht: de rotatie wint, tijdelijk. Omdat de rotatie wint, begint je ruimteschip naar buiten te bewegen, totdat het een afstand tot de ster bereikt waar de zwaartekracht en de nieuwe middelpuntvliedende kracht weer met elkaar in evenwicht zijn. Omdat de evenwichtssnelheid naar buiten toe afneemt (de differentieële rotatie) zal je nieuwe rotatiesnelheid uiteindelijk *lager* zijn dan je oorspronkelijke snelheid. Je voorligger begint op je uit te lopen!

De truc is, dat je in een differentieel roterende schijf moet *remmen* om te versnellen. Afremmen brengt je in een lagere baan van snelle rotatie, waarin je je voorligger luid toeterend kunt inhalen. Zodra je er voorbij bent, kun je weer *versnellen* om je ruimteschip terug te brengen in zijn oorspronkelijke baan. Een schijf is zeker geen saaie omgeving om in te wonen!



Figuur 2: Gasdichtheid in een schijf met een planeet zo zwaar als Jupiter. De planeet bevindt zich in $(x, y) = (-1, 0)$, en draait zijn rondjes tegen de klok in. De ster staat in de oorsprong (niet zichtbaar). Links: dichtheid na 120 jaar. De twee getijdengolven zijn duidelijk zichtbaar. Rechts: dichtheid na 2400 jaar. De planeet heeft een diep gat gegraven in de schijf.

PLANETEN IN SCHIJVEN

Planeten vormen zich dus in schijven van gas en stof rond jonge sterren. De schijf verdampt langzaam, totdat er vrijwel alleen planeten overblijven, zoals in ons zonnestelsel. Maar gedurende een lange periode draaien nieuw gevormde planeten rond in de schijf waaruit ze zijn gevormd. Het blijkt dat planeet en schijf een interessante relatie onderhouden, die soms zeer gewelddadig kan aflopen.

De zwaartekracht van de planeet verstoort de banen van de gas- en stofdeeltjes in de schijf. Op Aarde ontstaan getijden door de invloed van de zwaartekracht van de Maan (en, in mindere mate, van de Zon). Zowel aan de zijde van de Aarde die het dichtst bij de Maan is als aan de zijde die van de Maan is afgekeerd is het vloed. In het eerste geval trekt de Maan harder dan gemiddeld aan het water op Aarde, wat zorgt voor een hoge waterstand, en in het laatste geval trekt de Maan minder hard dan gemiddeld aan het water, waardoor de rotatie van het Aarde-Maan systeem het wint van de zwaartekracht en het water een beetje naar buiten geslingerd wordt.

Voor een planeet in een schijf geldt bijna hetzelfde verhaal, alleen nu voor het systeem planeet-ster in plaats van Aarde-Maan. Een tweede belangrijk verschil is dat de schijf van gas (die de rol speelt van de oceaan op Aarde) niet ophoudt aan het oppervlak van de planeet. Dit betekent dat de "oceaan" niet slechts een beetje vervormd

wordt, maar dat de getijde-verstoringen, die beginnen bij de planeet, zich voortplanten in de schijf.

Net als op Aarde zijn er twee van zulke getijde-golven: één naar de ster toe en één van de ster af. Nu komt weer de differentiële rotatie om de hoek kijken: terwijl de golf zich naar de ster toe beweegt neemt zijn rotatie alsmaar toe. Hierdoor krijgt de golf een spiraalvorm. Voor de naar buiten gerichte golf geldt hetzelfde, maar dan omgekeerd: deze komt in een gebied van langzamere rotatie, waardoor ook nu een spiraalvorm ontstaat, maar precies in de andere richting dan voor de binnenste spiraal. In het linker paneel van Fig. 2 zijn deze spiraalgolven duidelijk te zien.

Onder invloed van deze spiralen wordt gas en stof weggetransporteerd van de planeet. Hoe zwaarder de planeet, hoe sterker dit effect. Een planeet zo zwaar als Jupiter graaft een diep gat in de schijf waarin vrijwel geen gas of stof meer te vinden is. De precieze massa die nodig is voor zo'n drastische verminking van de schijf is één van de onderwerpen van dit proefschrift (Hoofdstukken 3, 6 en 8). Deze gaten zijn belangrijk voor toekomstige waarnemingen: zodra de telescopen sterk genoeg zijn om planeten in schijven te zoeken, zal er eerst gekeken worden of er gaten in de schijf gemaakt zijn. In het rechter paneel van Fig. 2 is het gat te zien wat door Jupiter gegraven wordt in een schijf rond de Zon.

De schijf laat deze verminking niet zomaar over zijn kant gaan: hij is uitstekend in staat zichzelf te verdedigen. Een beetje te goed zelfs. Omdat de differentiële rotatie niet lineair is, zijn de twee getijdegolven niet gelijk in sterkte. De (zwaarte-) krachten die deze golven op de planeet uitoefenen heffen elkaar dus niet op: de planeet zal van baan gaan veranderen onder invloed van de golven die hij zelf opwekt. Het blijkt dat voor een schijf met een vaste temperatuur-structuur (dat wil zeggen dat de aanwezigheid van de planeet geen invloed heeft op de temperatuur in de schijf) de planeet *altijd* in de richting van de ster beweegt.

Deze "migratie" van planeten is de verklaring voor de speciale klasse van exoplaneten (de "Hete Jupiters") die zeer dicht rond hun ster cirkelen. Zo dichtbij zelfs, dat het veel te heet is voor hen om daar gevormd te zijn: één van deze hete Jupiters is zelfs aan het verdampen onder invloed van de hitte van de ster. Migratie biedt de mogelijkheid dat deze planeten veel verder weg van de ster gevormd zijn, waar de schijf koeler is, waarna ze naar binnen gemigreerd zijn onder invloed van interactie met de schijf.

Het vervelende is echter, dat deze theorie voorspelt dat migratie erg snel gaat: in het extreme geval van een planeet zo zwaar als Neptunus in een schijf die 20 keer zo zwaar is als Jupiter duurt het slechts enkele tienduizenden jaren voor de planeet in de ster verdwijnt. Dit is veel te kort voor een planeet om uit te groeien tot een gasreus. Schijven verdampen slechts langzaam: het duurt miljoenen jaren voor al het gas is verdwenen. En al die tijd blijven planeten naar de ster toe bewegen. Het is zelfs zo erg, dat vrijwel *alle* planeten in de ster zouden verdwijnen voordat de schijf helemaal is verdampt. Probleem nummer één voor de theorie van planeet-schijf-interactie.

Een ander probleem is de hoge gemiddelde eccentriciteit van exoplaneten. Omdat de banen van de gas- en stofdeeltjes in de schijf vrijwel cirkelvormig zijn leidt de interactie van de planeet met de schijf tot circularisatie van de planeetbaan, mocht deze excentrisch zijn. Een uitzondering moet gemaakt worden voor zware planeten die

een diep gat in de schijf graven: als het gat diep en wijd genoeg is kan de eccentriciteit van de planeetbaan groeien. Helaas is dit alleen nog in simulaties waargenomen voor planeten die zo'n twintig keer zwaarder zijn dan Jupiter, terwijl er verschillende veel lichtere exoplaneten op zeer eccentriche banen gevonden zijn. Probleem nummer twee voor de theorie. In dit proefschrift bekijken we beide problemen nader.

DIT PROEFSCHRIFT

In dit proefschrift bekijken we de interactie tussen een planeet en de schijf waaruit deze geboren werd met behulp van gasdynamische computersimulaties. Met behulp van de computer worden de bewegingen van gas- en stofdeeltjes berekend terwijl ze reageren op de ster, op de planeet en op elkaar. De krachten die een rol spelen zijn de zwaartekracht, interne wrijving in het gas (de "stroperigheid"), wrijving tussen gas en stof, gasdruk en (soms) stralingsdruk. Het is duidelijk dat het samenspel van al deze krachten ingewikkelde patronen tot gevolg kan hebben.

Hoofdstuk 1

We beginnen in Hoofdstuk 1 met een algemene introductie, waarbij we wat dieper op de stof ingaan dan in deze Nederlandse Samenvatting.

Hoofdstuk 2

In Hoofdstuk 2 behandelen we de gebruikte numerieke methode in detail. Het is uiteraard zeer belangrijk om deze methode te testen, want we willen zeker weten dat alles wat we in de simulaties zien *echte* fysische effecten zijn, en geen fouten of tekortkomingen van de methode. Door alle hoofdstukken heen testen we de verschillende onderdelen van de methode grondig, maar in Hoofdstuk 2 leggen we de basis: de module die de beweging van het gas uitrekent. Deze module is speciaal ontworpen om *schokgolven* correct te behandelen. De bekendste vorm van een schokgolf is waarschijnlijk de knal die een vliegtuig veroorzaakt als hij door de geluidsbarrière gaat. Een schokgolf verschilt van een gewone (geluids-) golf in dat de verandering in snelheid en dichtheid veel heftiger is. Sterker nog: een schokgolf wordt meestal voorgesteld als een *discontinuïteit*, een punt waar het gas over een oneindig kleine afstand een sprong maakt van de ene naar de andere toestand. Discontinuïteiten zijn erg moeilijk te hanteren in een computer, want deze kan geen oneindig kleine (of oneindig grote) hoeveelheden aan. Een verkeerde benadering van schokken kan tot verkeerde antwoorden leiden, en zoals blijkt in Hoofdstuk 3 zijn schokken erg belangrijk.

Hoofdstuk 3

Vervolgens passen we de methode zoals beschreven in Hoofdstuk 2 toe op planeten van verschillende massa's om te zien waar de grens ligt tussen planeten die wel of geen gat graven in de schijf. Schokgolven blijken hier een essentiële rol bij te spelen. Door de invloed van de schokken kunnen *alle* planeten gaten graven in schijven, van Mercurius tot Jupiter. Het duurt alleen steeds langer voor lichtere planeten, zodanig dat de Aarde er eigenlijk al te lang over doet: voordat het gat diep genoeg is om te kunnen waarnemen is de schijf al verdampt.

Hoofdstuk 4

Een ander voordeel van de methode zoals beschreven in Hoofdstuk 2 is dat deze geschikt is voor een willekeurig systeem van coördinaten. De schijf is rond, dus het ligt voor de hand om in *poolcoördinaten* te werken. Verder is het verstandig om de planeet op een vaste plek in het coördinatensysteem te houden. Voor een cirkelbaan is dit simpel: we laten het coördinatensysteem gewoon mee roteren met de planeet, zodat de planeet ten opzichte van de coördinaten stil blijft staan. Maar zodra de planeet gaat migreren, en misschien wel een eccentriche baan krijgt, hebben we een probleem. In dit Hoofdstuk gebruiken we een coördinatensysteem dat zich aanpast aan de baan van de planeet. Hoe snel de planeet ook beweegt, en hoe eccentriche de baan ook wordt, de planeet staat stil in ons coördinatenstelsel. We gebruiken dit stelsel om migrerende en eccentriche planeten te bekijken. In het bijzonder proberen we of we een Jupiter op een eccentriche baan kunnen krijgen, onder de meest gunstige omstandigheden. Dit blijkt zeer moeilijk te zijn: alleen een hele dunne schijf is in staat Jupiter op een eccentriche baan te krijgen.

Hoofdstuk 5

In Hoofdstuk 5 gaan we in op het migratieprobleem. We bekijken in hoeverre de aanname dat de temperatuur in de schijf niet wordt beïnvloed door de planeet van belang is. De reden waarom dit nooit eerder is gedaan ligt in de enorme computerkracht die er voor nodig is. De verhitting van de schijf is niet het probleem; iedere hydrodynamica-methode kan die eenvoudig uitrekenen. De moeilijkheid ligt in de afkoeling die wordt veroorzaakt door straling. Fotonen ontsnappen uit de hete gebieden en transporteren hun energie naar de koelere gebieden. Fotonen bewegen zich echter veel sneller dan gasdeeltjes, wat de numerieke methode om fotonen te volgen heel duur maakt in termen van rekentijd.

Als de verhitting door de planeet en de koeling door straling met elkaar in evenwicht zijn gebeurt er niets bijzonders, maar het blijkt dat in veel gevallen de koeling ver achterblijft bij de verhitting. In gebieden van hoge dichtheid, waar de fotonen niet eenvoudig uit de hete stukken kunnen ontsnappen verandert het migratie-gedrag van kleine planeten drastisch: ze beginnen naar *buiten* te bewegen!

Het interessante is dat in een schijf de dichtheid vrijwel altijd toeneemt in de richting van de ster, zodat er in iedere schijf wel een gebied is waar kleine planeten stoppen naar binnen te bewegen. Ze kunnen zichzelf uitstekend redden: in plaats van in de ster te vallen, stoppen ze wanneer de gasdichtheid hoog genoeg is. Dit zou wel eens de oplossing kunnen zijn van het migratie probleem.

Hoofdstuk 6

Tot nu toe hebben we alleen over gas gepraat, en impliciet aangenomen dat het stof ongeveer hetzelfde doet. Vanaf Hoofdstuk 6 voegen we expliciet stof toe in de simulaties om te zien of dit echt zo is. Daarbij moeten we onderscheid maken tussen kleine en grote stofdeeltjes. Hoe groter een stofje, hoe minder deze aan het gas gekoppeld is. Terwijl minuscule pluisjes ver weg gedragen worden door een licht briesje, in er heel wat meer wind voor nodig om een auto te verplaatsen. Voor de allerkleinste deeltjes in de stofschijf (van minder dan één duizendste millimeter) geldt dat de wrijving met het gas zo groot is dat ze gewoon met het gas meebewegen. Niet zo interessant dus: als je weet waar het gas zich bevindt weet je ook waar deze kleine stofdeeltjes gebleven zijn. Grote rotsblokken daarentegen voelen weer bijna niets van het gas, tenzij ze zo groot worden dat getijden een rol gaan spelen; we hebben dan weer met migrerende planeten te maken.

Tussen deze twee extremen van groot en klein in bestaat er een populatie van stofdeeltjes van ongeveer 1 millimeter groot (zandkorrels) die nog wel sterk gekoppeld zijn aan het gas maar op de lange termijn toch interessant gedrag laten zien. Het blijkt dat middelgrote planeten, die niet zo snel een gat graven in de gasschijf, dit wel kunnen in de stofschijf. Dit komt door de aanwezige drukgradienten in het gas, die de stofdeeltjes niet direct voelen. Op Aarde waait de wind van hoge- naar lagedrukgebieden, maar over het algemeen trekken auto's en zandkorrels zich weinig aan van drukverschillen, tenzij ze meegevoerd worden door de wind. Mensen reizen meestal van lage- naar hogedrukgebieden om het mooie weer op te zoeken, precies tegen de beweging van het gas in. Zulke verschillen tussen gas en stof treden ook op rond een jonge planeet, wat leidt tot een diep stofgat waar er geen gat in het gas bestaat.

Hoofdstuk 7

In Hoofdstuk 7 bekijken we het effect van de stofgaten op de groei van gasreuzen. Uit waarnemingen blijkt dat Jupiter bijvoorbeeld relatief veel stof bevat vergeleken met de Zon. Beter gezegd: Jupiter bevat relatief meer zware elementen dan de Zon, waaruit kan worden afgeleid dat Jupiter relatief stofrijk is ten opzichte van de Zon. Dit kan enerzijds komen omdat Jupiter een stofkern heeft die langzaam erodeert, maar het is ook mogelijk dat Jupiter uit alleen gas is gevormd, waarna hij verrijkt is door het aantrekken van meer stof dan gas uit de schijf. In dit Hoofdstuk laten we zien dat stofgaten dit laatste verhinderen: het blijkt extreem moeilijk, zo niet onmogelijk te zijn een gasreus in stof te verrijken.

Hoofdstuk 8

Als laatste bekijken we planeten in schijven "in de overgang". Zoals gezegd verdampt de gasschijf langzaam, waarna slechts de planeten en wat stof overblijven. In schijven waaruit al een groot deel van het gas is verdwenen is de beweging van gas en stof heel anders dan in "gewone" schijven, waar ongeveer 100 keer meer gas is dan stof. In zulke jonge schijven voelt het gas eigenlijk weinig van het stof omdat het gas nu eenmaal veel meer massa heeft. Het is net als bij een wedstrijd touwtrekken: als de ene partij 100 keer zwaarder is dan de andere partij staat wel vast wie er gaat winnen. De zware partij, dus in dit geval het gas.

Als de andere partij bij het touwtrekken (het stof) veel zwaarder is, zal deze natuurlijk winnen. Maar als beide partijen even zwaar zijn is het niet meteen duidelijk wie de overhand krijgt. Dan komt het bij touwtrekken aan op techniek, ervaring, spierkracht, enzovoorts. Details worden erg belangrijk. Zo is het ook met gas en stof in overgangschijven, en het blijkt dat de onduidelijkheid ten aanzien van de "overwinning" leidt tot turbulente structuren in de schijf. Verder laten we zien dat het graven van een gat in deze schijven *makkelijker* gaat dan in jonge schijven, omdat het gas meegesleept wordt door het stof.

Omdat er al zo veel gas verdwenen is uit deze schijven kan de straling van de ster ver doordringen in de schijf. Deze straling botst met stofdeeltjes (niet met gasmoleculen; deze zijn veel kleiner) die daardoor naar buiten geduwd worden. Als de straling te sterk worden de stofdeeltjes weggeblazen uit het systeem, maar als dat *net* niet gebeurt kunnen interessante dichtheidsstructuren ontstaan, vergelijkbaar met wat we zien in waarnemingen van sommige van deze schijven.

TOEKOMST

En nu? De theorie van planeetvorming is met grote sprongen vooruit gegaan door de ontdekking van steeds nieuwe exoplaneten, maar er zijn nog verschillende tekortkomingen aan de modellen. Het is zeer waarschijnlijk dat het toevoegen van meer fysica nog meer inzicht geeft in de complexe relatie van planeten en schijven. Het moet echter wel stap voor stap gebeuren.

Allereerst hebben we niet gekeken naar de invloed van magneetvelden, terwijl het waarschijnlijk is dat deze wel degelijk belangrijk zijn. Magneetvelden veroorzaken turbulentie, en de interactie van een kleine planeet met deze turbulente structuren leidt tot stochastisch migratiegedrag. Specifieke geometrieën van een extern magneetveld zorgen voor extra golven dichtbij de planeet die migratie kunnen stoppen.

Dan is er de rol van de zwaartekracht van het gas. In de modellen reageert het gas op de zwaartekracht van de planeet en de ster, de planeet reageert op de zwaartekracht van het gas en de ster, maar het gas reageert niet op zijn eigen zwaartekracht. Nu is de schijf altijd zwaarder dan de planeet (want de planeet is tenslotte uit de schijf gevormd), dus het is zeker wel mogelijk dat de kracht van de schijf op zichzelf groter is dan de kracht van de planeet op de schijf. Nu is de massa van de planeet veel

meer geconcentreerd dan de massa in de schijf, maar toch is het belangrijk om de zelfgravitatie van het gas mee te nemen in de modellen.

Beide uitbreidingen van de modellen zijn duur, in de zin dat ze veel rekentijd vergen. Naast krachtige computers zijn er dus ook slimme methodes nodig om deze problemen te kraken. En dus ook slimme mensen die deze methodes kunnen bedenken. . .

Curriculum Vitae

Ik ben geboren op 30 juli 1979 te Alphen aan den Rijn, waar ik sindsdien heb gewoond. Het VWO heb ik doorlopen op het Scala College, de eerste twee jaar genaamd Albaniana, alwaar ik in 1997 mijn diploma behaalde. Geïntregeerd door vooral kosmologie begon ik in september van dat jaar aan de opleiding Sterrenkunde aan de Universiteit Leiden, en ik behaalde mijn propedeuse in de lente van 1998. Tijdens de doctoraalfase verschoof mijn interesse langzaam van kosmologie via extreem zware sterren naar planeten. Mijn klein onderzoek werd begeleid door dr. A. M. van Genderen en handelde over Wolf-Rayet sterren. Dit onderzoek leidde tot de ontdekking van een β -Cepheïde in het dubbelsysteem WR 86 en geheimzinnige lichtvariaties in WR 30a. Twee publicaties waren het gevolg van deze kennismaking met de observatieve sterrenkunde, overigens zonder zelf waarnemingen te doen. Mijn groot onderzoek naar planeten in schijven voltooide ik in de theoriegroep van prof. dr. V. Icke, onder begeleiding van dr. G. Mellema. In augustus 2002 studeerde ik cum laude in de Sterrenkunde af.

Sinds september 2002 ben ik als promovendus verbonden aan de Universiteit Leiden, in dezelfde groep en met dezelfde begeleiders als bij mijn groot onderzoek. Mijn afstudeeronderzoek, ook over planeten in schijven, vormde de basis voor de resultaten die zijn beschreven in dit proefschrift. De resultaten van dit promotieonderzoek heb ik op verschillende conferenties gepresenteerd in Nederland, Duitsland, België, Frankrijk en Zweden. Ik heb de afgelopen vier jaar met veel plezier vier keer geassisteerd bij het eerstejaarscollege "Speciale Relativiteitstheorie" van prof. dr. G. Nienhuis en één keer bij het college "Stereolutie" van prof. dr. P. T. de Zeeuw. Bovendien heb ik Siard van Boven begeleid bij zijn afstudeeronderzoek. Binnen de Sterrewacht was ik verantwoordelijk voor het organiseren van de studentencolloquia en heb ik twee jaar in de computercommissie gezeten.

Na mijn promotie zal ik voor twee jaar verbonden zijn aan het Department of Applied Mathematics and Theoretical Physics in Cambridge, UK, in de groep van Prof. dr. J. C. B. Papaloizou.

Nawoord

DE laatste bladzijde van dit proefschrift markeert het einde van mijn ruim 9 jaar in Leiden. Echter, voordat de definitieve punt onder dit werk gezet wordt, wil ik een aantal mensen bedanken die zeer belangrijk zijn geweest bij de totstandkoming ervan.

Sterrenkundig onderzoek is tegenwoordig ondenkbaar zonder de hulp van de computer. Sterker nog, numerieke astrofysica zou niet eens bestaan zonder. Daarom hier een speciaal woord van dank aan de leden van de computergroep, die er in geslaagd zijn om, naast alle "gewone" computers, een stabiele parallelle cluster te onderhouden. David, Tycho, Erik, Aart: bedankt! Ook ben ik veel dank verschuldigd aan hen die de Sterrewacht draaiende houden, het secretariaat: Kirsten, Jeanne, Elise, Liesbeth en Laura. Ik ben het Leids Kerkhoven Bosscha Fonds en het Europese netwerk "The Origin of Planetary Systems" zeer erkentelijk voor hun financiële ondersteuning.

De theoriegroep is misschien wel de leukste onderzoeksgroep van de Sterrewacht. Niet een gezamenlijk onderwerp vormt de binding, maar de nieuwsgierigheid om dingen te begrijpen. Van reïonisatie, via planetaire nevels, tot planeten; van stralingstransport, via N-deeltjes tot hydrodynamica. Deze verscheidenheid aan onderwerpen leidt tot interessante discussies en levendige bijeenkomsten. Erik-Jan, Inti en Jelle: het was een eer om samen met jullie het theoretisch promotietraject te doorlopen. Peter, I hope I have convinced you that planets are more interesting than stars :). Ook de wisselende groep van studenten die in de groep actief waren heeft een positieve bijdrage geleverd, aan de sfeer en aan het onderzoek. Franco, Huib, Jan-Pieter, Nathan, Tim en Paul: bedankt. Siard, het was fijn samenwerken. Het resultaat mag er zijn.

Promoveren doe je alleen. Maar met hulp. Het is fijn werken in een omgeving die zo open is als de Sterrewacht. Rowin, Dominic, Remco: bedankt voor de gezellige koffiepauzes en lunches. Stijn: ik heb nog nooit zo'n fijne dubbelganger gehad! Ik heb tijdens mijn promotie met veel plezier een kamer gedeeld met Michiel en Anne-Marie.

Naast werk is familie erg belangrijk. Soms zie je je familie op het werk, maar dat is niet erg. In ieder geval duurt het nog minstens vier jaar voor de Sterrewacht van de familie Paardekooper af is! Mijn ouders hebben mij altijd gesteund en zijn onmisbaar geweest in het ontwikkelen van een brede belangstelling en het doorzettingsvermogen wat nodig is voor het voltooien van een proefschrift. Ook mijn schoonfamilie, die al snel als "echte" familie voelde, ben ik veel dank verschuldigd.

Annemiek, zonder jou zou promoveren niet half zo leuk geweest zijn.

